Wave Propagation and Source Localization in Random and Refracting Media

by

David J. Geroski

A dissertation submitted in partial fulfillment
of the requirements for the degree of
Doctor of Philosophy
(Applied Physics)
in the University of Michigan
2021

Doctoral Committee:

Professor David R. Dowling, Co-Chair
Professor Kamal Sarabandi, Co-Chair
Assistant Professor Bogdan-Ioan Popa
Professor Leung Tsang
Professor Fawwaz T. Ulaby
Dr. Jacquelyn A. Vitaz

David J. Geroski
geroskdj@umich.edu
ORCID iD: 0000-0002-4559-2287

DEDICATION

To you, the reader.

ACKNOWLEDGMENTS

No list of the people who have contributed to this thesis would be complete without an acknowledgement of my two advisers, Professors David Dowling and Kamal Sarabandi. Each of them has served as a constant source of guidance and encouragement for the last five years to support my growth as a scientist and as a person.

Further, I would like to acknowledge the roles played, both inside of the classroom and on my doctoral committee, of Professors Bogdan Popa, Leung Tsang, and Fawwaz Ulaby, as well as the intellectual and professional mentorship that I have received from Dr. Jacquelyn Vitaz. I appreciate the willingness of each of you to serve on my doctoral committee, and the valuable feedback and mentorship that you have each provided.

Professionally, I have greatly benefited from collaborations with Dr. Matthew Dzieciuch, who has shared a significant amount of the data that is processed in this thesis and for his professional insights into the oceanographic community, and with Drs. Adib Nashishibi and Leland Pierce, for their combined dedication to both the intellectual and personal development of the students of the Radiation Laboratory.

Very little of this thesis would be possible without the financial support of

the Raytheon Company given through the Advanced Studies Scholarship Program over the last several years, as well as the financial support of the Applied Physics Department at the University of Michigan and the Office of Naval Research.

Maybe the clearest lesson that I have learned in graduate school is the extent to which science is a group effort. This thesis would certainly not exist without the input from the dozens of students around me, from those who were required to observe my laboratory skills with a straight face, to those who made life in- and outside of the office a little more fun.

Lastly, I think it is important to acknowledge the role that my family has played in this thesis. Most particularly, my mother, Barbara, my father, Andrew, and my sister, Kaitlyn. Thank you for all of the help over the last many years.

TABLE OF CONTENTS

LIST OF FIGURES

LIST OF TABLES

ABSTRACT

This thesis focuses on understanding the way that acoustic and electromagnetic waves propagate through an inhomogeneous or turbulent environment, and analyzes the effect that this uncertainty has on signal processing algorithms. These methods are applied to determining the effectiveness of matched-field style source localization algorithms in uncertain ocean environments, and to analyzing the effect that random media composed of electrically large scatterers has on propagating waves.

The first half of this dissertation introduces the frequency-difference autoproduct, a surrogate field quantity, and applies this quantity to passive acoustic remote sensing in waveguiding ocean environments. The frequency-difference autoproduct, a quadratic product of frequency-domain complex measured field values, is demonstrated to retain phase stability in the face of significant environmental uncertainty even when the related pressure field's phase is as unstable as noise. This result demonstrates that a measured autoproduct (at difference frequencies less than 5 Hz) that is associated with a pressure field (measured in the hundreds of Hz) and which has propagated hundreds of kilometers in a deep ocean sound channel can be consistently cross-correlated with a calculated autoproduct. This cross-correlation is shown to give a cross-correlation coefficient that is more than 10 dB greater than the equivalent cross-correlation coefficient of the measured pressure field, demonstrating that the autoproduct is a stable alternative to the pressure field for array signal processing algorithms. The next major result demonstrates that the frequency-difference autoproduct can be used to passively localize remote unknown sound sources that broadcast sound hundreds of kilometers to a measuring device at hun-

dreds of Hz frequencies. Because of the high frequency content of the measured pressure field, an equivalent conventional localization result is not possible using frequency-domain methods. These two primary contributions, recovery of frequency-domain phase stability and robust source localization, represent unique contributions to existing signal processing techniques.

The second half of this thesis focuses on understanding electromagnetic wave propagation in a random medium composed of metallic scatterers placed within a background medium. This thesis focuses on developing new methods to compute the extinction and phase matrices, quantities related to Radiative Transfer theory, of a random medium composed of electrically large, interacting scatterers. A new method is proposed, based on using Monte Carlo simulation and full-wave computational electromagnetics methods simultaneously, to calculate the extinction coefficient and phase function of such a random medium. Another major result of this thesis demonstrates that the coherent portion of the field scattered by a configuration of the random medium is equivalent to the field scattered by a homogeneous dielectric that occupies the same volume as the configuration. This thesis also demonstrates that the incoherent portion of the field scattered by a configuration of the random medium, related to the phase function of the medium, can be calculated using buffer zone averaging. These methods are applied to model field propagation in a random medium, and propose an extension of single scattering theory that can be used to understand mean field propagation in relatively dense (tens of particles per cubic wavelength) random media composed of electrically large (up to 3 wavelengths long) conductors and incoherent field propagation in relatively dense (up to 5 particles per cubic wavelength) media composed of electrically large (up to two wavelengths) conductors. These results represent an important contribution to the field of incoherent, polarimetric remote sensing of the environment.

CHAPTER 1

Overview

This thesis is written at the intersection of several disciplines, most notably acoustic and electromagnetic wave propagation in a random medium and nonlinear signal processing for remote sensing. This chapter serves to outline these fields individually, and to give an overview of the objectives of the thesis.

1.1 Remote Sensing

Remote sensing can generally be described as determining information from a distance in an uncontrolled environment [see: Ulaby, F.T. & Long, D.G. (2014), Urick (1976)]. This thesis limits its analysis to determining information about distant sources, such as a source location, using measurements of field quantities that are governed by the wave equation. The field quantities analyzed within this thesis are electromagnetic (light) fields, governed by Maxwell's Equations [Jackson, J.D. (1999)], and acoustic (sound) fields [Pierce, A.D. (1994)], a linear approximation to the Navier-Stokes equations. Remote sensing systems that work by analyzing electromagnetic waves are generally referred to as "Radio Detection and Ranging" (RADAR) systems, and systems that work by analyzing acoustic waves are, analogously, referred to as "Sound Navigation and Ranging" (SONAR) systems. Examples of each of these systems are used in many places and each occupies certain niches for studying the world. In places where both radar and sonar systems can operate, radars tend to be preferred, because of the relatively larger amount of available bandwidth

and the increased precision that is available to high-frequency electromagnetic waves. Radar systems are also exclusively deployed for extra-planetary exploration because acoustic waves cannot propagate in a vacuum. Sonar systems are preferentially deployed for ocean exploration, because electromagnetic waves cannot propagate over long distances in the water. This thesis explores both systems, radar systems in free-space propagation environments, and sonar systems in ocean environments.

Remote sensing systems are also typically characterized as being either "active" or "passive" remote sensing systems. Typically, active remote sensing systems are defined as systems that transmit a source signal and measure the response of the local environment to this source signal. This response can then be used to determine information about the environment. Passive remote sensing systems are typically defined as systems that only measure signals transmitted from sources of opportunity. Passive electromagnetic remote sensing systems are usually referred to as radiometers. One final type of remote sensing system, "cooperative" remote sensing, can be defined [Wu *et al.* (2019)]. Cooperative remote sensing systems are similar to passive remote sensing in that a receiver and a transmitter are far from one another. However, cooperative remote sensing systems typically assume significant knowledge about the transmitter that is not usually known in passive remote sensing systems. One example of a cooperative remote sensing system is the Global Positioning System (GPS), that can be used to locate a receiver on Earth. This thesis primarily focuses on developing the capability of passive remote sensing systems.

One major theme of this thesis is developing signal processing algorithms for the operation of remote sensing systems. Here, signal processing is roughly defined as the process of using a measurement to make an inference about the local environment. This thesis focuses on inferring information about a particular source (or target). In this case, signal processing can be described as four tasks [Skolnik, M.I. (1980), Dowling & Sabra (2015)]: Detection, or determining if a source is measured by a system, Classification, or identifying the likely source (biological, industrial, etc.), Localization, or identifying the spatial location of the source, and Tracking, or determining the time-evolution of the location of the source. This thesis exclusively examines the localization

task. Physics-based localization algorithms, such as beamforming [Jensen, F.B. *et al.* (2011)] and Matched Field Processing, are analyzed in this thesis. It is worth noting here that the formulation of these techniques is almost identical to the formulation of Synthetic Aperture Radar (SAR) [Ulaby, F.T. & Long, D.G. (2014)] in electromagnetic remote sensing, that is typically used for imaging in active remote sensing systems. The extension of these passive localization algorithms to the active imaging problem is not undertaken in this thesis.

The other major theme of this thesis is predicting wave propagation in a random medium. Predicting wave propagation in a medium relates to physics-based signal processing in that it provides the physics that can be used to evaluate the utility of a signal processing algorithm. Propagation in two types of random media are explored in this thesis [Ulaby, F.T. & Long, D.G. (2014)]: dynamic or scintillating random media, wherein multiple measurements are taken that are governed by the same statistics slightly differ from one another, and scattering random media, where a wave propagating through a random medium is impeded by many discrete objects in the medium. These two random media are intimately related to one another, the distinction that is drawn between them arises in the way that they are modeled (more precisely described in Section 1.2). Scintillating random media are defined herein by assuming that all variations in the local speed of propagation are smooth, and generally do not scatter incident energy in directions other than forward. Scattering random media are defined herein by assuming that variations are discrete, represented by distinct objects, and energy can be scattered away from the direction of wave propagation.

1.2 The Acoustic and Electromagnetic Wave Equation

Both acoustic and electromagnetic fields are governed physically by the wave equation [Jackson, J.D. (1999), Pierce, A.D. (1994)] in a wide variety of media. The wave equation, also referred to as D'Alembert's equation, is a partial differential equation that relates spatiotemporal propagation of a field quantity where the field quantities are expected to propagate over long distances and time-scales without dissipating. The simplest form of the wave equation is given in Eq. (1).

$$\nabla^2 W(\vec{x}, t) + \frac{1}{c^2}\frac{\partial^2 W(\vec{x}, t)}{\partial t^2} = S(\vec{x}, t) \tag{1.1}$$

Here, $\nabla^2 = \partial^2/\partial x^2 + \partial^2/\partial y^2 + \partial^2/\partial z^2$ is the (spatial) Laplacian operator, W is a general (scalar) field quantity at spatial location $\vec{x}$ and time t, c is the local speed of wave propagation, and S is the source function of the waves, generally assumed to be far from a measuring device in remote sensing. In the acoustic wave equation, W is a local (time-varying) pressure field, denoted p. The speed of sound in acoustics, c is well known in a variety of media. It is observed to be approximately 343 m/s in air and approximately 1500 m/s in water. The electromagnetic wave equation is a vector quantity. Provided that an electromagnetic field is propagating in a linear, isotropic medium, W typically represents each Cartesian spatial component of the electric vector field. Here, c is the speed of light, known to be 299792458 m/s, and S is more commonly denoted by the free current density $\vec{J}$.

This thesis analyzes the wave equation in the frequency, rather than the time domain. This is accomplished by taking the Fourier Transform of all quantities present in the wave equation. This analysis yields the Helmholtz Equation, given in Eq. (2).

$$\nabla^2 W(\vec{x}, \omega) + \frac{\omega^2}{c(\vec{x}, \omega)^2} W(\vec{x}, \omega) = S(\vec{x}, \omega) \tag{1.2}$$

Here, the variable ω represents the angular frequency of the field quantity, that all field quantities depend on. Further, the speed of wave propagation is here postulated explicitly to vary over space and time. In an infinitely large medium with no sources and a constant wave speed, the Helmholtz Equation is solved by a plane wave, as is given in Eq. (3).

$$W(\vec{x}, t) = W_0 exp\Big(i(\vec{k} \circ \vec{x} \pm \omega t)\Big) \tag{1.3}$$

The plane wave has a magnitude W_0, that has vector form in electromagnetics, and a phase defined by the argument of the exponential function. The plane wave is so named because it admits surfaces of constant phase defined by the argument. Here, $\vec{k}$ is the wavenumber of the field. The

magnitude of the wavenumber $\left|\vec{k}\right| = k_0$ defines the spatial frequency of the field, and the direction of the wavenumber $\hat{k} = \vec{k}/|\vec{k}|$ defines the direction of field propagation. This propagation direction is normal to the planar surfaces of constant phase.

The wave equation is a linear partial differential equation. Generally, this means [Strauss, W.A. (2008)] that the interrogated field quantity, W, is only found raised to the first power. Also, it means that separate field quantities, such as the electric $\vec{E}$ and magnetic $\vec{H}$ fields, are not multiplied against one another. Nonlinear analogues to the wave equation, termed integrable partial differential equations, are commonly analyzed [Hirota, R. (2004)] and also admit wave solutions, referred to as solitons. Nonlinear equations that aren't integrable, like the Navier-Stokes equations, are generally described as chaotic partial differential equations. The most important difference between linear and nonlinear partial differential equations is the principle of superposition, which states that two solutions to a linear partial differential equation can be added together and will exactly solve the same equation. Soliton solutions in integrable partial differential equations satisfy this condition only approximately, and nonlinear equations are always found to disobey the principle of superposition. Notably, this thesis does not analyze nonlinear field quantities, only nonlinear signal processing algorithms. Here, the distinction between linear and nonlinear signal processing algorithms is similarly defined by the principle of superposition.

1.3 Scintillating and Scattering Random Media

This thesis identifies two types of random media: scintillating and scattering random media. In principle, these media do not differ from one another. However, the phenomenological methods used to understand wave propagation in these media do differ from one another. Here, scintillating media may be better described as time-varying refracting media. Refracting media, exactly like scattering media, are composed of discrete scatterers placed in a background (or 'host') medium. However, in refracting media, scattering from all discrete scatterers can be understood as occurring in the Rayleigh regime [Jackson, J.D. (1999), Pierce, A.D. (1994)]. This occurs when all scatterers

are much smaller than the wavelength of propagating light. While propagation in such a medium can be understood using scattering simulations, this computationally expensive step is not typically undertaken because the theory governing propagation is seen to have strong predictive power. In this case, the propagation losses due to scattering are typically seen to be much smaller than the normal field spreading loss and the field quantity is understood to be propagating in an effective medium with a wave speed that differs from a nominal value. A medium is then said to be refracting when this wave speed varies gently in space and the field propagation can be understood locally using Snell's law of refraction. For the purpose of this thesis, a scintillating medium is identified as a time-varying refracting medium. Field propagation in a scattering medium, then, differs from this in that scatterers in the medium are not in the Rayleigh regime. Therefore, propagation in the medium is investigated using simulations of scattered fields.

Physics-based signal processing algorithms, like beamforming [Jensen, F.B. *et al.* (2011)], tend to depend on understanding both the relative magnitude and phase of a measured field quantity in the frequency domain. The measured magnitude and phase of field quantities that have propagated through a scintillating random medium are found to vary when multiple measurements of this quantity are taken over time. These variances cause physics-based signal processing algorithms to lack robustness when the field quantity in question loses stability. This loss of field stability is generally found to occur more often at higher frequencies. Signal processing algorithms explored in this thesis, specifically methods that interrogate the frequency-difference autoproduct of a field quantity, attempt to mitigate this loss of stability by reducing the frequency at which this processing is undertaken. These methods have been found to successfully increase the robustness of physics-based signal processing algorithms in scintillating media like the ocean [Worthmann *et al.* (2015)]. Scintillations in the ocean come from spatial and temporal variances in the local salinity, temperature, and pressure of ocean water, and these variations are generally understood to change the point-to-point propagation time of an acoustic field [Colosi *et al.* (2019)]. A physics-based signal processing algorithm that interrogates a particular field frequency is expected to fail when this change in the point-to-point propagation time is large compared to the temporal frequency of

the field. This assertion will be further assessed in Chapters 2-5 of this thesis.

Wave propagation in a scattering random medium is often found to mimic the same effects as wave propagation in a scintillating medium [Ulaby, F.T. & Long, D.G. (2014)]. This similarity makes physical sense, as these effects are understood to come from the same source (scattering from local fluctuations in a medium) at different (frequency) regimes. However, wave propagation in scattering random media is not well understood when the scatterers occupying a medium are electrically large and interact with one another. Further, when scatterers in a medium are not in the Rayleigh regime, meaning that they are not small compared to a wavelength of propagating light, losses due to scattering increase significantly. These losses can be used as a source for investigating the medium itself, but they can also cause localization algorithms to fail. This thesis investigates two problems associated with wave propagation in a scattering medium: it proposes a new method for predicting wave propagation in a random medium based on Monte Carlo simulation [Sarabandi & Siqueira (1997)] used in conjunction with computational scattering methods, and it assesses the effect that propagation in a scattering medium has on localization algorithms like beamforming.

1.4 Computational Acoustics and Electromagnetics Methods

Predictions made in this thesis draw on existing propagation and scattering codes to predict and assess the effects that propagation in random media will have on a field quantity, and to implement the Monte Carlo and signal processing methods outlined within it. While predictions made in Chapter 9 do utilize a homegrown code, all other results are obtained using freely- or commercially-available software packages to make all predictions. The methods that these software packages are based on are reviewed here.

1.4.1 Predicting Propagation in a Refracting Random Medium

Scintillating media in this thesis will be modeled as refracting media, with scintillation applied local to a receiver by either time-front or receiver range variation, as was observed in [Worcester

et al. (2013)]. The point-to-point response, or Green's function, of acoustic media can be predicted using several computational techniques. This thesis primarily considers acoustic refracting environments that are commonly observed in deep ocean, waveguiding environments. Such environments require simultaneous consideration of multiple physical phenomena [Jensen, F.B. *et al.* (2011)], including acoustic reflection from barriers, acoustic refraction, and diffraction. A general analytic method for determining the Green's function for such a medium does not exist. Because of this, numerical methods are commonly used to compute the Green's function for these media. This thesis makes use of the ONR Ocean Acoustics Toolbox [Heat (2021)] to predict the acoustic response of an ocean waveguide. Analogous methods for each numerical method included in the Ocean Acoustics Toolbox exist that can be used to predict electromagnetic propagation.

The most commonly used methods for predicting a Green's function in a refracting environment [Jensen, F.B. *et al.* (2011), Porter (1992), Porter & Bucker (1987)] are ray methods, mode-sum methods, and parabolic equation methods. The Ocean Acoustics Toolbox also contains a wavenumber integration technique. This author's work with the wavenumber integration techniques is limited and omitted from this thesis. Of the three more popular techniques, all results contained in this thesis are predicted using modal-sum methods. Similar results are available using ray methods [Geroski & Dowling (2019)] and parabolic equation methods, but are omitted from this thesis for the sake of brevity. Each of these three methods offers advantages and disadvantages. Ray-path predictions [Porter & Bucker (1987)] are made in the time-domain and offer incredible predictive power for wideband signals that have propagated over long distances. Ray-path predictions are also able to handle range-dependence. However, ray-path predictions fail to account for diffraction, leading to the existence of shadow zones where no sound is expected to propagate. In general, ray-path predictions apply best at high frequencies. Parabolic equation methods offer powerful predictions at all but the lowest frequencies and are also able to account for range dependence. However, predictions cannot be readily extended over a wide bandwidth of propagation. Mode codes [Porter (1992)] can be used to predict field propagation at any frequency. However, mode codes are found to have incredible computational complexity when making near-field pre-

dictions, or when working in media with range variation. The work contained herein finds that modal predictions are more computationally efficient at predicted frequencies, and that the range dependence does not need to be accounted for to make accurate predictions.

1.4.2 Predicting Propagation in a Scattering Random Medium

Scattering predictions in this thesis will be made using full-wave analysis software [Jin, J. (2010)] that can account for fully interacting systems. These methods tend to focus on relatively small spatial regions – at most tens of cubic wavelengths – in which a background medium can be thought of as constant. Discrete scatterers are placed into this background medium. Full-wave analysis of propagation and scattering in this medium starts by discretizing the medium itself. This discretization is primarily undertaken following two paths: Finite Differencing and Integral Equation Methods. Finite Differencing Methods, including Finite Differencing in the Time Domain (FDTD) and the Finite Element Method (FEM), work by discretizing all of the space in a scattering environment. Integral Equation Methods, including the Method of Moments (MoM), instead focus only on discretizing the scatterers themselves. Finite Differencing methods are generally able to predict scattering over larger regions and with more heterogeneous scatterers placed within them. However, this thesis focuses on computing the fields scattered by perfectly conducting bodies. For these types of problems, the Method of Moments is better able to predict scattering. Therefore, scattering predictions in this thesis are made entirely using the Method of Moments. While Finite Differencing methods would likely make equivalent predictions, this step is considered out of scope of the work contained herein.

The Method of Moments, first introduced in [Harrington (1967)] and well described in [Jin, J. (2010)], directly solves a scattering problem using the Green's function approach. This method works by using the Green's function for a given linear differential operator, in this case the Helmholtz operator, and a set of boundary conditions to solve for the interaction between different small sub-domains within a larger domain that represents all scatterers in the medium. The interactions are computed using the equivalence principle to represent each subdomain as a local current source

of variable magnitude and phase. The interactions between this basis function, that is the current induced on all basis functions by a current placed on any of them, are computed using the Green's function of the medium and are represented as an interactions or impedance matrix. Given this interaction matrix and an incident field, the scattered field can be computed by inverting the impedance matrix and multiplying it against the incident field. This thesis investigates scattering in two- and three-dimensional media. For two-dimensional media, a homegrown scattering code is implemented in MATLAB. For analysis of three-dimensional media, a commercial software package [Altair Engineering (2014)] is used.

1.5 Thesis Objectives

The overarching goal of this thesis is to understand and expand the limitations of remote sensing systems that are operating in random media. Understanding the limitations of remote sensing systems is undertaken by attempting to expand the theory of wave propagation in random media to account for inter-particle interaction in random media composed of discrete scatterers using a combination of Monte Carlo simulation and existing computational methods. Expanding the limitations of remote sensing systems is undertaken via the proposal and application of a surrogate field quantity, the autoproduct, to problems in both acoustic and electromagnetic wave propagation and remote sensing in free space and in an ocean waveguide.

The first major objective of this thesis, that uses Monte Carlo simulation in conjunction with numerical methods to better understand wave propagation in a scattering random medium, focuses on developing Radiative Transfer theory. Radiative Transfer fundamentally applies to (passive) polarimetric remote sensing in radar, and is based on solving for the intensity of a field quantity propagating through a random medium using the conservation of energy. At the outset of this study, in 2016, this technique had been used to numerically validate the predictions offered by mixing formulae in two-dimensional random media propagation and to experimentally validate the predictions offered by the same methods in three-dimensional random media propagation. Ini-

tially, the goal of this research was to apply this method to expand the theory of Radiative Transfer to account for interactions between electrically large particles. This particular goal, and the prior work in this area, primarily focused on solving for the extinction matrix of Radiative Transfer (see: Chapter 6 of this thesis) that is related to mean field propagation. The success of this method for predicting mean field propagation in a random medium composed of electrically large, interacting scatterers represents an expansion of Radiative Transfer theory. This study was then expanded to attempt to expand Radiative Transfer theory to solve for the phase matrix of the random medium. Previously, this step was not undertaken because of the presence of significant numerical noise arising from the assumptions used to implement this method that prevents convergence of an estimated phase function. Therefore, this question had been left open for some time. This thesis proposes a simple method, referred to herein as "buffer zone averaging" that removes this numerical noise and leads to the convergence of the phase function. As of the writing of this thesis, the exact interpretation of the buffer zone averaging concept remains an open question. But, this is method is shown to offer repeatable predictions from a numerical standpoint. One final goal of this thesis is undertaken to use the intuition provided by Monte Carlo simulation to design a random medium to have a particular, in this case a narrowband, response. These methods represent an interesting development in Radiative Transfer theory, and a method for expanding extant models, both those derived from theory and from measured data, of random media propagation in polarimetric remote sensing.

The second major objective of this thesis, that defines and explores the utility of the frequency-difference autoproduct in remote sensing, was undertaken primarily to increase the robustness of matched-field style source localization algorithms to the environmental (or channel) mismatch problem in acoustic remote sensing of the ocean. This study began in 2016 by attempting to expand the prior autoproduct-processing source localization algorithm, termed Frequency Difference Matched Field Processing, to localize sources transmitting over long ranges and at high frequencies in the deep ocean. This algorithm would ultimately prove to be ill-suited to solving this problem and would require to proposal and development of several new source localization algorithms that

are suited to working over long distances in time-varying, refracting, waveguiding environments. These new algorithms are termed ”autoproduct matching” methods, in contrast to ”field matching” methods that existed prior to this body of work. These methods ultimately proved to offer solutions to the (long-range, high-frequency) source localization problem that are both accurate and consistent. The success seen in this method led to further investigation of the problem of cross-terms in autoproduct-processing methods, which arise from the nonlinear (quadratic) product of field solutions used to calculate the autoproduct from measured data. These cross-terms, that arise in both the signal and from the presence of an interferer, are generally thought to degrade the performance of autoproduct-processing algorithms. This thesis rigorously analyzes the form of both types of cross-term, proposes several (related) methods for removing cross-terms, and quantifies the effect that cross-terms have on autoproduct-processing algorithms and the effectiveness of the methods proposed to remove them. One final goal of this study was to define the frequency-difference autoproduct as a surrogate to a polarized field quantity and to use such a definition to analyze the utility of autoproduct processing in remote sensing systems that operate outside of the ocean. Each of these studies represents a development of the capability of passive remote sensing systems to understand their environment and to determine the location of a source.

1.6 Thesis Overview

Overall, the work contained in this thesis reviews two major contributions to remote sensing theory: the theory of wave propagation in scattering random media, and the contribution that frequency-differencing can make to solving problems in source localization in dynamic random media. The first of these contributions is made to extend the theory of Radiative Transfer to account for incoherent wave propagation in a scattering random medium that is composed of electrically large, interacting scatterers using Monte Carlo simulation and the Method of Moments in conjunction with one another. Frequency-differencing methods are used to extend existing nonlinear signal processing methods in beamforming and source localization. The utility of frequency-differencing

methods is assessed in both scintillating and scattering random media. This chapter serves as an introduction to the content of this thesis, outlining the background information that is relevant to understanding the content of the thesis itself. Chapters 2 and 6 outline the theory of the frequency-difference autoproduct and Radiative Transfer. Chapters 3-5 and 7-9 outline original research contributions made in this thesis. To better understand each content chapter, the overview chapter should be read first. For Chapters 3-5, and Chapter 9, this means reading Chapter 2, and for Chapters 7 and 8, this means reading Chapter 6. Chapter 10 summarizes the overall conclusions of this work and recommends follow-on efforts that would extend the utility of these methods.

Chapter 3 first analyzes the propagation of a bandwidth-averaged frequency-difference autoproduct in a scintillating, deep-ocean environment. This chapter serves to demonstrate the utility of the frequency-difference autoproduct in scintillating random media, and shows that frequency-differencing can be used to recover coherent field stability in both simulated and measured pressure fields. The primary contribution of this chapter has been published in the Journal of the Acoustical Society of America in [Geroski *et al.* (2021b)].

Chapter 4 further analyzes the frequency-difference autoproduct, focusing on the existence and form of cross-terms that are induced in the autoproduct as an artifact of the nonlinear processing used to form the autoproduct. These cross-terms, both those endemic to a signal [Worthmann *et al.* (2015)] and those that arise from the presence of a loud interferer [Worthmann *et al.* (2017)], have been suggested previously to negatively impact the performance of autoproduct-processing algorithms. This chapter analyzes the form of these cross-terms, demonstrates the difficulty that exists in coherently subtracting them from an autoproduct Cross Spectral Density Matrix, and proposes six methods for removing cross-terms from a measurement. The primary contribution of this chapter has been published in the Journal of the Acoustical Society of America in [Geroski & Worthmann (2021)].

Chapter 5 evaluates the performance of frequency-differencing methods in localizing distant sources that are transmitting in the deep ocean. It goes farther, evaluating the capacity of frequency-differencing methods to localize sources in the presence of a loud interfering (noise-like) source.

This chapter also evaluates the effect that cross-terms have on the autoproduct in the context of the source localization algorithm. Generally, this chapter finds that frequency-differencing can be used to overcome significant environmental mismatch, related to wave scintillation, to successfully localize sources transmitting at high frequencies and over long ranges. This chapter also finds that cross-terms generally have a minimal, although a measurable, effect on the performance of localization algorithms. The primary technical contribution of this chapter can be found in the Journal of the Acoustical Society of America in [Geroski & Dowling (2019), Geroski & Dowling (2021), Geroski & Worthmann (2021)]. The final contribution of this chapter is expected to be submitted to the same journal later this year as [Geroski *et al.* (2021a)].

Chapter 7 is the first chapter that analyzes electromagnetic wave propagation in a three-dimensional random medium populated with many discrete scatterers. This chapter focuses on using Monte Carlo simulation in conjunction with the Method of Moments to predict the coherent and incoherent part of a field scattered by such a random medium. These objects are expected to offer insight into expanding Radiative Transfer theory to account for interactions between electrically large scatterers. Here, the coherent portion of the scattered field is expected to represent the existence of an effective medium in which the field propagates on average. This effective medium is calculated using inverse scattering, and the solution to this inverse scattering problem is shown to be consistent in many results. The incoherent portion of the scattered field is expected to represent the phase matrix of the medium that governs incoherent emission of field power that is absorbed by the random medium. The incoherent scattering coefficient of the medium, linearly related to the phase matrix, is shown to be computable using Monte Carlo simulation in a variety of problems. Each of these contributions is outlined in the IEEE Transactions on Antennas and Propagation in [Geroski & Sarbandi (2020), Geroski & Sarabandi (2020)].

Chapter 8 serves to apply the predictions made in Chapter 7 of this thesis. Here, Monte Carlo simulation is used in conjunction with the Method of Moments to predict the coherent and incoherent portion of the field scattered by media composed of many types of scatterers. First, the intuition provided by single scattering is used to design a random medium that has a desirable re-

sponse. This design is followed by predicting both the effective permittivity and the phase function of a chaff-like random medium. This prediction is made for a wide variety of particle lengths, occupying densities, and curvatures and forms the basis of a macromodel that governs propagation in chaff. The contributions of this chapter are also primarily published in IEEE Transactions on Antennas and Propagation in [Geroski & Sarbandi (2020), Geroski & Sarabandi (2020)]. Understanding the methods that are implemented in this chapter to derive models is best undertaken by first reading Chapter 7.

Chapter 9 analyzes the performance of frequency-difference beamforming using electromagnetic waves in a two-dimensional scattering random medium. This chapter serves to extend previous studies in scattering random media that used acoustic waves [Douglass & Dowling (2019), Worthmann & Dowling (2020b)]. This chapter represents the first study of its kind that directly analyzes the performance of autoproduct-processing algorithms using polarized waves. This chapter defines the autoproduct for polarized waves as a dyadic product of measurements. The performance of this algorithm is interrogated using the Method of Moments, and it is found to perform similar to or better than conventional in-band processing. This work has not yet been published outside of this thesis.

CHAPTER 2

Definition of the Autoproduct Formed from a Scalar Field

2.1 Introduction

Autoproduct processing, encompassing both frequency-differencing and frequency-summing techniques, was originally proposed as a concept [Abadi *et al.* (2011)] that fits entirely into the field of signal processing for improving either the robustness (using frequency-differencing) or precision (using frequency-summing) of extant frequency-domain signal processing routines like beamforming. Since its proposal, the autoproduct has been extended from being a signal processing technique to being defined as a field quantity [Worthmann & Dowling (2017)] in its own right that has applications in studying oceanography [Geroski *et al.* (2021b)]. This chapter lays out the theory that has been developed to understand the exact form of the autoproduct, particularly when it comes to the frequency-difference autoproduct. This theory includes the idea behind the frequency-shifting that occurs when using autoproduct processing, as well as the emergence of field corrections. Computational methods for calculating autoproducts are discussed, undesirable side effects of autoproduct processing, termed 'cross-terms' are derived and discussed. The form of cross-terms is investigated and methods for cancelling these is discussed. Each aspect of this chapter will be quantitatively investigated and applied to real world signal processing problems like cross correlation and passive source localization in the following chapters, but this chapter stands as a full description of the current state of the art for autoproduct processing methods using scalar fields.

The frequency-difference autoproduct was first proposed in the context of sparse array blind deconvolution [Abadi *et al.* (2013), Abadi *et al.* (2012)], beamforming and source localization [Abadi *et al.* (2011)] in the near field of an array and was found to effectively downshift the frequency content of a measured field. During this time, the frequency-sum autoproduct was also investigated [Abadi *et al.* (2013), Abadi *et al.* (2015)] for the purpose of improving precision of signal processing algorithms. While the frequency-sum autoproduct is capable of effectively upshifting the frequency content of a measured field and allow for more precise predictions to be made than traditionally thought possible, this improvement in precision tends to come at the expense of robustness and it is therefore not quantitatively investigated in this thesis. The improved robustness that frequency-difference beamforming offers was further investigated in other environments [Douglass *et al.* (2017), Lipa *et al.* (2018)], is found to mitigate negative effects associated with strong random scattering [Douglass & Dowling (2019)], to be useful in treating the acoustic trip wire problem, and to extend array coherence lengths in the ocean. Given this improved robustness, the frequency-difference autoproduct was explored as a vehicle for improving the robustness of matched field processing [Worthmann *et al.* (2015), Worthmann *et al.* (2017)]. Given the success seen here, the autoproduct was abstracted from a signal processing technique to an independent field quantity [Worthmann & Dowling (2017)] and the effect that complex wave propagation phenomena including diffraction [Worthmann & Dowling (2020a)], multipath, caustics [Worthmann & Dowling (2020b)], and reflection at a barrier have on the frequency-difference autoproduct were investigated. These predictions were confirmed using data measured in a controlled environment [Lipa *et al.* (2018)], as well as in an oceanographic study on an (uncontrolled) deep ocean environment [Geroski *et al.* (2021b)] and in passive source localization [Geroski & Dowling (2019), Geroski & Dowling (2021), Geroski & Worthmann (2021)] contexts. In all of these studies, the frequency-difference autoproduct is found to offer improved robustness compared to conventional signal processing methods like matched field processing.

The idea behind the autoproduct is not unique to the studies conducted at the University of Michigan over the last decade. An earlier related concept, referred to as Δk-radar [Popstefanija

et al. (1993), Sarabandi (1997), Tatarskii & Clifford (1995)] and -sonar [Silva *et al.* (2008)] was popularized in the two decades before the autoproduct was defined. The autoproduct itself was defined independently of these studies as a natural progression from the blind deconvolution problem [Abadi *et al.* (2012)], and carries several features that are unique to its construction. This idea has also been compared to the idea of frequency interferometry, as in [Weissman (1973)], or the idea of the parametric acoustic array [Westervelt (1963)] but differs from these ideas in its fundamental construction in that it looks at the spatial coherence of its output and does not produce a low frequency sound as a part of an acoustic field.

The frequency-difference autoproduct is applied to scalar fields primarily as a new tool for use in studying acoustic pressure fields propagating in uncertain ocean sound channels. Acoustic propagation in the ocean is generally studied because long distance propagation is possible over a wide frequency band in a variety of environments [Flatte, S.M. (1979)] and is governed only by the scalar Helmholtz equation. Despite this advantage, ocean environments represent a variety of complex problems to study from a wave propagation standpoint: they represent a wide variety of refraction phenomena [Pierce, A.D. (1994), Kinsler, L.E. *et al.* (1999), Brekhovskikh, L.M. & Lysanov, Y.P. (2003)] that include, among other phenomena, the presence of caustics [Zhuravlev *et al.* (1989), Kratsov, Y.A. & Orlov, Y.I. (1999), D'Spain *et al.* (2002)], and the dynamics of the ocean lead to time-dependence of acoustic propagation [Colosi *et al.* (2013), Flatte *et al.* (1983), **?**]. This time dependence has been demonstrated to affect the spatiotemporal coherence of acoustic fields [Wan *et al.* (2009), Morgan & Smith (1990), Lunkov & Petnikov (2014), Duda *et al.* (2012), Cox (1973)] that leads to robustness issues in any array signal processing problems that rely on this coherence [Greene & Moller (1962)]. Because of this loss of coherence in the frequency domain, acoustic fields are commonly studied in the time-domain [Munk, W., Worcester, P. & Wunsch, C. (1995)] using acoustic tomography as acoustic propagation is found to be more stable in the time domain than it is in the frequency domain. Frequency-differencing methods have proven to be an alternative approach to stabilizing frequency domain acoustic field information, because these methods are applied as a post-processing step and therefore can be used to provide information

that is supplementary to tomographic methods provided that the effect that all physical phenomena seen in wave propagation in the ocean have on autoproducts are well understood.

This chapter discusses matrix-based noise rejection algorithms and suggests their use to isolate the parts of the frequency-difference autoproduct that are spatiotemporally coherent from incoherent parts. These algorithms are adapted from their use in conventional acoustic signal processing [Hald (2019)], and they generally make use of available averaging information to distinguish between parts of a signal that are coherent or incoherent on the Cross-Spectral Density Matrix (CSDM) of a field quantity. It is well known in physics-based signal processing that averaging usually needs to be employed to have a robust understanding of a measured quantity, and each of these algorithms accomplishes this in different ways. Riemannian manifolds can be used to understand the representational differences of acoustic fluctuation [Cao *et al.* (2019), Finette & Mignerey (2018)] and to stochastically estimate their effects. The Riemannian manifold approaches are not implemented here because of the computational complexity, both in data-storage requirement and in terms of raw calculation, of these algorithms in inverse-problem based source localization algorithms. Understanding of the algebraic differences between coherent and incoherent phenomena [Aravkin *et al.* (2014), Dinsenmeyer *et al.* (2018), Wright *et al.* (2009), Hald (2017)] can be used to decompose CSDM into signal- and noise-like parts. Canonical coherence over portions of the CSDM [Hald (2019)] can also be used to emphasize coherent portions of a measured CSDM over incoherent portions. Of these approaches, the linear-algebra- and coherence-based methods are implemented in this thesis. These algorithms mostly make use of repeated measurements, usually termed 'snapshots' in acoustic remote sensing, to provide the averaging that is necessary to distinguish between the coherent and incoherent portions of a measurement. In addition to being able to take advantage of snapshot averaging, frequency-differencing algorithms can make use of bandwidth averaging for implementing these methods. This means that frequency-differencing algorithms can make use of noise rejection techniques for improving their performance even when only using a single snapshot.

The remainder of this chapter is broken into four sections. Section 2.2 defines the frequency-

difference and frequency-sum autoproducts, as well as their related bandwidth averages and cross-spectral density matrices. It also covers the ways in which field phenomena affect autoproduct propagation and how these differences are addressed when implementing autoproduct processing algorithms. Section 2.3 explores the emergence of cross-terms when calculating an autoproduct, makes quantitative predictions about the form of these cross-terms in multipath environments and in the presence of interference, and distinguishes the cross-term presentation from more desirable self-terms. Section 2.4 explores how to distinguish between self- and cross-terms using noise rejection algorithms, and explains where each of these algorithms is expected to fail. Section 2.5 draws what conclusions are available from these definitions, and points an interested reader to what chapters make predictions relevant to each of the phenomena explored herein.

2.2 Definition of Autoproducts

The frequency-difference (Eq. 2.1) and frequency-sum (Eq. 2.2) autoproducts were originally defined in the context of (scalar) acoustic fields propagating in an ocean sound channel [Abadi *et al.* (2011), Abadi *et al.* (2012)] as a quadratic product of pressure fields represented in the frequency domain, measured at the same spatial location and at two different frequencies. Both autoproducts were initially postulated to also be solutions to the scalar Helmholtz equation at either the difference or the sum of the frequencies used to construct them.

$$AP_{\Delta}(\vec{r}, \Delta\omega, \omega) = P^{*}\left(\vec{r}, \omega - \frac{\Delta\omega}{2}\right) P\left(\vec{r}, \omega + \frac{\Delta\omega}{2}\right) \tag{2.1}$$

$$AP_{\Sigma}(\vec{r}, \Sigma\omega, \omega) = P\left(\vec{r}, \omega - \frac{\Delta\omega}{2}\right) P\left(\vec{r}, \omega + \frac{\Delta\omega}{2}\right) \tag{2.2}$$

Here, AP_{Δ}, AP_{Σ} are the frequency-difference and frequency-sum autoproducts at location $\vec{r}$, respectively, and are formed from pressure measured pressure fields, P, that are represented in the frequency domain. Here, P is assumed to be defined over a measured bandwidth $\Omega_L \leq \omega \leq \Omega_H$.

The defined autoproducts vary at difference or sum frequency, $\Delta\omega, \Sigma\omega$, and have center frequency ω. Thus far, the definition of the autoproduct is identical to the formulation of frequency interferometry [Weissman (1973)] and of the related concepts of Δk-radar [Sarabandi (1997)] and -sonar [Silva *et al.* (2008)]. In the context of frequency-difference and frequency-sum beamforming on relatively short arrays, where pressure fields can be locally represented as a sum of plane waves of constant amplitude over the span of the array, this postulate is sufficient for making many successful predictions [see: Douglass *et al.* (2017), Douglass & Dowling (2019)]. When this formulation was first extended to the question of source localization using a matched-field style algorithm [Worthmann *et al.* (2015)], the bandwidth-averaged autoproduct was introduced, as in Eq. (2.3), for the purpose of suppressing cross-terms that were postulated to reduce the stability of the proposed source localization algorithm, Frequency Difference Matched Field Processing.

$$\langle AP_{\Delta}(\vec{r}, \Delta\omega)\rangle_{\omega} = \frac{1}{\Omega_{BW}} \int_{\Omega_L + \frac{\Delta\omega}{2}}^{\Omega_H - \frac{\Delta\omega}{2}} d\omega \frac{AP_{\Delta}(\vec{r}, \Delta\omega, \omega)}{S^*\left(\omega - \frac{\Delta\omega}{2}\right) S\left(\omega + \frac{\Delta\omega}{2}\right)} \tag{2.3}$$

Here, $\langle AP_{\Delta}(\vec{r}, \Delta\omega)\rangle$ is the bandwidth-averaged frequency-difference autoproduct. It is formed by averaging through all available measured bandwidth, $\Omega_{BW} = \Omega_H - \Omega_L - \Delta\omega$. This bandwidth-averaged frequency-difference autoproduct is not typically used to make source localization predictions because of its dependence on the source waveform, $(S(\omega))$, which is typically not assumed to be known for passive source localization. Instead, the bandwidth average of the Cross-Spectral Density Matrix (CSDM) of the frequency-difference autoproduct, given in Eq. (4), was used to make the source localization predictions.

$$R^{\Delta}_{mn}(\Delta\omega, \vec{r}_m, \vec{r}_n) = \langle AP^*_{\Delta}(\vec{r}_m, \Delta\omega, \omega) AP_{\Delta}(\vec{r}_n, \Delta\omega, \omega)\rangle_{\omega} \tag{2.4}$$

The bandwidth-average of the autoproduct CSDM, R^{Δ}_{mn}, is independent of the transmitted source waveform, and is able to serve as the basis for successful matched field-style localization in the shallow ocean. Later investigation found that the initial postulate, that the autoproduct is well represented as a pressure field, is incorrect in many tactically relevant acoustic environments.

Some of these investigations discovered that the autoproduct resembled an acoustic pressure field with some corrections, and other investigations found that this model is insufficient and produces incorrect results.

The first difference that was found to arise between an autoproduct and a pressure field was discovered in the context of source localization [Worthmann *et al.* (2015)] and theoretically explored first in [Worthmann & Dowling (2017)]. This difference occurs in the neighborhood of a reflecting barrier. Specifically, in ocean acoustics it is common to model the surface of the ocean as a pressure release barrier [Jensen, F.B. *et al.* (2011)] since the speed of sound in air is so much lower than the speed of sound in water. In a locally flat region of the ocean surface, some power from an incident plane wave will be reflected and transmitted from the surface, as in Eq. (2.5) and (2.6).

$$P\Big(x,y,z,\vec{k}\Big)\Big|_{z\to 0^-} = A\Big(exp\Big(i(k_x x + k_y y + k_z z)\Big) + \widetilde{R} exp\Big(i(k_x x + k_y y - k_z z)\Big)\Big) \tag{2.5}$$

$$P\Big(x,y,z,\vec{k}\Big)\Big|_{z\to 0^+} = A\widetilde{T} exp\Big(i(k_x x + k_y y - k_z z)\Big) \tag{2.6}$$

Here, P represents the pressure field in the neighborhood of the boundary, $A, \vec{k}$ represent the amplitude and direction of propagation for the incident plane wave, and $\widetilde{R}, \widetilde{T}$ represent the reflection and transmission coefficients of the planar surface that divides the two semi-infinite media, defined by the sound speeds and densities of each medium. Eq. (2.5) captures the incident and reflected field, and Eq. (2.6) represents the transmitted field. For a pressure release surface, as the ocean surface is typically modeled, $\widetilde{R} = -1, \widetilde{T} = 0$. Using this understanding, a frequency-difference autoproduct can be calculated, as in Eq. (2.7) and (2.8).

$$\begin{aligned} AP_\Delta\Big(x,y,z,\vec{,}k_z\Big)\Big|_{z\to 0^-} &= |A|^2 \Big(exp\Big(i(\Delta k_x x + \Delta k_y y + \Delta k_z z)\Big) + \\ \Big|\widetilde{R}\Big|^2 exp\Big(i(\Delta k_x x + \Delta k_y y - \Delta k_z z)\Big) &+ 2Re\Big(\widetilde{R}\Big) exp\Big(i(\Delta k_x x + \Delta k_y y - k_z z)\Big)\Big) \end{aligned} \tag{2.7}$$

$$AP_{\Delta}\left(x, y, z, \vec{,} k_z\right)\Big|_{z\to 0^+} = A\left|\widetilde{T}\right|^2 exp\left(i(\Delta k_x x + \Delta k_y y + \Delta k_z z)\right) \tag{2.8}$$

Here, AP_{Δ} is the frequency-difference autoproduct, and Δk is the spatial difference frequency of the rays. Initially, Eq. (2.7) and Eq. (2.8) present much differently than do Eq. (2.5) and Eq. (2.6). When considering reflection and transmission from a pressure release surface, however, the transmitted fields are the same ($\widetilde{T} = \left|\widetilde{T}\right|^2 = 0$). Also, for a plane wave that is locally constant, the difference between A and $|A|^2$ doesn't affect beamforming and source localization. The third term in the reflected field is a cross-term, that will be treated in depth in Section 2.3. The biggest difference in the neighborhood of a pressure release surface is that ($\widetilde{R} = -1 \neq \left|\widetilde{R}\right|^2 = 1$) the autoproduct responds to a pressure release boundary as though it is a perfectly rigid surface. This is a seemingly non-physical result, but it is used successfully in short-range source localization scenarios like the shallow ocean experiment KAM11.

A more important difference between a frequency-difference autoproduct and a pressure field is found for rays that are propagating over long distances in a refracting environment. Here, the problem occurs where rays cross over one another forming a so-called 'caustic' [see: Kratsov, Y.A. & Orlov, Y.I. (1999)]. Caustics are also found to arise in refracting environments outside of the ray approximation, [Zhuravlev *et al.* (1989), D'Spain *et al.* (2002)] and are here referred to as field dislocations. The difference between a bandwidth-averaged frequency difference autoproduct and a pressure field at the difference frequency was first defined in [Worthmann & Dowling (2020b)], and is most easily described using the ray approximation. The ray approximation assumes that a pressure field can be represented as a sum of eigenray paths between a source and a receiver, as in Eq. (2.9).

$$G_{rays}\left(\vec{r}, \vec{r}_s, \omega\right) = \sum_{n=1}^{N} A_n exp\left(i\left(\omega\tau_n + \frac{m_n\pi}{2}\right)\right) \tag{2.9}$$

Here, N is the number of eigenrays connecting position $\vec{r}$, nominally a receiver location, and $\vec{r}_s$, nominally the position of the source. Eigenray paths and associated amplitudes A_n are found to

be nondispersive, meaning that they do not vary with frequency ω, provided that the local speed of sound in the medium is also nondispersive. For the frequencies investigated in this thesis, the speed of sound in the ocean is found to be nondispersive. Here, τ_n represents the travel time of each eigenray, and m_n represents the number of caustics [see: Jensen, F.B. *et al.* (2011)] that this eigenray passes through between the source and receiver position. The bandwidth-averaged frequency-difference autoproduct, given in Eq. (2.10), shows different behavior than does a pressure field when passing through a caustic.

$$\begin{aligned} \langle AP_{\Delta}(\vec{r},\Delta\omega)\rangle_{\omega} = \sum_{n=1}^{N}\left|A_n\right|^2 exp(i\Delta\omega\tau_n) - \\ -2i\sum_{n'\neq n}^{N,N} A_n^* A_{n'} exp\left(\frac{i\pi}{2}(m_{n'}-m_n)\right) exp\left(\frac{i\Delta\omega}{2}(\tau_{n'}-tau_n)\right)\times \\ exp\Big(i\Omega_C(\tau_{n'}-tau_n)\Big) sinc\left(\frac{\Omega_{BW}(\tau_{n'}-tau_n)}{2}\right) \end{aligned} \tag{2.10}$$

Here, the most important term in the bandwidth-averaged autoproduct is the first summation or 'self-term' of the autoproduct because it best resembles the pressure field ray path summation given in Eq. (2.9). Here, we can see that each eigenray carries no dependence on m_n. While the second term, or 'cross-term' of the autoproduct depends on the number of caustics, these terms are not found to be beneficial in autoproduct processing algorithms. Therefore, frequency-difference autoproducts that propagate over long distances in refracting environments, like an ocean waveguide, are expected to differ in form from a pressure field at the difference frequency.

One final difference that is found between a frequency-difference autoproduct and a pressure field is that their magnitudes differ. This phenomenon was known to exist in the earliest studies on frequency-differencing [Abadi *et al.* (2011), Worthmann *et al.* (2015)] but was not found to have a significant negative impact on results. In these studies, low-frequency pressure field computation is much simpler than computing a frequency-difference autoproduct and this computational simplicity makes this model significantly more desirable to use when it is expected to work. In fact, all

studies on autoproduct matching [Geroski *et al.* (2021b), Geroski & Worthmann (2021), Geroski & Dowling (2021)] have found that replicating the magnitude of an autoproduct is much more challenging than replicating its phase and has only marginal impact on the performance of algorithms that were tested. In general, the magnitude differences between an autoproduct and a pressure field are important in two contexts: environments where plane wave amplitudes vary significantly over an array, as would be observed when a long vertical receiving array is used in the deep ocean, or when a significant portion of the pressure field comes from diffraction [Worthmann & Dowling (2020a)]. The second point bears mentioning here: the frequency-difference autoproduct generally only stabilizes the phase of field quantities. It is not expected to recover magnitude as a part of its processing. Therefore, a shadow zone in a pressure field is expected to persist when autoproduct processing is undertaken. Accurately predicting the magnitude of the frequency-difference autoproduct that is propagating in a general environment remains an open question as of the writing of this thesis. Failing to accurately predict the magnitude is not currently found to aversely impact results given by autoproduct processing algorithms explored herein.

2.3 Existence of Cross-Terms

Cross-terms in an autoproduct are one of the reasons that many members of the remote sensing community stopped using Δk-radar and -sonar processing techniques. The word cross-term is used to refer to two similar phenomena: that can be called 'signal cross-terms,' as in [Geroski & Worthmann (2021)], or 'interferer cross-terms', as in [Worthmann *et al.* (2017)], as terms that do not arise from a physical source or singular eigenray path. The first type of cross term, a signal cross-term, can be understood using the ray approximation, given in Eq. (2.11), for intuition as terms in the autoproduct that do not vary at the difference frequency, that are shown in Eq. (2.12) and (2.13).

$$P(\vec{r}, \omega) = \sum_n A_n exp(i\omega\tau_n) \tag{2.11}$$

$$AP_{\Delta}(\vec{r},\Delta\omega) = \sum_{n=m} |A_n|^2 exp(i\Delta\omega\tau_n) + \sum_{n\neq m} A_n^* A_m exp\Big(i\omega(\tau_n-\tau_m)\Big) exp\left(\frac{i\Delta\omega}{2}(\tau_n+\tau_m)\right) \quad (2.12)$$

$$\langle AP_{\Delta}(\vec{r},\Delta\omega)\rangle_{\omega} = \sum_{n=m} |A_n|^2 exp(i\Delta\omega\tau_n) + \sum_{n\neq m} A_n^* A_m exp\left(\frac{i\Delta\omega}{2}(\tau_n+\tau_m)\right) sinc\left(\frac{\Omega_{BW}(\tau_n-\tau_m)}{2}\right) \quad (2.13)$$

Here, P represents a pressure field at spatial location $\vec{r}$ and frequency ω that can be represented as a sum of incident plane waves with amplitudes A_n and travel times τ_n. The frequency-difference autoproduct of this pressure field, AP_{Δ}, and its related bandwidth average, $\langle AP_{\Delta}\rangle_{\omega}$, are given in Eq. (2.12) and Eq. (2.13). Both the autoproduct and its bandwidth average are split into two different summations. The first summation in each is described as the self-term because it arises purely from ray paths multiplying against themselves. The second summation in each is described as a cross-term summation because it arises from each ray path multiplying against every other ray path. As is seen in Eq. (2.13), bandwidth averaging can be employed to coherently remove the effects of these cross-terms except when two ray paths arrive at the same time. Signal cross-terms have a more significant presentation when the autoproduct cannot be directly averaged over the measured frequency band, when the CSDM of the autoproduct must be investigated instead. The presentation of cross-terms in an autoproduct CSDM is given in Eq. (2.14)-(2.18), and is found to be much more complex than the autoproduct because the CSDM is a quadratic product of values. The autoproduct, already a quadratic quantity, has a CSDM that presents as a quartic quantity, which squares the number of relevant terms.

$$\left\langle R_{mn}^{\Delta}(\Delta\omega)\right\rangle_{\omega} = \left\langle R_{mn}^{SS}(\Delta\omega)\right\rangle_{\omega} + \left\langle R_{mn}^{SC,1}(\Delta\omega)\right\rangle_{\omega} + \left\langle R_{mn}^{SC,2}(\Delta\omega)\right\rangle_{\omega} + \left\langle R_{mn}^{CC}(\Delta\omega)\right\rangle_{\omega} \quad (2.14)$$

This analysis finds that the bandwidth average of the frequency-difference autoproduct CSDM,

R^{Δ}_{mn}, can be broken into three types of terms: self-self terms (R^{SS}_{mn}), that arise from multiplying the self-term of an autoproduct with another self-term, self-cross terms (R^{SC}_{mn}), that arise from multiplying the self-term of an autoproduct with a cross-term, and cross-cross terms (R^{CC}_{mn}), that arise from multiplying two cross-terms together. Of these terms, only the self-self term, given in Eq. (2.15) are found to vary entirely at the difference frequency.

$$\left\langle R^{SS}_{mn}(\Delta\omega)\right\rangle_{\omega} = \sum_{j,l}\left|A^n_j\right|^2\left|A^m_l\right|^2 exp\left(i\Delta\omega\left(\tau^n_j - \tau^m_l\right)\right) \tag{2.15}$$

Here, R^{SS}_{mn} is the self-self term of the autoproduct CSDM, n, m are receiver indices, and j, l are ray path indices. The self-cross and cross-cross terms, given in Eq. (2.16)-(2.18), are still more complex.

$$\left\langle R^{SC,1}_{mn}(\Delta\omega)\right\rangle_{\omega} = \sum_{j,L} 2\left|A^n_j\right|^2\left|A^m_L\right|^2 exp\left(i\Delta\omega\left(\tau^n_j - \tau^m_L\right)\right)cos\left(\Omega_C\Delta\tau^m_L + \Delta\phi^m_L\right)sinc\left(\frac{\Omega_{BW}\Delta\tau^m_L}{2}\right) \tag{2.16}$$

$$\left\langle R^{SC,2}_{mn}(\Delta\omega)\right\rangle_{\omega} = \sum_{J,l} 2\left|A^n_J\right|^2\left|A^m_l\right|^2 exp\left(-i\Delta\omega\left(\tau^n_J - \tau^m_l\right)\right)cos\left(\Omega_C\Delta\tau^n_J + \Delta\phi^n_J\right)sinc\left(\frac{\Omega_{BW}\Delta\tau^n_J}{2}\right) \tag{2.17}$$

$$\begin{aligned}\left\langle R^{CC}_{mn}(\Delta\omega)\right\rangle_{\omega} = \sum_{J,L} 4\left|A^n_J\right|^2\left|A^m_L\right|^2 exp\left(i\Delta\omega\left(\tau^n_J - \tau^m_L\right)\right)\\ cos\left(\Omega_C\left(\Delta\tau^n_J \pm \Delta\tau^m_L\right) + \left(\Delta\phi^n_J \pm \Delta\phi^m_L\right)\right)sinc\left(\frac{\Omega_{BW}\left(\Delta\tau^n_J \pm \Delta\tau^m_L\right)}{2}\right)\end{aligned} \tag{2.18}$$

Here, $R^{SC,2}_{mn}$,$R^{SC,2}_{mn}$ represent the two self-cross term components. These are represented by a triple sum over singular indices represented by lower case letters (j, l) and double summations over capital letters (J, L). The most important part of these terms is found in the *sinc* function. Here, the argument of the *sinc* function depends on the difference of two ray path arrival times $\Delta\tau_{J,L}$. When

two ray paths arrive at the same time, this term cannot be integrated to zero. More problematic than these terms is R_{mn}^{CC}, the cross-cross term. This term presents as a quadruple summation, and this term is guaranteed to be non-zero on the diagonal of the CSDM, where $m = n$. These terms are generally found to dominate other terms on and near the diagonal of the CSDM. For more precise analysis of these terms, see the appendix of [Geroski & Worthmann (2021)] or Chapter 4 of this thesis. Signal cross-terms are found to cause measurable degradation to the performance of autoproduct processing algorithms, but are generally not found to cause failure of these algorithms.

The second type of cross term, that arises when a measured pressure field is generated by two distinct sources, is referred to as an interferer or interference cross-term. The most commonly analyzed source of interference is random noise [Worthmann *et al.* (2017), Geroski *et al.* (2021a)]. These terms arise starting from Eq. (2.19).

$$P(\vec{r}, \omega) = P_1(\vec{r}, \omega) + P_2(\vec{r}, \omega) \tag{2.19}$$

Here, P is a measured pressure field, and P_1,P_2 are two different sources of the pressure field. This analysis could describe either a two-source problem, which could be further generalized into a multi-source problem, or the signal in noise problem. The bandwidth-averaged frequency difference autoproduct is given in Eq. (2.20), and its CSDM is given in Eq. (2.21).

$$\langle AP_\Delta(\vec{r}, \Delta\omega)\rangle_\omega = \langle AP_\Delta^{11}(\vec{r}, \Delta\omega)\rangle_\omega + \langle AP_\Delta^{12}(\vec{r}, \Delta\omega)\rangle_\omega + \langle AP_\Delta^{21}(\vec{r}, \Delta\omega)\rangle_\omega + \langle AP_\Delta^{22}(\vec{r}, \Delta\omega)\rangle_\omega \tag{2.20}$$

$$\left\langle R_{mn}^{\Delta}(\Delta\omega)\right\rangle_\omega = \sum_{a,b,c,d=1,2} \left\langle R_{abcd}^{\Delta}(\Delta\omega)\right\rangle_\omega \tag{2.21}$$

Technically, the CSDM given in Eq. (2.21) is a summation of 16 different terms. In most autoproduct-processing scenarios, the goal is to make remote sensing predictions about only one of these terms. When one of these terms is considered to be emanating from a noise source that is incoherent in space and time, 12 of these terms go to zero, as in Eq. (2.22). Here, the lack of

coherence between the signal and interferer is defined as $\int_\Omega d\omega P_1^*\left(\omega - \frac{\Delta\omega}{2}\right) P_2\left(\omega + \frac{\Delta\omega}{2}\right) = 0$.

$$\left\langle R^{\Delta}_{mn}(\Delta\omega)\right\rangle_\omega = \left\langle R^{\Delta}_{1111}(\Delta\omega)\right\rangle_\omega + \left\langle R^{\Delta}_{1212}(\Delta\omega)\right\rangle_\omega + \left\langle R^{\Delta}_{2121}(\Delta\omega)\right\rangle_\omega + \left\langle R^{\Delta}_{2222}(\Delta\omega)\right\rangle_\omega \tag{2.22}$$

This makes terms like R_{1112} go to zero with sufficient averaging. The remaining four terms are expected to be non-zero even when infinite averaging is employed. The effect that these terms have on autoproduct processing algorithms is more closely explored in Chapters 4 and 5.

2.4 Methods for Rejecting Cross-Terms

Because both signal- and interferer-cross-terms are postulated to degrade the effectiveness of autoproduct-processing algorithms, methods that can remove these cross-terms from autoproduct fields or their CSDM's should improve their effectiveness. The simplest idea for accomplishing this is to use knowledge of the source to estimate and coherently subtract the cross-terms from either the autoproduct or its CSDM. This idea is found to not remove signal cross-terms in the presence of environmental mismatch in [Geroski & Worthmann (2021)] because signal cross-terms vary at the field frequency and not at the difference frequency. This environmental mismatch causes field quantities propagating at the field frequency to lose their coherence where field quantities at the difference frequency may recover it. In general, coherent subtraction only works to remove cross-terms in scenarios where conventional signal processing algorithms are expected to make a successful prediction because the in-band field is coherent. In this case, it is unlikely a user would opt to use a frequency-differencing algorithm because of the greater complexity of these methods. However, the loss of coherence of the cross-terms turns out to be a discriminating factor between the self-terms and the cross-terms that can be used to remove the cross-terms in any number of ways.

Many noise rejection methods exist that can differentiate between signals that are coherent or incoherent on an array. These methods are termed 'noise rejection' methods because noise is the

most common source of incoherent signal in signal processing algorithms. One simple method that can be used to coherently remove incoherent signals is simply to take multiple measurements of a signal and to average them together, [see: Geroski & Dowling (2021)]. It is notable here that this step is not strictly possible in many conventional signal processing applications when the desirable part of the field quantity has lost coherence. Frequency-differencing, as will be shown in Chapter 3, promotes the long-term coherence or stability of a measured field quantity. In this case, the coherent portion of the measurement will add constructively and the incoherent portion of the measurement will add destructively, effectively cancelling some of the cross-terms. While this method is robust, relying on multiple measurements in passive remote sensing is not ideal because the signal could lose coherence for reasons other than environmental mismatch. Additionally, passive remote sensing relies on signals of opportunity to function, and such signals could conceivably fade in time. Therefore, noise rejection algorithms that can be implemented on a single measurement are preferred to those that require multiple measurements.

Generally, the noise rejection methods that are explored in this thesis rely on having access to the statistics of their measurements [Hald (2017), Hald (2019)]. The statistics of the measurements can then be used to differentiate between the coherent and incoherent part of the measurements in question. These methods generally rely on taking multiple measurements to access the statistics of their measurements, but frequency-differencing is able to use the bandwidth-averaging process to implement these methods successfully on a single measurement. This thesis explores differentiating between the coherent (self-term) and incoherent (cross-term) portions of a CSDM using five different techniques.

The first noise rejection algorithms that were found to be useful for rejecting cross-terms in an autoproduct CSDM took advantage of the algebraic difference of the presentation of each term [Geroski & Worthmann (2021)]. Because cross-terms are expected to be incoherent, they are found to be emphasized on the diagonal of the CSDM. Using this observation, the first idea, called 'diagonal zeroing' simply sets all values on the diagonal of the CSDM to zero. This idea can also be found in the original [Bucker (1976)] paper on Matched Field Processing. Diagonal zeroing is

also related to 'diagonal subtraction' [Hald (2017)] that subtracts a matrix whose only non-zero entries are on the diagonal but whose entries vary over the CSDM to preserve the desirable positive semidefinite property of the CSDM. Implementing diagonal subtraction methods, as opposed to diagonal zeroing, is not found to noticeably improve the performance of autoproduct-processing methods.

Two more noise rejection schemes that are inspired by the algebraic form of self- and cross-terms are Robust Principal Component Analysis (RPCA) [Wright *et al.* (2009)] and eigen- decomposition [Geroski & Worthmann (2021)]. Here, it is noted that a coherent quantity is not expected to vary when averaging is applied. When processing a CSDM, which is constructed from a vector outer product of measurements and is therefore rank-1, this means that the coherent portion of the matrix is expected to remain rank-1 or, at least, low rank. The incoherent portion of the CSDM, which is found to only sparsely populate the matrix, is by definition high-rank or complete. RPCA seeks to decompose a CSDM into two components using an optimization problem given in Eq. (2.23).

$$\min_{S,N} rank(S_{mn}) + \gamma \|N_{mn}\|_0 \tag{2.23}$$

$$\text{given: } S_{mn} + N_{mn} = R_{mn}$$

Here, the CSDM, R_{mn}, is postulated to be composed of two principal components: a signal component, S_{mn}, and a noise component N_{mn}. The signal component is postulated to be low rank and the noise component is postulated to be sparse, and so the CSDM can be composed into these two matrices as the solution to the (nonconvex) optimization problem given in Eq. (2.23). Here, $rank\,()$ measures the rank of its argument, or the minimum number of eigenvectors required to represent it, γ is an optimization variable, and $()_0$ is the sparsity of the argument, or number of non-zero entries. This equation is exact, but is found to be nonconvex for variable γ, and so is exchanged for Eq. (2.24).

$$\min_{S,N} \|S_{mn}\|_* + \lambda \|N_{mn}\|_1 \tag{2.24}$$

$$\text{given: } S_{mn} + N_{mn} = R_{mn}$$

Eq. (2.24) minimizes the nuclear norm, $\|_*$, of the signal matrix and the L_1 norm of the noise matrix, $\|_1$ with respect to optimization variable λ. This problem is found to be solvable using convex optimization, and is found to converge to the exact same solution as Eq. (2.23) provided that the noise matrix, N_{mn} is truly sparse. RPCA is expected to fail when the noise matrix is not sparse, and this will be seen in Chapters 4 and 5. Eigen-decomposition seeks to avoid the optimization problem by simply postulating that the self-term of the CSDM is represented by its largest (principal) eigenvector. While this hypothesis is never explicitly tested, this method is found to succeed at rejecting cross-terms and improving cross-correlation and source localization results in many contexts.

The remaining noise rejection algorithms seek to separate the coherent and incoherent components of a CSDM on the basis of whether or not the signals are coherent on either different portions of the array [Hald (2019)] or in different portions of the measured bandwidth. The first of these algorithms, which isolates the signals based on their coherence over the array works by splitting the array, X, into two subarrays α,β. These subarrays should span X. When α,β are not overlapping, this means that the CSDM can be represented as in Eq. (2.25).

$$\alpha \in X, \beta = X - \alpha$$

$$R^{\Delta}_{mn} = \begin{bmatrix} R_{\alpha\alpha} & R_{\alpha\beta} \\ R_{\beta\alpha} & R_{\beta\beta} \end{bmatrix} \tag{2.25}$$

When α,β overlap, there is a more complicated representation of the CSDM. The canonical coherence between the three independent portions of the CSDM can be computed using Eq. (2.26).

$$K = G^{1/2}_{\alpha\alpha} G_{\alpha\beta} G^{1/2}_{\beta\beta} \tag{2.26}$$

Here, K represents the canonical coherence between these three matrices, and it can be decomposed using an SVD algorithm, as in Eq. (2.27).

$$K = U\Sigma V^T \tag{2.27}$$

Using these matrices, reconstructions of the principal blocks of the CSDM, $R_{\alpha\alpha}$ and $R_{\beta\beta}$, can be made using Eq. (2.28) and can be substituted back into Eq. (2.25) for a denoised CSDM.

$$P = G_{\alpha\alpha}^{1/2} U\Sigma^{1/2}, Q = G_{\beta\beta}^{1/2} V\Sigma^{1/2} \tag{2.28}$$

$$\tilde{R}_{\alpha\alpha} = PP^T, \tilde{R}_{\beta\beta} = QQ^T \tag{2.29}$$

This algorithm can be implemented successfully using conventional signal processing algorithms. Another version of this algorithm that works only with frequency-differencing algorithms is proposed to nearly mirror this algorithm. Here, α,β instead of being spanning subarrays of a receiving array are proposed to be spanning sub-bands of a measured bandwidth Ω_{BW}. In this case, $R_{\alpha\alpha}$, $R_{\alpha\beta}$, and $R_{\beta\beta}$ can be defined using Eq. (2.30).

$$\begin{aligned} R_{\alpha\alpha} &= \langle AP_{\Delta}^{*}(\vec{r}, \Delta\omega, \omega \in \alpha) AP(\vec{r}, \Delta\omega, \omega, \omega \in \alpha) \rangle_{\omega} \\ R_{\alpha\beta} &= \langle AP_{\Delta}^{*}(\vec{r}, \Delta\omega, \omega \in \alpha) AP(\vec{r}, \Delta\omega, \omega, \omega \in \beta) \rangle_{\omega} \\ R_{\beta\beta} &= \langle AP_{\Delta}^{*}(\vec{r}, \Delta\omega, \omega \in \beta) AP(\vec{r}, \Delta\omega, \omega, \omega \in \beta) \rangle_{\omega} \end{aligned} \tag{2.30}$$

These matrices can be used as the basis for a new algorithm by substituting them into Eq. (2.26)-(2.29). Here, however, the final representation of the CSDM comes using Eq. (2.31).

$$\tilde{R}_{mn}^{\Delta} = \tilde{R}_{\alpha\alpha} + \tilde{R}_{\beta\beta} \tag{2.31}$$

2.5 Conclusion

This chapter provides the theoretical basis for understanding the next three chapters of this thesis. In it, the autoproduct and its related quantities are defined. The effects that various wave phenomena have on autoproducts are explored in a theoretical context to build intuition that will be useful in the succeeding chapters. The frequency-difference autoproduct is postulated to have greater coherence than the pressure fields that are conventionally investigated using signal processing algorithms, and therefore algorithms that process the frequency-difference autoproduct are expected to be more robust than conventional signal processing algorithms. The hypothesis that the frequency-difference autoproduct offers greater stability than a measured pressure field will be assessed in Chapter 2. This chapter then proceeds to define the difference between a self-term and a cross-term, and to explain why self-terms are thought to be beneficial for autoproduct-based signal processing algorithms and cross-terms are not. Two forms of cross-terms, those arising from multipath signals and those arising from the presence of an interferer, are explored. The primary difference between self- and cross-terms is postulated to be that self-terms have greater spatiotemporal coherence than cross-terms, and several noise rejection algorithms are proposed to remove cross-terms from a CSDM. These algorithms have been found in other studies to remove incoherent signals from a CSDM with some level of effectiveness. The effect that cross-terms have on signal processing concepts like cross-correlation and source localization will be assessed in Chapters 4 and 5, as well as the benefits of using noise rejection algorithms to improve their operation.

CHAPTER 3

Measurement and Stability Analysis of the Frequency-Difference Autoproduct in Ocean Environments

3.1 Introduction

Array Signal Processing techniques are often used to study acoustic fields propagating in an ocean sound channel, as well as to infer information about sources of the sound and/or the ocean environment in general [see: Dowling & Sabra (2015)]. For an array signal processing technique to be scientifically useful, it generally must meet three criteria: it must use a measurable quantity, the quantity must be stable, and the quantity must offer identifiable information that is of interest to an operator. Here, a quantity is said to be measurable if a process exists by which the quantity can be directly determined. One such example is an acoustic pressure field, that can be measured using a transducer. The quantity is further said to be stable if measurements that are taken near to one another, either spatially or in the time domain, are predictably related. The quantity is said to offer identifiable information if it reliably provides quantitative physical indication of interest to the observer. Acoustic fields propagating over long distances or at high frequencies in the ocean are generally found to be unstable in both the spatial and frequency domain, making it difficult to infer information from them [Urick (1976) Tolstoy (1989)]. This lack of stability does not arise from either a physical or numerical limitation on predicting the pressure field [Porter (1992)], but

rather from a lack of knowledge of the environment that an observer is operating in [**?**, Flatte *et al.* (1983)]. The frequency-difference autoproduct was originally proposed as a stable surrogate to the pressure field for identifying information when the pressure field is unstable [Abadi *et al.* (2011), Worthmann *et al.* (2015), Douglass *et al.* (2017)]. This chapter uses both synthetic and experimental data to test the hypothesis that the frequency-difference autoproduct is more stable than a measured pressure field, proposes a simple model of environmental mismatch for understanding autoproduct stability, and conclusively demonstrates that the frequency-difference autoproduct differs fundamentally from a low-frequency pressure field.

One of the common tasks in array signal processing related to inferring information about a source is localization, that is, determining the location of a source based on a successful detection. The classic method used for ocean source localization, Matched Field Processing (MFP) [see: Bucker (1976), Baggeroer *et al.* (1993)], fails to be robust when the pressure field information used to make this prediction is unstable. In acoustic array signal processing in the ocean, this instability tends to arise from a variety of environmental factors, including noise and interference [Jensen, F.B. *et al.* (2011)], and dynamic variation and static uncertainty in the sound speed within the bulk of the ocean [Colosi *et al.* (2019), Dzieciuch *et al.* (2013), Worcester *et al.* (2006)] and uncertainty related to the ocean boundary conditions [Hamilton (1978), Dong *et al.* (2010), Jiang *et al.* (2007)]. These factors arise from a number of physical characteristics, including seasonal and tidal variations, and internal waves. To accurately localize a source, MFP relies upon cross correlating [Urick (1976)] a measurement taken over an array with a predicted Green's function that is made using an operator's knowledge of the environment. MFP is found to be unreliable due to instability in the measured pressure field in the deep ocean when attempting to localize a source that is transmitting at or above 10 Hz at a range greater than or equal to 50 km from a receiving array [Tolstoy (1989)]. More generally, pressure field quantities are more likely to be unstable when transmitted at higher frequencies and/or over longer distances. The frequency-difference autoproduct attempts to use the bandwidth transmitted by a given source to force measured field information to appear at a frequency that is lower than that transmitted, ideally stabilizing the field

information.

The frequency-difference autoproduct has been studied in a variety of contexts before. It was first used to mitigate the effects of array sparseness in plane- and spherical-wave beamforming [Abadi *et al.* (2011), Douglass *et al.* (2017)]. It was next studied for source localization in a refracting waveguide environment in first the shallow [Worthmann *et al.* (2015), Worthmann *et al.* (2017)], and then the deep [Geroski & Dowling (2019), Geroski & Worthmann (2021), Geroski & Dowling (2021)], oceans. The bandwidth-averaged frequency-difference autoproduct was first measured explicitly in a laboratory water tank [Lipa *et al.* (2018)] meant to emulate predictions made in a Lloyd's Mirror environment [Worthmann & Dowling (2017)], and then later measured in the deep ocean [Geroski *et al.* (2021b)]. This chapter focuses on studying the stability of measurements of the bandwidth-averaged frequency-difference autoproduct propagating at a variety of difference frequencies in the deep ocean. Further, this chapter demonstrates that thinking about the frequency-difference autoproduct as a pressure field propagating at the difference frequency provides useful, but limited intuition about this object. Looking towards using the autoproduct as the basis of a matched field-style source localization algorithm, the stability and exact form of the autoproduct in this environment will be assessed by cross correlating a measured autoproduct field with an autoproduct field predicted using numerical acoustic propagation software [Porter (1992)]. Such cross-correlation is equivalent to measuring the Euclidean distance metric [Finette & Mignerey (2018)] between the two quantities at a single difference frequency. Where cross-correlation is high, the Euclidean (and geodesic) distance between the two vectors is small in complex space. Where cross-correlation is low, the Euclidean (not necessarily geodesic) distance between the two vectors is larger. When correlating an unstable measurement to a constant vector, the magnitude and phase of this cross correlation is expected to be a zero-mean Gaussian process. Evidence of this is presented in Section 3.5. This chapter demonstrates that the cross correlation between a predicted and a measured bandwidth-averaged frequency-difference autoproduct at single Hz difference frequencies is far higher and far more stable than the cross correlation between a measured and predicted pressure field measured propagating in the hundreds of Hz.

Predicting a Green's function in a general ocean environment can be accomplished in a number of ways. In particular environments, like the Lloyd's Mirror, exact Green's functions [Pierce, A.D. (1994)] exist that can be used to directly compute a measured pressure field. For slightly more general media, like the isovelocity or Pekeris waveguide, the method of images [Kinsler, L.E. *et al.* (1999)] can be used to estimate the Green's function numerically using an infinite sum. When the environment is sufficiently complicated, as it is in the deep ocean, it is common to use a variety of other techniques to predict the Green's function. The most popular methods used in ocean acoustics today [Jensen, F.B. *et al.* (2011)] are ray codes [Porter & Bucker (1987)], mode codes [Porter (1992)], Wavenumber Integration Codes, and parabolic equation codes. Free and Open Source implementations of each of these methods can be found in [Heat (2021)]. This study focuses on using frequency-domain mode codes, specifically the open-source KRAKEN [Porter (1992)] toolbox, to predict the Green's function of the deep ocean because of the speed and accuracy of the computations in the simplified model environment used for the calculations (see: Section 3.4). This model is deemed to be sufficient for the purposes of showing the increased stability of the autoproduct to both synthetic and measured pressure field mismatch in the deep ocean.

The model for environmental mismatch that is used in this study is derived from observations made during tomographic experiments, like the North Pacific Acoustic Library's 2010-2011 Philippine Sea Experiment (PhilSea10) [Worcester *et al.* (2013)]. Other analyses of this experiment are conducted using time-front analysis [Munk, W., Worcester, P. & Wunsch, C. (1995)]. This method pulse compresses measurements [Birdsall & Metzger (1986)] taken from a cooperating source to infer the time-domain Green's function for the deep ocean. Changes in this measured Green's function over the course of the experiment mostly correspond to variances in the time that pressure field information is measured. In a tomographic setting, this time-of-arrival variance can be directly related to changing environmental factors such as internal waves [Colosi *et al.* (2013), Colosi *et al.* (2019)]. To mimic this effect in the time domain, zero-mean Gaussian time delays can be added to the time-of-arrival of rays at each receiver, altering the phase of each ray as it is

measured at the receiver. Mimicking this effect using a mode code is accomplished by slightly shifting each receiver spatially. While this model ignores the effect of shifting two ray path arrival times relative to one another, it is found to be sufficient for the purpose of assessing the stability of the frequency-difference autoproduct in the deep ocean.

The remainder of this chapter is divided into six sections. Section 3.2 lays out the theory that is relevant to understanding the time- and frequency-domain implications that our model of environmental mismatch should have on a field quantity, as well as the cross correlation metric that is used to assess the stability of both pressure fields and autoproducts. Section 3.3 provides simple verification of these predictions using both synthetic and measured data in a controlled, Lloyd's Mirror environment. Section 3.4 introduces the PhilSea10 experiment, which will be used for validation of the mismatch model and verification of the increased stability provided by the autoproduct. Section 3.5 shows the results of cross correlating all relevant field quantities in a synthetic environment and demonstrates the instability of cross correlating the autoproduct with a pressure field at the difference frequency. Section 3.6 shows the results of cross correlating measured and predicted autoproduct fields, demonstrating the increased robustness that the frequency-difference autoproduct shows to measured environmental mismatch relative to the pressure field. Section 3.7 draws what conclusions are available from this experiment.

3.2 Theory

3.2.1 Cross-Correlation Metrics

One of the most common ways to compute similarity between two vectors in a $\mathbb{C}^N$ space is cross-correlation. In this thesis, compared vectors will be solutions to the time-harmonic wave equation or a related equation, and the cross-correlation will be performed over space. Cross-correlation is usually defined [see: Bracewell, R. (1965)] as a convolution process between two vectors as in Eq. (3.1). The time-domain cross-correlation can be converted, for the purposes of computational convenience, using a Fourier Transform as is shown in Eq. (3.2). For this thesis, the frequency-

domain representation is preferred. For correlating two related vectors at a single frequency across space, Eq. (3.3) can be defined equivalently. This equation can be approximated over a discretely sampled array in Eq. (3.4).

$$\chi(\tau) = \int_T dt w_1^*(t) w_2(t+\tau) \tag{3.1}$$

$$\chi(\omega) = F\Big(\chi(\tau)\Big) = F\Big(w_1^*(t)\Big)F\Big(w_2\Big) \tag{3.2}$$

$$\chi(\omega) = \int_V d^3\vec{x} w_1^*(\vec{x},\omega) w_2(\vec{x},\omega) \tag{3.3}$$

$$\chi(\omega) = \frac{w_1^*(\vec{x},\omega) \circ w_2(\vec{x},\omega)}{\sqrt{w_1^*(\vec{x},\omega) \circ w_1(\vec{x},\omega)}\sqrt{w_2^*(\vec{x},\omega) \circ w_2(\vec{x},\omega)}} \tag{3.4}$$

This normalized cross-correlation coefficient, $\chi(\omega)$ in (3.4), is a complex quantity in general. Here, variables t, τ represent time-domain variables, ω represents the angular (temporal) frequency of the field, F is the Fourier Transform, $\vec{x}$ is a spatial variable, and $\circ$ represents an inner or "dot" product between two vectors. The domain of integration in Eq. (3.1) and Eq. (3.3), TV, represent all time or all space. Here the inner product is taken over the spatial domain. The goodness of the matching between two vectors, w_1 and w_2, is typically assessed using the complex magnitude of the cross correlation coefficient itself, which is bounded between 0 and 1, $0 \leq |\chi| \leq 1$. The complex argument of χ represents the average phase between the two quantities. Three versions of this complex correlation coefficient are explored in the remainder of this chapter: correlation between measured and predicted pressure fields, correlation between measured and predicted autoproducts, and measured autoproducts and predicted pressure fields.

For the remainder of this chapter, w_1 will represent the measured quantity and w_2 the predicted quantity. For synthetic tests, w_1 will be calculated using KRAKEN and corrupted according to

the environmental model used for mismatch, while w_2 will never be altered. The autoproduct and pressure field calculations will be computed following Eq. (3.5) and (3.6).

$$w_1(\omega, \vec{x}_t, \vec{x}_r) = G(\omega, \vec{x}_t, \vec{x}_r) \tag{3.5}$$

$$w_1(\Delta\omega, \vec{x}_t, \vec{x}_r) = \left\langle G^*\left(\omega - \frac{\Delta\omega}{2}, \vec{x}_t, \vec{x}_r\right) G\left(\omega + \frac{\Delta\omega}{2}, \vec{x}_t, \vec{x}_r\right)\right\rangle_\omega \tag{3.6}$$

In both equations, $G(\omega, \vec{x}_t', \vec{x}_r')$ represents a time-harmonic, pressure field Green's function in the environment under investigation. To compute a time-harmonic Green's function, both analytic Green's functions, as in the Lloyd's Mirror environment, and computational Green's functions, in the deep ocean environment, can be used. Here, $G(\omega, \vec{x}_t', \vec{x}_r')$ depends on all environmental information available to the operator. Its explicit dependence on the field frequency, ω, and source and receiver locations, $\vec{x}_t'$ and $\vec{x}_r'$, are outlined because they are varied throughout the computational process. In Eq. (3.6), the bandwidth-averaged autoproduct is computed by averaging over all available bandwidth. That is, for a source transmitting over all ω such that $\Omega_L \leq \omega \leq \Omega_H$, the bandwidth average is computed for all $\omega, \Delta\omega$ such that $\Omega_L \leq \omega \pm \Delta\omega/2 \leq \Omega_H$.

3.2.2 Expected Effect of Synthetic Mismatch Model

The mismatch model that will be used as the basis for a synthetic test of the stability of both pressure fields and autoproducts is drawn directly from tomography experiments. Similar understanding can be gleaned from other fields of random media propagation such as optical scintillation in astronomy [Carroll, B.W. (1996)]. Given a single eigenray propagating from a source to a receiver in the ocean, effects of environmental mismatch can be understood using concepts like the Time and Intensity Sensitivity Kernels [Skarsoulis & Cornuelle (2004), Skarsoulis *et al.* (2009), Dzieciuch *et al.* (2013)] that can be related directly to acoustic sound speed variations in the ambient environment. Here, the effects of these constructs are simplified to provide an easily understood synthetic test in Eq. (3.7) and (3.8).

$$G(\omega, \vec{x}_t, \vec{x}_r) = Aexp(i\omega(\tau + \Delta\tau)) \tag{3.7}$$

$$\chi(\omega) = exp(i\omega\Delta\tau) = exp\left(i2\pi\left(\frac{\Delta\tau}{T}\right)\right) \tag{3.8}$$

Here, Eq. (3.7) gives a field quantity that can be represented locally as a single eigenray between a source at location $\vec{x}_t$ and receiver at location $\vec{x}_r$. The field amplitude, A, and travel time τ can be solved in a general acoustic operating environment using a ray code, like BELLHOP [Porter & Bucker (1987)]. Here, $\Delta\tau$ is a variable that can be parametrically varied to understand the effect that time-front mismatch has on cross correlation for solutions to the wave equation. Eq. (3.8) represents the result of cross correlating Eq. (3.7) with non-zero $\Delta\tau$ with another sample of itself with $\Delta\tau = 0$ (see: Eq. 3.4). Here, it can be seen that there is little effect on cross correlation when the mismatch parameter is small compared to a temporal period, T. This equation represents the simple case where this correlation is computed for an array with one receiver. For computing a spatial cross correlation where $\Delta\tau$ varied over the array, the cross correlation is expected to decrease as many elements will destructively add together. For the synthetic test in Section 3.3, this test is directly compared. Section 3.4, that instead uses a mode code, uses the spatiotemporal equivalence in the wave equation to understand the same effect.

Time-front mismatch, for this study, is modeled in a mode code by introducing small amounts of receiver displacement, Δr into receivers on the array. This can be understood using Eq. (3.9), which explicitly outlines the local dependence of a field quantity on range.

$$G(\omega, \vec{x}_t, \vec{x}_r) = Aexp\left(i\left(\omega\tau - \vec{k} \circ \vec{x}_r\right)\right) \tag{3.9}$$

Here, the local wavenumber, $\vec{k}$ is also assumed to be available using a ray code or a mode code. By introducing receiver displacement, $\Delta\vec{r}$, instead of arrival time displacement, $\Delta\tau$, the effect on cross correlation seen in Eq. (3.8) can be mimicked, as in Eq. (3.10).

$$\chi(\omega) = exp\left(i\vec{k} \circ \Delta\vec{r}\right) = exp\left(\frac{i2\pi\left(\hat{k} \circ \Delta\hat{r}\right)|\Delta r|}{\lambda}\right) \tag{3.10}$$

Here, the effect of displacement is seen to be small provided that the magnitude of the spatial displacement parameter, Δr, is small compared to a wavelength (λ) of the field quantity. For the purpose of making comparisons with the tomography literature [Munk, W., Worcester, P. & Wunsch, C. (1995), Colosi *et al.* (2019)], this effect will be described herein as time-front mismatch.

3.3 Lloyd's Mirror Simulation and Experiment

A controlled-environment test of autoproduct stability compared to pressure field stability is conducted prior to working in an uncontrolled environment like the deep ocean. For this purpose, verification of predictions made in Section 3.2 are made in a simulated Lloyd's Mirror environment and in a water tank experiment wherein recordings have been trimmed to resemble a Lloyd's Mirror environment. This test is also used to demonstrate effects that will be further explored in Chapters 4 and 5. Here, the goal is to examine the effect that environmental mismatch has on cross correlation between a predicted pressure field and measured pressure field at in-band frequencies, between predicted and measured autoproducts at varied difference frequencies, and between a predicted pressure field at the difference frequency and measured autoproduct in an environment where such a comparison can be successfully made.

The details relevant to understanding the simulation and experiment, originally conducted by Jessica Lipa in 2018 [see: Lipa *et al.* (2018)], are summarized in Fig. 3.1. Receivers are shown on the left side of the figure as yellow dots arranged in a vertical line array. The source is shown as a black dot on the right, $r = 32.5$ cm from the receiving array, and at $z = 20.4$ cm from the surface.

The sound speed profile is constant for $z \geq 0$ as $c_0 = 1500\ m/s$, and the surface boundary condition is assumed to be a pressure release, (corresponding to $c = 0\ m/s$, or a reflection coefficient of $R = -1$). The source transmits a modulated Gaussian wave packet with center frequency of $f_c = 70\ kHz$ and a nominal bandwidth of 60 kHz. This means that the autoproduct can be

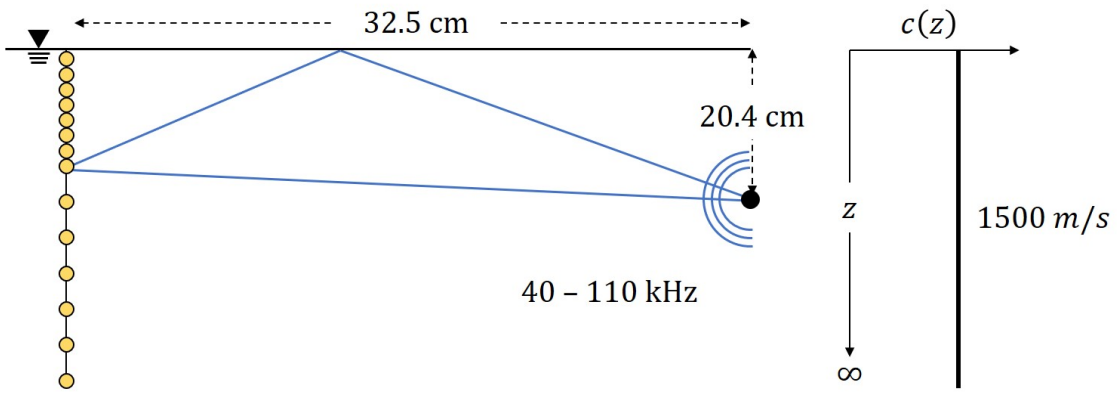

Figure 3.1: Schematic of the acoustic environment with a monopolar acoustic source placed at depth ($d = 20.36\ cm$), and range ($r = 32.46\ cm$) away from an array with N receivers. Source transmission is processed in frequency range $40 - 110\ kHz$. The array is 40 cm long, and is sampled at $\Delta z = 0.1\ cm$ for $z < 10\ cm$ and at $\Delta z = 0.5\ cm$ to a depth of $z = 40\ cm$. Surface boundary condition is assumed to be a pressure release.

computed over difference frequencies of $0 \leq \Delta f \leq 60\ kHz$. When modeling an autoproduct as a pressure field propagating at difference frequency Δf, it is common to model the surface boundary condition reflection coefficient as $R_{AP} = |R|^2$, as in [Worthmann & Dowling (2017)]. Here, this corresponds to placing an effective perfectly rigid boundary at the surface ($c = \infty,\ R = 1$) on the surface in place of a pressure release boundary.

Initially, a simulated comparison of time-harmonic field magnitude is explored in this environment. This comparison is shown in Fig. 3.2. Here, the pressure field at $f = 40\ kHz$ is shown in a blue line, with an autoproduct at $\Delta f = 40\ kHz$ in red. Initially, the comparisons demonstrate a problem: the fields are out of phase. This is initial verification of the need to correct the boundary condition for the matching field.

Beyond the phase difference between the fields, the autoproduct shows much higher frequency behavior near the surface. This behavior primarily arises from the presence of cross-terms, explored in Chapter 4, and can be observed in the experimental data, as well as in the simulation. The presence of cross-terms cannot be replicated by making the boundary condition adjustment, but is generally understood to play a minor role in the overall stability of the autoproduct, as will be shown in Sections 3.4 and 3.5.

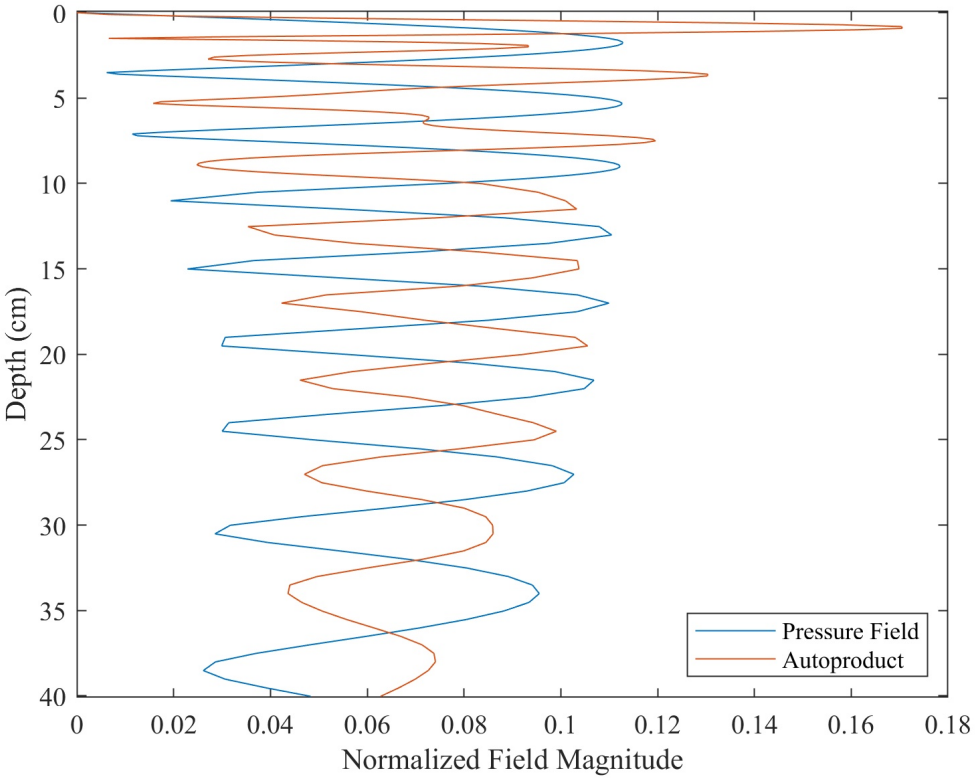

Figure 3.2: Comparison of calculated pressure fields and autoproducts at same (difference) frequecy of 25 kHz in the Lloyd's Mirror environment

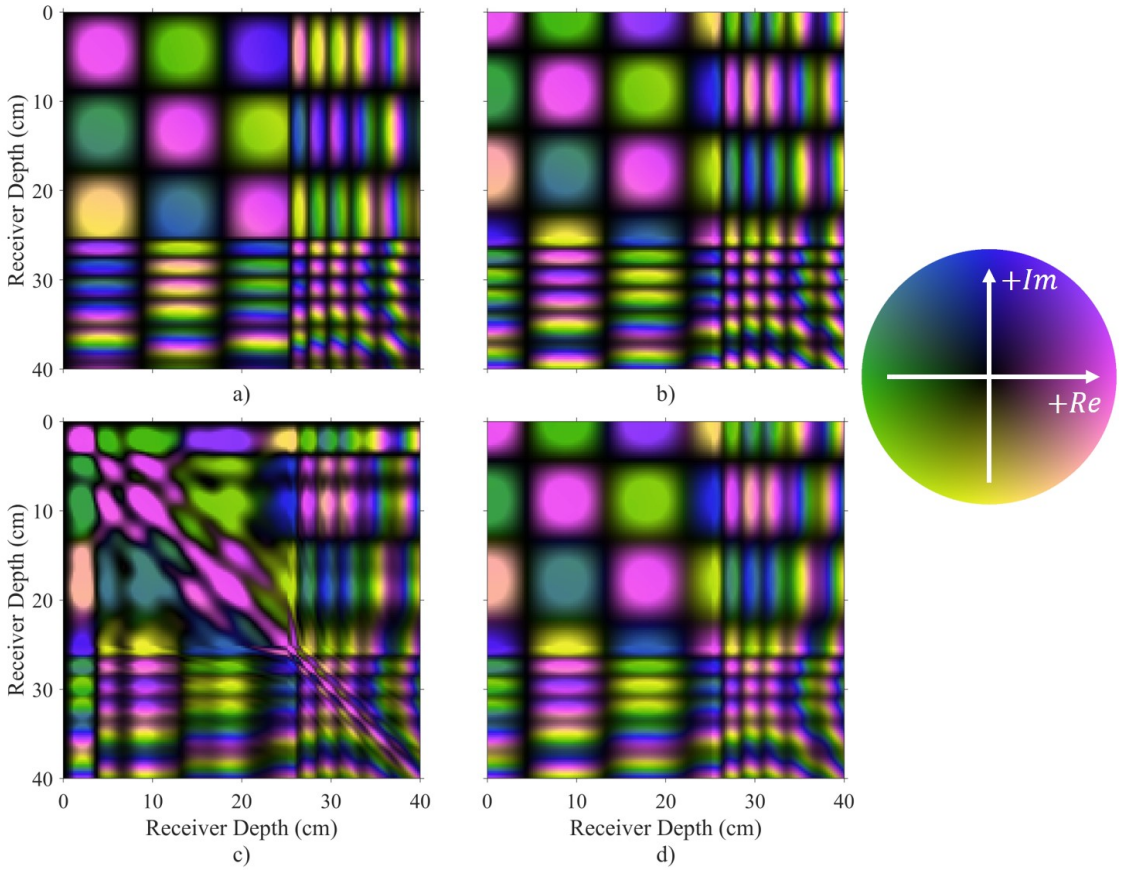

Figure 3.3: Measured pressure field and autoproduct cross-spectral density matrices, (a) Pressure field at the difference frequency with normal boundary conditions, (b) Pressure field at the difference frequency with rectified boundary conditions, (c) Bandwidth-averaged autoproduct CSDM, (d) CSDM constructed with bandwidth-averaged autoproduct fields.

Another way to look at field quantities that is common in passive remote sensing is to form an array Cross-Spectral Density Matrix (CSDM). This chapter does not focus on the form of CSDM's, but rather uses them as a different way to look at autoproduct and pressure field forms. The procedure for calculating a CSDM is given in Chapter 2. CSDM's relevant to this portion of the thesis are given in Fig. 3.3. The CSDM's displayed in all areas of this text use domain coloring [Wegert, E. (2012)] to simultaneously convey complex magnitude and phase information of the CSDM using a cyclic colorbar that varies in hue for complex phase and brightness for magnitude.

Here, the unit circle in Fig. 3.3 gives the colorbar. Magenta (green) represents the positive (negative) part of the real axis, and Blue (yellow) represents the positive (negative) part of the imaginary axis. This cyclic colorbar is chosen to be perceptually uniform [Kovesi (2015)] over

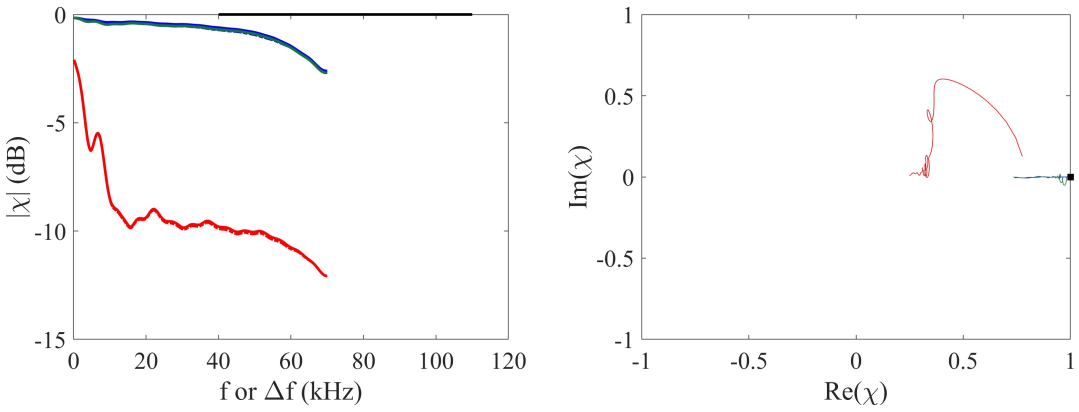

Figure 3.4: (a) Magnitude and (b) Phase of cross correlation coefficient of all field quantities in Lloyd's Mirror environment. Black lines represent pressure-to-pressure cross correlation, blue lines represent autoproduct-to-autoproduct cross correlations, green lines represent autoproduct-to-pressure field with rectified boundary conditions, and red lines represent autoproduct-to-pressure field without rectified boundary conditions.

2π. Black corresponds to low magnitude. In Fig. 3.2, it can be observed that Figs. 3.2b, 3.2c, and 3.2d all resemble one another more closely than they do Fig. 3.2a. This provides further demonstration for the need to rectify boundary conditions when matching an autoproduct. Further, Fig. 3.2c retains a significant amount of high frequency behavior that is not seen in any other figure panel. This behavior is governed by the presence of CSDM cross-terms (see: Chapter 4). These cross-terms can be mitigated somewhat using bandwidth averaging, but must mostly be subtracted using advanced techniques. The implementation and utility of several of these techniques will be explored in the next chapter.

To better explore the effect that the visual comparisons shown in Fig. 3.2 and 3.3 have on array signal processing problems like source localization, cross correlation is explored next. To understand the ideal case of cross correlation in the Lloyd's Mirror, this effect is first explored absent mismatch in a synthetic test. The results here are shown in Fig. 3.4.

Fig. 3.4a plots only the magnitude of the cross correlation coefficient as a function of pressure field frequency or autoproduct difference frequency. In this plot, the black line, which represents $\chi(\omega)$ between pressure fields is unity at all points. The red line, which represents cross correla-

tion between an autoproduct and a pressure field without rectified boundary conditions at Δf is much lower, dropping to $|\chi| \leq -10\ dB$ for most difference frequencies. The last two lines, green and blue, represent cross correlations between an autoproduct and a pressure field with rectified boundary conditions and an autoproduct, respectively. Here, the blue line is seen to always outperform the green line slightly, which can be explained by the slight improvement in magnitude matching. Both cross correlations tend to fall off at high difference frequency because there is little bandwidth to average over to suppress signal cross terms. Fig. 3.4b shows the phase of the cross correlation at all frequencies. Here, the black, blue, and green lines generally show little to no phase difference at every frequency, and the red line shows significant phase variation over the difference frequency range explored. Because of the necessity of rectifying boundary conditions in even the simplest synthetic experiment, cross correlation between an autoproduct and pressure field with non-rectified boundary conditions will not be explored further in this thesis.

Absent mismatch, the presence of cross terms seem to force the autoproduct to behave as a worse alternative to in-band processing. The autoproduct is expected to provide greater stability in the face of environmental mismatch than is an in-band pressure field. This effect is explored in Fig. 3.5. Here, the figure panels and lines represent the same quantities as they did in Fig. 3.4. However, zero-mean, Gaussian random time delays with standard deviation of $\Delta\tau = 5\ ms$ are applied to the arrival time of each ray path.

In Fig. 3.5a, the presence of time-front mismatch causes all field quantities to decorrelate similar to one another. However, the autoproduct, because it is governed at difference frequency Δf instead of measured frequency f, has greater cross correlation than the in-band pressure field. The phase, shown in Fig. 3.4b, tells effectively the same story. Considering the hypothesis given in Eq. (3.8), the temporal period of the autoproduct can be made larger than the in-band field used to form it. This effectively mitigates the effect of arrival time fluctuations.

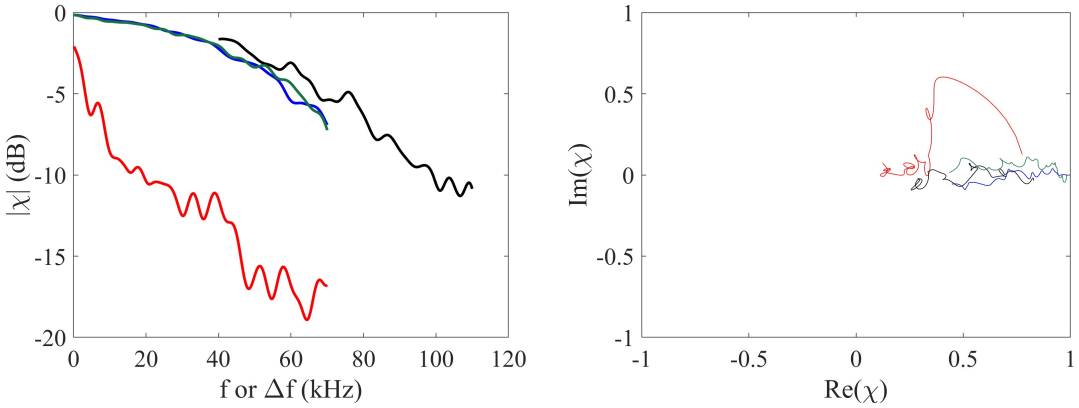

Figure 3.5: Magnitude and phase of cross correlation of all field quantities in a Lloyd's Mirror environment in the presence of environmental mismatch modeled as arrival time fluctuations. Black lines represent pressure-to-pressure cross correlation, blue lines represent autoproduct-to-autoproduct cross correlations, green lines represent autoproduct-to-pressure field with rectified boundary conditions, and red lines represent autoproduct-to-pressure field without rectified boundary conditions.

3.4 PhilSea10 Experiment

Given the greater stability that was offered by the autoproduct field to a synthetic model of mismatch, the next step is to examine the stability of the autoproduct in the deep ocean. To provide the best test of this stability, a dataset measured in the Philippine Sea was identified and a simulated environment was constructed to mimic it. This experiment [Worcester *et al.* (2013)], the North Pacific Acoustic Library 2010-2011 Philippine Sea Experiment (designated: PhilSea10), included thousands of measurements taken on a water-column spanning Distributed Vertical Line Array (DVLA) from both moored and towed sources in the Philippine Sea between April 2010 and April 2011. The data was provided to the author by Drs. Matthew Dzieciuch and Peter Worcester. A two-dimensional rendering of this environment is shown in Fig. 3.6.

Here, the receivers are shown as yellow dots on the left side of the schematic, and a source is shown on the right. Source range and depth information, as well as transmitting bandwidth information and source level are given in Table 3.1. The acoustic sound speed profile, measured near to the DVLA at the outset of the experiment, is shown on the right. This information will be

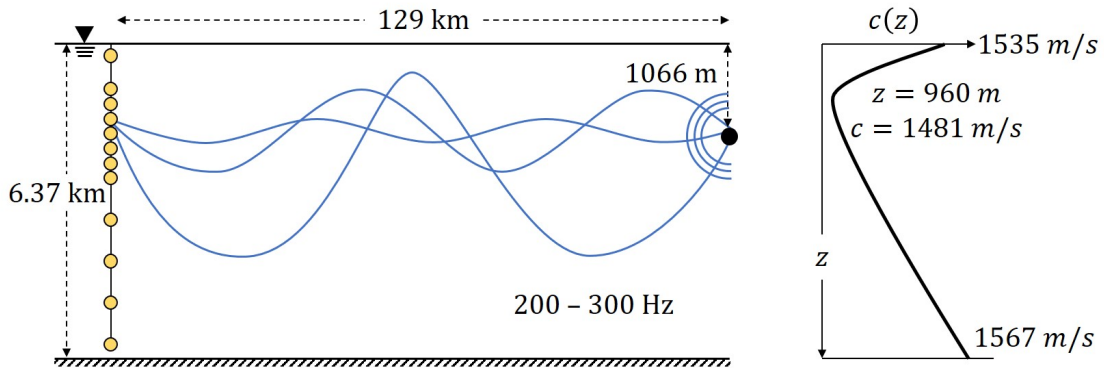

Figure 3.6: Nominal PhilSea10 deep-ocean experimental geometry and coordinate system showing a vertical array at $r = 0$, a sound source at range $r = r_s$ and depth $z = z_s$, both in an ocean water column of depth $D = 6.37$. The sound speed profile at the right with a minimum at a depth of 960 m was measured near the vertical array.

PhilSea10 Source Designation	Source-to-Array Range (km)	Source Depth (m)	Source Transmitting Bandwidth (Hz)	Source Level ($dBre1\mu Paat1m$)
T6	129.4	1066	200-300	185.8
T5	210.1	1062	205-305	184.0
T1	224.8	1069	200-300	184.4
T4	379.1	1065	225-325	182.7
T2	395.9	1070	140-205	183.8
T3	450.1	1062	225-325	181.9

Table 3.1: Relative source location and signal bandwidths from the PhilSea10 experiment. Information available in (Worcester et. al. 2013).

used to construct all matching vectors. Here, it should be noted that the closest source, designated T6, stopped transmitting in the middle of the experiment. For quantitative predictions of cross correlation and source localization, only successful transmissions will be used.

The measured data was provided to the author as a set of matched filtered and pulse compressed measurements in the time domain. These outputs represent the measured time-domain Green's function of the medium. Example measurements, taken from the farthest source ($T3, r_s = 450\ km$) near the beginning of the experiment (immediately after array timing calibration) are shown in Fig. 3.7, along with related pressure field simulations.

Here, Fig. 3.7a shows the pressure field measured during the experiment. The pattern, colloquially referred to as a "double accordion" pattern, is characteristic of operation in an environment

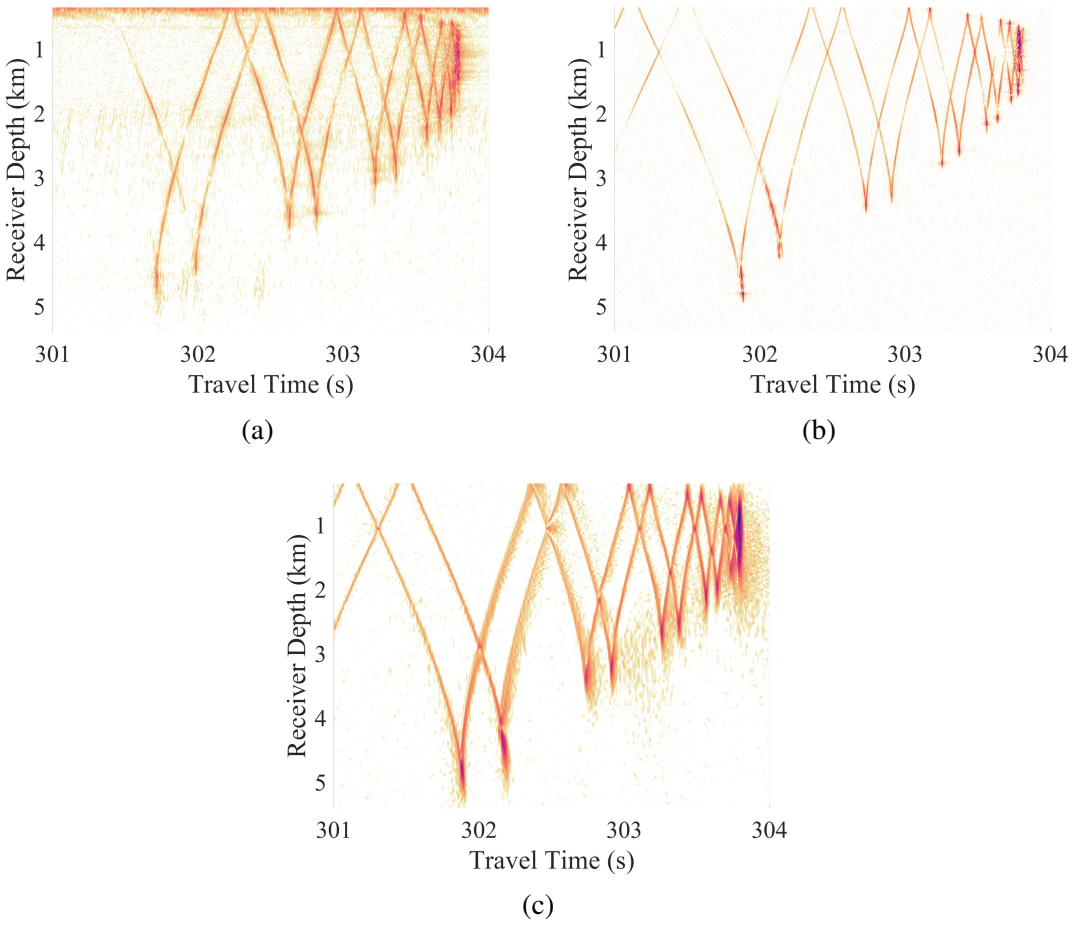

Figure 3.7: Example time-domain pressure field measurements and simulations at in-band and difference frequencies. (a) Pressure field measured during the PhilSea10 experiment, (b) pressure field predicted using parameters from the PhilSea10 experiment, (c) pressure field at the difference frequency predicted to mimic the PhilSea10 experiment

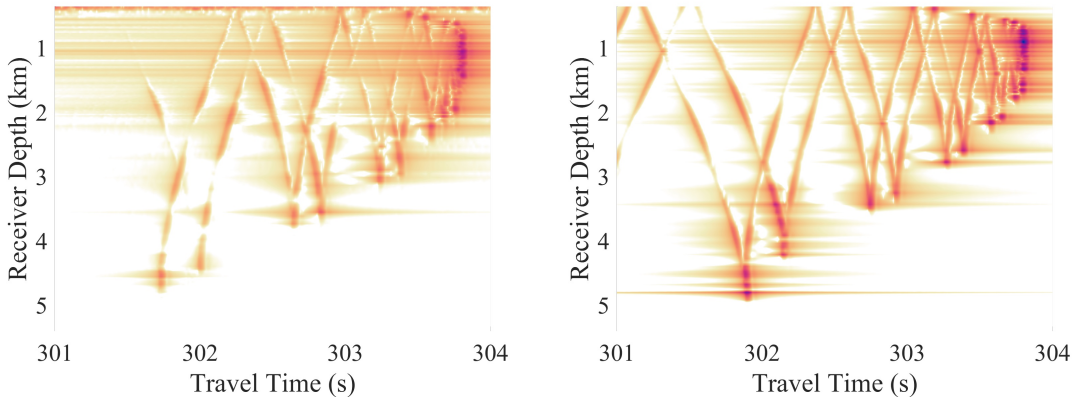

Figure 3.8: Example time-domain autoproduct measurements and simulations at difference frequencies. (a) Autoproduct measured during PhilSea10 experiment, (b) Autoproduct predicted using simulation

with a sound speed minimum in the bulk of the medium. Fig. 3.7b and 3.7c represent simulations, calculated using KRAKEN, of the same quantity. Fig. 3.7b represents the in-band field, with $f = 225 - 325\ Hz$, and Fig. 3.7c represents an out-of-band pressure field at $f = 1/16 - 5\ Hz$ that will be matched to an autoproduct in Section 3.4. Here, the fields show some differing characteristics. The measurements show greater noise outside of the arrivals. Additionally, the top several receivers show continuous noise identified during the experiment as strumming noise. Most importantly, there are differences in arrival time and amplitude character. Lastly, arrivals in Fig. 3.7c are wider than the other two panels. This width is not primarily governed by the field frequency, but rather by the bandwidth of the plotted field quantity.

Given pressure field measurements and predictions, the next step was to examine the character of measured and predicted autoproducts. For this purpose, autoproducts at difference frequencies of $\Delta f = 1/16 - 5\ Hz$ are calculated from measured and simulated pressure fields shown in Fig. 3.7a and 3.7b. Low difference frequencies are accessed using zero-padding [Jensen, F.B. *et al.* (2011)].

Here, Fig. 3.8a shows a measured (calculated using measured data) autoproduct, and Fig. 3.8b shows a predicted autoproduct. Notably, calculation is applied as a post processing step, and, therefore, an autoproduct can be measured using the same procedure as is used to measure

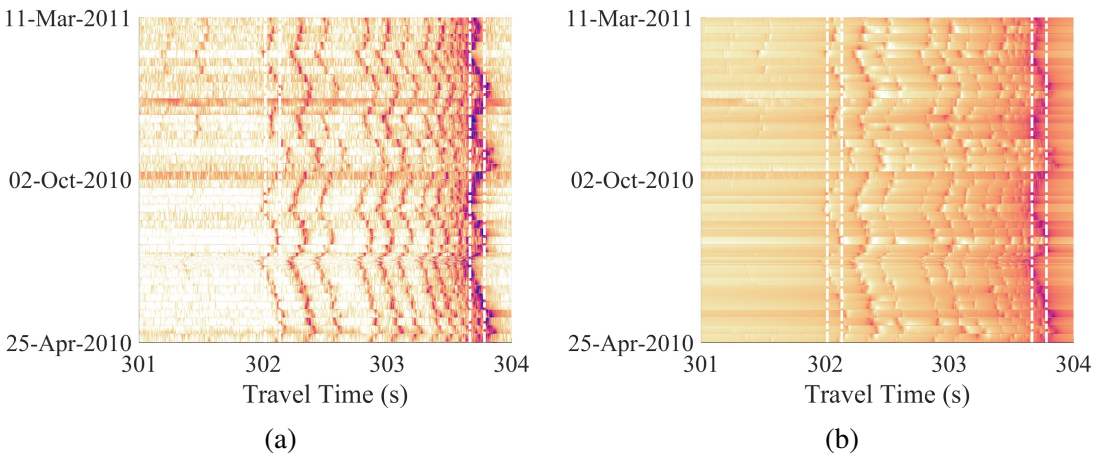

Figure 3.9: Example Arrival time fluctuations in PhilSea10 experiment, (a) pressure field fluctuations, (b) autoproduct fluctuations.

a pressure field. The autoproduct differs from the pressure field measurement primarily in the presence of the horizontal streaks that arise near to the convergence of ray-path arrivals. These streaks are postulated to be related to cross-terms, and are not explored further in this chapter.

Next, the measured data was used to provide insight into the environmental mismatch model that was applied in Section 3.3 and which will be applied in Section 3.5. To do this, measurements taken from a single receiver during multiple trials (snapshots) of the experiment are displayed graphically on top of one another in Fig. 3.9. This is referred to hereafter as a 'long-time/short-time plot' where "long-time" refers to the vertical axis (that encompasses several months) and "short-time" refers to a horizontal axis (that encompasses 3 seconds).

Fig. 3.9a shows the arrival time variation of the 35^{th} receiver in the array over all transmissions recorded from the T3 source (r_s = 450 km) for the pressure field, and Fig. 3.9b shows the same information for the autoproduct. Here, it is shown that the primary effect of environmental mismatch is to alter the time of arrival. This demonstrates the validity of using a time-front mismatch model as the basis for a synthetic test of the stability of the autoproduct in the presence of environmental mismatch in the deep ocean. The magnitude of the time delays measured during this experiment over the DVLA are given in Table 3.2.

	Number of Pings	$\Delta\tau$ Time Front Mismatch (ms)	Signal Start Time (s)	Signal End Time (s)	Transmission Start Date	Transmission End Date
T6	224	26.8	79	95	04/25/10	10/26/10
T5	376	33.0	134	150	04/25/10	03/25/11
T1	374	29.2	144	160	04/25/10	03/25/11
T4	376	73.0	247	263	04/25/10	03/25/11
T2	376	51.5	259	275	04/25/10	03/25/11
T3	376	86.2	294	310	04/25/10	03/25/11

Table 3.2: Source Timing and propagation information from PhilSea10 experiment (sources listed in order of increasing ground range from array).

3.5 Simulated Test of Autoproduct Stability in the Deep Ocean

Cross correlation between two unrelated vectors is a random process, and so two "unrelated" vectors are expected to have a non-zero cross correlation. The first step in the synthetic test is to determine the level of accidental matching that occurs between vectors that are different from one another. To accomplish this, each matching vector is correlated against a randomly generated noise vector. Noise vectors have zero-mean Gaussian random real and imaginary parts, and (because they are truly randomly generated) are expected to be completely unstable. These noise vectors are then cross correlated with calculated pressure field and autoproduct weight vectors that are calculated using the measured acoustic environmental information from the PhilSea10 experiment repeatedly to assess the probability density function (PDF) of this result. These results are shown in Fig. 3.10.

Fig. 3.10a shows the PDF of cross correlation magnitude from all cross correlation experiments. Here, all PDF's are roughly in line with one another, and show a general Rayleigh character [Pierce, A.D. (1994)]. Fig. 3.10b shows the phase of each trial, and the phases are seen to be generally uniformly distributed. This establishes two important results: first, an average cross correlation magnitude, $|\chi| \approx 0.1$ is no more stable than noise, and, second, that a cross correlation that is uniformly distributed in phase also resembles random correlation. These two criteria will be used to distinguish whether or not a cross correlation result is more stable than noise.

Synthetically testing the stability of pressure fields and autoproducts in the face of time-front mismatch is first undertaken by calculating three time-harmonic cross correlations for each sim-

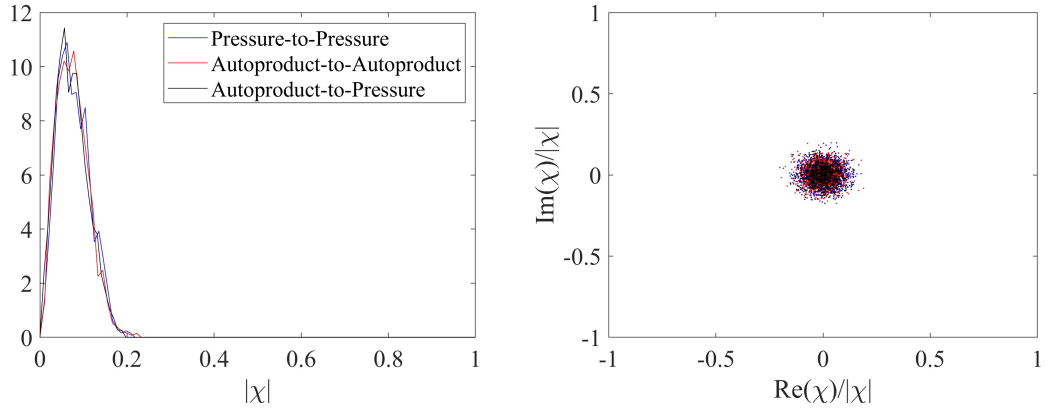

(a) (b)

Figure 3.10: Cross correlation between random noise and weight vectors, (a) PDF of cross-correlation magnitudes, (b) Cross-correlation magnitude/phase

ulated source in the face of varying levels of time front mismatch. The first cross correlation is pressure field to pressure field at the transmitting center frequency of the source, the second is between an autoproduct and pressure field at $\Delta f = 1\ Hz$, and the third is between an autoproduct and an autoproduct at $\Delta f = 1\ Hz$. The results of this calculation are shown in Fig. 3.11.

Fig. 3.11a and 3.11b both show the average magnitude of all cross correlation coefficients shown in this test. The difference between these plots is the x-axis. Fig. 3.11a plots the average correlation, $\langle|\chi|\rangle$ vs. $\log_{10}(\Delta\tau)$, and Fig. 3.11b non-dimensionalizes the x-axis by plotting $\log_{10} f\Delta\tau$. These plots demonstrate that both pressure fields and autoproducts decorrelate similar to one another in the presence of time-front mismatch. However, the relevant quantity here is the size of the arrival-time fluctuations relative to the temporal period of the carrying field (as given in Eq. (3.4)). The black lines, which represent average cross correlation between an autoproduct and a pressure field show much lower cross correlation on average, and also show a correlation that changes at different source ranges. This suggests that cross correlating autoproducts and pressure fields is an unstable process in the deep ocean. Fig. 3.11c displays the average phase of the cross correlation coefficient in all trials. This tells a similar story to Fig. 3.11a and 3.11b, that the correlation between like field quantities is stable in this synthetic test but the cross correlation between autoproduct and pressure field is unstable with respect to source range. This suggests that

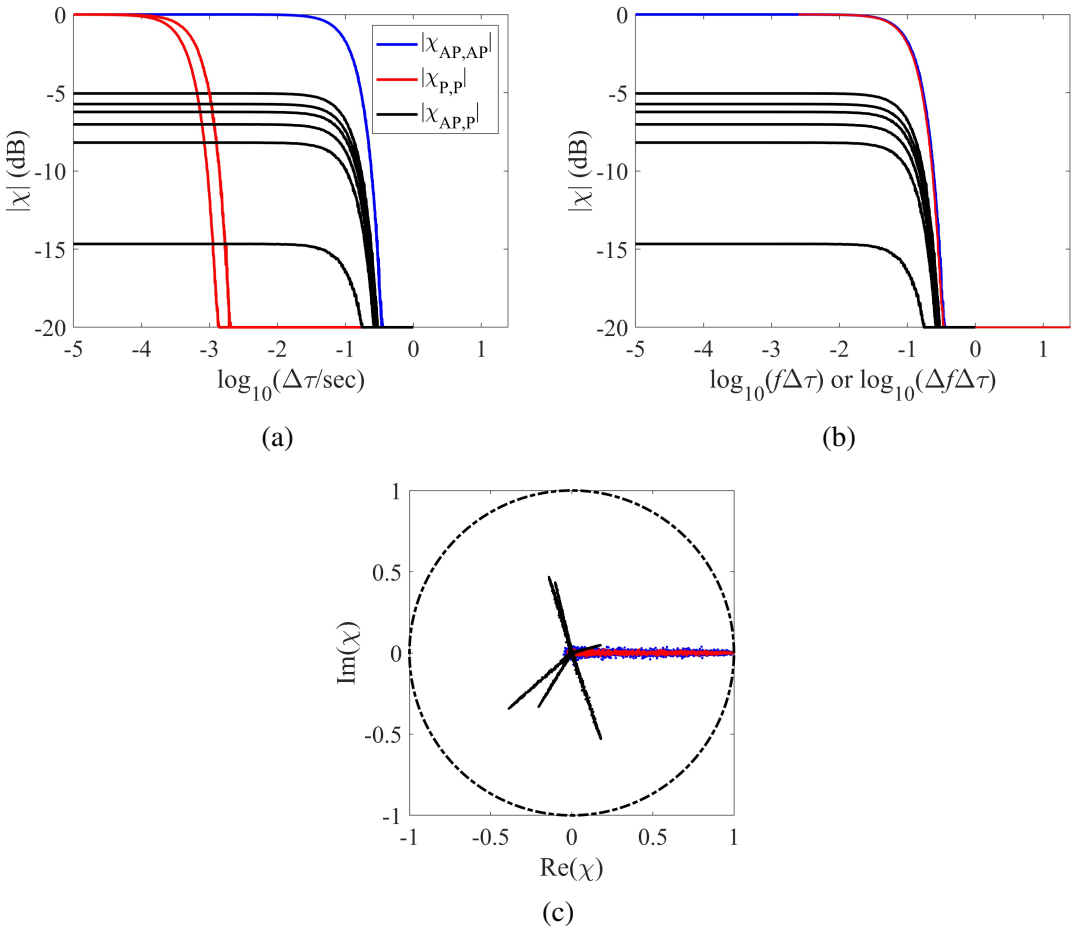

Figure 3.11: Cross correlation of all field quantities for varied levels of environmental mismatch. (a) Decorrelation of field quantities with respect to varied levels of arrival time fluctuation, (b) Decorrelation of field quantities compared to non-dimensionalized arrival time fluctuation, (c) Magnitude/Phase of cross-correlation for varied amounts of arrival time fluctuations.

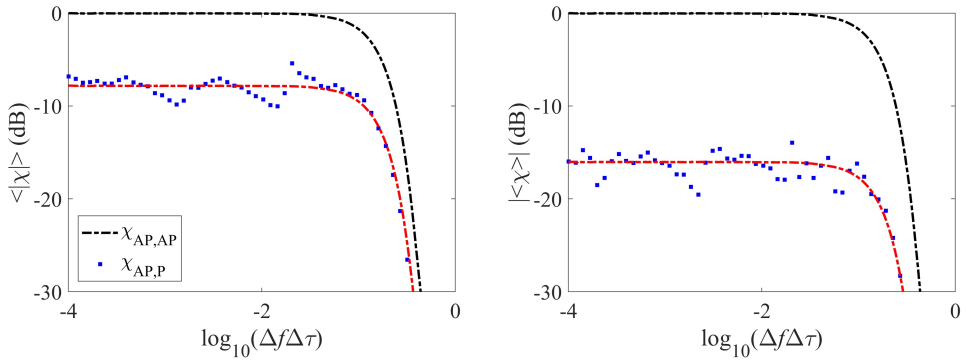

(a) (b)

Figure 3.12: Effect of autoproduct-to-field mismatch in refracting environment on magnitude of a cross correlation coefficient. (a) Incoherent average of cross-correlations, (b) Coherent average of cross correlations.

previous autoproduct matching algorithms, like Frequency Difference Matched Field Processing [Worthmann *et al.* (2015), Worthmann *et al.* (2017)], will struggle to perform source localization in the deep ocean because the underlying cross correlation of the field quantities is unstable.

To further investigate the stability of the autoproduct and pressure fields using cross correlation in a synthetic environment, a second test, intended to better mimic the experimental scenario, is undertaken. Here, the amount of random time delay at each source is held fixed and cross correlation is calculated over either a difference frequency bandwidth from $1/16$ to 5 Hz, or over the transmitting bandwidth of the pressure field. These quantities are plotted in Fig. 3.12 (magnitude only) and Fig. 3.13 (magnitude/phase). Cross correlations calculated between the pressure field are noise-like, and therefore unstable, at any frequency calculated. Hence, these do not appear in Fig. 3.12 and Fig. 3.13.

The remaining two cross correlations, cross correlation between two autoproducts and between an autoproduct and a pressure field at the difference frequency, are both shown in Fig. 3.12. In Fig. 3.12a and 3.12b, the behavior of these correlations is examined more closely. The difference between the plots is that Fig. 3.12a incoherently averages all cross correlations, and 3.12b coherently averages all correlations. In both plots, the black dashed curve is very consistent, which suggests that cross correlations at all ranges have similar average magnitude and phase. The red curve is the

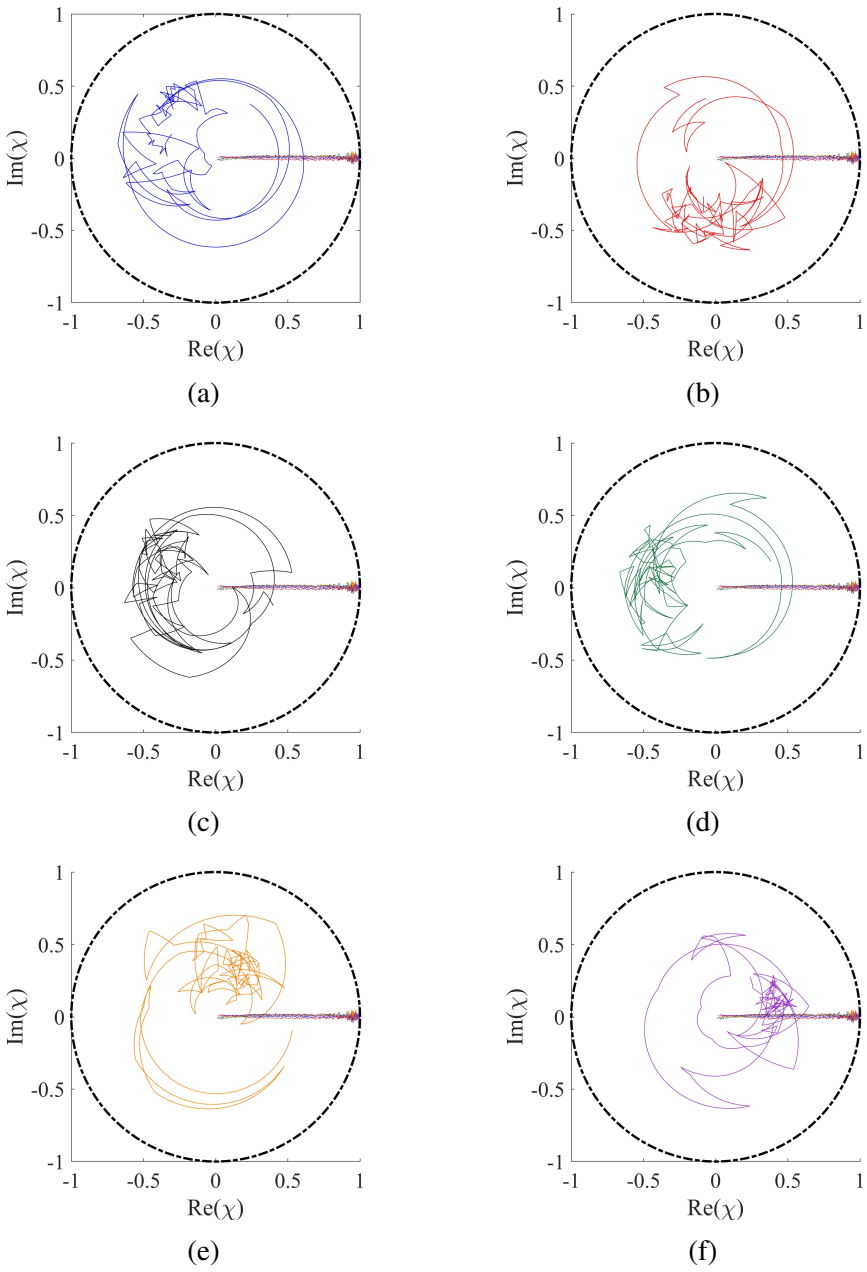

Figure 3.13: Effect of autoproduct-to-field mismatch in refracting environment on magnitude and phase of a cross correlation. (a) T6, r_s = 129 *km*,(b) T5, r_s = 210 *km*,(c) T1, r_s = 225 *km*,(d) T4, r_s = 379 *km*,(e) T2, r_s = 390 *km*,(f) T3, r_s = 450 *km*.

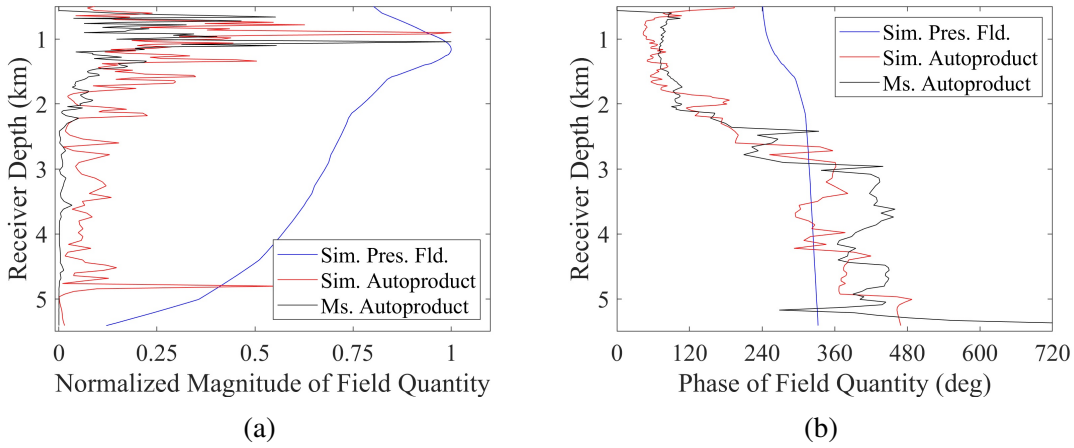

Figure 3.14: Plotted field quantity (a) magnitude and (b) phase values at $\Delta f = 0.5\ Hz$.

same as the black curve, downshifted by 8 and 16 dB in Fig. 3.12a and 3.12b respectively, and is meant to go through the middle of the blue dots. The blue dots represent average cross correlation between an autoproduct and pressure field at varied difference frequencies, and show significant fluctuation over the explored difference frequencies. Fig. 3.13 again tells a similar story, with autoproduct to autoproduct cross correlations stubbornly showing almost no average phase, and autoproduct to pressure field cross correlation showing little rhyme or reason in the face of varied Δf.

3.6 Measured Test of Autoproduct Stability in the Deep Ocean

Given the impressive stability of the autoproduct to time front mismatch in a synthetic deep ocean environment, pressure field to pressure field cross correlation and autoproduct to autoproduct cross correlation are explored using measured data. To start this experiment, a simple comparison between measured and predicted autoproduct quantities was undertaken to calibrate expectations and determine appropriate time conventions. This comparison is shown in Fig. 3.14, between a time-harmonic measurement of an autoproduct at $\Delta f = 0.5\ Hz$ taken from the measurement used to construct Fig. 3.8, a prediction of the same autoproduct made using KRAKEN [Porter (1992)], and a prediction of a pressure field at the difference frequency made using KRAKEN.

Fig. 3.14a shows the comparison between these three field quantities in magnitude, and Fig. 3.14b shows this comparison in phase. Initially, the red and black curve, that represent predicted and measured autoproducts, resemble one another while the blue curve, which represents a pressure field at the difference frequency, is visually different. Closer inspection demonstrates that there is significant magnitude mismatch between the autoproduct quantities in Fig. 3.12a, but the phase between these two quantities is very close. Phase is a more important factor in determining high cross correlation, in that it determines whether each individual cross correlation on the array adds constructively or destructively. However, the magnitude mismatch will be found to cause an issue for source localization. Strategies for mitigating this problem can be found in Chapter 5.

Given the generally positive results obtained by comparing the magnitude and phase of autoproducts, a test of measured cross correlation at a single difference frequency, $\Delta f = 0.5\ Hz$, was undertaken. Equivalent in-band pressure field tests are also calculated at the transmitting center frequency of each source. The results of this are shown in Fig. 3.15.

Fig. 3.15a shows the PDF of cross correlation magnitude between measured and predicted autoproducts at $\Delta f = 0.5\ Hz$ for all transmissions measured from all moored sources in the PhilSea10 experiment, and Fig. 3.15c shows the phase of each of these results. Fig. 3.15b and 3.15d are equivalent results for pressure fields. Here, it is clear the measured pressure field cross correlations are unstable at all ranges over the course of the experiment, in that they resemble the noise trials shown in Fig. 3.10 almost exactly. The autoproduct to autoproduct cross correlations, on the other hand, noticeably differ from noise and seem to truly offer increased stability in the face of environmental mismatch compared to their in band counterparts.

Given the success seen from cross correlating autoproducts at a difference frequency of $\Delta f = 0.5\ Hz$, the difference frequency was varied between $1/16\ Hz$ and $5\ Hz$ to see how this affects cross correlation at multiple difference frequencies. The result of this test is shown in Fig. 3.16 and 3.17. Here, Fig. 3.16 shows the average magnitude of this cross correlation for all sources over the explored difference frequency bandwidth.

The different colored markers shows the average cross correlation of each source over the

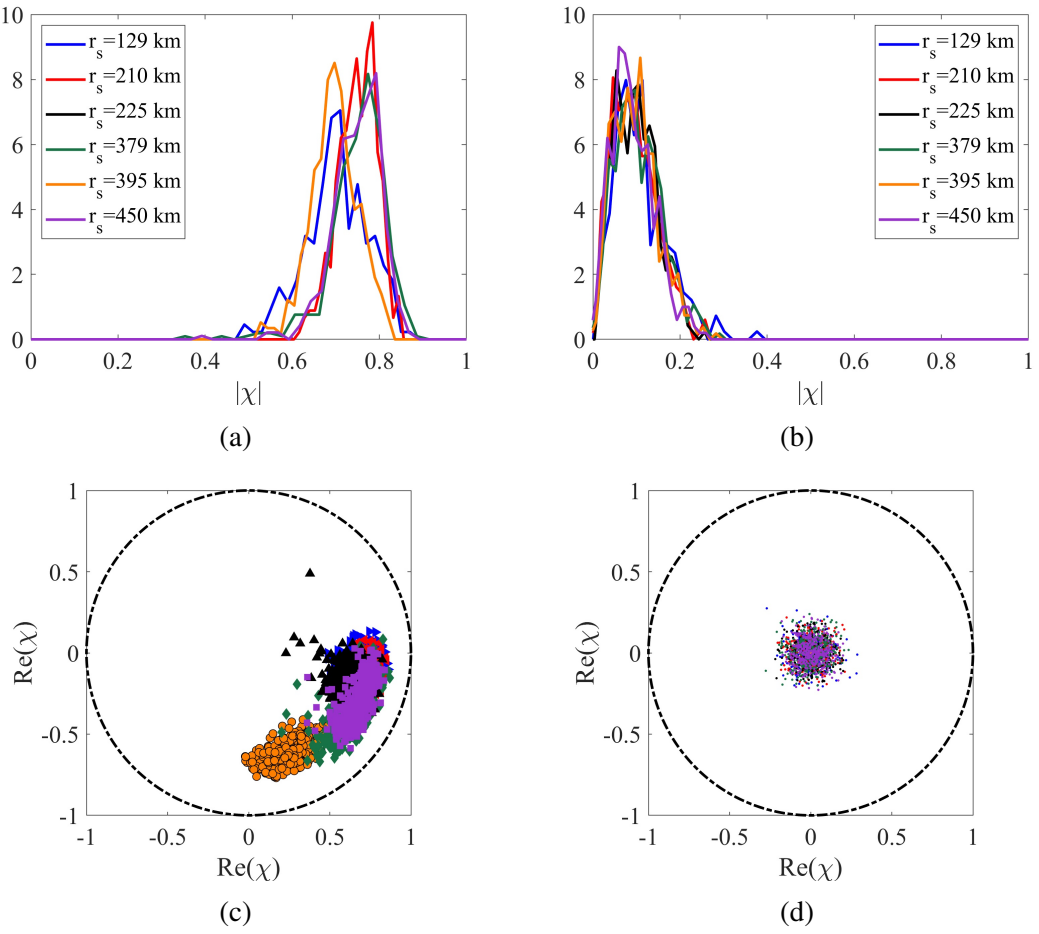

Figure 3.15: Probability density functions of cross correlation magnitude and phase for measured PhilSea10 data at $\Delta f = 0.5\ Hz$ or $f = f_c$. (a) Magnitude for autoproduct-to-autoproduct cross correlation, (b) Magnitude for pressure-to-pressure cross correlation, (c) Phase for AP-AP cross correlation, (d) Phase for P-P cross correlation.

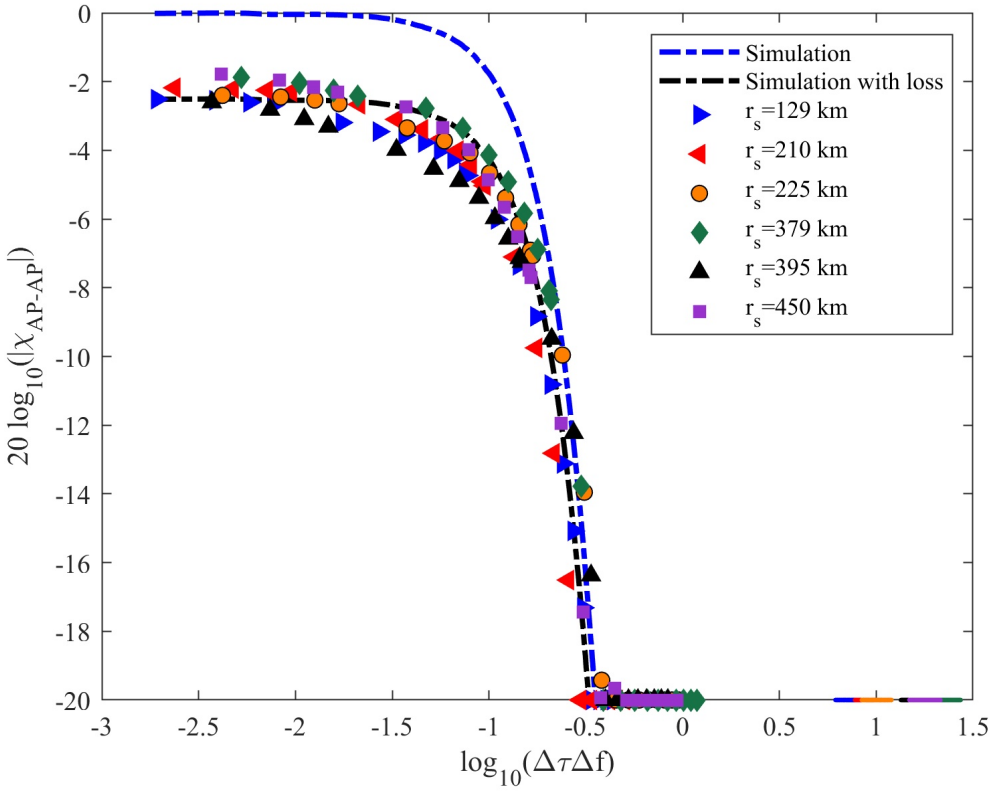

Figure 3.16: Magnitude of coherent average of cross correlation between measured and calculated autoproducts for all six PhilSea10 sources across many difference frequencies.

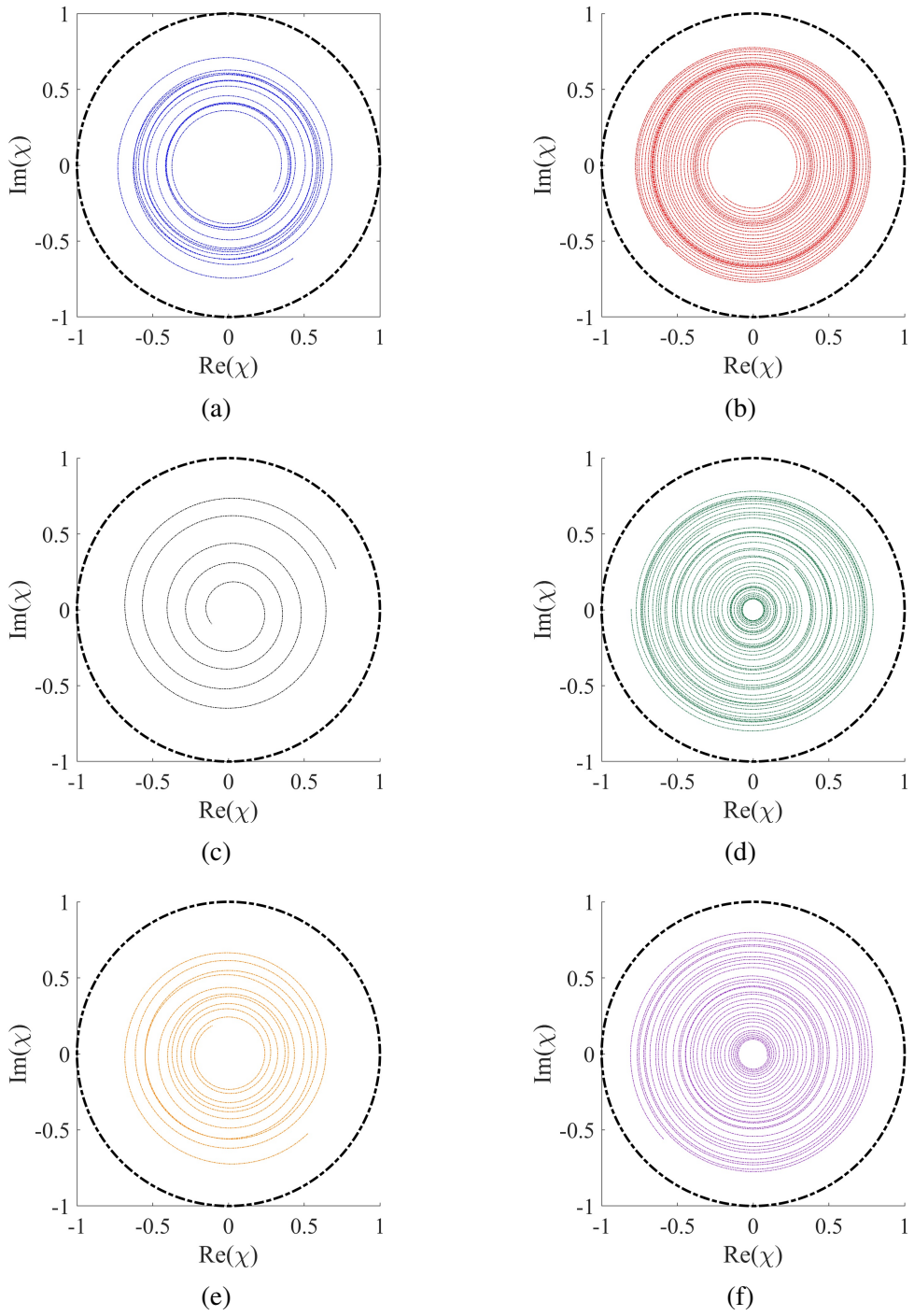

Figure 3.17: Magnitude/Phase of coherent average of cross correlation between measured and calculated autoproducts for all six PhilSea10 sources across many difference frequencies for (a) T6, r_s = 129 *km*,(b) T5, r_s = 210 *km*,(c) T1, r_s = 225 *km*,(d) T4, r_s = 379 *km*,(e) T2, r_s = 390 *km*,(f) T3, r_s = 450 *km*.

difference frequency bandwidth explored, with some smoothing undertaken to avoid saturating the plot. The blue dashed line is the simulated result, and the black dashed line is the same as the blue with 2.3 dB subtracted to go through the middle of the markers. In band results are shown with colored dots in the bottom right of the plot, and are generally all bad. Fig. 3.17 shows the average phase of the cross correlation coefficient for each source. Here, each curve looks like a spiral that decreases in magnitude with increasing Δf. While this initially doesn't indicate stability, the consistency of the phase change, $\partial(\arg(\langle\chi\rangle))/\partial\Delta f$, suggests that this data may actually provide further physical insight that is beyond the scope of this thesis. Overall, this result demonstrates that the autoproduct offers greatly increased stability compared to in-band pressure fields in the face of environmental mismatch.

3.7 Conclusion

The purpose of this chapter is to demonstrate that the autoproduct offers increased robustness to environmental mismatch relative to conventional pressure fields. This increased stability is demonstrated by cross correlating measured and predicted autoproduct fields because of the eventual goal of using the autoproduct as the fundamental element of a matched field-style source localization algorithm. The results of this study lend themselves to four conclusions. First, that the autoproduct is measurable in both refracting environments, like the deep ocean, and non-refracting environments, like the Lloyd's Mirror. Second, that it is possible to learn useful information by cross correlating an autoproduct and a pressure field at the difference frequency in a non-refracting environment like the Lloyd's Mirror, but that this cross correlation is not expected to yield useful information in a refracting environment like the deep ocean. Third, this chapter provides a model for environmental mismatch, time front mismatch, that is based on tomographic experiments that is easy to implement and seems to accurately represent physical mismatch in the deep ocean. Finally, this chapter demonstrates that the autoproduct can offer stability in the face of challenging levels of both modeled and physical environmental mismatch that would de-stabilize a measured pressure

field without requiring any additional work on the part of an operator.

CHAPTER 4

Autoproduct Cross-Term Analysis and Cancellation

4.1 Introduction

Autoproduct processing methods, including frequency-differencing, have been postulated to lose their featured robustness [Worthmann *et al.* (2015), Worthmann *et al.* (2017), Geroski & Dowling (2019)] in the face of cross-terms that arise as an unintended artifact of the nonlinear processing that make autoproducts more robust. These cross-terms can be categorized as either signal cross-terms, which are present in any multipath environment, and interferer cross-terms, that are present when other signals are measured along with a desired source. Initially, signal cross-terms were thought to be the cause of the low peak value, dynamic range, and peak-to-sidelobe ratio (PSR) that is observed in Frequency-Difference Matched Field Processing (FDMFP) results [Worthmann *et al.* (2015), Geroski & Dowling (2019)], but their effects were not severe enough to lead to failure. Interferer cross-terms, on the other hand, were thought to lead to a significant decrease in the noise rejection capacity of autoproduct based methods [Worthmann *et al.* (2017)], leading to their being undesirable for use outside of controlled experimental scenarios. These undesirable effects: low peak value, low dynamic range, low PSR, and low noise rejection capability, are found to be addressed by switching from field processing methods like FDMFP to autoproduct processing methods like FDSL [Geroski Dowling 2019] and Phase-Only Matched Autoproduct Processing [Geroski & Dowling (2021)]. Also, studies into the forms of signal [Geroski & Worthmann (2021)] and interferer [Geroski *et al.* (2021a)] cross-terms show that noise rejection methods can be used

to further mitigate the effects of cross-terms. This chapter explores and demonstrates the existence of cross-terms and analyzes their exact form, as well as demonstrating one of the major effects that cross-terms are expected to have on autoproduct processing methods and quantifies the improvements that can be achieved by using noise rejection methods to remove them.

Autoproduct cross-terms were known to exist both in early studies on frequency-difference beamforming [Abadi *et al.* (2011)] and in studies on k-radar and -sonar [Popstefanija *et al.* (1993), Silva *et al.* (2008)]. In early studies into frequency-differencing, the exact form of cross-terms was not analyzed because the cross-terms did not seem to be hindering the performance of the algorithms in question. Cross-terms were also observed to exist in [Lipa *et al.* (2018), Douglass *et al.* (2017), Worthmann & Dowling (2020a)], but were found to not affect the successful results that were found in each of these studies. Mitigation of signal cross-terms was discussed as the reason for implementing the bandwidth-averaging step of FDMFP [Worthmann *et al.* (2015)] and FD beamforming [Douglass *et al.* (2017)], but exact analysis of these terms in the context of frequency-differencing was not undertaken in the open literature until [Worthmann & Dowling (2017)] and their effect on source localization was not explored until [Geroski & Worthmann (2021)]. These studies precisely define the existence of signal cross-terms in a refracting environment that is well described using ray theory [Porter & Bucker (1987)], and finds that these terms appear to be both unstable and to mimic noise in a source localization context in that they seem to be coming from all places in the sound channel [Snieder *et al.* (2008), Ozanich *et al.* (2017)]. Because of this property, matrix-based noise rejection techniques are found to be useful in removing some of the negative effects of both signal- and interferer-cross terms in autoproduct processing methods.

Given the unstable and noise-like behavior of cross-terms in autoproduct processing, any number of methods are expected to remove their effects provided averaging can be employed. The simplest method for differentiating between stable and unstable signals in remote sensing is to coherently average several measurements [Usher (1964)]. This method is undesirable in matched-field-style localization algorithms for two reasons: (1) that in-band pressure fields are not expected to be stable when propagating over long distances [Finette & Mignerey (2018)], and (2) that pas-

sive remote sensing should not rely upon a source giving more than one signal. The first issue can be mitigated somewhat by employing incoherent processing [Dosso & Wilmut (2012), Fialkowski *et al.* (2001), Tollefsen *et al.* (2017)] if the received signal is expected to be unstable, but a calculated ambiguity surface is expected to be stable. This is the method that is used to find success in [Geroski Dowling 2019] for deep ocean source localization. Mitigating cross-terms coherently, however, is best achieved in a manner that is similar to compressive sensing [Gerstoft & Mecklenbauker (2015)] by taking advantage of available bandwidth to produce a better result. Specifically, in matrix processing methods, coherent and incoherent signals are found to differ significantly from one another in terms of their rank and sparsity in matrix representation and so can be removed using diagonal subtraction [Hald (2017)] or subarray coherence [Hald (2017), Quijano & Zurk (2017)]. Further, these two signals can be separated from one another using Robust Principal Component Analysis (RPCA) [Wright *et al.* (2009), Aravkin *et al.* (2014)], or Probabilistic Factorial Analysis [Dinsenmeyer *et al.* (2018)]. This chapter will show that it is also possible to distinguish these signals from one another using their spatial frequency, but further exploration of this idea is not undertaken because of the difficulty of representing spatial frequency information in a nonuniformly sampled array. These methods are found to perform well in removing cross-terms from autoproduct processing methods.

The remainder of this chapter is divided into five sections. Section 4.2 reviews the relevant theory, including the emergence of cross-terms in both the frequency-difference autoproduct and its Cross-Spectral Density Matrix (CSDM), the generalization of cross-correlation from Chapter 3 for CSDM processing, and the noise rejection techniques that will be used to remove cross-terms from the CSDM. Section 4.3 shows the emergence of signal- and interferer-cross-terms in a simple multipath environment, the Lloyd's Mirror, and quantifies the expected effects of cross-terms in this environment. Section 4.4 quantifies the improvements offered by using noise rejection techniques in the Lloyd's Mirror environment in using both synthetic and measured signals. Section 4.5 demonstrates the existence of cross-terms in the deep ocean, and shows the improvements offered when using noise rejection techniques to coherently remove either signal- or interferer-cross-terms.

Section 4.6 draws what conclusions are available from this chapter.

4.2 Theory

4.2.1 Autoproduct Theory and Emergence of Cross-Terms

Cross-terms in the frequency difference autoproduct arise because of the quadratic product used to construct them. The frequency-difference autoproduct, as given in Eq. (4.1), and the bandwidth-averaged frequency-difference autoproduct, given in Eq. (4.2), are both acknowledged to contain both signal- and interferer-cross terms.

$$AP_{\Delta}(\vec{r},\Delta\omega,\omega) = P^{*}\left(\vec{r},\omega-\frac{\Delta\omega}{2}\right)P\left(\vec{r},\omega+\frac{\Delta\omega}{2}\right) \tag{4.1}$$

$$\langle AP_{\Delta}(\vec{r},\Delta\omega)\rangle_{\omega} = \frac{1}{\Omega_{BW}}\int_{\Omega_L+\frac{\Delta\omega}{2}}^{\Omega_H-\frac{\Delta\omega}{2}} d\omega \frac{AP_{\Delta}(\vec{r},\Delta\omega,\omega)}{S^{*}\left(\omega-\frac{\Delta\omega}{2}\right)S\left(\omega+\frac{\Delta\omega}{2}\right)} \tag{4.2}$$

Here, AP_{Δ} is the frequency-difference autoproduct, P is a pressure field, measured at spatial location $\vec{r}$, and frequency ω. Here, the pressure field is assumed to be detected over a bandwidth $\Omega_L \leq \omega \leq \Omega_H$ and the bandwidth usable in constructing a bandwidth averaged autoproduct is $\Omega_{BW} = \Omega_H - \Omega_L - \Delta\omega$. When measuring a bandwidth-averaged frequency-difference autoproduct, the effect of a source signal waveform must be removed, as in [Lipa *et al.* (2018), Geroski & Worthmann (2021)]. However, when working with either an impulsive signal or when directly computing the Green's function of a medium [Porter & Bucker (1987), Porter (1992)], the bandwidth-average is an ensemble average. When the source waveform is unknown, as in most passive remote sensing applications, the CSDM of a frequency-difference autoproduct, given in Eq. (4.3) can be used instead.

$$R^{\Delta}_{mn}(\Delta\omega,\vec{r}_m,\vec{r}_n) = \langle AP^{*}_{\Delta}(\vec{r}_m,\Delta\omega,\omega)AP_{\Delta}(\vec{r}_n,\Delta\omega,\omega)\rangle_{\omega} \tag{4.3}$$

Here, R^{Δ}_{mn} is the CSDM of the frequency-difference autoproduct, measured on receivers at spatial locations $\vec{r}_m$,$\vec{r}_n$. Often, spatial arguments are omitted and represented instead in the m, n indices of the CSDM. Using the CSDM, incoherent cross correlation can be computed using Eq. (4.4).

$$\chi(\omega) = w_m(\omega) R_{mn}(\omega) w^*_n(\omega) \tag{4.4}$$

Eq. (4.4) uses Ricci tensor notation [Bishop, R.L. & Goldberg, S.I. (1968)] to concisely express an implied double summation. In this convention, repeated indices (in this case, m, n) are summed over. This is considered an incoherent cross correlation between CSDM R_{mn} and weight vector w_m,w_n because it is a real, positive definite number. And, when each object is normal in an L_2 sense [Finette & Mignerey (2018)], the number is bounded $0 \leq \chi \leq 1$. It should be noted here that the cross correlation in Chapter 3 uses two vectors that are normal in an L_2 sense. This metric will be used to compare a measured autoproduct CSDM and calculated weight vector w in this chapter. Cross-terms that cannot be removed from a CSDM are expected to match a weight vector only incidentally (see: relevant discussion in Chapter 3), and so to decrease the expected value of cross-correlation.

Signal cross-terms arise in autoproducts, and their related bandwidth-averages and CSDM's. They are most easily understood by assuming that a measured pressure field obeys ray theory [see: Jensen, F.B. *et al.* (2011)] and can be decomposed into a sum of incident ray paths, as in Eq. (4.5).

$$P(\vec{r}, \omega) = \sum_n A_n exp(i\omega\tau_n) \tag{4.5}$$

Here, A_n,τ_n are calculated eigenray path amplitudes and travel times. These can be explicitly computed using image theory in simple environments like the Lloyd's Mirror, isovelocity sound channel, Pekeris waveguide, or others, and can be calculated using software like BELLHOP [Porter & Bucker (1987)] in more general refracting environments. Given a set of eigenrays with computed amplitudes and travel times, the pressure field can be analytically computed. Using this pressure

field, the autoproduct can be computed using Eq. (2), and decomposed into (desirable) self-terms and (undesirable) cross-terms, as in Eq. (4.6).

$$\langle AP_{\Delta}(\vec{r},\Delta\omega)\rangle_{\omega} = \sum_{n=m}|A_n|^2 exp(i\Delta\omega\tau_n) + \sum_{n\neq m}A_n^* A_m exp\left(\frac{i\Delta\omega}{2}(\tau_n+\tau_m)\right)sinc\left(\frac{\Omega_{BW}(\tau_n-\tau_m)}{2}\right) \quad (4.6)$$

In Eq. (4.6), the original postulate of the frequency-differencing field, that the frequency-differencing autoproduct resembles a pressure field at the difference frequency, can be understood. The first summation, referred to hereafter as a 'self-term,' has the same number of ray paths as the pressure field used to construct the autoproduct and these paths seem to vary in travel time at the difference frequency, $\Delta\omega$, as opposed to the in-band frequency ω. This hypothesis is found to break down [see: Worthmann & Dowling (2020b)] in refracting environments where $A_n \in \mathbb{C}$, such as arises when ray paths pass through a caustic. The second summation is the cross-term summation, and the *sinc* function is the un-normalized cardinal *sinc* function [Geroski & Worthmann (2021)]. These terms are seen to be mitigated when a greater amount of bandwidth, Ω_{BW}, is used to calculate the bandwidth average providing that two ray paths do not arrive at a receiver at the same time. Additionally, the bandwidth average is found to provide diminishing returns with increasing bandwidth when $\Omega_{BW}(\tau_n - \tau_m) > 2\pi$. While it is possible to creatively choose the amount of bandwidth to average over to completely cancel a cross term ($\Omega_{BW}(\tau_n-\tau_m) = 2\pi n : n \in \mathbb{Z}$) at a specific receiver in an array, in practice it is best to use all bandwidth available. While these terms are suppressed in the infinite bandwidth limit, removal of cross-terms from an autoproduct CSDM is not necessarily possible even using infinite bandwidth.

Both signal- and interferer-cross-terms in an autoproduct CSDM are significantly more complicated to compute analytically. Full expressions for signal cross-terms can be found in [Geroski Worthmann 2021] and interferer cross-terms can be found in [Geroski *et al.* (2021b)]. For the sake of brevity, detailed derivations are omitted from this thesis. Both signal- and interferer-cross-terms can be analyzed as arising from a measured pressure field with two components, as in Eq. (4.7).

$$P(\vec{r},\omega) = P_1(\vec{r},\omega) + P_2(\vec{r},\omega) \tag{4.7}$$

$$SIR(P_1,P_2) = 10log_{10}\frac{\int_{V,\Omega} d\vec{x}d\omega|P_1(\vec{r},\omega)|^2}{\int_{V,\Omega} d\vec{x}d\omega|P_2(\vec{r},\omega)|^2} \tag{4.8}$$

Here, P_1 and P_2 are the first and second components of a pressure field. In signal cross-term language, these can be considered eigenray paths. In interferer cross-term language, these are emitted by separate sources: one of which is considered signal in an application and the other of which is considered interference or noise. Their relative contribution is given in Eq. (4.8), here dubbed "SIR" for signal-to-interferer ratio, and is referred to as SNR (for signa-to-noise-ratio) when P_2 is a noise field. Naturally, multi-source configurations can be considered. Using Eq. (4.3), the bandwidth-averaged autoproduct and CSDM of this measurement will approach the results given in Eq. (4.9) and Eq. (4.10).

$$\langle AP_\Delta(\vec{r},\Delta\omega)\rangle_\omega = \langle AP_\Delta^{11}(\vec{r},\Delta\omega)\rangle_\omega + \langle AP_\Delta^{12}(\vec{r},\Delta\omega)\rangle_\omega + \langle AP_\Delta^{21}(\vec{r},\Delta\omega)\rangle_\omega + \langle AP_\Delta^{22}(\vec{r},\Delta\omega)\rangle_\omega \tag{4.9}$$

$$\left\langle R_{mn}^\Delta(\Delta\omega)\right\rangle_\omega = \left\langle R_{1111}^\Delta(\Delta\omega)\right\rangle_\omega + \left\langle R_{1212}^\Delta(\Delta\omega)\right\rangle_\omega + \left\langle R_{2121}^\Delta(\Delta\omega)\right\rangle_\omega + \left\langle R_{2222}^\Delta(\Delta\omega)\right\rangle_\omega \tag{4.10}$$

In Eq. (4.9) and Eq. (4.10), terms labelled "1" or "2" represent the result that comes out of multiplying pressure terms (from Eq. 4.7) in the given order. Hence, $\langle AP_\Delta^{11}(\vec{r},\Delta\omega,\omega)\rangle$ arises from the term $\langle P_1^*(\omega-\Delta\omega/2)P_1(\omega+\Delta\omega/2)\rangle_\omega$. Therefore, in Eq. (4.9), $\langle AP_\Delta^{11}(\vec{r},\Delta\omega,\omega)\rangle$ and $\langle AP_\Delta^{22}(\vec{r},\Delta\omega,\omega)\rangle$ represent the self-term component, and the other terms represent the cross-terms. The autoproduct CSDM, given in Eq. (4.9), ought to have sixteen terms, but the four that are given are the ones that are not expected to vanish from the bandwidth average assuming: $\langle P_1^*(\vec{r},\omega-\Delta\omega/2)P_2(\vec{r},\omega+\Delta\omega/2)\rangle_\omega \to 0$ that the two components of the pressure field are incoherent in

frequency. Hence, terms like $\langle R_{1112} \rangle$ are expected to not contribute to the final form of the CSDM except in circumstances beyond the scope of this thesis. One example of this would be attempting to simultaneously localize multiple sources. These terms can be further classified into "self-self," "self-cross," and "cross-cross" terms within the CSDM, as in Eq. (4.11).

$$\left\langle R^{\Delta}_{mn}(\Delta\omega) \right\rangle_{\omega} = \left\langle R^{SS}_{mn}(\Delta\omega) \right\rangle_{\omega} + \left\langle R^{SC}_{mn}(\Delta\omega) \right\rangle_{\omega} + \left\langle R^{CC}_{mn}(\Delta\omega) \right\rangle_{\omega} \tag{4.11}$$

Here, the S and C represent "self" and "cross" terms. In general, the self-self terms are considered desirable in autoproduct processing methods. Care is taken in all methods to not remove these terms. The self-cross terms are primarily found to vanish except near a reflecting boundary (see: Section III, Lipa et. al. 2018), and can be avoided by not using receivers positioned near a known reflecting boundary. Cross-cross terms, on the other hand, are found to be present in all receiving geometries explored and must be removed using advanced methods. These terms are found to only sparsely populate the CSDM, and can be coherently removed using advanced noise rejection methods.

4.2.2 Noise-Rejection Techniques

Any number of techniques can be used to distinguish between signals as they are measured on an array. In general, this paper focuses on differentiating between the signals using either spatial frequency or matrix rank. The first method, dubbed Δk filtering, comes from another noise rejection technique [Carriere *et al.* (2014)] that is usually implemented in conventional CSDM-based signal processing using vertical arrays. This technique recognizes that, in an acoustic waveguide like the ocean, rays are only expected to propagate over long distances at certain angles. A ray traveling horizontally (broadside to a vertical array) when it arrives at the array will have a wavenumber (or spatial frequency) of zero. The maximum spatial frequency a ray can carry occurs when it is traveling vertically in the sound channel (referred to as array end fire). This spatial frequency can be determined over the CSDM by taking an FFT in each dimension. Any sound above the end fire

spatial frequency can be digitally filtered. If the user expects that the waveguide will attenuate ray paths that would arrive at an angle above a critical angle, a sharper filter can be applied. This technique is not often used in conventional array signal processing because the array doesn't sample near the Nyquist frequency of rays traveling at many angles and frequencies. Given that concern, this technique is much more applicable to frequency-differencing, which accesses low frequencies. However, the FFT is only used for uniformly sampled signals. So, realistic implementation of this idea is only mentioned here in examining the presentation of the cross terms, rather than in the context of improving array signal processing techniques.

All noise rejection algorithms in this thesis that are explored arise from the idea of rejecting random noise from a CSDM that has been ensemble averaged in time, as in [Hald (2019)]. The idea in these cases is that a user is distinguishing between two signals: a coherent signal that is useful, and a fluctuating signal that is not. Repeated averaging over the measurements is found to cause the coherent signal to remain more or less the same, and the incoherent signal to destructively interfere everywhere except for the diagonal. Given this, a first attempt at removing the incoherent signal is found in diagonal subtraction or diagonal zeroing [Hald 2017], described using Eq. (4.12).

$$R^1_{mn}(\omega) = R_{mn}(\omega) - R_{m=n}(\omega) \tag{4.12}$$

Here, a calculated CSDM has its diagonal elements set to zero. It should then be re-normalized using the L_2 convention. This technique is approximate, but was notably also used in the original paper on Matched Field Processing [Bucker (1976)] to improve dynamic range and PSR of a calculated ambiguity surface. This technique can be replicated in autoproduct CSDM's in exactly the same way as in conventional CSDM's. Here, autoproduct CSDM's do not necessarily require snapshot averaging as they can take advantage of bandwidth averaging.

Another analysis of the differing forms of signal and noise in a CSDM comes from considering the algebraic structure of each portion of the CSDM. A CSDM constructed from a single field sample is a matrix outer product (see: Chapter 2, Eq. 2.4) that is rank-1 by definition. If the signal portion of the CSDM is thought to be static, then adding many samples of it together is expected

to remain rank-1. The noise portion of the CSDM, which is fluctuating over time, is expected to approach a full-rank representation with sufficient averaging. This intuition about the two signals is borne out by the previous observation: that the signal term is complete in the CSDM, and the noise is sparse and primarily is represented on the diagonal. Robust Principal Component Analysis (RPCA) [Wright *et al.* (2009), Aravkin *et al.* (2014)] seeks to decompose a noisy CSDM into two parts: a complete, low-rank "signal" part and a sparse, full-rank "noise" part. This is accomplished using Eq. (4.13)-(4.15) to form this observation into a convex optimization problem that can be solved on modern computers.

$$\min_{S,N} rank(S_{mn}) + \gamma ||N_{mn}||_0 \tag{4.13}$$

$$\text{given: } S_{mn} + N_{mn} = R_{mn}$$

$$\min_{S,N} ||S_{mn}||_* + \lambda ||N_{mn}||_1 \tag{4.14}$$

$$\text{given: } S_{mn} + N_{mn} = R_{mn}$$

$$R^2_{mn}(\omega) = S_{mn} \tag{4.15}$$

Here, Eq. (4.13) postulates that a CSDM, R_{mn}, decomposes into two matrices that are the solution to the given constrained (nonconvex) optimization problem. The function $rank(\circ)$ identifies the rank of the matrix, or the minimum number of eigenvectors required to represent it. The sparsity of the matrix is measured by $\| \circ \|_0$ and γ is the optimization variable. This optimization problem is found to be intractable for variable γ, and so is re-posed in Eq. (4.14) where $\| \circ \|_*$ is the nuclear norm of the matrix, $\| \circ \|_1$ is the 1-norm of the matrix, and λ is the new optimization variable. It ought to be noted that a free and open-source implementation of RPCA [Aravkin *et al.* (2014)] is used in this thesis for the purpose of easy replicability by an interested member of the community. One more technique is used to accelerate this process in this thesis, which assumes

that the desired part of a CSDM that is represented by a single eigenvector dominates the CSDM. Therefore, the principal (largest) eigenvector is used in place of the full CSDM, as in Eq. (4.16).

$$R^3_{mn}(\omega) = v^*_{1,m} v_{1,n} \tag{4.16}$$

Here, v_1 is the principal (represented by the largest eigenvalue) eigenvector of the initial CSDM, R_{mn}. This matrix does not need to be re-normalized when using standard eigenvector conventions. These techniques are generally found to be successful in eliminating both signal and interferer cross-terms. Generally, the eigendecomposition method given in Eq. (4.16) is found to be better than RPCA in scenarios where both succeed, but is less robust than RPCA.

One final noise rejection technique, outlined in [Hald (2019)], is used in this study. This uses canonical coherence to determine which part of a measured signal is important on a subarray and which is not. This algorithm can be implemented following Eq. (4.17)-(4.21).

$$\alpha \in X, \beta = X - \alpha$$

$$R^{\Delta}_{mn} = \begin{bmatrix} R_{\alpha\alpha} & R_{\alpha\beta} \\ R_{\beta\alpha} & R_{\beta\beta} \end{bmatrix} \tag{4.17}$$

$$K = G^{1/2}_{\alpha\alpha} G_{\alpha\beta} G^{1/2}_{\beta\beta} \tag{4.18}$$

$$K = U \Sigma V^T \tag{4.19}$$

$$P = G^{1/2}_{\alpha\alpha} U \Sigma^{1/2}, Q = G^{1/2}_{\beta\beta} V \Sigma^{1/2} \tag{4.20}$$

$$\tilde{R}_{\alpha\alpha} = PP^T, \tilde{R}_{\beta\beta} = QQ^T \tag{4.21}$$

Here, X represents the full array that is used to measure the CSDM, and α,β represent subarrays that span X. If the subarrays are continuous, the CSDM can be represented as in Eq. (4.17). The

representation is more complex if the subarrays are not continuous, but the decomposition method does not require such a choice. Given the decomposition, the subarray coherence can be measured using the definition of canonical coherence, given in Eq. (4.18) and defined in a coherence matrix K. This matrix is then decomposed using an SVD algorithm, as in Eq. (4.19), and can be used to reconstruct matrices P,Q (as in Eq. 4.19) that represent original input block matrices $R_{\alpha\alpha}$,$R_{\beta\beta}$ from Eq. (4.17) that have their incoherent components suppressed. This decomposition method works for both conventional and autoproduct processing methods. A similar algorithm is here proposed in Eq. (4.22)-(4.27) that only works for autoproduct processing methods and arises through sub-band processing.

$$\alpha \in \Omega, \beta = \Omega - \alpha$$

$$\begin{aligned} R_{\alpha\alpha} &= \langle AP^*_\Delta(\vec{r}, \Delta\omega, \omega \in \alpha) AP(\vec{r}, \Delta\omega, \omega, \omega \in \alpha) \rangle_\omega \\ R_{\alpha\beta} &= \langle AP^*_\Delta(\vec{r}, \Delta\omega, \omega \in \alpha) AP(\vec{r}, \Delta\omega, \omega, \omega \in \beta) \rangle_\omega \\ R_{\beta\beta} &= \langle AP^*_\Delta(\vec{r}, \Delta\omega, \omega \in \beta) AP(\vec{r}, \Delta\omega, \omega, \omega \in \beta) \rangle_\omega \end{aligned} \tag{4.22}$$

$$K = G^{1/2}_{\alpha\alpha} G_{\alpha\beta} G^{1/2}_{\beta\beta} \tag{4.23}$$

$$K = U \Sigma V^T \tag{4.24}$$

$$P = G^{1/2}_{\alpha\alpha} U \Sigma^{1/2}, Q = G^{1/2}_{\beta\beta} V \Sigma^{1/2} \tag{4.25}$$

$$\tilde{R}_{\alpha\alpha} = PP^T, \tilde{R}_{\beta\beta} = QQ^T \tag{4.26}$$

$$\tilde{R}^\Delta_{mn} = \tilde{R}_{\alpha\alpha} + \tilde{R}_{\beta\beta} \tag{4.27}$$

Here, Ω represents the measured frequency of the source, and α,β are sub-bands that cover the entirety of Ω. This works in frequency-differencing because the self-terms are expected to be coherent over a bandwidth where cross-terms are not (see: Eq. 4.6). When these canonical coherence methods are utilized in the thesis, they are calculated for three equal subarrays/sub-bands each: first with continuous division of the space, second with interlocked elements of the space, and third with random elements of the space. The recommendation to choose these three is given first in [Hald (2019)]. Each of these methods is implemented in this chapter. They are found to reject cross-terms well, provided that the cross-terms are not sufficiently well resolved to be coherent over the array.

4.3 Emergence of Signal and Interferer Cross Terms Lloyd's Mirror

Analysis of the emergence of signal- and interferer-cross-terms is most easily conducted in the simplest multipath environment: the Lloyd's Mirror [Pierce, A.D. (1994)]. This environment is chosen because a simple analytic solution based on the Method of Images exists, and similar analyses with other wave propagation phenomena like electromagnetics [Jackson, J.D. (1999)] and vibrational waves [Maurice, E.W. *et al.* (1957)] can be carried out following the same methodology. This environment places a source in a semi-infinite, homogeneous environment with sound speed $c_0 = 1500\ m/s$ chosen to match the nominal sound speed in water. This medium is bounded above by a planar, pressure release surface with a nondispersive reflection coefficient $R = -1$. This environment is shown in Fig. 4.1.

The source is placed $z = 20.4\ cm$ from the reflecting boundary and $r = 32.5\ cm$ from a vertical receiving array. This environment is chosen initially because of its simplicity and because of the existence of a dataset that was measured in a controlled, laboratory water tank for the purpose of analyzing autoproducts [Lipa *et al.* (2018)]. The number of receivers and their separation is varied during this analysis, based on whether a synthetic or measured test is being conducted.

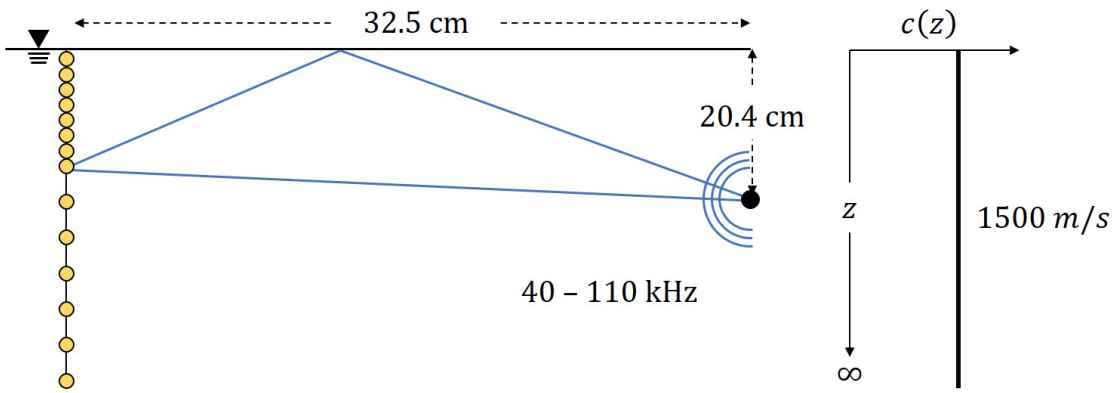

Figure 4.1: Schematic of the acoustic environment with a monopolar acoustic source placed at depth ($d = 20.36\ cm$), and range ($r = 32.46\ cm$) away from an array with N receivers. Source transmission is processed in frequency range $40 - 110\ kHz$. The array is 40 cm long, and is sampled at $\Delta z = 0.1\ cm$ for $z < 10\ cm$ and at $\Delta z = 0.5\ cm$ to a depth of $z = 40\ cm$. Surface boundary condition is assumed to be a pressure release.

Acoustic pressure fields are generated using this environmental description for an array of $N = 161$ receivers positioned from the reflecting boundary down to a depth of $z = 40\ cm$ for frequencies $f = 40 - 110\ kHz$. Using these measured pressure fields, frequency-difference auto-product CSDM's are calculated at $\Delta f = 25\ kHz$, and are decomposed into self-self, self-cross, and cross-cross term components in Fig. 4.2.

Each panel of Fig. 4.2 shows a CSDM, and uses domain coloring [Wegert, E. (2012)] to simultaneously convey both complex magnitude and phase information. A phase colorbar, chosen to be perceptually uniform [Kovesi (2015)] over all angles is appended on to the right side of the figure, and the brightness of each color conveys the magnitude of each bin. In Fig. 4.2, it can first be seen that Figs. 2b-2d can be added together coherently to produce Fig. 4.2a. It should further be noted that each component of the CSDM cannot be readily accessed outside of a controlled synthetic test. One goal of this chapter is to isolate an equivalent of Fig. 4.2b from an equivalent of Fig. 4.2a without using information not directly embedded into the measured pressure field. Here, it can be seen that Fig. 4.2b obeys the intuition given in Section 4.2 in that it is complete and visually possesses lower spatial frequency content. The spatial frequency content will be examined more closely in Section 4.4. Fig. 4.2c seems to only have definition near the reflecting boundary of

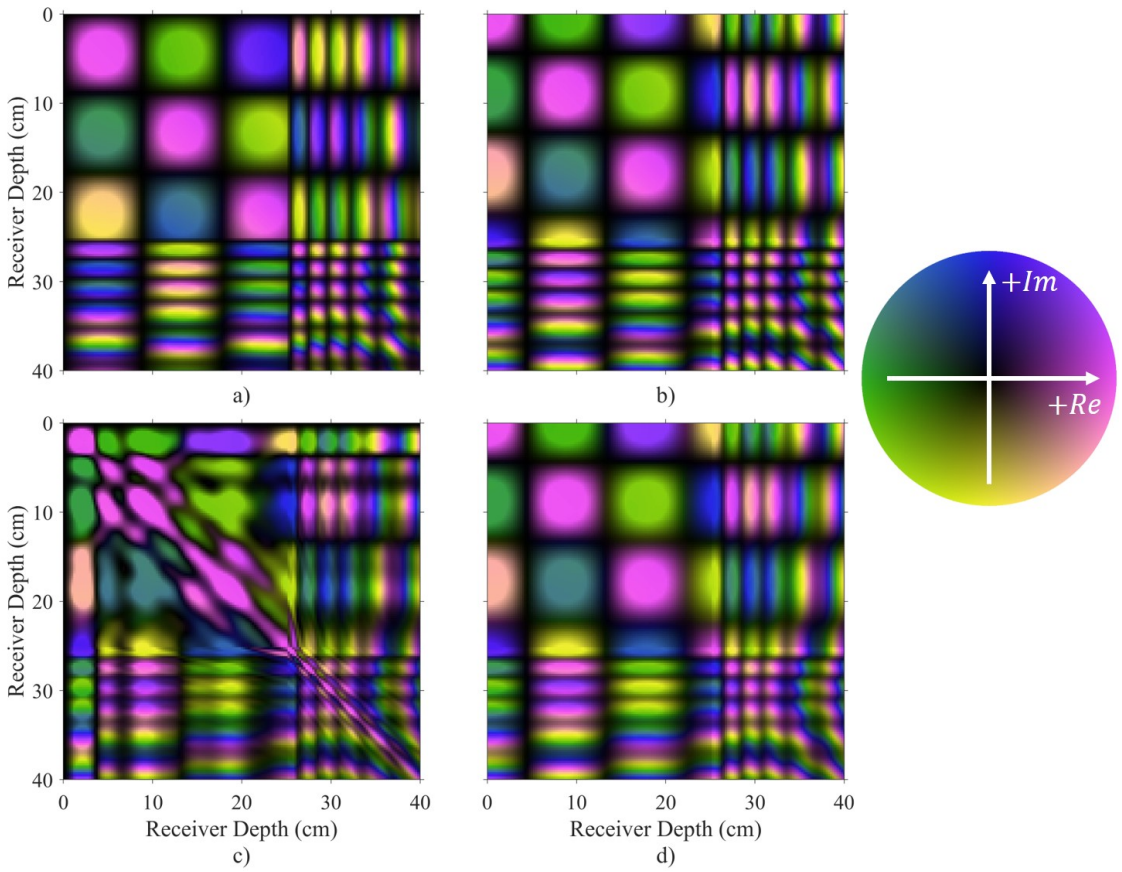

Figure 4.2: Simulated Autoproduct CSDM in a Lloyd's Mirror at $\Delta f = 25\ kHz$ environment normalized by source-receiver distance, (a) full CSDM, (b) isolated self-self-terms, (c) isolated self-cross terms, (d) isolated cross-cross terms

the environment. This result is also given in [Worthmann & Dowling (2017), Lipa *et al.* (2018)]. Fig. 4.2d is similarly confined, but this time near the primary diagonal of the CSDM. It should be noted that the self-cross terms are less concerning than cross-cross terms, because receivers near reflecting boundaries can be removed and can show higher noise levels in the field because of the presence of strong surface interference [Blae & Chase (1971)] like shipping noise and precipitation. Additionally, the deep ocean measurements analyzed in other parts of this thesis [Worcester *et al.* (2013)] showed significant strumming noise near the surface. The cross-cross terms, shown in Fig. 4.2d, cannot be removed in the same manner.

Given the existence of signal cross-terms, the next step was to examine the form of cross-terms that arise from the presence of an interferer. Here, the interfering source is chosen to be white noise that is spread evenly over the array. This choice is made because noise is an omnipresent interferer in signal processing, and the white noise model is the most commonly used one. Here, the relative strength of signal and interference is categorized using Eq. (4.8), and here signal-to-interferer ratio becomes "signal-to-noise ratio" (SNR). The form of a CSDM is tested in a synthetic environment using an SNR of 0 dB, and the results of this test are displayed in Fig. 4.3.

Here, Fig. 4.3b exactly corresponds to Fig. 4.2a. Figs. 4.3c and 4.3d represent the interferer cross terms, and are not seen to have the same desirable properties that were seen when analyzing signal cross-terms. Most particularly, neither of these terms presents as sparse. These two terms become more prominent as SNR is decreased, and this will lead to the downfall of diagonal zeroing, RPCA, and eigen-decomposition at low SNR as the noise terms come to dominate larger portions of the CSDM. At higher SNR, these cross-terms are only seen to present sparsely and will not affect autoproduct processing techniques. One final aspect of this study should be noted here, that any noise rejection algorithm that is able to reject signal cross-terms and interferer cross-terms separately is expected to be able to do so simultaneously.

Given the success in simulating both signal and interferer cross-terms, the next step was to attempt to reconstruct them using measured data. In this case, the data measured and originally published in Lipa *et al.* (2018)] was used to calculate a CSDM at $\Delta f = 25\ kHz$. The CSDM

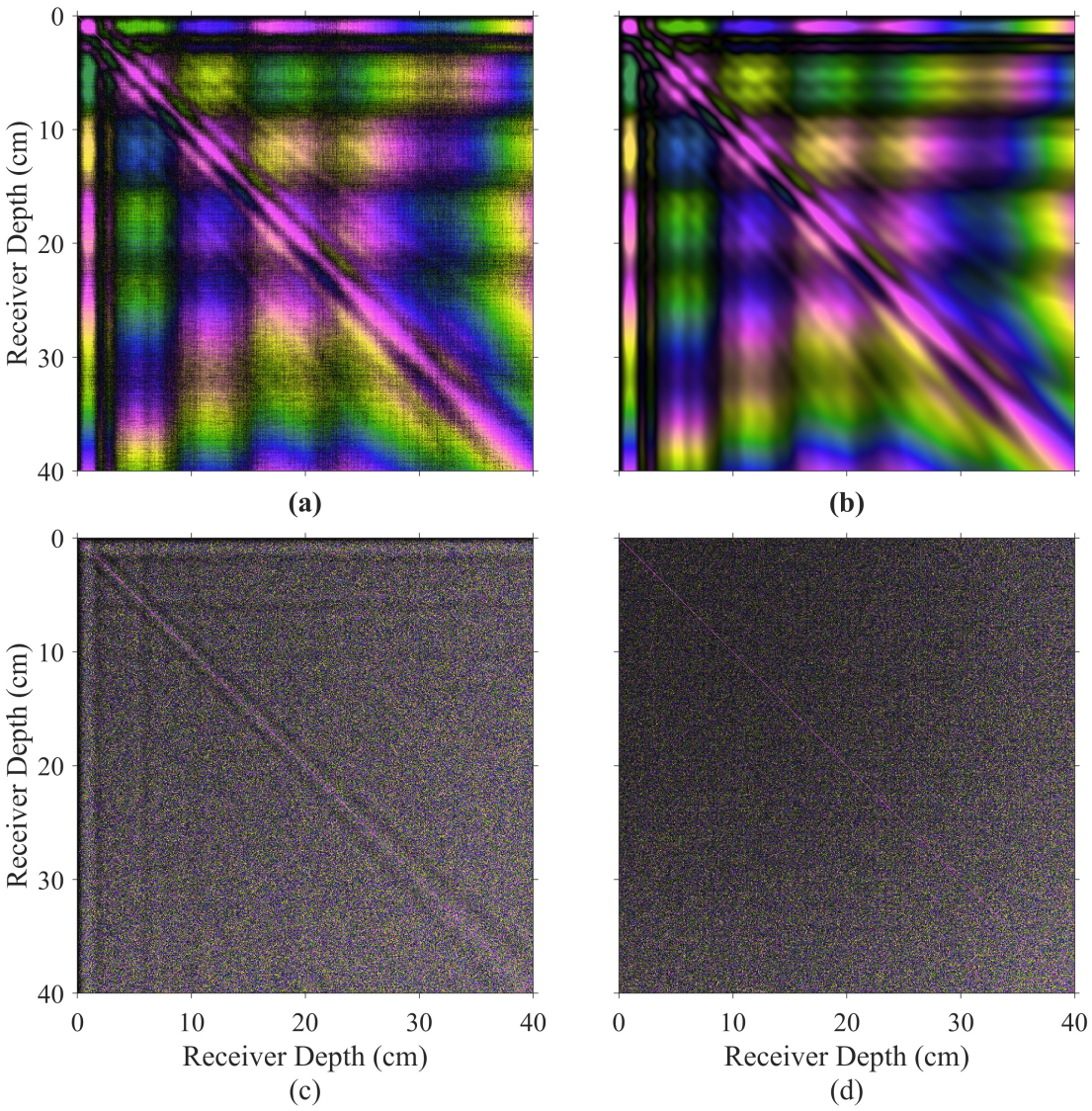

Figure 4.3: Simulated Autoproduct CSDM at $\Delta f = 25\ kHz$ in presence of noise with pressure field $SNR = 0\ dB$, (a) Full CSDM, (b) Isolated signal-signal term, (c) isolated signal-noise cross-terms, (d) isolated noise-noise cross-terms

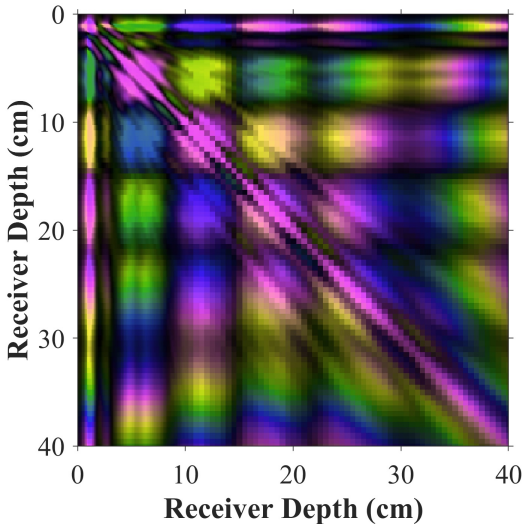

Figure 4.4: Measured autoproduct CSDM at $\Delta f = 25\ kHz$. Resembles Fig. 2b almost exactly, with greater discretization at deeper hydrophone depths due to coarser sampling

calculated using this data is shown in Fig. 4.4.

The CSDM displayed in Fig. 4.4 bears strong resemblance to the simulated results shown in Figs. 4.2a and 4.3b. Here, the most noticeable difference is that the discretization of the CSDM is shown more clearly in the lower-right hand corner of the plot. This discretization arises because of the coarser sampling in the measurements. The initial experiment was conducted to focus on resolving the frequency-difference autoproduct cross-terms that arise near a reflecting boundary, emphasizing the need to measure more finely at shallow depths.

Given that signal cross-terms compare well visually between synthetic and measured data, the next step was to quantitatively predict the effect that cross-terms would have on the cross-correlation between the autoproduct CSDM and a weight vector. Here, it is important to remember that cross-correlation values near unity are desired for matched-field style localization algorithms, and low ($|\chi| < 0.1$) cross correlation values generally indicate failure of matched field localization. This correlation study was conducted for $0 < \Delta f < 60\ kHz$ and for signal-to-noise ratios $-40 < SNR < 30\ dB$.

In Fig. 4.5a, the presence of cross-terms degrades cross correlation somewhat. The primary loss of correlation that is seen here comes from there being limited bandwidth to average over in

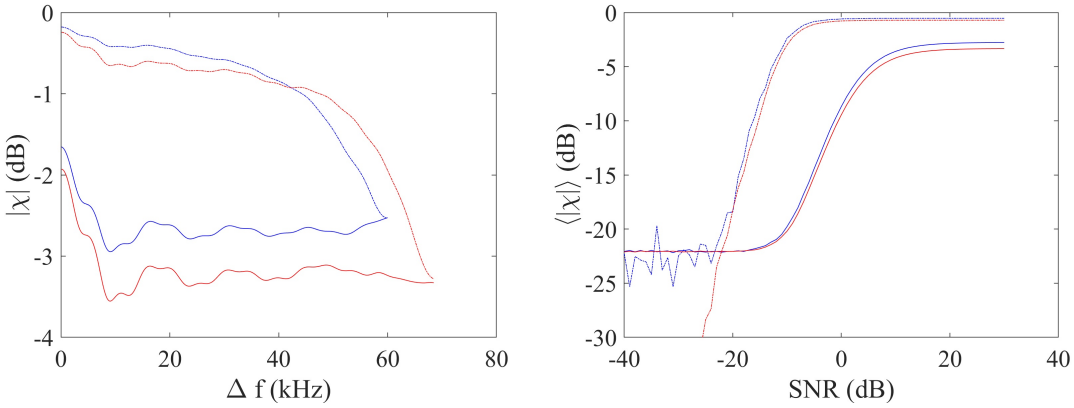

Figure 4.5: Effect of cross-terms on cross correlation between autoproduct field and CSDM's. Blue lines are calculated using synthetic data, and red lines are calculated using measured data. These values are found to agree with one another. Dashed lines have cross-terms coherently suppressed, solid lines have cross-terms incoherently suppressed. (a) Signal cross-terms, which are found to remove less than 4 dB of cross correlation for all Δf (b) Interferer cross-terms at varied SNR, represent an average across all Δf. These are found to cause failure ($\chi < 0.1$) at low SNR.

calculating the autoproduct CSDM. However, even with no extra bandwidth to average over, cross correlation in this environment still shows $\chi \approx -3\ dB >> 0.1$. Fig. 4.5b tells another story, with cross correlation degrading from $\chi \approx -3\ dB$ to $\chi < -20\ dB = 0.1$ as SNR is decreased. Successful cross term cancellation, shown in this plot, is projected to cause cross-correlation to carry physical meaning ($\chi > 0.1$) for 10 dB more SNR. Given these results, it is desired to remove both signal and interferer cross-terms using noise rejection algorithms.

4.4 Cancellation of Cross-Terms

Given the existence of cross-terms and the detrimental effect that they have on cross-correlation, the next step is to attempt to remove the terms using noise rejection methods. The first method attempted here is Δk filtering. This method is challenging to implement using the data that is measured on a non-uniform array, but this method is used to examine the spatial frequency content of the synthetically generated CSDM. The spatial frequency data is investigated by taking a two-dimensional Fourier transform over the measured CSDM, and is shown in Fig. 4.6.

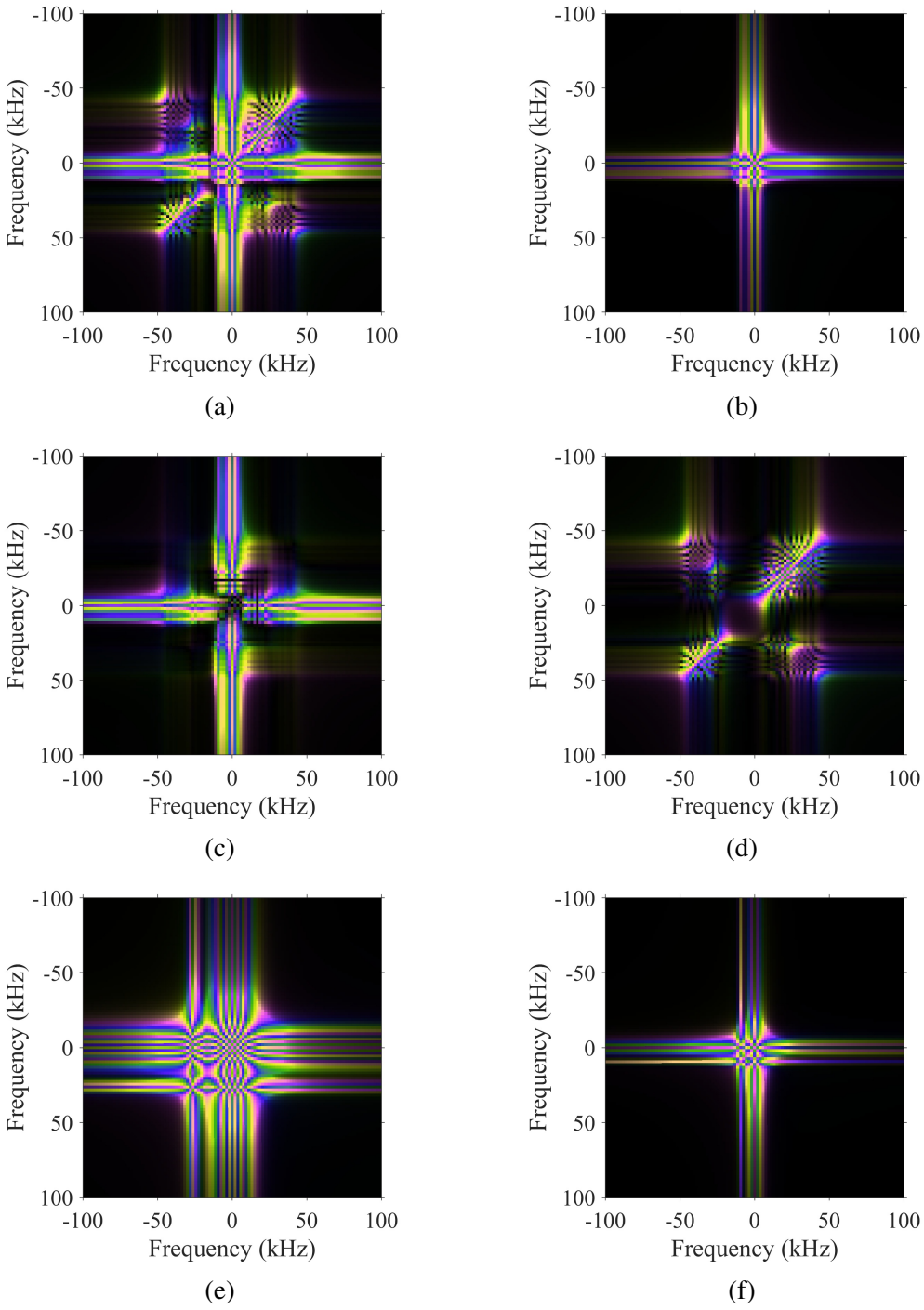

Figure 4.6: Frequency domain (k-space) representation of CSDM's. (a) Autoproduct CSDM at $\Delta f = 25\ kHz$, (b) self-self term of autoproduct CSDM, (c) self-cross term of autoproduct CSDM, (d) cross-cross term of autoproduct CSDM, (e) in-band ($f = 70\ kHz$) CSDM, (f) pressure field at Δf CSDM.

In these spatial spectrograms, data at the center of the spectrogram is lower in frequency than data that is nearer to the border. Of these, Figs. 4.6b and 4.6f are best localized in the middle of the spectrogram, indicating the lowest spatial frequency data. The similarity in spatial frequency content indicates that the self-self term of the frequency-difference autoproduct does truly contain lower frequency data than the pressure fields used to form it. Implementing Δk filtering on these spectra can be done by weighting the coefficients in the (spatial) frequency domain and then inverse transforming them back into the spatial domain. This step is not undertaken in this thesis because this step is difficult to replicate in non-uniformly sampled arrays, and all data that will be used in this thesis was measured on non-uniformly sampled arrays.

Given the difficulty of implementing Δk filtering using the measured data, the next step was to implement the noise rejection methods described in Section 4.4(B). This implementation was first undertaken using synthetic data, and the result of this calculation is shown in Fig. 4.7. Here, Fig. 4.7a shows a CSDM that has not been processed using a noise rejection technique and that exactly mirrors Fig. 4.2a.

The remaining subfigures show the result of using noise rejection methods to remove signal cross-terms. Fig. 4.7b represents the CSDM using only its principal eigenvector, and it noticeably suppresses the cross-cross terms that are evident in Fig. 4.7a. Fig. 4.7c uses diagonal zeroing, which only removes the diagonal of the CSDM. Fig. 4.7d uses RPCA to reconstruct the CSDM, and this result resembles that shown in Fig. 4.7b, except magnitude on all receivers is generally increased because RPCA is posed to increase completeness of the signal representation, rather than simply reducing rank. Fig. 4.7e shows the least change from Fig. 4.7a. This arises because the cross-terms, absent expected environmental mismatch, are coherent on these subarrays. This method will prove more successful when working with deep ocean data in Section 4.5. Lastly, Fig. 4.7f, that is calculated using bandwidth canonical coherence, also shows significant rejection of signal cross-terms relative to the basic CSDM. In general, each of these methods are capable of imperfectly removing signal cross-terms from the CSDM.

Following the successful cancellation of signal cross-terms using noise rejection, the same

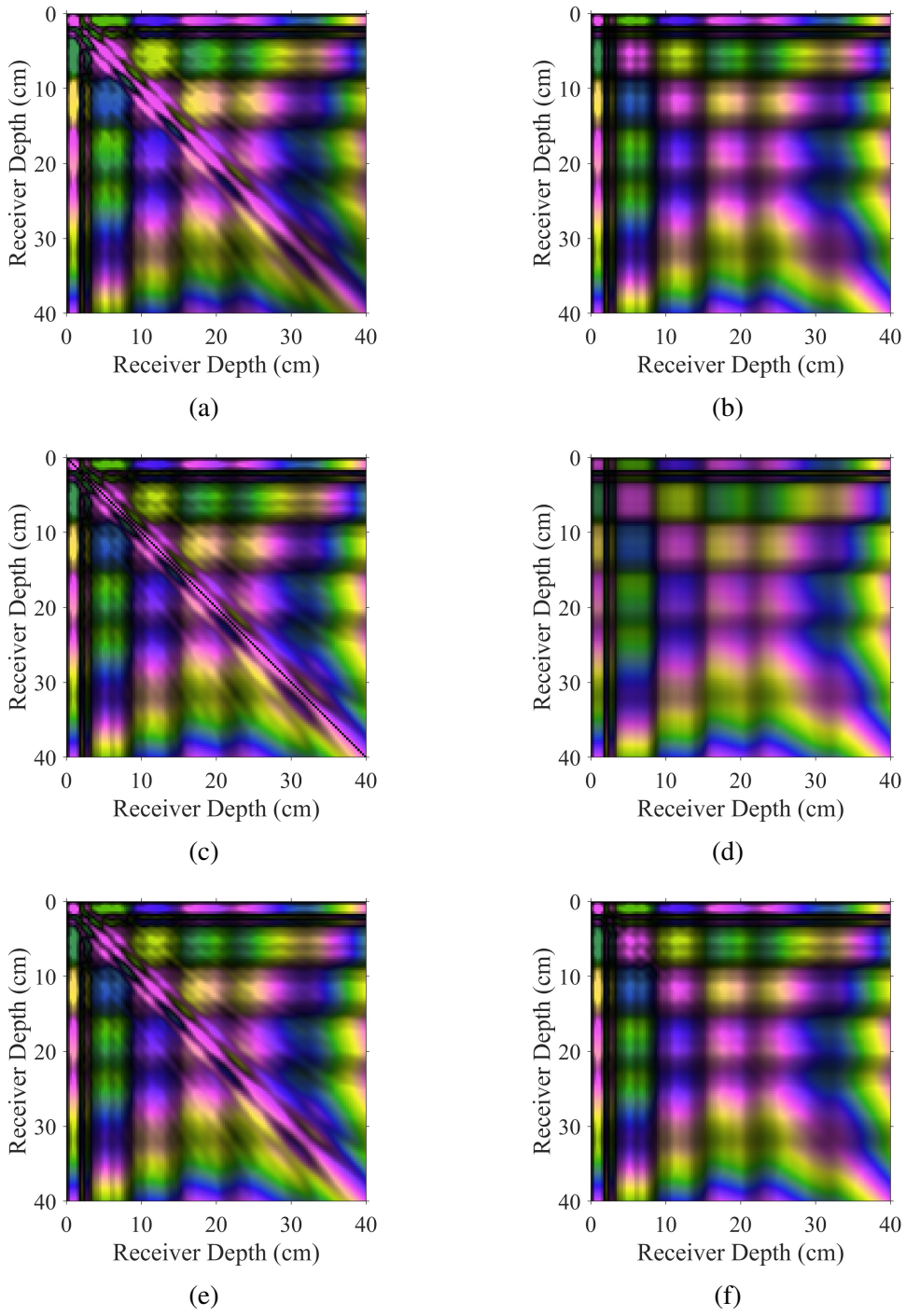

Figure 4.7: Effect of noise rejection algorithms on cancelling signal cross-terms in a CSDM, (a) Full CSDM, (b) Eigen-decomposition, (c) Diagonal zeroing, (d) RPCA, (e) Array Canonical Coherence, (f) Bandwidth Canonical Coherence

algorithms were used to attempt to cancel interferer cross-terms that arise from a corrupting noise source. For this test, a signal-to-noise ratio of 0 dB was used. The results of this test are shown in Fig. 4.8. The subfigure panels in Fig. 4.8 correspond to the same algorithms as were shown in Fig. 4.7.

In Fig. 4.8, all noise rejection techniques are shown to remove some amount of the noise cross terms that are seen in the first figure. Also, all of the techniques are able to simultaneously remove cross-terms arising from interference and the cross-terms that primarily arise from signals. Of these noise rejection algorithms, eigen-decomposition and RPCA seem to be doing the best job of cancelling interferer cross-terms from a visual perspective.

Given that both signal cross-terms and interferer cross-terms can be cancelled simultaneously using noise rejection techniques, the effect that noise rejection techniques have on removing signal cross-terms from measured data is explored to verify that the algorithms behave similarly. The measurements, taken from [Lipa *et al.* (2018)] do not include the presence of significant measured noise or interference. Therefore, this dataset cannot be used to assess the ability of noise rejection algorithms to remove measured noise from a CSDM. That will be tested in Chapter 5. The effect of using noise rejection to remove signal cross-terms from measured data is shown in Fig. 4.9.

Here, the subfigures correspond to the same algorithms that they did in Figs. 4.7 and 4.8. Here, it can clearly be seen that the results of noise rejection algorithms on measured data closely follows the intuition built up employing these algorithms to remove cross-terms from synthetic data. Here, subarray canonical coherence and diagonal zeroing have the least effect in visually suppressing cross-terms. In less controlled environments, subarray canonical coherence will perform better. Given the success seen here, it seems that the existence and exact form of both signal and interferer cross-terms in autoproduct CSDM's is well understood, and that these cross-terms can be at least partially removed using noise rejection algorithms using both synthetic and measured data.

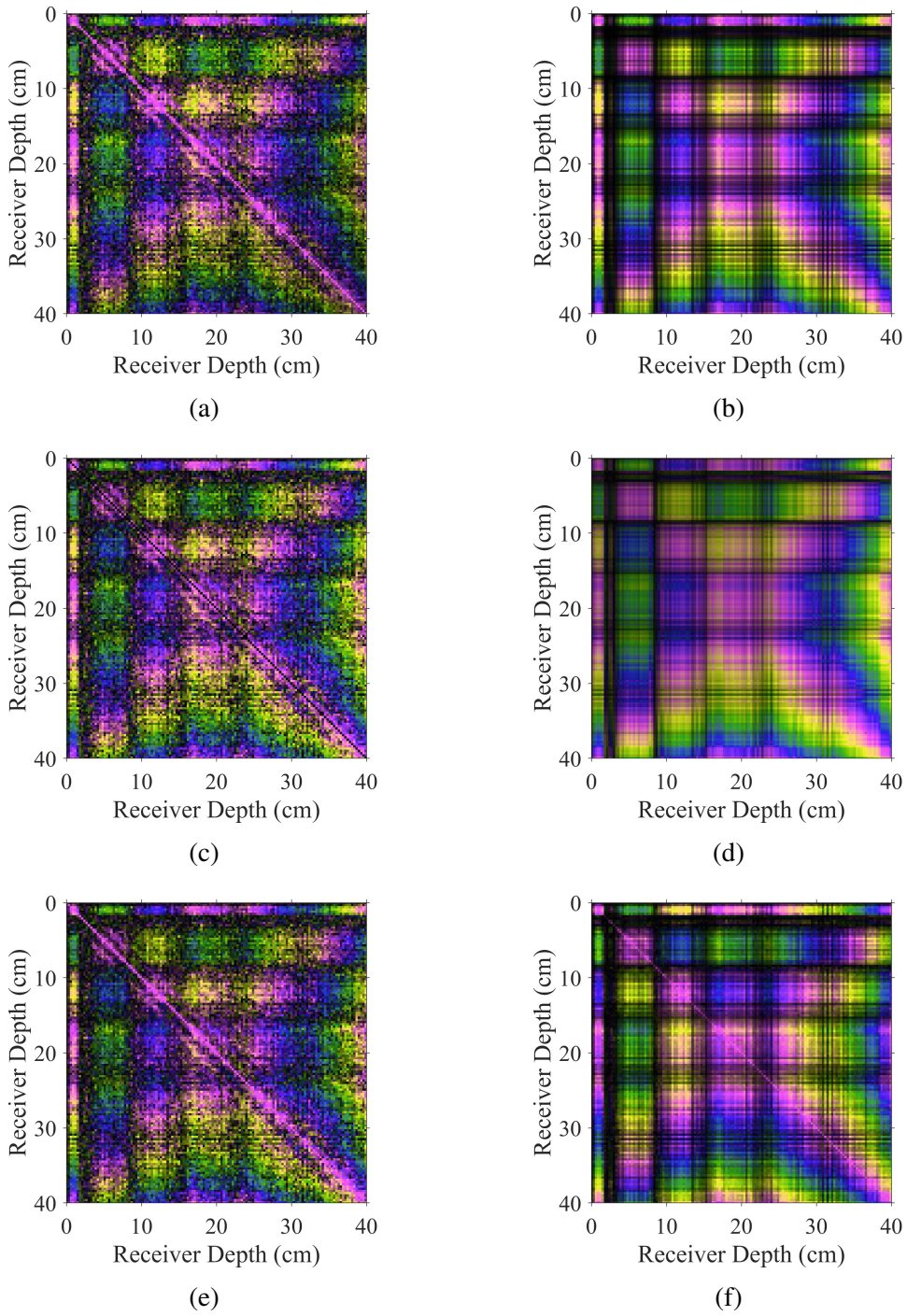

Figure 4.8: Effect of noise rejection algorithms on cancelling noise cross-terms in a CSDM with pressure field $SNR = 0\ dB$. (a) Full CSDM, (b) Eigen-decomposition, (c) Diagonal zeroing, (d) RPCA, (e) Canonical Coherence, (f) Bandwidth Canonical Coherence

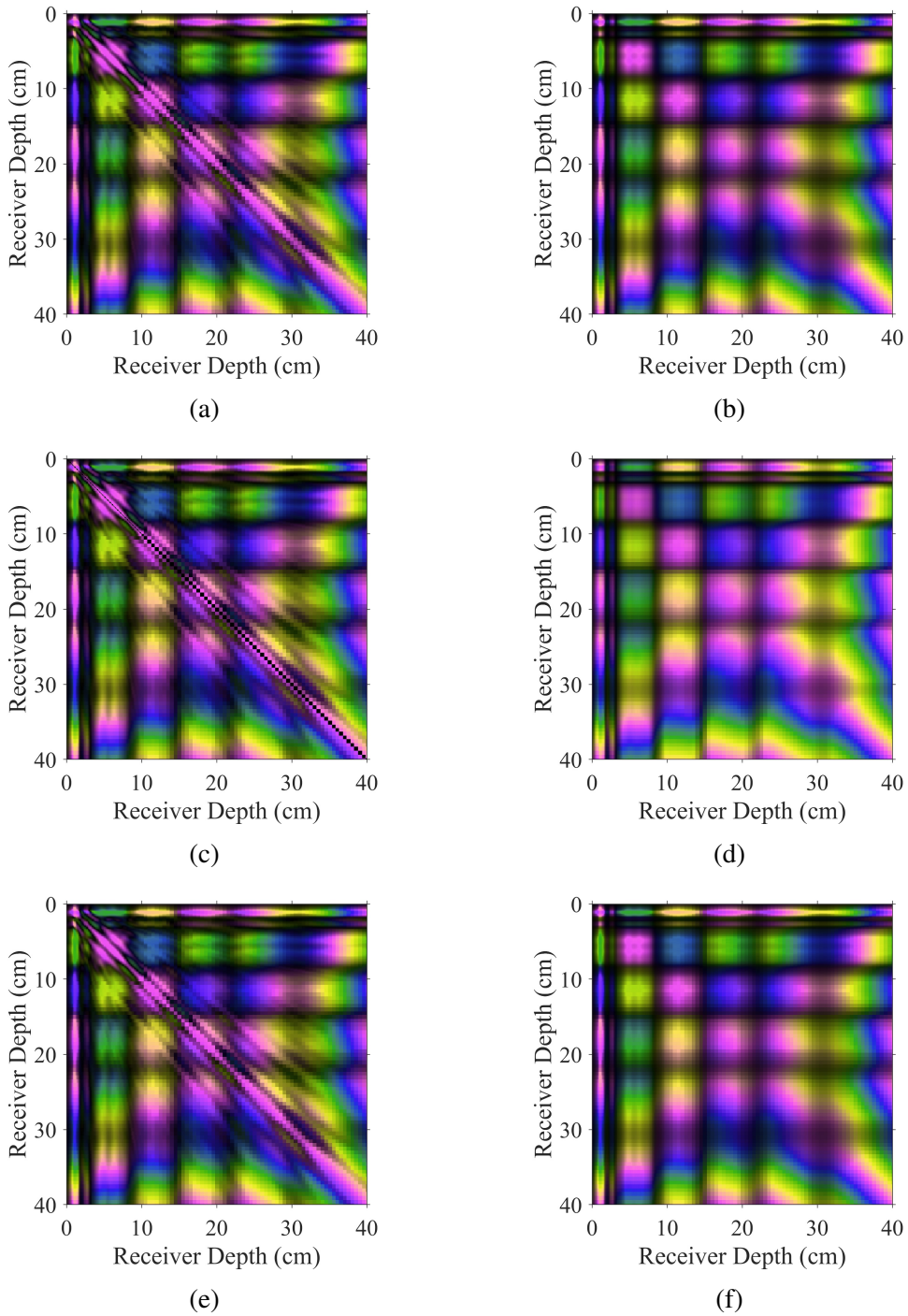

Figure 4.9: Effect of noise rejection algorithms on cancelling cross-terms in measured CSDM. (a) Full CSDM, (b) Eigen-decomposition, (c) Diagonal zeroing, (d) RPCA, (e) Canonical Coherence, (f) Bandwidth Canonical Coherence

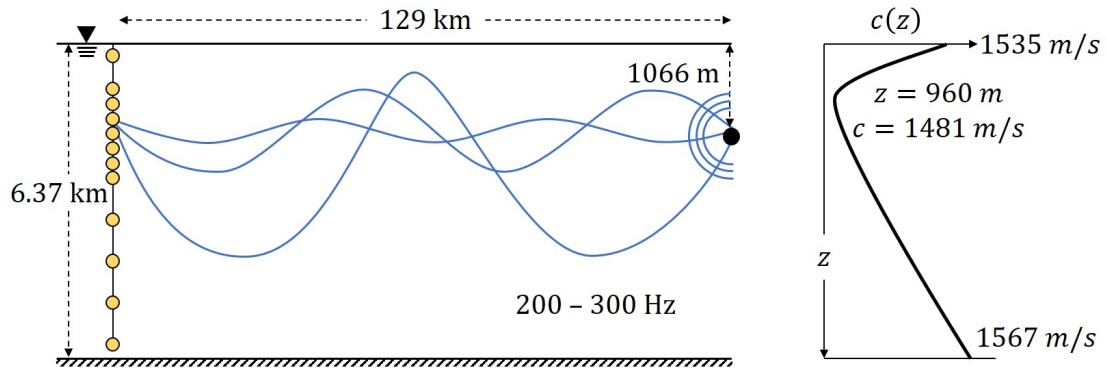

Figure 4.10: Schematic of the acoustic environment from the PhilSea10 experiment. Acoustic source placed at depth ($d = 1066\ m$) and range ($r = 129\ km$) from the DVLA with 149 receivers. For calculating the weight vector, the bottom boundary is modeled as a planar, nondispersive surface with complex reflection coefficient $R = 0.5$ and the surface is modeled as a pressure release boundary. Acoustic rays are not calculation, and are shown for illustration purposes only.

4.5 Emergence of Cross-Terms in the Deep Ocean

Given confirmation of the existence of cross-terms, quantitative understanding of their negative effects on autoproduct processing methods, and the capacity of noise rejection algorithms to remove some cross-terms in a controlled environment, cross-term presentation and analysis was extended into the deep ocean. To investigate this environment, data measured from a single moored source during the PhilSea10 [Worcester *et al.* (2013)] experiment will be used. This source, designated T6, is the closest ($r_s = 129\ km$) moored source to the Distributed Vertical Line Array (DVLA) that was measured during PhilSea10. A two-dimensional rendering of the experimental geometry is shown in Fig. 4.10.

The source transmitted a Linear Frequency Modulated chirp signal with a center frequency $f_c = 250\ Hz$ and nominal bandwidth of 100 Hz. The DVLA consisted of some 149 receivers grouped into five subarrays with varying receiver spacing and spanning depths from approximately 500 meters to 5.5 km. For the purpose of computing cross correlation results, the acoustic sound speed profile shown is used in conjunction with KRAKEN [Porter (1992)]. This measured sound speed profile is typical of the deep ocean [Brekhovskikh, L.M. & Lysanov, Y.P. (2003)], with the characteristic sound speed minimum measured at a depth of 960 m. The acoustic sound speed

profile was measured near the location of the DVLA at the beginning of the experiment, and will be assumed constant in range and time over its entirety.

All data measured from the source was used to investigate the existence and effect of cross-terms in the deep ocean. For this purpose: 220 measurements from the PhilSea10 experiment were taken and used to compute bandwidth averaged autoproduct CSDM's with a difference frequency of $\Delta f = 5\ Hz$. The CSDM's were then averaged over all measurements to produce the CSDM's shown in Fig. 4.11. It should be noted here that snapshot averaging the pressure fields prior to computing an autoproduct leads to a CSDM that lacks any coherence because the pressure field is not stable over the course of the experiment.

Here, each panel in Fig. 4.11 corresponds to the same panels as in Fig. 4.7. In Fig. 4.11, to equalize magnitude over the CSDM, some weighting is provided to different parts of the array. Fig. 4.11a shows clear signs of signal cross-terms along the diagonal of the CSDM. Because all receivers are more than 500 meters removed from reflecting boundaries near the ocean surface and floor, there is little evidence of self-cross terms in this CSDM. Each of the algorithms removes some of the cross-term that is evident on the diagonal of the CSDM. Here, it should be noted that the subarray canonical coherence algorithm is working much better than it did in the Lloyd's mirror environment. This visual evidence of cross-term suppression provides qualitative evidence that the noise rejection algorithms are working to suppress cross-terms.

A more quantitative evaluation of the effect of the noise rejection algorithms is given by cross-correlating a measured CSDM and a calculated weight vector. For this portion of the experiment, snapshot averaging of the measurements is not employed. Rather, cross correlations of individual trials are computed, and then average cross correlations are reported. The results of this study, for difference frequencies $\Delta f = 0.25, 0.5, \ldots, 5\ Hz$ are shown in Fig. 4.12.

Fig. 4.12 shows the operation of all noise rejection algorithms and the effect that these have on the cross-correlation between a measured CSDM and a calculated bandwidth-averaged autoproduct weighting vector. It can be seen that all cross correlations do better than the nominal expected cross-correlation between a weight vector and noise $\chi(\omega) \approx 0.1$. All noise rejection algorithms

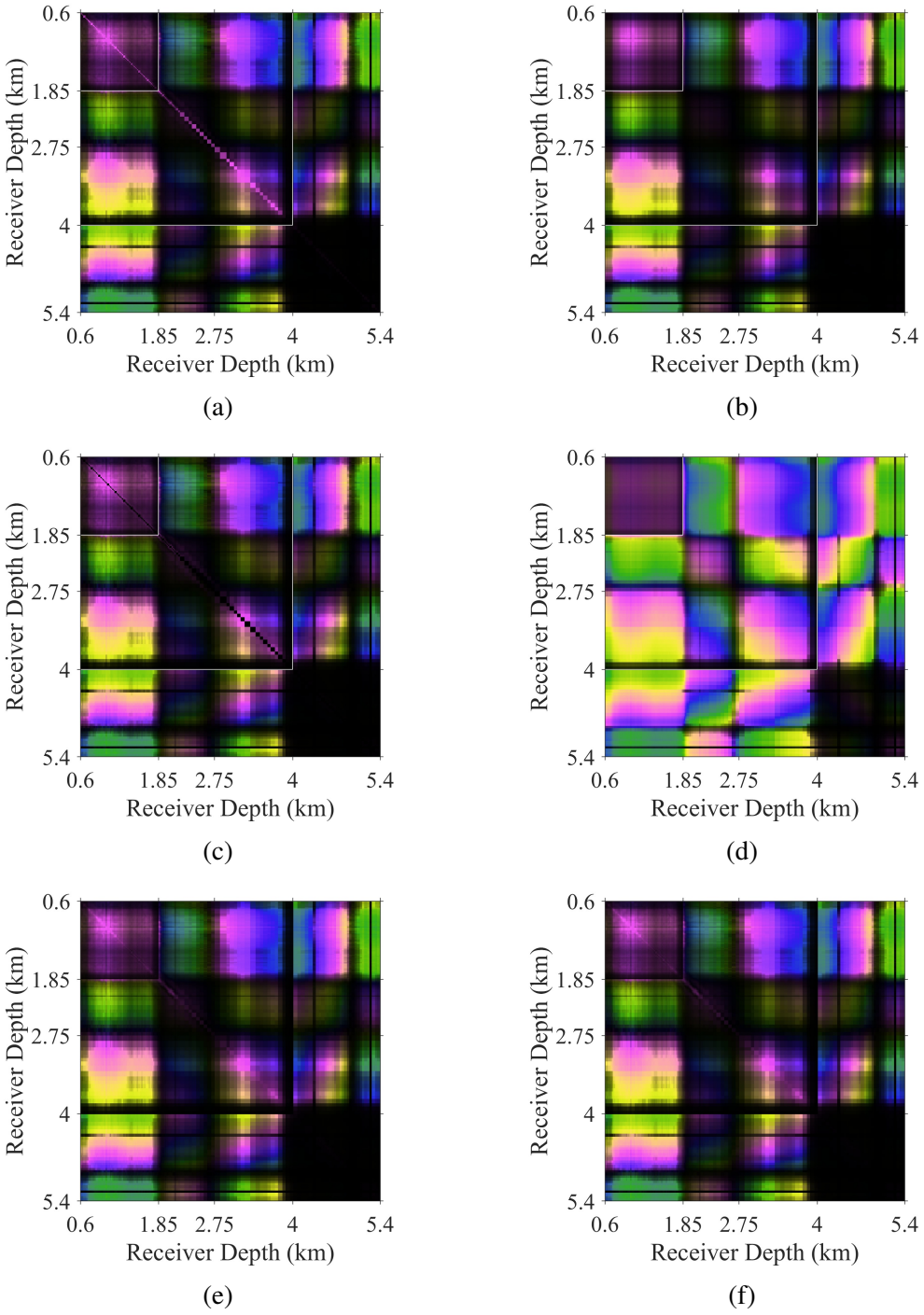

Figure 4.11: Effect of noise rejection algorithms on measured, snapshot-averaged CSDM's from PhilSea10 experiment. (a) Full CSDM, (b) Eigen-decomposition, (c) Diagonal Zeroing, (d) RPCA, (e) Canonical Coherence, (f) Bandwidth Canonical Coherence. To equalize observed magnitude over the CSDM, receivers in the array are multiplied by different magnitudes to increase the constant. Receivers in the top left corner ($z < 1.85$ *km*) receive a magnitude weight of unity, receivers in the middle of the array ($1.85 < x < 4$ *km*) receive a weight of 10, and receivers in the bottom of the array ($z > 4$ *km*) receive a weight of 1000.

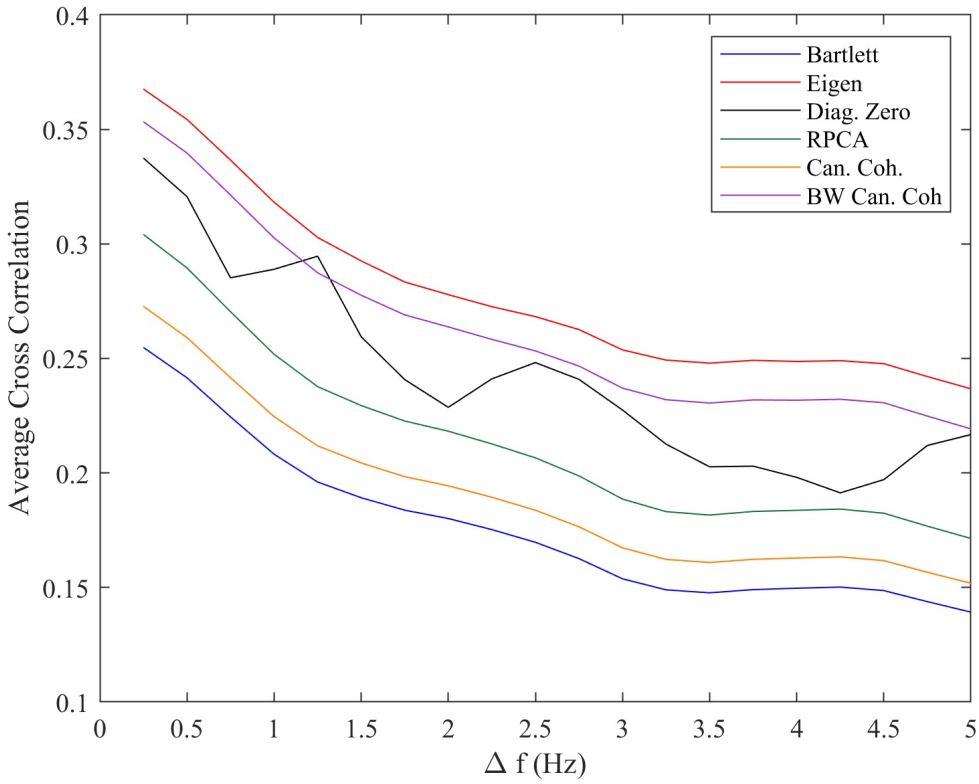

Figure 4.12: Cross Correlation Improvement over many difference frequencies offered by employing noise rejection algorithms to cancel cross-terms.

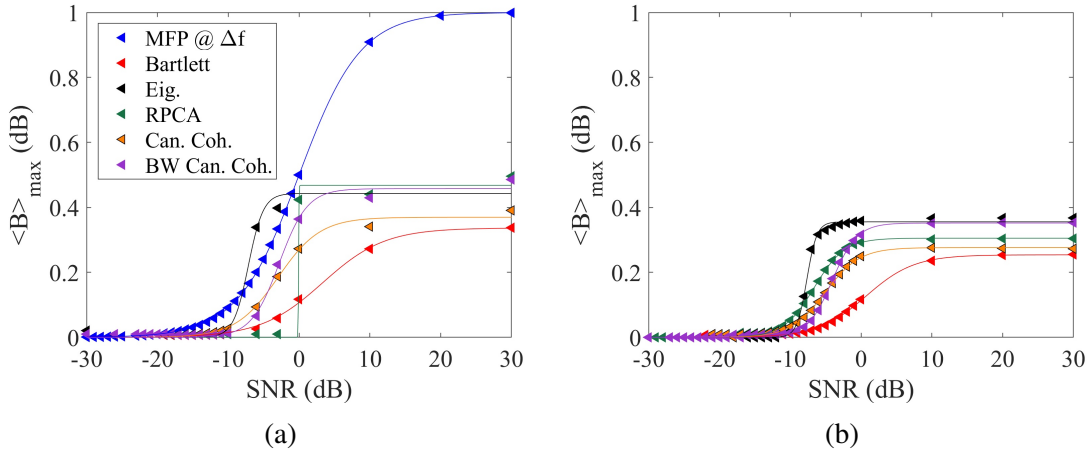

Figure 4.13: Cross Correlation improvement in the presence of noise. Here, autoproduct CSDM is seen to maintain relatively high cross-correlation (peak of ambiguity surface) to lower SNR values than the in-band field at the difference frequency. Noise rejected CSDMs are shown to keep high cross correlation values at even lower signal-to-noise ratios

increase the cross-correlation metric compared to Bartlett processing, which suggests that they are working. However, given that signal cross-terms do not, for this environmental description and source-array geometry, cause cross-correlation to go below the noise level expectation for any difference frequency the results provided by all noise rejection algorithms are considered to be sufficient to proceed.

Given that the noise rejection algorithms seem to be removing the signal cross-terms, the next step was to test removing white noise that was applied over the whole array and the strength of varying noise rejection algorithms in removing these interferer cross terms. This study was conducted for $-30 \leq SNR \leq 30\ dB$, and the results are shown in Fig. 4.13.

Fig. 4.13a shows the result of using synthetic signals to calculate cross correlation. In this plot cross-correlation between a pressure field and a pressure field is found to have the best cross correlation at high SNR. This cross correlation is found to degrade as SNR is decreased. While pressure-to-pressure field cross correlation is found to be highest at high SNR, all autoproduct methods predict consistent cross correlation values down to lower SNR before falling off rapidly. The noise rejection methods show this fall off later. Fig. 4.13b uses measured data to confirm the predictions made in the synthetic study. The data from both plots is fitted to a sigmoid curve,

Algorithm	Mean	Roll-off	Peak
Sim. Bart. MFP	0.00 dB	4.34 dB	1.00
Sim. Bart. POMAP	3.35 dB	4.39 dB	0.34
Sim. Eig. POMAP	-7.15 dB	1.05 dB	0.44
Sim. RPCA POMAP	-0.06 dB	0.03 dB	0.47
Sim. Can. Coh. POMAP	-2.96 dB	2.99 dB	0.36
Sim. BW Can. Coh. POMAP	-2.79 dB	1.99 dB	0.46
Ms. Bart. MFP	N/A	N/A	N/A
Ms. Bart. POMAP	0.71 dB	3.41 dB	0.26
Ms. Eig. POMAP	-7.66 dB	0.71 dB	0.36
Ms. RPCA POMAP	-6.63 dB	2.16 dB	0.31
Ms. Can. Coh. POMAP	-5.06 dB	2.43 dB	0.28
Ms. BW Can. Coh. POMAP	-4.05 dB	1.75 dB	0.35

Table 4.1: Parameters for fitting simulated and measured cross-correlation results in presence of simulated white noise at varied SNR.

and the fitted parameters governing this curve are given in Table 4.1. The results of the synthetic and measured study seem to agree with one another. At this point, the results are promising and suggest that autoproduct-processing methods may reject noise more successfully than conventional methods. That hypothesis will be tested for the source localization problem in Chapter 5.

4.6 Conclusion

This chapter provides analytic descriptions of two types of cross-terms, signal- and interferer-cross-terms, that are expected to degrade the performance of autoproduct-based processing methods. The emergence of these cross-terms is explored analytically, and the exact form of them is explored using both synthetic and measured data in a Lloyd's Mirror environment, and the intuition built up in this environment is extended into a more scientifically interesting and tactically relevant environment using data measured in a deep ocean environment during the PhilSea10 experiment. In both environments, signal-based cross-terms are found to have some measurable effect on cross-correlation using autoproduct processing methods. This effect is generally found to have little tactical relevance. In both environments, cross-terms that arise from having a noisy interferer is found to have tactical relevance for the cross-correlation problem. Given the intuition

built about cross-terms several noise rejection algorithms are proposed. One, k filtering, is found to be inappropriate for working with the measuring arrays that are used in both the Lloyd's Mirror experiment and PhilSea10, but is shown to provide evidence that frequency-differencing truly changes the frequency content of a measured field. All other noise rejection algorithms are implemented, and are found to have an effect in removing both types of cross-term introduced in this chapter in the context of cross-correlation. These promising results will be further explored in the context of source localization in Chapter 5.

CHAPTER 5

Applications of Autoproduct Theory: Passive Acoustic Source Localization

5.1 Introduction

One acoustic signal processing method that requires field quantity stability to work is Matched Field Processing (MFP) [Bucker (1976)]. This algorithm, which can generally be described as an inverse problem, works by correlating the relative magnitude and phase of a measured field quantity to the relative magnitude and phase of a predicted field quantity for the purpose of determining the likely location that the source is transmitting from. Unfortunately, MFP is found to lose its robustness [Baggeroer *et al.* (1993)] when a measured source is transmitting in an environment that is not well known to an operator, and that these robustness issues are found to be more problematic when the source is farther away or is transmitting at higher frequency. These issues are postulated to arise because a time-harmonic pressure field, the quantity that is fundamentally being interrogated by MFP, is not stable over space and time. The frequency-difference autoproduct was originally postulated [Abadi *et al.* (2011)] to effectively lower the frequency of a measured pressure field. This effective lower frequency is postulated to help recover field quantity stability when the fields have propagated over long distances or at high frequencies in an uncertain acoustic environment and, in so doing, to increase the robustness of MFP-style source localization algorithms to these uncertainties. The frequency-difference autoproduct was demonstrated to be a viable candidate for shallow ocean source localization [Worthmann *et al.* (2015)] at high frequencies over

short distances using Frequency-Difference MFP, and frequency-differencing methods were found to help the autoproduct recover stability [Geroski *et al.* (2021b)] for fields propagating in the deep ocean. This chapter extends this analysis to show that acoustic source localization is possible in both simple and complicated environments using autoproduct-processing methods, and quantifies the increased robustness that is available using these methods. It also quantifies the effect that autoproduct cross-terms and their removal have on the source localization problem in the context of these algorithms.

Passive source localization is a common problem in acoustic array signal processing, with MFP being one of the most common methods that is used to address the problem [Baggeroer *et al.* (1993)] over the course of the last several decades. MFP is able to provide meaningful predictions of source localization in any refracting environment [see: Jensen, F.B. *et al.* (2011)] and is robust in the face of significant interference from undesired sources. While MFP is robust in the presence of random mismatch, as would be seen from a noise source or from an interferer, it is not robust to deterministic mismatch [Tolstoy (1989)] as would be seen in the deep ocean for sources transmitting over 10 Hz that are at least 50 kilometers from an array. Many attempts have been taken since the proposal of MFP to mitigate its robustness issues and to propose a version of MFP that is tolerant to environmental mismatch. Of these methods, the most successful methods tend to attempt localization in the time domain [Hursky *et al.* (2004)], but such methods either require operator knowledge of the source spectrum (not typically assumed in passive source localization) or a solution to the blind deconvolution problem [Dowling & Sabra (2015)]. Other methods attempt to use a more mismatch-tolerant beamformer [Schmidt *et al.* (1990), Krolik (1992), Gingras & Gerr (1993), Song *et al.* (2003)], or to use simultaneous, dual-band measurements to recover high-frequency field stability [Soares *et al.* (2002)]. These methods are found to increase the robustness of MFP to environmental mismatch to some extent, but are still found to fail for measurements taken from sources at tactically relevant ranges and transmitting at tactically relevant frequencies. Other signal processing algorithms attempt to increase the robustness of MFP using Bayesian signal processing [Richardson & Nolte (1991), Spiesberger (2005)], but are again found to fail when

the measure field is too high in frequency or is transmitted from a source that is far from the array. Another approach taken to improve the robustness is to process the measured field information in another domain that is expected to be more robust to environmental mismatch, such as in the modal domain (referred to as Matched Mode Processing) [Yang (1990)], or by calculating either the waveguide or array invariant of the environment [Lee & Makris (2006)]. While algorithms like these do offer stable alternatives to using MFP, Matched Mode Processing is also found to lose robustness at high frequencies as modes become non-dispersive. Also, the array invariant becomes challenging to compute outside of specific, typically shallow, ocean environments.

More modern extensions of MFP are currently being developed and understood in the literature. Time domain localization methods are currently being explored for their applications in cooperative source localization [Van Uffelen *et al.* (2013), Wu *et al.* (2019)] for the purpose of extending the useful deployment time and range of unmanned undersea vehicles. While important for the development of greater autonomy in cooperative source localization, these methods do not fundamentally address the blind deconvolution problem that makes them undesirable for passive source localization. Another method works by changing the metric space that is used to compare measurement and prediction in MFP [Finette & Mignerey (2018)] from Euclidean to Riemannian to make the comparison more stable in passive source localization. This method is found to be comparably robust to MFP in measured environments [Cao *et al.* (2019)] but its full potential and capacity to overcome the stability problem has not been assessed as of the writing of this thesis. Compressive processing has also been proposed as a more stable alternative to MFP [Mantzel *et al.* (2011)], but has been found to offer similar performance. The waveguide invariant is being explored for the purpose of passively ranging acoustic sources in the shallow ocean [Byun *et al.* (2018), Cho & Song (2017)], but the complexity inherent in computing the waveguide invariant of a deep ocean environment is expected to make this method challenging to implement in these environments. One final class of methods that is showing promise for solving the passive source localization method takes advantage of advances in machine learning computations [Niu *et al.* (2017), Bianco *et al.* (2019)] or performance blending [Tucker & Wage (2019)] to attempt to simultaneously solve for

a source location using data-driven methods. As of the writing of this thesis, the capacity of these methods to localize acoustic sources transmitting in the deep ocean has not been assessed. All of these methods differ fundamentally from the approach taken in autoproduct processing in that they do not directly process a measured field quantity to attempt to recover stability that has been lost over a propagation path.

Autoproduct processing methods, starting with [Abadi *et al.* (2011)], work by attempting to change the frequency that a source emitted. Frequency-differencing techniques work by attempting to decrease the measured signal frequency to increase the robustness of the signal processing at the expense of precision. This is found, in frequency-difference beamforming [Abadi *et al.* (2011), Douglass *et al.* (2017)], to overcome the issues associated with processing a signal measured on an array that is sparse at the measured frequency. The bandwidth-averaged frequency-difference autoproduct was first measured in a controlled water tank environment in [Lipa *et al.* (2018)] and was successfully used as the basis for near-field localization in a two-path beamforming experiment in [Geroski & Worthmann (2021)]. Frequency-differencing techniques were first extended to the source localization problem in the shallow ocean [Worthmann *et al.* (2015)] using Frequency Difference Matched Field Processing (FDMFP), and then were later extended for deep ocean localization [Geroski & Dowling (2019), Geroski & Dowling (2021)] using a variety of matched autoproduct processing methods. While these methods are found to increase the robustness of MFP to deterministic mismatch, this is postulated to come at the expense of robustness to random mismatch in [Worthmann *et al.* (2017)]. These methods were also investigated outside of the University of Michigan in [Xie *et al.* (2020)]. This chapter summarizes source localization results to quantify the state of the art in using autoproduct-processing methods for source localization in both controlled laboratory and uncontrolled ocean environments.

The deep ocean represents a rich acoustic environment that is subject to two physical effects that are not typically explored in the same environment: the presence of caustics and the dynamic nature of the ocean. The deep ocean, as defined in [Jensen, F.B. *et al.* (2011)], describes a significant ($> 50\%$) of the Earth's ocean environments from an acoustic standpoint. The shallow part of

the deep ocean, which extends from the surface down to approximately 1 kilometer in depth, is warmed by the sun's rays and is generally marked as having high sound speed. Below this portion of the ocean, the temperature of the water is more or less static, but the salinity and hydrostatic pressure of the water both continue increasing, which leads to the acoustic sound speed of the deeper part of the ocean increasing as well. These competing physical effects lead to the existence of a sound speed minimum, referred to as the Sound Fixing and Ranging (SOFAR) channel, in the bulk of the ocean. Because of this channel, acoustic energy is found to propagate in the bulk of the medium over long distances without interacting with the boundaries of the environment. Acoustic rays that do not interact with the boundaries, termed 'waterborn rays,' are found to pass through caustics [D'Spain *et al.* (2002), Zhuravlev *et al.* (1989)] over long distances. At the same time, the dynamic nature of the deep ocean can lead to fluctuating pressure fields that do not have temporal coherence [Greene & Moller (1962)] in the frequency domain. This loss of coherence, related to stability, leads many oceanographic researchers to perform tomographic experiments [Worcester *et al.* (2013)] that are stable over long time periods. While each of these effects are found to occur in other areas of remote sensing [Skolnik, M.I. (1980)] they are not often present in the same environment. This study makes use of free and open source software [Porter (1992)], based on computing modal sums, to compute the Green's function of the deep ocean to test matched autoproduct processors in solving the source localization problem.

The remainder of this chapter is divided into five sections. Section 5.2 gives an overview of inverse problem-based methods and their use in solving the source localization problem. Section 5.3 shows the operation of matched-autoproduct processing methods in a controlled, Lloyd's Mirror environment. Section 5.4 extends these results to quantify the performance, including both the stability and the robustness, of autoproduct-processing methods for solving the source localization problem in the deep ocean in the face of significant deterministic mismatch. Section 5.5 quantifies the robustness of autoproduct processing methods to random mismatch and shows the effect of using noise rejection methods to improve source localization. Section 5.6 draws what conclusions are available from this chapter.

5.2 Source Localization as an Inverse Problem

Inverse-problem based localization algorithms were first proposed as a nonlinear extension to passive beamforming. Following onto this idea, autoproduct-processing schemes were also originally assessed for their applicability in passive beamforming [Abadi *et al.* (2011)]. Beamforming works by spatially correlating frequency-domain measurements over an array with calculated incident plane waves. Because of the linearity of the wave equation, this method can be used to find the local incidence structure of many plane waves. This solution can be calculated for measurements taken over a bandwidth using Eq. (5.1), which represents the complex square of the magnitude of the cross correlation calculated in Chapter 3.

$$B\left(\vec{\theta}\right) = \left\langle w_m^*\left(\omega, \vec{\theta}\right) R_{mn}\left(\omega\right) w_n\left(\omega, \vec{\theta}\right) \right\rangle_\omega \tag{5.1}$$

In Eq. (5.1), R_{mn} represents the cross-spectral density matrix of the measured pressure field, given in Eq. (5.2), w_m represents a weight vector that is a plane wave incident at angle $\vec{\theta}$ relative to the array in beamforming, ω is the measured field frequency, m, n are spatial indices that index along the measuring array, and B represents a positive-definite scalar ambiguity surface. Here, Ricci summation notation [Bishop, R.L. & Goldberg, S.I. (1968)] is used to simplify the equation and suppress the implied double summation over indices m, n. In this beamforming convention, both the CSDM and the weight vector are computed to have an L_2 norm of 1, as in Eq. (5.3) and (5.4), which guarantees $0 \leq B \leq 1$. This means that B represents the relative power contained in the incident plane waves along the array.

$$\widetilde{R}(\omega) = P_n^*(\omega) P_m^*(\omega) \tag{5.2}$$

$$w_n\left(\omega, \vec{\theta}\right) = \frac{\widetilde{w}_n\left(\omega, \vec{\theta}\right)}{\sqrt{\widetilde{w}_n^*\left(\omega, \vec{\theta}\right) \widetilde{w}_n\left(\omega, \vec{\theta}\right)}} \tag{5.3}$$

$$R_{mn}(\omega) = \frac{\widetilde{R}_{mn}(\omega)}{\sqrt{\widetilde{R}^{*}_{mn}(\omega)\widetilde{R}_{mn}(\omega)}} \tag{5.4}$$

These equations describe plane-wave beamforming. This can be applied to solve the source localization problem in the near field by substituting the weight vector for a spherical wave, and altering the search parameter $\vec{\theta}$ to be a search over space. This concept is referred to as spherical wave beamforming, and that can be extended using image theory for the purpose of source localization in the Lloyd's Mirror using Eq. (5.5).

$$\widetilde{w}_n(\omega, \vec{x}_t) = \frac{exp\left(i\frac{\omega}{c}\left|\vec{x}_n - \vec{x}_t\right|\right)}{\left|\vec{x}_n - \vec{x}_t\right|} + \widetilde{R}\frac{exp\left(i\frac{\omega}{c}\left|\vec{x}_n - \vec{x}_{im}\right|\right)}{\left|\vec{x}_n - \vec{x}_{im}\right|} \tag{5.5}$$

Here, $\vec{x}_n$ is the spatial location of elements of the receiving array, $\vec{x}_t$ is a so-called "test" source location that is used as the basis for the inverse problem, c is the acoustic speed of sound in the operating environment, and $\widetilde{R}$ is the (complex) reflection coefficient of the surface. This complex reflection coefficient is $\widetilde{R} = -1$ in the Lloyd's Mirror environment, which has a pressure release surface. This equation forms the basis for using Matched Field Processing for source localization in the Lloyd's Mirror, and ambiguity surface values represent the (relative) likelihood of finding a source at each test location. In this case, the MFP prediction for the true location of the source is the spatial location of the maximal value of B for any calculated test locations. It is possible that this process could be accelerated using convex optimization rather than a brute force search, however, environmental mismatch causes this processing to fail to predict an accurate location in tactically relevant scenarios. This thesis primarily focuses on improving the accuracy and precision of source localization predictions, rather than accelerating a calculation process. Matched Autoproduct Processing (MAP) can be computed in the Lloyd's Mirror environment using the weight vector given in Eq. (5.6) with a frequency-difference autoproduct CSDM given in Eq. (5.7).

$$\widetilde{w}_n(\omega, \vec{x}_t) = \frac{exp\left(i\frac{\Delta\omega}{c}\left|\vec{x}_n - \vec{x}_t\right|\right)}{\left|\vec{x}_n - \vec{x}_t\right|} + \left|\widetilde{R}\right|^2 \frac{exp\left(i\frac{\Delta\omega}{c}\left|\vec{x}_n - \vec{x}_{im}\right|\right)}{\left|\vec{x}_n - \vec{x}_{im}\right|} \tag{5.6}$$

$$\widetilde{R}^{\Delta}_{mn}(\Delta\omega) = \langle AP^*_m(\Delta\omega, \omega)AP_n(\Delta\omega, \omega)\rangle_\omega \tag{5.7}$$

Here, $\Delta\omega$ is the difference frequency of the autoproduct. This version of MAP will be computed in Section 5.3.

Source localization using matched-field style algorithms can be extended into more complex environments by replacing the weight vector that is used in calculating plane-wave and spherical-wave beamforming with a Green's function that has an L_2-norm of unity. In MFP, the unnormalized weight vector is a Green's function, as in Eq. (5.8), that can be computed using computational acoustics methods [see: Jensen, F.B. *et al.* (2011)].

$$MFP : \widetilde{w}_n(\omega, \vec{x}_t) = G(\omega, \vec{x}_t, \vec{x}_n) \tag{5.8}$$

For the purposes of this study, all Green's functions will be computed using the KRAKEN mode code [Porter (1992)]. Frequency-differencing methods were first introduced for solving the source localization problem in the shallow ocean using Frequency Difference Matched Field Processing (FDMFP) [Worthmann *et al.* (2015)], that postulates that the frequency-difference autoproduct ought to resemble a pressure field at the difference frequency, as in Eq. (5.9).

$$FDMFP : \widetilde{w}_n(\Delta\omega, \vec{x}_t) = G(\Delta\omega, \vec{x}_t, \vec{x}_n) \tag{5.9}$$

This postulate is found to be sufficient for solving the source localization in refracting environments provided that the measured pressure fields have not passed through too many caustics between the source and the receiver. When pressure fields have propagated through many caustics in a waveguide, there is expected to be a fundamental mismatch between the autoproduct and a low frequency pressure field [Worthmann & Dowling (2020b)] and cross-correlation between

these two objects is expected to lack stability [Geroski *et al.* (2021b)]. For solving a long-range source localization problem in a refracting waveguide, several autoproduct processors have been proposed. The most straightforward proposal is to use Matched Autoproduct Processing (MAP), as in Eq. (5.10), but this algorithm is found to lack robustness due to the magnitude mismatch that was shown in Chapter 3.

$$MAP : \widetilde{w}_n(\Delta\omega, \vec{x}_t) = \left\langle G^*\left(\omega - \frac{\Delta\omega}{2}, \vec{x}_t, \vec{x}_n\right) G\left(\omega + \frac{\Delta\omega}{2}, \vec{x}_t, \vec{x}_n\right)\right\rangle_\omega \tag{5.10}$$

Two more source localization algorithms were proposed to mitigate the magnitude mismatch problem. The first successful algorithm, given in Eq. (5.11), is termed 'Frequency Difference Source Localization' [Geroski & Dowling (2019)] (FDSL), and works by combining the magnitude of the weight vector used in FDMFP and the phase of the weight vector computed for MAP. The second successful algorithm, termed 'Phase-Only Matched Autoproduct Processing' (POMAP) [Geroski & Dowling (2021)] simply removes magnitude information from the computed weight vector and attempts localization using only relative phase information, as in Eq. (5.12).

$$FDSL : \widetilde{w}_n(\Delta\omega, \vec{x}_t) = \left|G(\Delta\omega, \vec{x}_t, \vec{x}_n)\right| \left(\frac{\left\langle G^*\left(\omega - \frac{\Delta\omega}{2}, \vec{x}_t, \vec{x}_n\right) G\left(\omega + \frac{\Delta\omega}{2}, \vec{x}_t, \vec{x}_n\right)\right\rangle_\omega}{\left|\left\langle G^*\left(\omega - \frac{\Delta\omega}{2}, \vec{x}_t, \vec{x}_n\right) G\left(\omega + \frac{\Delta\omega}{2}, \vec{x}_t, \vec{x}_n\right)\right\rangle_\omega\right|} \right) \tag{5.11}$$

$$POMAP : \widetilde{w}_n(\Delta\omega, \vec{x}_t) = \left(\frac{\left\langle G^*\left(\omega - \frac{\Delta\omega}{2}, \vec{x}_t, \vec{x}_n\right) G\left(\omega + \frac{\Delta\omega}{2}, \vec{x}_t, \vec{x}_n\right)\right\rangle_\omega}{\left|\left\langle G^*\left(\omega - \frac{\Delta\omega}{2}, \vec{x}_t, \vec{x}_n\right) G\left(\omega + \frac{\Delta\omega}{2}, \vec{x}_t, \vec{x}_n\right)\right\rangle_\omega\right|} \right) \tag{5.12}$$

Each of these source localization algorithms: MFP, FDMFP, FDSL, and POMAP, is tested using data measured in PhilSea10 in Sections 5.4 and 5.5. Of these, POMAP is currently thought

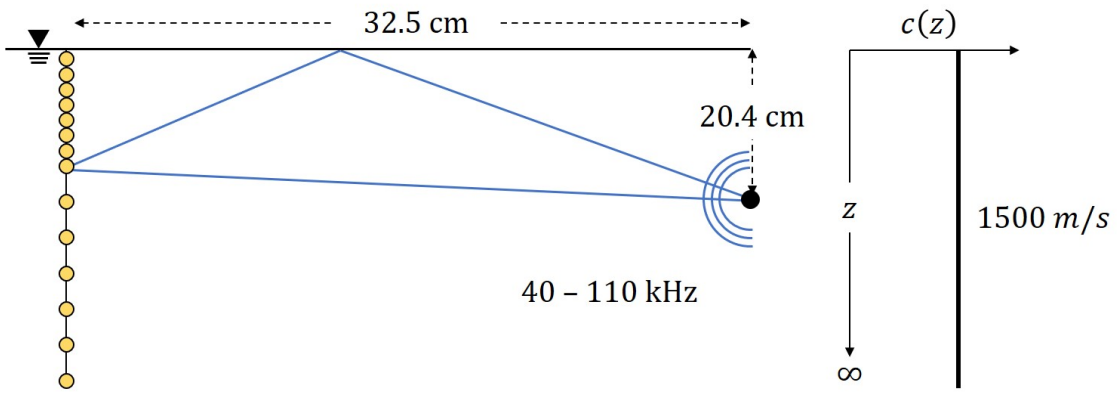

Figure 5.1: Schematic of the acoustic environment with a monopolar acoustic source placed at depth ($d = 20.36\ cm$), and range ($r = 32.46\ cm$) away from an array with N receivers. Source transmission is processed in frequency range $40 - 110\ kHz$. The array is 40 cm long, and is sampled at $\Delta z = 0.1\ cm$ for $z < 10\ cm$ and at $\Delta z = 0.5\ cm$ to a depth of $z = 40\ cm$. Surface boundary condition is assumed to be a pressure release.

to be the easiest to deploy in the field because its results seem to be stable across a user's choice of difference frequency. The success of algorithms like FDSL and POMAP indicate that MAP could be improved by using a better probabilistic representation of the magnitude, such as that proposed in [Finette (2006)]. However, these algorithms are found to be robust to the types of mismatch observed in the deep ocean.

5.3 Source Localization in the Lloyd's Mirror Environment

Acoustic source localization is first attempted using data measured [Lipa *et al.* (2018)] in the near field of an array in a controlled, laboratory water tank environment meant to emulate the Lloyd's Mirror. Here, a source was placed in the water tank at a depth of $z_s = 20.4\ cm$, and transmitted to a single receiver in a vertical array with variable depth, z, where all receivers had a source-array range of $r = 32.5\ cm$. This measurement was then repeated 161 times to effectively capture 161 receivers occupying a single vertical line array. For the purpose of computing source localization results, image theory (Eq. 5.6) was used to calculate weight vectors assuming that the test source existed in a semi-infinite medium with sound speed $c_0 = 1500\ m/s$ bounded above by a pressure release surface. The environment used to calculate weight vectors is given in Fig. 5.1.

In Fig. 5.1, the receivers in the vertical array are shown as yellow dots. The receivers had two different spacings in different parts of the array: the top 101 receivers had a separation of $\Delta z = 0.1\ cm$, and the remaining 60 receivers had a separation of $\Delta z = 0.5\ cm$. The source broadcast a modulated Gaussian signal, but the details of this are not included in this chapter as this information is not necessary for computing source localization results.

The model environment was used to calculate autoproduct matching vectors to compute Matched Autoproduct Processing ambiguity surfaces for source localization in the measured Lloyd's Mirror environment. Because of the size of the environment in question and the level of control employed in measuring the data, it is expected that source localization schemes will both work and be stable. In addition to calculating MAP results, the noise rejection algorithms described in Chapter 3 were used to pre-process the autoproduct CSDM's. Here, source localization results calculated with synthetic and measured data are visually identical and are all successful, therefore synthetic results are omitted from this document for the sake of brevity. The source localization results obtained using the data measured in [Lipa *et al.* (2018)] are shown in Fig. 5.2.

In Fig. 5.2, all plots have mostly the same structure: the underlying surface plot represents the calculated ambiguity surface, normalized to have values $0 \leq B \leq 1$, that is shown with a 10 dB dynamic range. The colorbar here is given in [Kovesi (2015)], and is chosen to be perceptually uniform over the 10 dB range. Here, white indicates regions of low matching where the source is unlikely to be and dark purple indicates regions of high matching where the source is likely to be. The peak of the ambiguity surface is indicated with a white cross (or 'x') shape, and the true source location is indicated by a white circle. Fig. 5.2a represents MAP results with no noise rejection algorithm used to pre-process the CSDM for the purpose of rejecting signal cross-terms, Figs. 5.2b-5.2f indicate MAP results with varying noise rejection algorithms used for the purpose of rejecting signal cross-terms. The ambiguity surfaces calculated using noise rejection algorithms, with the exception of Fig. 5.2e, generally resemble Fig. 5.2a with increased values added everywhere on the ambiguity surface. This indicates that the cross-terms are being rejected from the signal, because cross-terms do not come from a physical source and so provide essentially

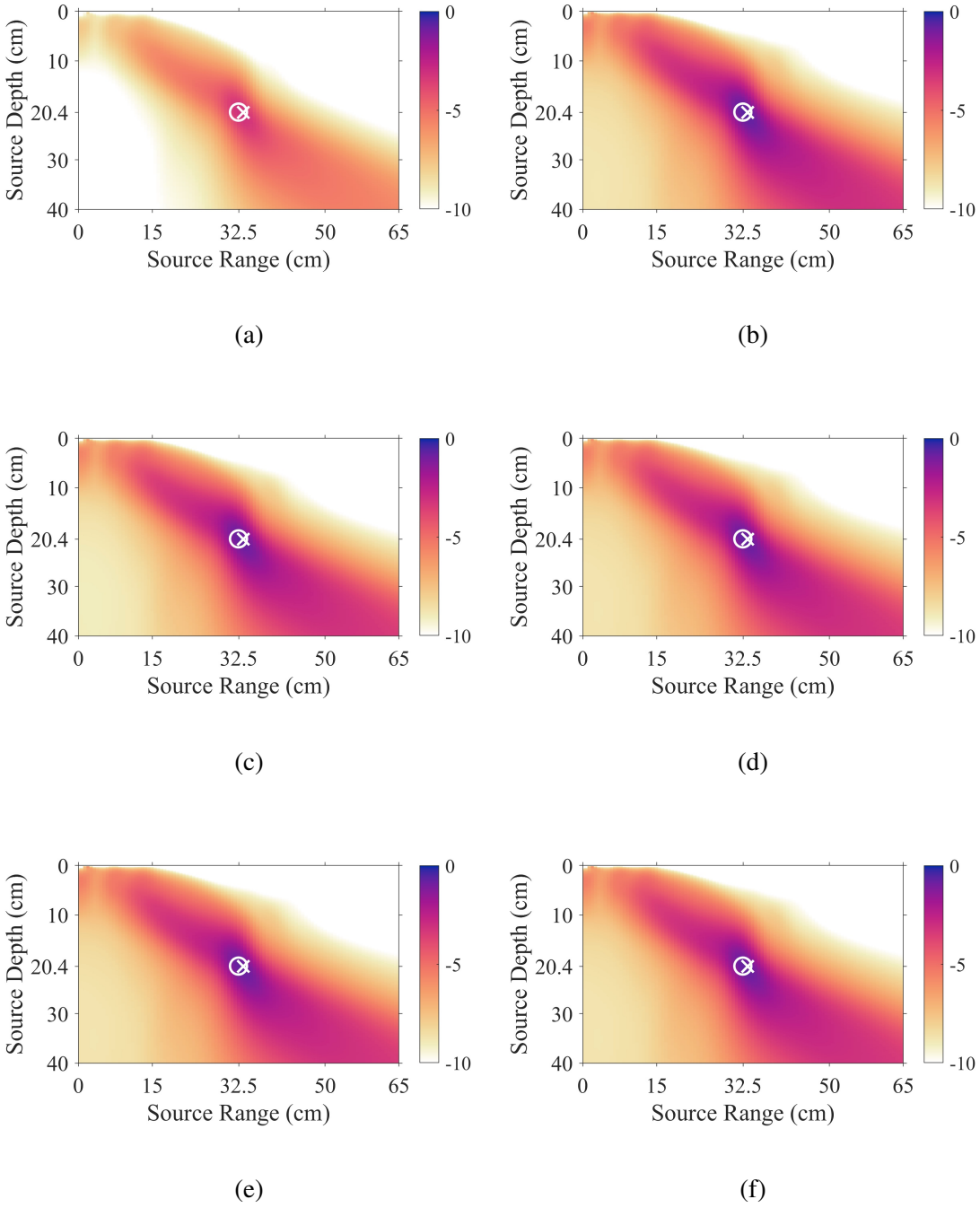

Figure 5.2: Ambiguity surfaces calculated using measured data from Lloyd's Mirror environment. All plots are surfaces with 10 dB of dynamic range, the white cross and white circle indicate the ambiguity surface peak and true source location, respectively. (a) MAP without noise rejection processing. (b) MAP with eigen-decomposition, (c) MAP with diagonal zeroing, (d) MAP with RPCA, (e) MAP with Canonical Coherence, (f) MAP with bandwidth canonical coherence.

	Basic	Eig.	Diag.	RPCA	Can. Coh.	BW Can. Coh.
Avg. B (Sim.)	-2.1 dB	-0.3 dB	-0.5 dB	-1.8 dB	-2.1 dB	-0.2 dB
Min B (Sim.)	-3.1 dB	-0.4 dB	-0.6 dB	-3.0 dB	-3.0 dB	-0.4 dB
Max B (Sim.)	-1.6 dB	-0.2 dB	-0.3 dB	-1.2 dB	-1.5 dB	-0.1 dB
Avg. B (Ms.)	-3.1 dB	-0.6 dB	-0.8 dB	-0.7 dB	-3.0 dB	-0.51dB
Min B (Ms.)	-3.5 dB	-0.8 dB	-1.0 dB	-0.9 dB	-3.5 dB	-0.7 dB
Max B (Ms.)	-1.9 dB	-0.3 dB	-0.3 dB	-0.3 dB	-1.9 dB	-0.3 dB
Dyn. Rng. (Ms.)	6.1 dB	7.4 dB	6.5 dB	7.1 dB	7.0 dB	7.5 dB

Table 5.1: Results of Lloyds Mirror study for both simulated and measured Lloyd's Mirror environments. Table summarizes the improvement in average cross correlation (peak value of ambiguity surface if localization is successful), the best/worst case for observed cross correlations in this study for each method, and the dynamic range expansion in each method. Dynamic range is here defined as the peak of the ambiguity surface minus the average value of the ambiguity surface.

even matching everywhere in the searched area. Removing the cross-terms and renormalizing the CSDM increases the amount of power in the self-terms, and gives almost perfect matching (see: Table 5.1) at the peak of the ambiguity surface. The exception to this is shown in Fig. 5.2e, that was calculated by pre-processing the array using subarray canonical coherence, that was shown in Chapter 4 to not reject signal cross-terms in this environment. While it was hoped that cross-term rejection would improve the peak-to-sidelobe ratio (PSR) of the ambiguity surface, these ambiguity surfaces do not show noticeable sidelobes in the near field of the array and this dataset is insufficient for this purpose. Given these successful results, source localization was next attempted in an uncontrolled, deep ocean, environment.

5.4 Acoustic Source Localization in the Deep Ocean

Given the successful MAP results that were seen when attempting source localization in a controlled, Lloyd's Mirror environment, source localization was next attempted using signals measured in the PhilSea10 environment [Worcester *et al.* (2013)]. For this portion of the experiment, source localization of six moored sources will be attempted. These sources, termed T1-T6 in the oceanographic literature, transmitted linear frequency modulated chirp signals with $60 - 100$ Hz of bandwidth at transmitted center frequencies $172.5 \leq f_c \leq 275$ Hz to a single receiving

Src. Name	Src. Rng. (km)	Src. Dpt. (m)	Src. BW (Hz)	Meas. $\Delta\tau$ (ms)
T6	129.4	1066	200-300	26.8
T5	210.1	1062	205-305	33.0
T1	224.8	1069	200-300	29.2
T4	379/1	1065	225-325	73.0
T2	395.9	1070	140-205	51.5
T3	450.1	1062	225-325	86.2

Table 5.2: Relative source location and signal bandwidths from the PhilSea10 experiment.

vertical line array, termed the Distributed Vertical Line Array (DVLA) in the oceanographic literature, over propagation distances $129 \leq r_s \leq 450$ *km*. Each source nominally transmitted almost 400 signals over the course of a year, though the closest source, T6, stopped transmitting approximately halfway through the experiment and only transmitted some 220 usable measurements. Exact source-array geometries are given in Table 5.2. Each measurement was matched filtered and pulse compressed using factor inverse filtering [Birdsall & Metzger (1986)] to increase the signal-to-noise ratio of the measurements. While the particular waveform is important for this step, autoproduct-processing itself does not depend on using a particular waveform, as was demonstrated in [Worthmann *et al.* (2015)], and the pulse compression is simply used for the increased signal-to-noise ratio. To localize sources, measurements from all receivers in the array are used. It is likely that fewer receivers would produce a successful result. However, the requisite number of receivers is not investigated in this thesis. Here, it should be noted that PhilSea10 is fundamentally a tomography experiment [Munk, W., Worcester, P. & Wunsch, C. (1995)] because the time-domain Green's function is stable when transmitted over hundreds of kilometers at high (hundreds of Hz) frequencies and the time-harmonic Green's function is not stable. Because of the instability of the frequency-domain Green's function, the success of matched-field style source localization algorithms is not expected.

The PhilSea10 experiment collected thousands of measurements of acoustic propagation in the deep-ocean, Philippine Sea, environment. The moored sources measured during this experiment were positioned in many azimuthal directions relative to the vertical receiving array. These differing positions lead to differences in the bathymetry of the ocean floor between the sources and the

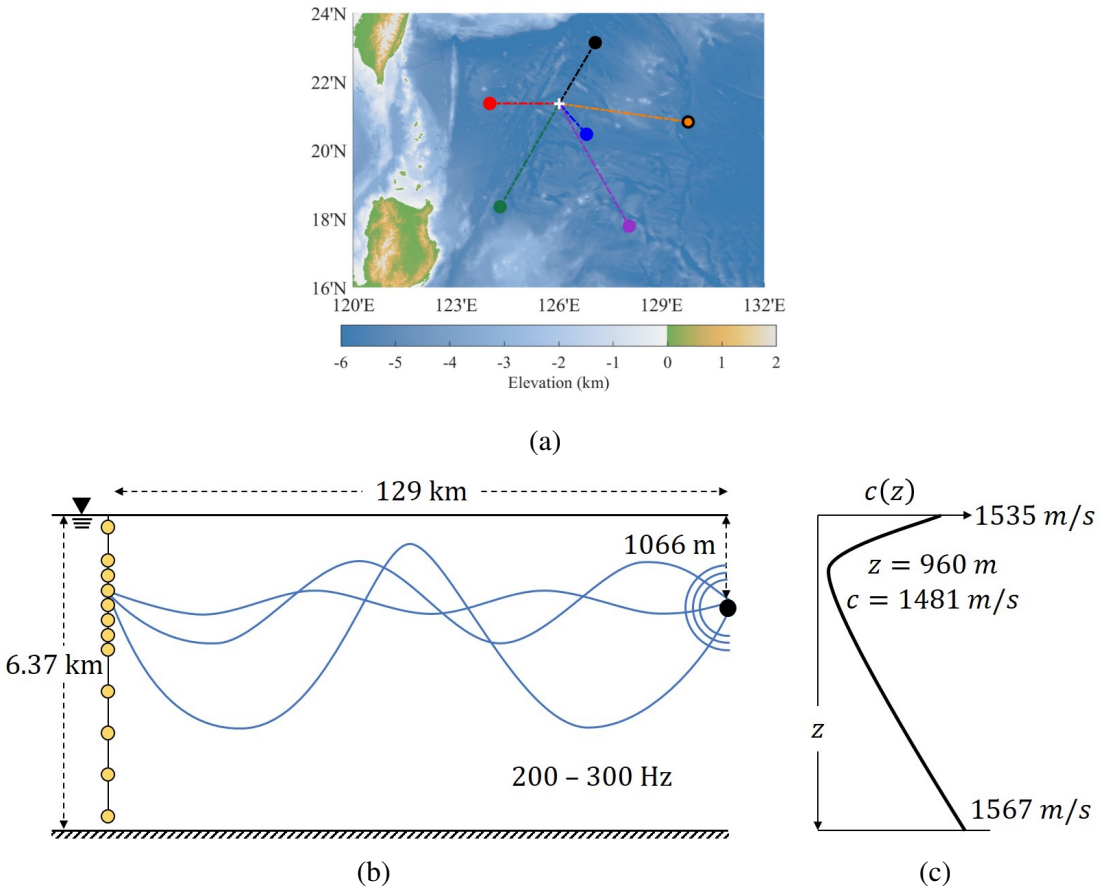

Figure 5.3: PhilSea10 (a) experimental environment, showing local altitude relative to sea-level and source- (colored circles) array (white plus +) geometry, (b) model environment used to calculate weight vectors.

array, as well as differences in the local sound speed of the environment. The local operating environment of the experiment, as well as the model environment used to calculate the weight vectors, are shown in Fig. 5.3.

Fig. 5.3a shows the operating environment of the PhilSea10 experiment, including the local altimetry and bathymetry of the Earth's surface relative to sea level [GEBCO (2021)]. The six moored sources are indicated as filled colored circles, and they are connected by dashed lines of the same color to the position of the DVLA, that is indicated with a white plus (+) sign. Because the receiving array is vertical, matched-field style localization algorithms cannot easily distinguish arrivals azimuthally. Therefore, source localization will be attempted in a two-dimensional, range-depth plane that is shown in Fig. 5.3b. Here, the receiver position is assumed to be known at

Subarray	Receiver Depth (m)	Receiver Spacing (m)	Number of Receivers
1, 1.5	180-540, 580-1180	40,20	10,31
2, 2.5	1200-2120, 2160-2200	20,40	47,2
3	2280-3240	60	17
4	3360-4320	60	17
5	4383-5381	40	26

Table 5.3: Nominal hydrophone depths on the DVLA in PhilSea10 experiment.

depths given in Table 5.3, all at range $r_s = 0$. The surface of the model environment is assumed to be a pressure release when calculating MFP and POMAP results, is assumed to be perfectly rigid when computing FDMFP results, and is assumed to be a pressure release surface when computing the phase of FDSL results and rigid when computing the magnitude of FDSL results. The bottom boundary is always assumed to be perfectly planar, at a depth of $z = 6.37$ km, and to have a non-dispersive reflection coefficient of $R = 0.5$. This choice is made to gradually decrease the amount of boundary interacting sound that is seen from sources at varying ranges. The acoustic sound speed profile used to calculate the matching vectors is shown in Fig. 5.3c, and it was obtained by directly measuring the acoustic sound speed near to the DVLA at the beginning of the experiment. This sound speed profile is assumed to be constant over all space for the entirety of the experiment, and no attempt is made to compensate for seasonal and tidal variations of the operating environment.

The operating environment was used to compute weight vectors that were correlated with pressure field and autoproduct measurements to attempt source localization. As a first step, pressure field and autoproduct CSDM's were computed for a wide (difference frequency) bandwidth, and then were snapshot averaged over all measurements taken from the closest source ($T6, r_s = 129$ km). Pressure field CSDM's were computed in 5 Hz increments over the whole bandwidth, $f = 200, 205, \ldots, 300$ Hz, and autoproduct CSDM's were calculated in quarter Hz increments, $\Delta f = 1.25, 1.5, \ldots, 5$ Hz, so that many ambiguity surfaces would be calculated for all methods. All source localization algorithms were calculated for all snapshot-averaged CSDM's, and then the ambiguity surfaces were averaged over continuous bandwidths. No source localization algorithm

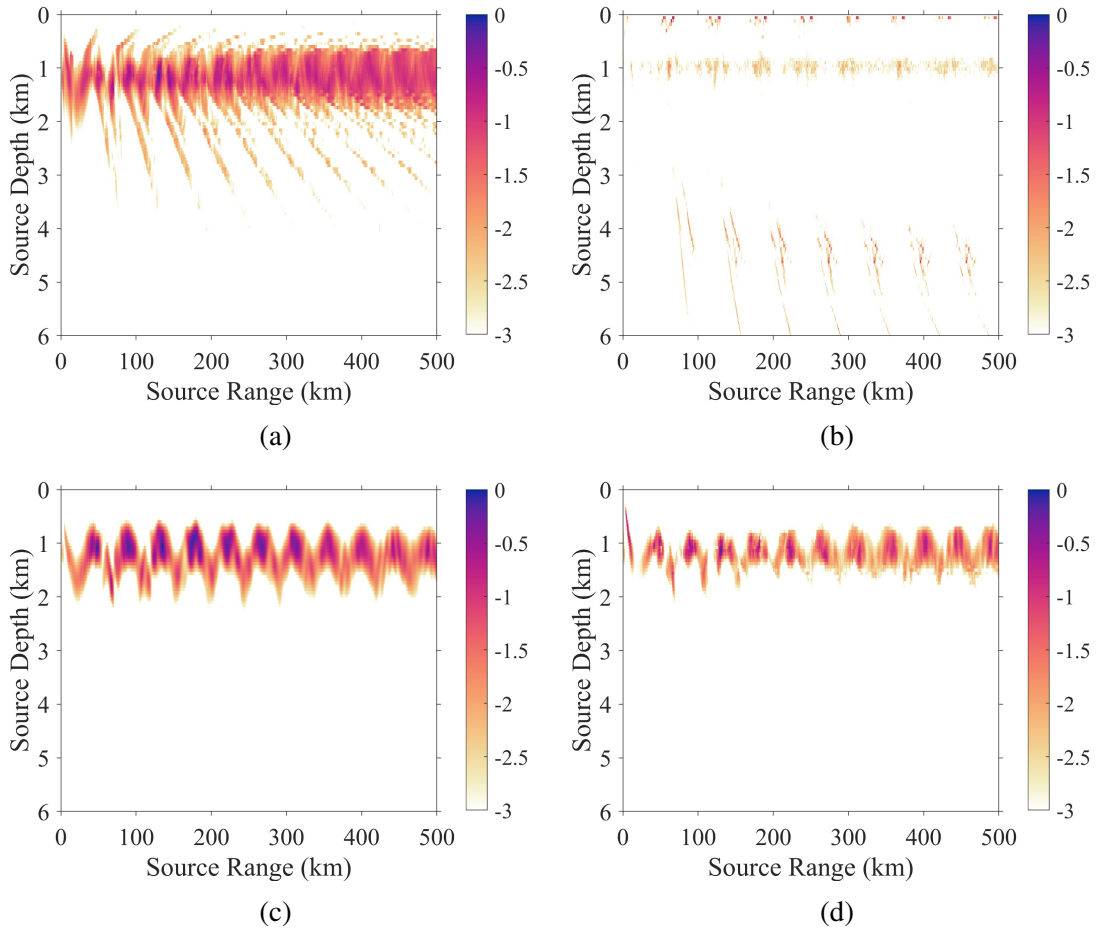

Figure 5.4: Source Localization attempted using four matched field style algorithms. Bandwidths for successful localization given in Table 5.4. Ambiguity surfaces calculated with 3 dB dynamic range using (a) Phase-Only Matched Autoproduct Processing (b) Matched Field Processing, (c) Frequency-Difference Matched Field Processing, (d) Frequency Difference Source Localization.

is found to have much success using an ambiguity surface with no (difference-frequency) bandwidth averaging, therefore only ambiguity surfaces with some bandwidth averaging are considered. This means that 210 ambiguity surfaces were computed for MFP, and 120 ambiguity surfaces were calculated for all autoproduct-processing methods. The calculated ambiguity surfaces with the smallest miss distance for each method are shown in Fig. 5.4.

Here, Fig. 5.4 displays all source localization algorithms shown in this study. POMAP results are shown first because they are found to provide the most robust results for autoproduct-processing, and the next three are arrayed in order of earliest publication (MFP, FDMFP, FDSL). Of these source localization algorithms, all autoproduct-processing methods are found to be suc-

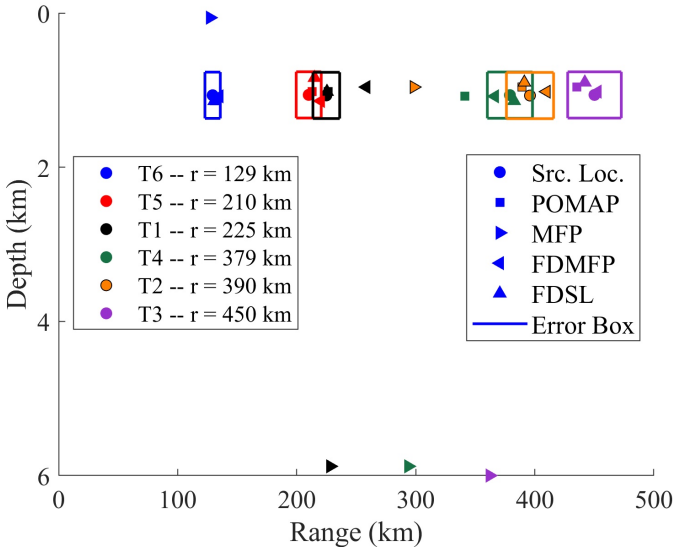

Figure 5.5: : Scatter plot of ambiguity surface peaks computed using all source localization algorithms for all sources. Peaks have the smallest miss distance from the relevant source for each algorithm over the bandwidths that were searched.

cessful for given Δf-bandwidths (given in Table 5.4) where MFP is not successful for any tested frequency bandwidth. The lack of success seen using MFP suggests that autoproduct-processing methods are doing better than simple luck, since luck should favor each of these algorithms equally, but these results do not provide insight into choosing a difference-frequency bandwidth for successful source localization.

The next step in this study was to attempt source localization of all moored sources in the PhilSea10 experiment. This step is undertaken in the same way as the step for localizing the closest source, using all available snapshot averaging for each source and the defined bandwidth-averaging procedure. Each autoproduct-processing algorithm produces 120 ambiguity surfaces, and each field processing algorithm produces 210 ambiguity surfaces, except for the fifth closest source ($T2, r_s = 390\ km$) that transmitted a chirp with 60 Hz of bandwidth that produces 78 ambiguity surfaces. The ambiguity surface with the smallest miss distance for each source and algorithm pairing is shown in Fig. 5.5.

Fig. 5.5 shows the true source position (filled colored circles), and smallest miss distance result for each source localization algorithm and source pairing. The colored lines are centered on

	T6	T5	T1	T4	T2	T3
Src. Rng.	129 km	210 km	225 km	379 km	390 km	450 km
Src. Dpt.	1.1 km	1.1 km	1.1 km	1.1 km	1.1 km	1.1 km
PO-MAP Δf BW (Hz)	1.25-5	1.25-5	1.25–5	1.25-1.75	1.25-2.25	1.25-1.75
MFP f BW (Hz)	255-290	230-235	200-220	225-245	175-180	240
FDSL Δf BW (Hz)	3.25-5	1.25	2.75-5	2.25-2.5	4-5	3.75-5
FDMFP Δf BW (Hz)	3.25-5	4.5-5	1.5	3	3.25	3-3.25
PO-MAP Robustness	0.98	0.8	0.58	0.0	0.03	0.01
MFP Robustness	0	0	0	0	0	0
FDSL Robustness	0.24	0.18	0.22	0.06	0.09	0.04
FDMFP Robustness	0.08	0.01	0	0.02	0.02	0.02

Table 5.4: Source Localization with snapshot averaging information. Table lists the true source location from the experiment, the difference-frequency bandwidths used to compute the best localization results shown graphically in Fig. 5.5, and the bandwidth success fraction, defined as the number of bandwidths that produce successful localization divided by the number of bandwidths tested.

the true source positions, have dimensions of ±2.5% of source range and ±2.5% of search depth, and represent the nominal boundaries by which successful localization is determined. These dimensions are chosen to be reasonable, and, given that very few source localization predictions fall near to this success boundary, do not seem to affect the quality of the results. Of these algorithms, all autoproduct-processing results are found to successfully localize 5 out of 6 sources for a difference-frequency bandwidth given in Table 5.4, where MFP is never found to successfully localize the moored sources. This demonstrates that autoproduct-processing algorithms can be used to successfully localize sources in the deep ocean for well-chosen difference-frequency bandwidths using significant snapshot averaging. This thesis only shows successful source localization of sources transmitting near to the sound channel axis. Simulation results suggest that successful source localization results are for sources transmitting away from this access, but data from such sources is not available to the author at this time. These simulation results are omitted for brevity.

Given that autoproduct processing algorithms can be used to successfully localize transmitting sources at appropriate difference frequency bandwidths given sufficient snapshot averaging, the ease of choosing the appropriate difference frequency bandwidth was next investigated. For this purpose, the success fraction, the number of successful ambiguity surfaces divided by total num-

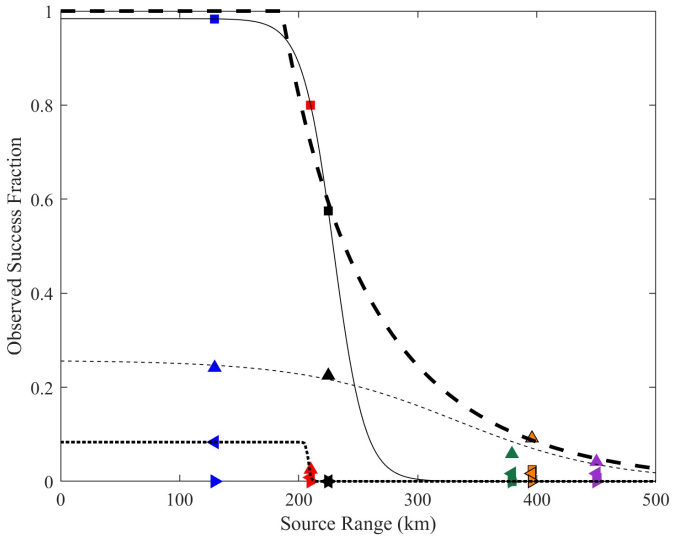

Figure 5.6: Observed success fraction for each source compared to predicted maximal possible success fraction for each source using all snapshots measured during the PhilSea10 experiment.

ber of ambiguity surfaces, of the explored difference frequency bandwidths was calculated using synthetic data for each source-algorithm pairing. These results are shown in Fig. 5.6.

The synthetic test results are indicated by the heavy black-dashed line in Fig. 5.6. These results are calculated entirely using KRAKEN to establish upper- and lower-bound predictions for successful source localization in the deep ocean. The lower-bound is given as $\Delta f = 1$ Hz, and ambiguity surfaces calculated below this point are found to be unsuccessful when calculated using both synthetic and measured data. The upper-bound for localization is found from time-front mismatch (explained in Chapter 3) where receivers are shifted in range by small amounts to mimic environmental-mismatch-induced changes in arrival time ($\Delta\tau$) of propagating rays. This mismatch induces a phase error, $\omega\Delta\tau$ in the local measured field quantity. Matched-field style algorithms are all found to fail 50% of the time for phase errors $\omega\Delta\tau > 65°$. Combining these two predictions with the amount of observed time-front mismatch given in Table 5.2 yields the expected success fraction for calculated $1.25 \leq \Delta f \leq 5$ Hz. All MFP results are expected to fail given the amount of observed time-front mismatch.

Given a prediction of the source localization success fraction that is possible using autoproduct-processing algorithms, the measured success fraction of each source-algorithm pairing is compared

to this predicted possible success in Fig. 5.6. Here, the measured success fraction for all sources (T1-T6) is displayed for all four algorithms (POMAP, MFP, FDMFP, FDSL) using colored markers that match the source-algorithm pairing convention used in Fig. 5.5. The measured success fractions for each source-algorithm pairing are given in Table 5.4. These markers are fitted to a sigmoid for the purpose of guiding a reader's eye, rather than for any quantitative prediction. Of these four methods, MFP perfectly matches the predicted success fraction obtained using measured data in that no successful source localization prediction was made. All of the autoproduct processing methods are found to have low success fractions for the farthest three sources, indicating that the current state of the art in autoproduct processing is not expected to consistently localize sources that are at least 379 km away from a receiving array. The results for the closest three sources are much more telling: POMAP is found to localize the three closest sources with: 98% (118 successes out of 120 trials), 80%, and 60% success fractions, respectively. This metric significantly outperforms the observed success fractions for FDSL and FDMFP. Therefore, it seems that POMAP is the most robust option of these choices for computing source localization results in the deep ocean given sufficient snapshot averaging.

Having observed the success of POMAP for localizing acoustic sources transmitting in the deep ocean with significant snapshot averaging, the final step undertaken in this portion of the study is to assess how many measurements of a single source are required to make a successful localization prediction using POMAP. This can be assessed in two ways: the success rate of given difference-frequency bandwidth, and the average success rate of all difference-frequency bandwidths. The first of these metrics, the localization success rate obtained using a single bandwidth is shown in Fig. 5.7.

In Fig. 5.7, the percentage of successful localizations is shown for the number of snapshots used to compute these successful localizations. Here, snapshot averaging was computed only over neighboring measurements, so, for example, two snapshot averaging is computed for measurements 1&2, 2&3, and so on. It is seen here that the closest source is 98% successful using no snapshot averaging and 100% successful using four or more snapshots to compute source local-

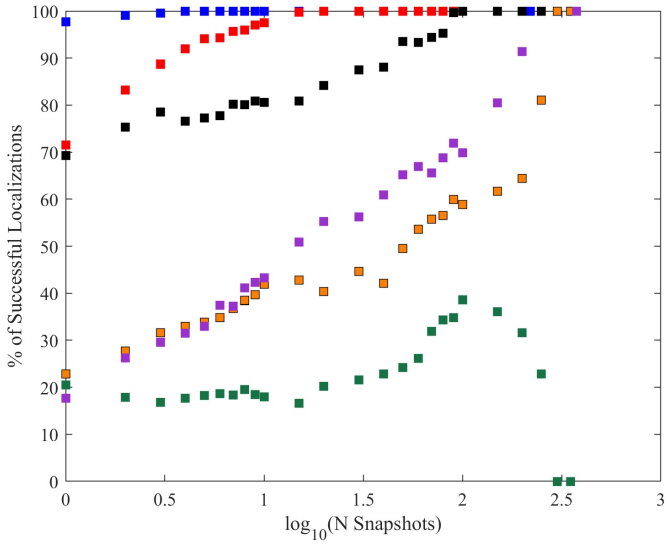

Figure 5.7: Observed most successful localization using reduced amounts of snapshot averaging for each source. Four sources reach 100% success rate without using all snapshots. One source ($T4,\ r_s = 379\ km$) sees less success when using more than 100 snapshots to calculate the CSDM

ization results at the difference frequency bandwidth given in Table 5.5. Also notable here is that the second closest ($T5, r_s = 210\ km$), third closest ($T1, r_s = 225\ km$), and farthest ($T3, r_s = 450\ km$) all achieve 100% success rates using sufficient snapshot averaging. The fourth closest source ($T4, r_s = 379\ km$) actually sees nominally decreasing success when too many snapshots are used. This indicates that the difference frequency bandwidth used to compute the source localization results loses coherence over the time-scale of the experiment. The average success of all bandwidths for a given amount of snapshot averaging is investigated in Fig. 5.8.

In Fig. 5.8, a difference-frequency bandwidth is considered successful if it is at least 75% as successful for a given amount of snapshot averaging as the best difference-frequency bandwidth for this source (shown in Fig. 5.7, given in Table 5.5). Several features of this plot are notable: the three farthest sources do not have high success fraction and instead have successful bandwidths. This could likely be addressed by using a more complicated acoustic environment to calculate the weight vectors, but this study is not undertaken in this thesis for the sake of brevity. The third closest source, ($T1, r_s = 225\ km$) shows a generally increasing success fraction up until 8 snapshots are used to calculate source localization, and then stays generally low until sufficient (at least

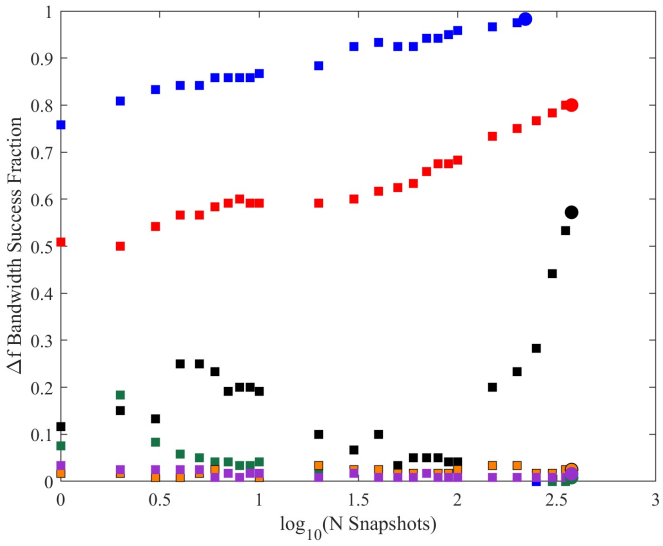

Figure 5.8: Effective success fraction of the results shown in Fig. 5.7. Here, a bandwidth is considered successful if it is at least 75% as successful as the most successful bandwidth. Here, the two nearest sources have success fractions that increase predictably to their observed values obtained using all available snapshot averaging. The third farthest source requires significant snapshot averaging to approach its true robustness. Three farthest sources steadily decrease in robustness.

	Best Δf BW (Hz)	N snapshots for 100% Success	Δf BW Suc. Frac. at N snapshots	Sngl. Snap. Succ. 100 Trials	Sngl. Snap. Δf BW Suc. Frac.
T6	1.25-5	4	0.84	100	0.86
T5	1.25-5	15	0.59	78	0.78
T1	1.25-5	90	0.04	92	0.81
T4	2.25-2.75	N/A	N/A	36	0.38
T2	1.25-2.25	N/A	N/A	23	0.07
T3	1.25-1.75	300	0.01	28	0.03

Table 5.5: POMAP Source localization using successive snapshot averaging results. Lists the Δf bandwidth used to localize each source, the number of snapshots (if applicable) at which the method achieves 100% success, the Δf bandwidth success fraction at this number, and the single snapshot localization success and Δf bandwidth success fraction for only the first 100 measurements.

100) snapshots are used to make localization predictions. This can be observed by looking at the time series of localization predictions, where successful and unsuccessful predictions are grouped together. This grouping is thought to come from seasonal variations in the acoustic sound speed profile, and could possibly be overcome by introducing these into the acoustic environment used to calculate the matching vector. The two closest sources are seen to have monotonic increasing

behavior in this metric. Given these two datapoints, successful source localization can be obtained by taking the consensus estimate of the source's location offered by many different bandwidths.

5.5 Acoustic Source Localization in a Noisy Deep Ocean

Given the successful source localization results shown in Section IV, the final step undertaken in this chapter is to address the effect that noise rejection algorithms have on removing cross-terms from autoproduct ambiguity surfaces in the deep ocean. This study extends the analysis given in Chapter 4 to quantify the effect that both signal- and interferer-cross-terms have on the success of autoproduct based localization methods and their associated ambiguity surfaces. For brevity, this study is only conducted on signal samples measured from the closest ($T6, r_s = 129$ km) moored source measured in the PhilSea10 experiment. This source is chosen for two reasons: its high localization success rate and robustness to the user's choice of difference frequency, and the existence of measured noise samples for corrupting the measurements when studying the effect that interfering-cross-terms have on localization success. Example signal and noise measurements taken from this source during the PhilSea10 experiment are given in Fig. 5.9.

Fig. 5.9 shows example measurements that will be used to understand localization success in the presence of signal- and interferer-cross-terms. Fig. 5.9a shows an example signal measurement taken from source T6, the first taken after array calibration had been completed. This measurement shows significant strumming noise on the top 10 receivers in the array, and, therefore, measurements from these receivers are not used for source localization. Fig. 5.9b shows an example measurement taken after this source had stopped transmitting. Fig. 5.9c shows all measurements taken on the 35^{th} receiver in the DVLA during the PhilSea10 experiment. The black box in Fig. 5.9c shows the measurements after the source had stopped transmitting. Of the 220 measurements where the source did transmit, the first 100, outlined in white, will be used to evaluate cross-term and noise rejection capability of POMAP.

The measurements taken from the T6 source, both the signal measurements and the noise

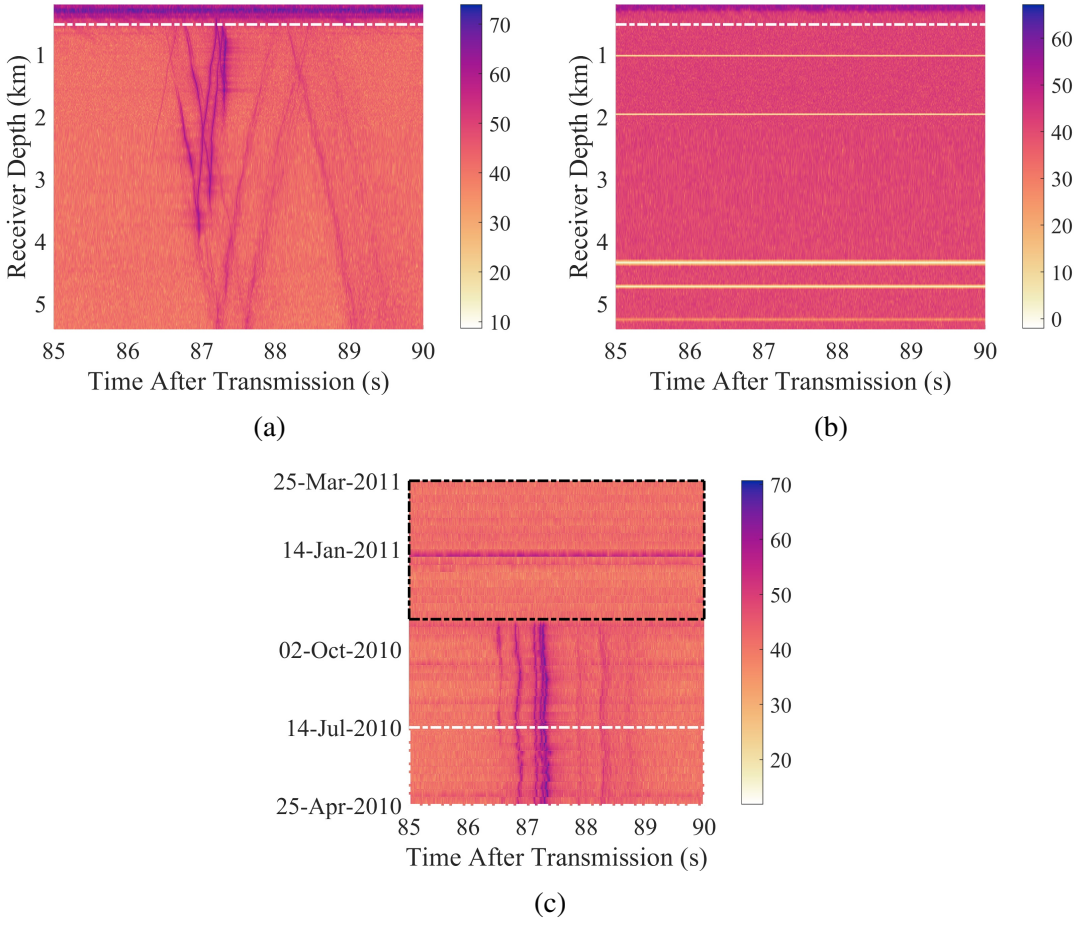

Figure 5.9: Example measurements taken from closest source ($T6, r_s = 129\ km$) during PhilSea10 experiment. (a) Signal measurement, third measurement event taken during experiment, (b) noise measurement, 225th measurement event taken during experiment (after T6 had stopped transmitting), (c) Arrival statistics of 35th receiver ($z = 1020\ m$) over entire experiment. First 100 measurements that will be used for studying noise rejection shown in white box, last 150 measurements that are used to determine statistics of measured noise shown in black box.

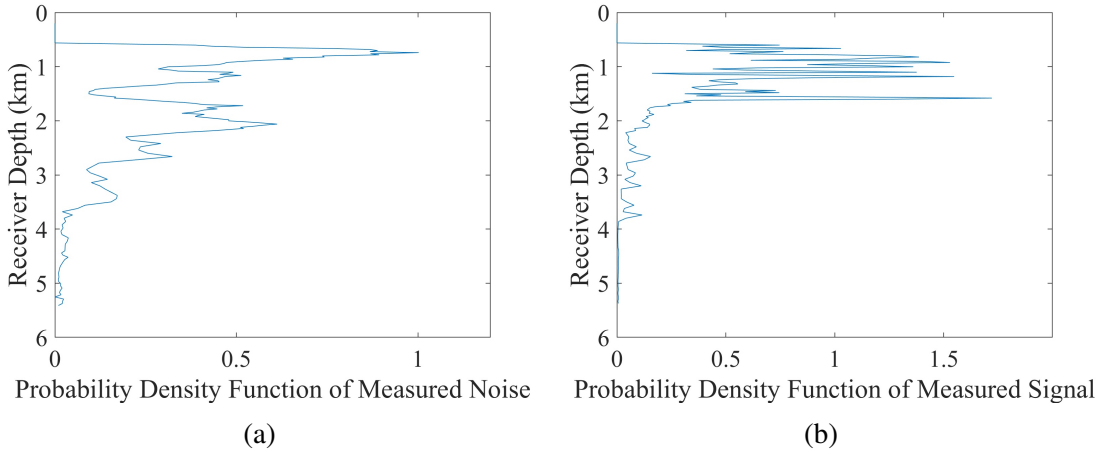

Figure 5.10: PDF of (a) noise and (b) signal measurements taken from T6 during PhilSea10 experiment.

measurements taken after the source had stopped transmitting, are comparable to one another. Generally, the PDF of both the signal- and noise-power measured over the length of the DVLA is found to vary significantly over the array. These PDF's are shown in Fig. 5.10.

Fig 5.10a shows the PDF of measured noise power from the last 150 measurements taken during the PhilSea10 experiment, and Fig. 5.10b shows the PDF of signal power measured over the array during the first 100 transmissions of the T6 source. Most importantly, the significant variance in observed noise power over the array suggests that the white noise model used to corrupt the measurements in Chapter 4 is insufficient. The phase of these measurements is still found to be uncorrelated in space and time. Therefore, the PDF and standard deviation of the measured magnitude and random phase will be used to lower the effective SNR of the measurements taken during the PhilSea10 experiment.

The effect that signal-cross-terms have on localization performance was first evaluated at very high SNR. Noise rejection algorithms were found in Chapter 4 to increase the expected peak value at high SNR across all measured difference-frequencies. Ambiguity surfaces were calculated for $1.25 \leq \Delta f \leq 5$ Hz and incoherently averaged both with and without noise rejection at high SNR to determine the effect that signal-cross-terms have on localization performance using synthetic data. This is shown in Fig. 5.11.

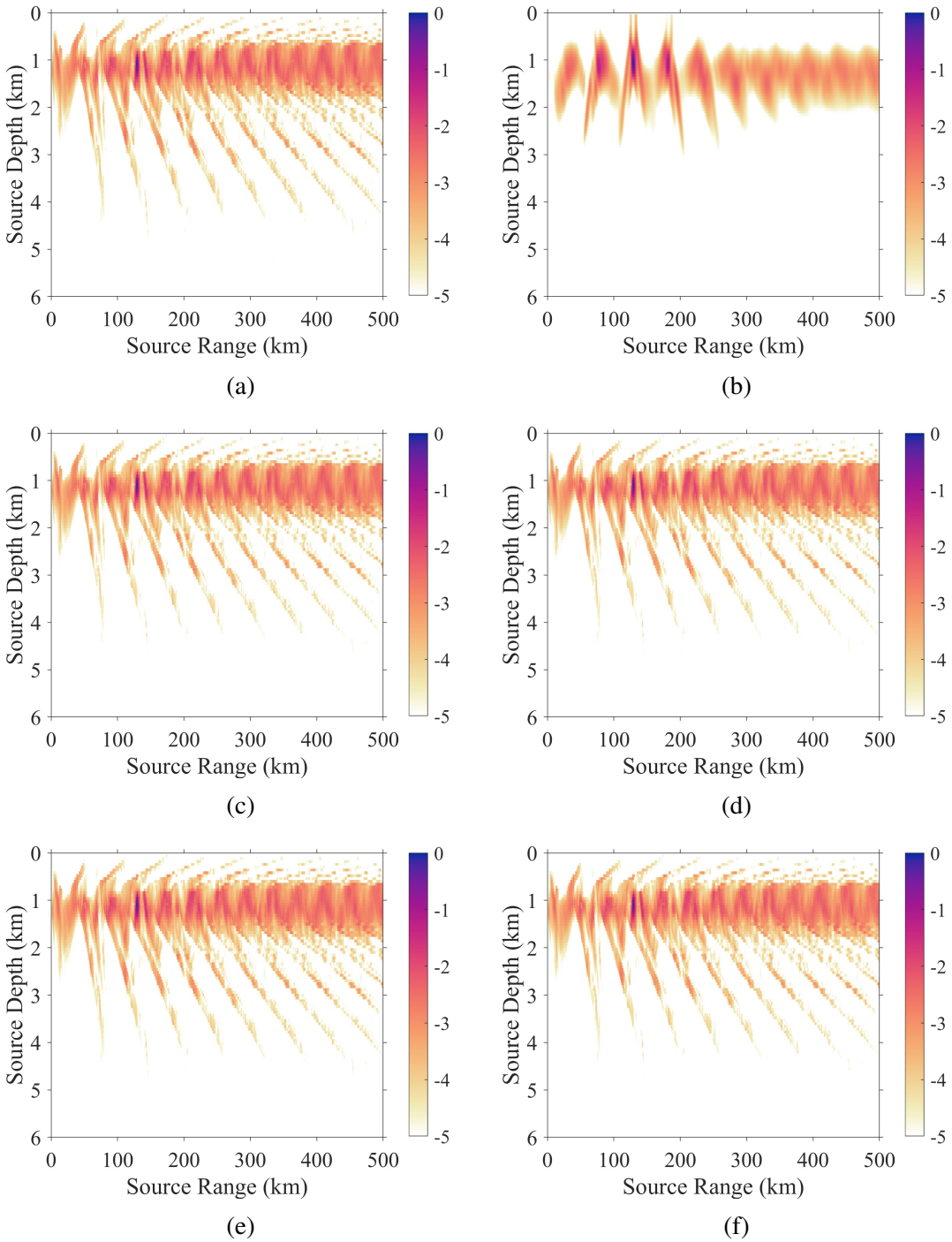

Figure 5.11: Simulated ambiguity surfaces for this sound channel at high (30 dB) SNR. (a) POMAP with no noise rejection, (b) MFP at Δf, (c) POMAP with eigen-decomposition, (d) POMAP with RPCA, (e) POMAP with Canonical Coherence, (f) POMAP with Bandwidth Canonical Coherence

Fig. 5.11 shows the simulated performance of POMAP for all noise rejection algorithms, and compares this performance to simulated MFP calculated at the difference frequencies. Here, it is found that signal-cross-terms do not greatly affect localization performance. While the ambiguity surface peak is somewhat reduced by the presence of signal-cross-terms, this effect can be accounted for by a user who sets their expectations appropriately. Also, each of the ambiguity surfaces calculated using POMAP is observed to have a PSR that is higher, if less spatially structured, than MFP at the difference frequency. Given this successful result, the effect that interferer cross-terms have on POMAP (and autoproduct processing algorithms in general) is evaluated next.

Given that noise rejection algorithms seem to successfully cancel signal-cross-terms that are measured using autoproduct-processing techniques in the deep ocean, and that these cross-terms are not seen to have a major effect on localization performance, interferer-cross-terms that arise from the presence of noise are investigated. This study is first computed using synthetic data over the same difference frequency bandwidth $1.25 \leq \Delta f \leq 5$ Hz for $-30 \leq SNR \leq 30$ dB. The noise character in this first trial is computed using the PDF of the noise measurements given in Fig. 5.10 and then altered to give the appropriate SNR for the pressure field. Four ambiguity surfaces calculated at varying SNR during this study are given in Fig. 5.12.

Fig. 5.12 shows POMAP localization performance across three decades of SNR. Here, little to no difference can be seen when reducing SNR from 10 dB to 0 dB, shown in Figs. 5.12a and 5.12b. Reducing SNR down to -10 dB, in Fig. 5.12c, shows a significant increase in the noise floor, although POMAP is still giving the correct localization prediction at this SNR. The noise floor seen in Fig. 5.12c increases more in Fig. 5.12d, representing localization performance at an SNR of -20 dB, and produces an incorrect localization prediction. This suggests that POMAP is expected to fail to successfully localize sources in the presence of significant interfering noise.

The failure of POMAP in the presence of significant noisy interference was investigated using synthetic signals in a Monte Carlo simulation. Here, 100 Monte Carlo trials of simulated localization were calculated for $-30 \leq SNR \leq 30$ dB for all source localization algorithms shown in Fig. 11. The result of this Monte Carlo trial is shown in Fig. 5.13.

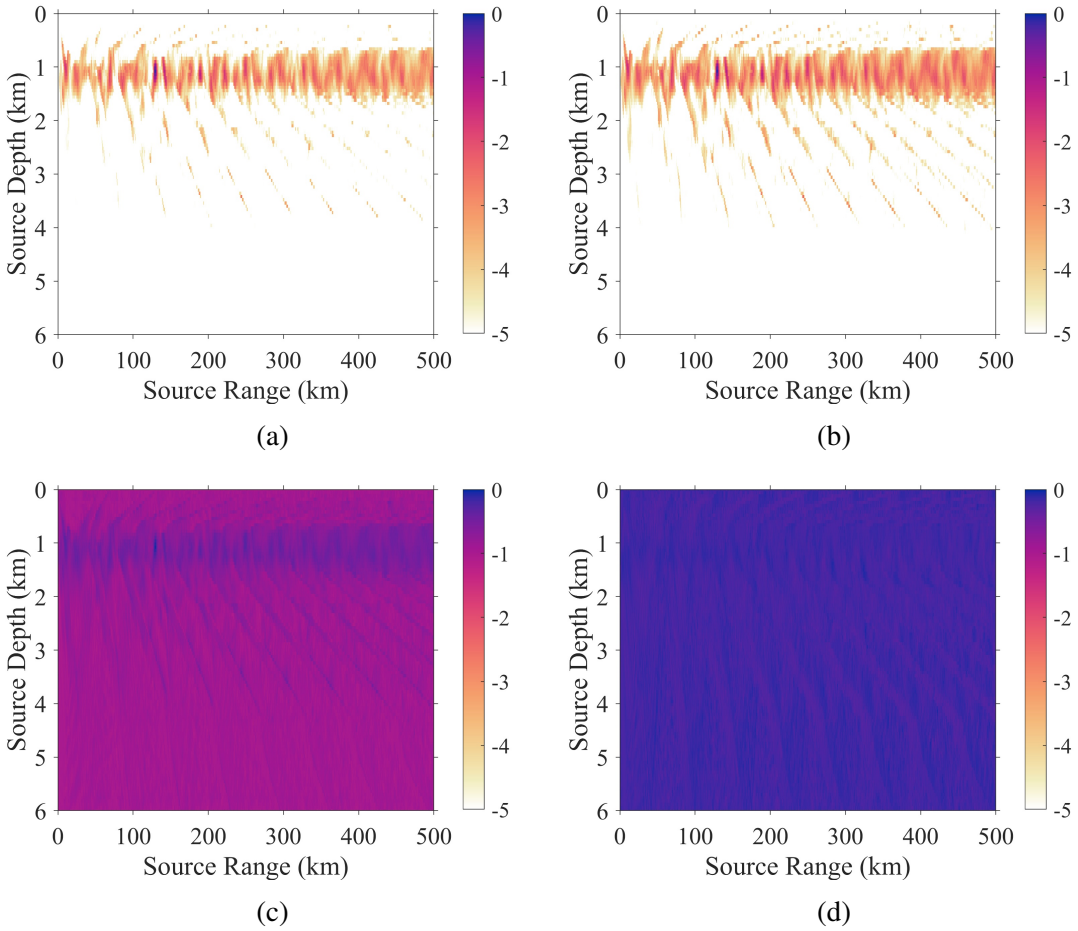

Figure 5.12: Simulated ambiguity surfaces calculated using POMAP with no noise rejection at varying SNR levels, (a) SNR=10 dB, (b) SNR=0 dB, (c) SNR=-10 dB, (d) SNR=-20 dB.

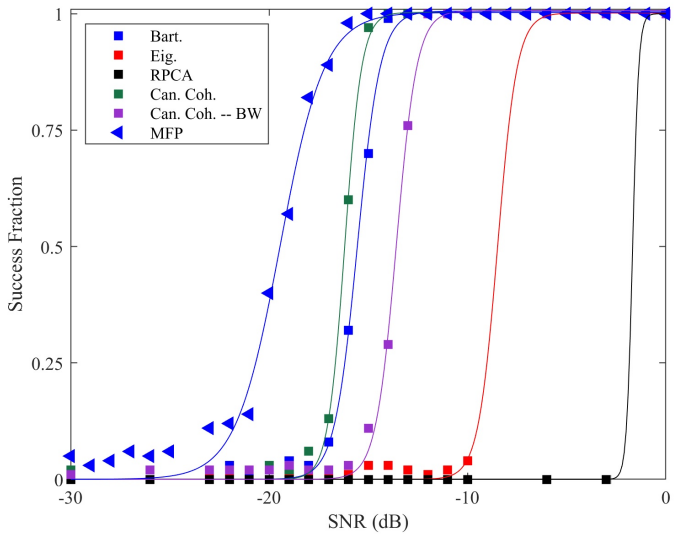

Figure 5.13: Average localization success rate using 100 Monte Carlo trials for all methods shown in Fig. 5.11. MFP at the difference frequency is noticeably better than other methods, and most noise rejection methods fail to improve localization success. Parameters governing fitted curves given in Table 5.6.

	Sim. Max.	Sim. 50%	Sim. Rate	Ms. Max	Ms. 50%	Ms. Rate
MFP Δf	1	-19.5 dB	4.48 dB	N/A	N/A	N/A
POMAP (Bart).	1	-15.6 dB	2.16 dB	1	-14.5 dB	2.88 dB
Eig.	1	-8.5 dB	1.96 dB	1	-8.9 dB	2.36 dB
RPCA	1	-1.7 dB	0.6 dB	1	-13.0 dB	3.80 dB
Can. Coh.	1	-16.2 dB	1.72 dB	1	-14.9 dB	3.80 dB
BW Can. Coh.	1	-13.6 dB	2.08 dB	1	-13.1 dB	3.76 dB

Table 5.6: Fitted sigmoid parameters for simulated and measured source localization in noise performance. Here, the max of the sigmoid represents the success rate at high SNR, the 50% of the sigmoid represents the point of algorithmic failure at which success rate is 0.5, and the rate of the sigmoid represents the 10-90 fall off rate of the fitted function.

Fig. 5.13 compares the performance of six localization algorithms, five of these algorithms are POMAP with noise rejection algorithms applied prior to calculating the ambiguity surface, and the sixth is MFP at the difference frequency. All algorithms produce 100% successful localization results for $SNR \geq 0$ dB, and are seen to fail between this point and $SNR = -20$ dB. Of these algorithms, the best performing is MFP at the difference frequency. This can be understood because MFP doesn't have the interferer cross-terms affecting its performance. The best noise rejection algorithm seems to be the one that takes advantage of array canonical coherence to reject noise,

which is found to fail at 1 dB lower SNR than does POMAP with no pre-processing. The remaining algorithms offer worse performance in the presence of noise. In general, this suggests that noise rejection algorithms will struggle to reject interferer-cross-terms and that more research may be warranted in this area. The current conclusion here is that POMAP loses approximately 3 dB of noise rejection performance compared to MFP at the difference frequency using synthetic data.

The predictions made using synthetic data for signal- and interferer-cross-term rejection were next evaluated using measured data. For this study, each of the first 100 measurements taken from the closest source during the PhilSea10 experiment were corrupted by adding noise to the measured pressure fields at a given SNR. The noise was generated randomly according to the observed statistics of the noise given in Fig. 5.10 for each measurement. From here, the frequency-difference CSDM was computed for $1.25 \leq \Delta f \leq 5$ Hz, and then was processed using a given noise rejection algorithm. The capacity of noise rejection algorithms to coherently remove signal-cross-terms from a measured autoproduct CSDM was tested by computing these results at high SNR. The ambiguity surfaces computed using POMAP to predict the source location of the first measured signal are given in Fig. 5.14.

The results shown in Fig. 5.14 are almost directly comparable to those shown in Fig. 5.11. It is worthwhile to note here that Fig. 5.14b is completely white because the source is not transmitting at the difference frequency. Thus, while the impressive performance of MFP at the difference frequency may be preferred to the performance of POMAP, this information is not actually accessible using data measured during the PhilSea10 experiment. This demonstrates that it is possible to reject signal-cross-terms using noise rejection algorithms.

Given that signal-cross-terms were rejected well even using measured data, the noise rejection capability of POMAP using measured data was next explored. First, the SNR of the measurements was degraded to give an idea of where the localization performance is expected to fail for a given measurement. These results are shown for the first signal measurement in Fig. 5.15.

These results are directly comparable to the synthetic study: POMAP is found to successfully localize at positive SNR, and this successful performance seems to extend down to $SNR = -10$

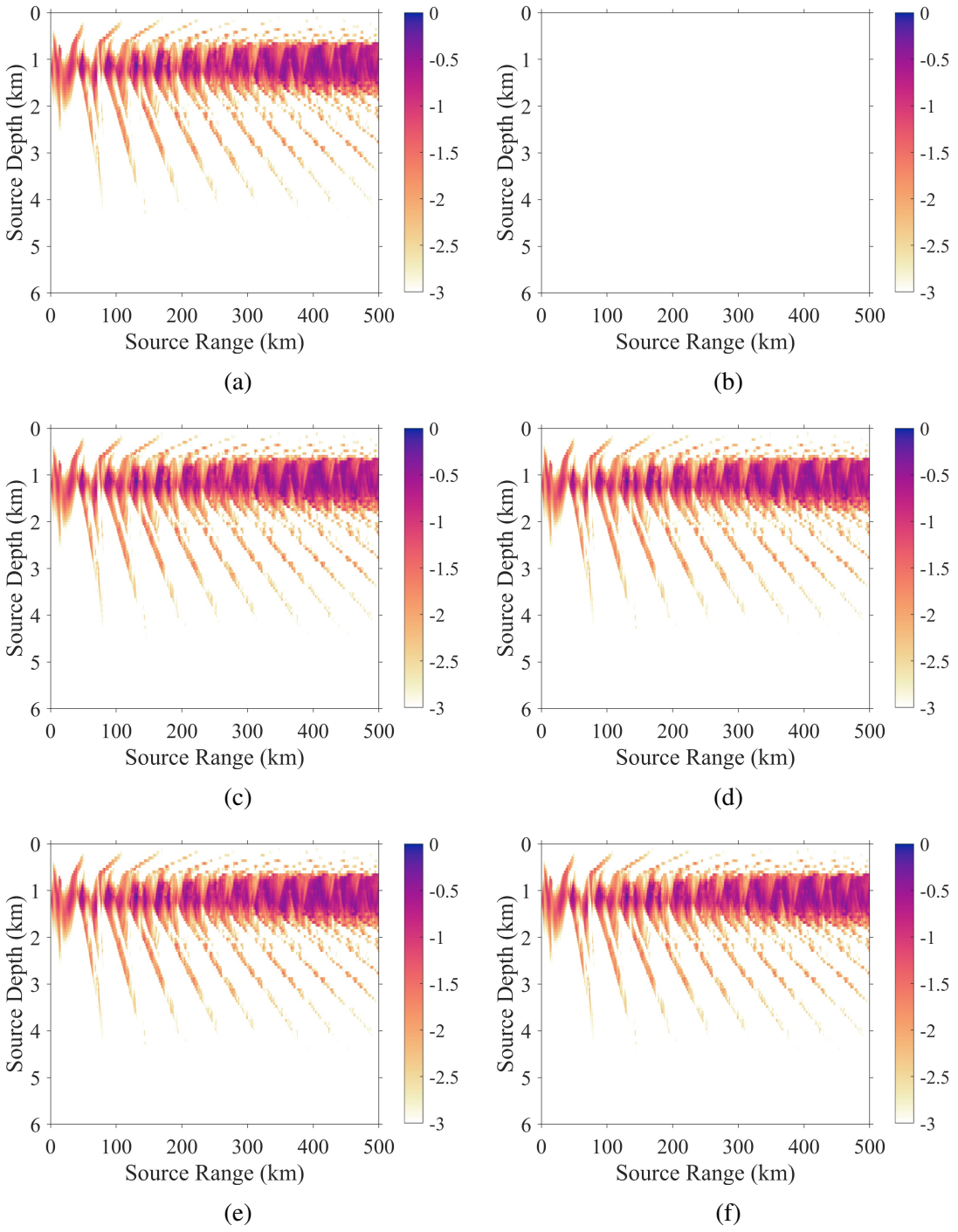

Figure 5.14: Measured ambiguity surfaces for (a) POMAP with no noise rejection, (b) MFP at Δf with no noise rejection, (c) POMAP with Eigen-decomposition, (d) POMAP with RPCA, (e) POMAP with subarray canonical coherence, (f) POMAP with bandwidth canonical coherence

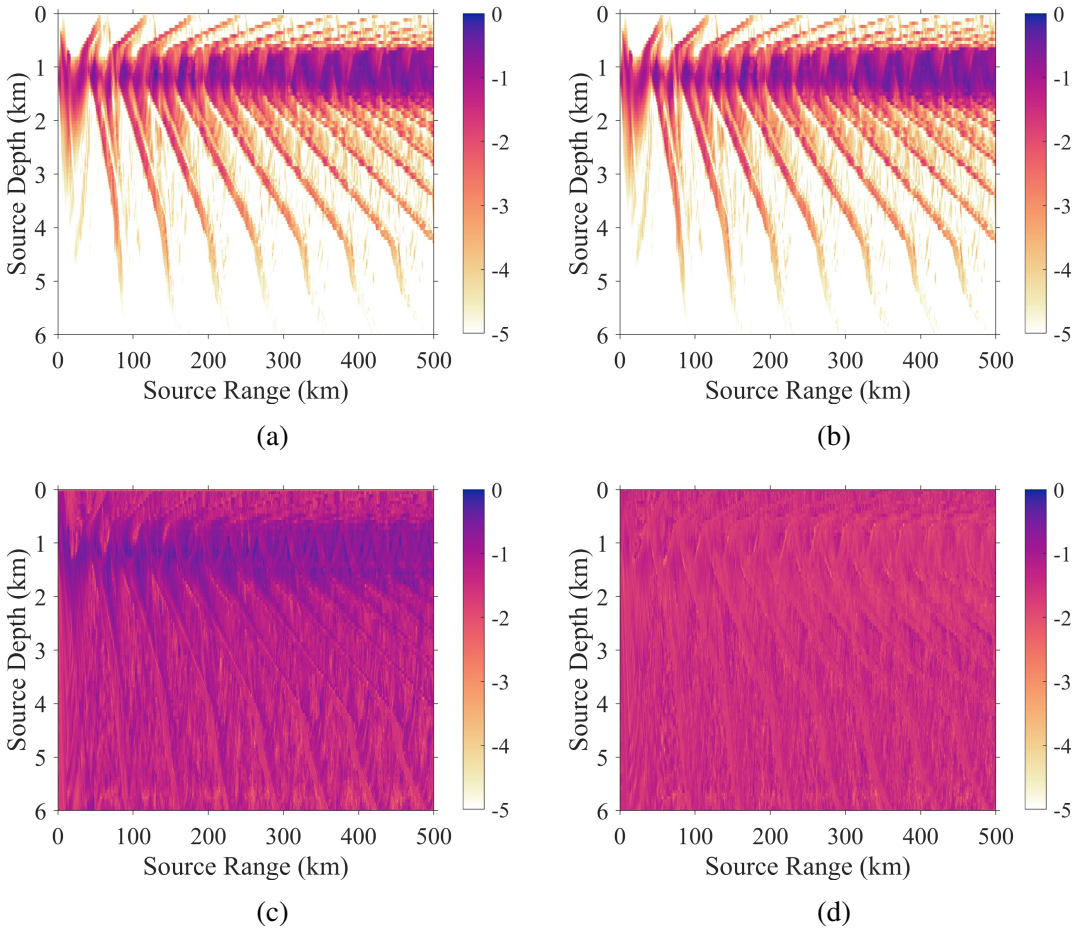

Figure 5.15: Measured ambiguity surfaces calculated using POMAP with no noise rejection at varying SNR levels, (a) SNR=10 dB, (b) SNR=0 dB, (c) SNR=-10 dB, (d) SNR=-20 dB.

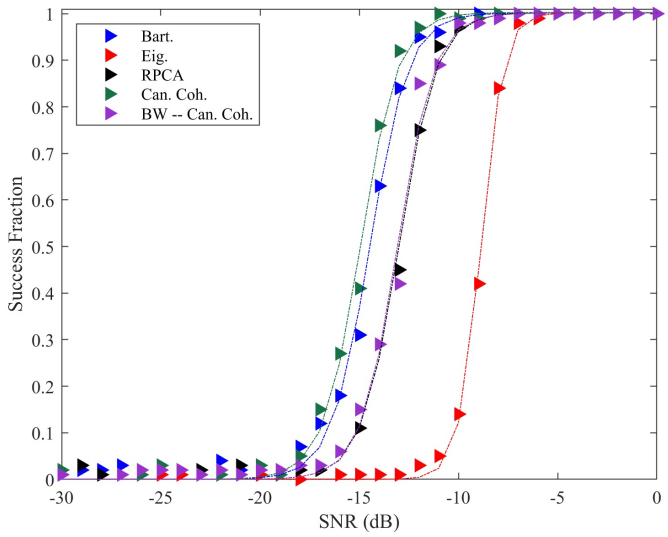

Figure 5.16: Average localization success rate using first 100 measurements taken during PhilSea10 experiments for all methods shown in Fig. 14. This figure is almost directly comparable to Fig. 5.13. Parameters governing fitted curves given in Table 5.6.

dB, where the localization prediction is still successful. At $SNR = -20$ dB, there is little to no observable character in the ambiguity surface. The average localization performance of these 100 measurements was computed for varied SNR, and this result is shown in Fig. 5.16.

Fig. 5.16 shows very similar character to Fig. 5.13. Five of the noise rejection algorithms are mostly equal to their counterparts in the synthetic prediction, although they lose approximately 1 dB of noise rejection capability. RPCA improves significantly relative to the synthetic test, suggesting that this algorithm actually improves somewhat in the presence of measured mismatch. Likely this improvement is seen because of the perfect, rank-1 nature of the synthetic data. Because RPCA still represents a performance degradation for POMAP relative to the unprocessed CSDM, this disparity is not investigated further. Again, the only noise rejection algorithm that seems to successfully reject interferer-cross-terms utilizes subarray canonical coherence.

5.6 Conclusion

This chapter lends itself to three conclusions. Firstly, this chapter demonstrates that autoproduct processing methods can be used as the basis for successful source localization predictions in both controlled and uncontrolled environments. Here, it should be noted that successful passive source localization results for the moored sources in PhilSea10 have not been published using any other method, and so these results seem to stand in a class of their own for deep ocean source localization. Of the explored autoproduct-processing algorithms, Phase-Only Matched Autoproduct Processing seems to be the most robust, and offers consistent localization results for many difference-frequencies and difference-frequency-bandwidths outlined in this study. Further, this chapter demonstrates that it is possible to use noise rejection algorithms to remove signal-cross-terms from a measured autoproduct CSDM. This successful removal does not seem to alter POMAP predictions of source location or increase peak-to-sidelobe ratio, but does increase the peak value of the ambiguity surface somewhat. Lastly, POMAP is found to lose some noise rejection capability relative to MFP at the difference frequency. While one explored noise rejection algorithm is found to increase the noise rejection capability of POMAP, this improvement is found to be marginal.

CHAPTER 6

Theory of Radiative Transfer

6.1 Introduction

Wave propagation in random media composed of discrete scatterers, referred to herein as a 'scattering' random medium, is of interest in both active and passive remote sensing. An operator working on such a system may wish to use their physical understanding of the phenomenology of wave propagation in such a medium to understand the mechanics of the medium itself, or to compensate for the propagation effects to investigate a part of the local environment. One powerful method for investigating these effects for incoherent, polarimetric remote sensing using electromagnetic waves is Radiative Transfer [Ulaby, F.T. & Long, D.G. (2014)]. Radiative Transfer postulates that an electromagnetic wave propagating in a scattering random medium undergoes scattering as a Gaussian process. The first moment of this Gaussian process, that arises from the mean scattered field, attenuates the wave propagating in the medium, and the second moment of this Gaussian process, that arises from the fluctuating scattered field, governs the radiation of this power out of the medium. This thesis chapter lays out the theory governing vector Radiative Transfer, as well as its scalar simplification. It then establishes the physical Gaussian process that is postulated to be governing Radiative Transfer via the extinction and phase matrices, and approximate methods for calculating these objects. This chapter then discusses using Monte Carlo simulation to calculate the extinction and phase matrices for Radiative Transfer, as well as approaches to use these objects to predict the field scattered by a random medium whose scattering statistics are governed by these

objects.

An observable quantity that is found to obey Gaussian statistics, which is to say that it can be characterized solely by two statistical moments, is said to arise as the result of a Gaussian process. Measured quantities governed by a Gaussian process are likely to have non-zero higher statistical moments, but these non-Gaussian moments do not carry physical meaning. The field scattered from a random medium is found to obey an underlying Gaussian process in many fields of random media propagation including polarimetry [Ulaby, F.T. & Long, D.G. (2014), Fante (1975)], and active remote sensing in cluttered environments [Lewinski (1983), Stark, H. & Woods, J.W. (1986)]. Here, both the real and imaginary parts of the scattering matrices are found to obey Gaussian statistics, allowing for meaningful information to be inferred by examining the relative magnitude and phase scattered from these media.

One of the best methods based on assuming that scattering from a random medium is a Gaussian process is Radiative Transfer [see: Ulaby, F.T. & Long, D.G. (2014), Tsang & Kong (1978)]. This method takes advantage of the principle of conservation of energy to understand how the intensity of a propagating wave will change as it traverses a random medium. In Radiative Transfer theory, two things happen to the propagating wave, typically referred to as the coherent intensity [Ishimaru (1977), Tsang & Ishumaru (1987)]: the wave is attenuated, and the attenuated power is re-radiated in many directions. Attenuation in Radiative Transfer is governed by the mean scattered field, the first moment of the Gaussian process, that works by effectively shadowing the propagating intensity. Re-radiation is governed by the fluctuating component of the scattered field, the second moment of the Gaussian process, that takes the power absorbed from the propagating field and scatters it to conserve energy. Radiative Transfer has been used to predict field propagation in a variety of interesting random media, including inside of a forest [Ulaby *et al.* (1990a)], and inside of a wheat field [Huang *et al.* (2017)]. The power of Radiative Transfer, as a tool, fundamentally rests upon the strength of the methods used to understand the mean and fluctuating components of the field scattered by the random medium itself.

The mean and fluctuating components of the field scattered by a random medium are governed

in Radiative Transfer by the extinction matrix and the phase matrix. The extinction matrix, related to the mean scattered field, absorbs intensity from the propagating field, effectively attenuating and eventually extinguishing it. This quantity is well understood in a variety of random media. For random media that are sparsely populated by non- or weakly-interacting particles, single scattering and the Foldy-Lax approximation can be used [Foldy (1945), Lax (1952)]. For random media that are composed of electrically small particles, mixing formulae [Polder & van Santen (1946), De-Loor (1953)] can be applied to predict attenuation of the propagating field. Mixing formulae work by suggesting that the extinction matrix represents an effective medium, and attenuation of the propagating wave can be understood as the loss factor in the effective medium. More modern interpretations of the Foldy approximation [Brown & Curry (1982)] also find that this understanding can be applied to single scattering. The phase function, that governs re-radiation is more difficult to predict theoretically. Many mixing formula calculations assume that the phase function is zero everywhere. Predictions of the bistatic scattered power in single-scattering systems can also be used to understand the phase matrix in media composed of non- or weakly-interacting particles [Foldy (1945)]. Each of these approximations is found to successfully predict propagation of fields in applicable random media.

Extending Radiative Transfer to predict scattering from a random medium that is densely occupied by electrically large scatterers generally relies on using a numerical method to predict the scattered field, since no analytic solution to a general electromagnetic scattering problem exists. Here, it is postulated that Monte Carlo simulation can be used to calculate the incoherent and the coherent portion of the fields scattered by a random medium. Using this methodology in two-dimensional random media propagation [Siqueira & Sarabandi (1996), Sarabandi & Siqueira (1997)] demonstrated that the coherent scattered field can be used to understand the effective medium parameter that governs the extinction matrix of the medium. This concept was then measured [Sarabandi & Nashishibi (1996)] in three-dimensional random media propagation by measuring the field scattered by many dielectric spheres placed inside of a container sphere. This notion was extended into random media propagation in media of interacting, electrically-large particles in [Geroski &

Sarabandi (2020)]. These studies give significant evidence that wave attenuation in random media propagation for all kinds of media can be understood as the existence of an effective medium. In this methodology, the phase function of the random medium can be calculated from the incoherent portion of the scattered field [Geroski & Sarbandi (2020)]. Given these methods for computing the extinction and phase matrices, all quantities that carry physical meaning in Radiative Transfer can be computed using Monte Carlo simulation.

The remainder of this chapter is divided into four sections. Section 6.2 defines the Radiative Transfer equations in their vector form, as well as introducing their scalar simplifications. Section 6.3 lays out the single scattering approach to calculating the extinction and phase matrices, the physical intuition behind this theory, and approaches for expanding single scattering predictions. Section 6.4 outlines the approach for using extinction and phase matrices to solve the Radiative Transfer equations using perturbation theory. Section 6.5 draws what conclusions are available from this chapter.

6.2 Radiative Transfer Theory

For electromagnetic remote sensing of random media that are too large to solve directly using computational electromagnetics routines, typically media that are tens of wavelengths long in every dimension, Radiative Transfer can be used to predict incoherent field propagation through the medium using the conservation of energy [Ulaby, F.T. & Long, D.G. (2014)]. While Radiative Transfer theory is fundamentally an incoherent theory of random media propagation, it can predict the relative phase between elements of the scattering matrix for polarimetric remote sensing. Radiative Transfer theory fundamentally solves for the Stokes vector of a field quantity, rather than the electric field, propagating in a random medium. The Stokes vector, related to the field intensity, is given in Eq. (6.1).

$$\vec{I} = \begin{bmatrix} I_v \\ I_h \\ U \\ V \end{bmatrix} = \begin{bmatrix} |E_v|^2 \\ |E_h|^2 \\ 2Re(E_v E_h^*) \\ 2Im(E_v E_h^*) \end{bmatrix} \tag{6.1}$$

Here, $\vec{I}$ is the Stokes vector, which has 4 elements constructed from the two polarizations of a measured electric field, E_v, E_h. The quantity Z_0 represents the impedance of free space. All elements of the Stokes Vector are real, but can lend insight into the relative phase between the different polarizations of the electric field.

The intensity propagating in a random medium is modeled, in Radiative Transfer, as changing as a function of extinction and emission, that are most generally considered to be taking place simultaneously as a wave propagates. The first of these phenomena, extinction, is modeled as an extinction matrix, where the random medium apparently absorbs energy that is propagating within it and, in so doing, attenuates the propagating wave. This absorption and attenuation occurs in all highly scattering random media, and is generally found in electromagnetic propagation in a random medium with a background of free space to be emitted (or scattered) out of the medium in question, rather than absorbed and dissipated as heat. The nature of this emission is governed by the phase matrix. This is modeled in Radiative Transfer using Eq. (6.2), in the form of an integral equation.

$$\frac{\partial \vec{I}(\vec{r}, \hat{s})}{\partial s} = -\bar{\bar{\kappa}}_e \vec{I}(\vec{r}, \hat{s}) + \int_\Omega d\Omega' P_b(\hat{s}, \hat{s}') \vec{I}(\vec{r}, \hat{s}') \tag{6.2}$$

The Radiative Transfer equation is defined by the expected change in intensity along a direction of propagation, $\hat{s}$, of a coherent field. This change is governed by the extinction matrix, $\bar{\bar{\kappa}}_e$, and a phase matrix, P_b. The extinction matrix serves to attenuate the propagating field, and the phase matrix, that represents bistatic power scattered from incident direction $\hat{s}'$ or Ω' to scattered direction $\hat{s}$ or Ω, serves to emit the absorbed power in every direction.

The Radiative Transfer equations fundamentally arise from the conservation of energy. From

a scattering perspective, all electromagnetic energy is initially contained in the incident field, that can be decomposed into a sum of plane waves. The extinction matrix serves to absorb power from this incident wave. While power can be absorbed into the medium itself and dissipated as heat, it is more commonly seen to be scattered out as incoherent energy. The extinction matrix, then, predicts the length scale (or skin depth) over which an incident field can propagate in the medium. All power that is not dissipated as heat in the random medium is re-radiated according to the bistatic scattering predictions modeled in the phase function. Because of the simplicity of the equations and the existence of solutions to integral equations of the form of the Radiative Transfer equation, the strength of the predictions made using Radiative Transfer theory rest entirely on the strength of the methods used to predict the extinction and phase matrices.

6.3 Single Scattering Prediction of Extinction and Phase Matrices

This thesis focuses on solving for extinction and emission from sparsely populated random media composed of electrically large, interacting scatterers. The natural place to start such an analysis is with the single scattering approximation to Radiative Transfer [Ulaby, F.T. & Long, D.G. (2014)]. Single scattering theory postulates that the inclusions populating a random medium do not interact with one another, and therefore the scattering matrix of the overall random medium can be considered as being the sum of the scattering matrices of each individual particle. Given this observation, and following the Radiative Transfer equation, the extinction matrix of the random medium is given in Eq. (6.3).

$$\bar{\bar{\kappa}}_e = \begin{bmatrix} 2Re(m_{vv}) & 0 & Re(m_{vh}) & Im(m_{vh}) \\ 0 & 2Re(m_{hh}) & Re(m_{hv}) & Im(m_{hv}) \\ 2Re(m_{hv}) & Re(m_{vh}) & Re(m_{vh}+m_{hh}) & Im(m_{vh}-m_{vv}) \\ -2Im(m_{hv}) & Im(m_{vh}) & Im(m_{vh}-m_{hh}) & Re(m_{vv}+m_{hh}) \end{bmatrix} \tag{6.3}$$

$$m_{pq} = -\frac{2\pi i}{k} n \langle S_{pq}(\Omega = \Omega') \rangle \tag{6.4}$$

Here, $\bar{\bar{S}}$ is the bistatic scattering matrix of the medium, pq are the scattered and incident polarizations of the field quantity, Ω,$\Omega\prime$ are the scattered and incident directions of the field quantity, n is the number density of particles in the medium, and k is the wavenumber of the propagating field. The matrix m_{pq} is found to depend on the ensemble average, over both particle type and orientation, of the forward-scattering direction of the scattering matrices of all particles in the medium. The extinction matrix, $\bar{\bar{\kappa}}_e$, is defined relative to m_{pq} and can serve both to attenuate the power of the propagating field (seen primarily in the first block of the matrix) and to change the relative phase between the field quantities. Here, the single scattering approximation explicitly depends only on the forward scattered field to shadow the propagating field quantity. This is to say that the scattered fields of non-interacting particles are expected to be incoherent in every direction except for forward scattering.

The phase matrix, that governs emission of the power absorbed in the medium by the extinction matrix, is defined as all power that is scattered incoherently in the medium. According to single scattering theory, power scattered in all directions except forward scattering is incoherent. The phase matrix, then, is found by relating the incident and scattered intensities of the propagating field quantity. These quantities are related most generally by the modified Mueller matrix, given in Eq. (6.5).

$$\bar{\bar{M}} = \begin{bmatrix} |S_{vv}|^2 & |S_{vh}|^2 & Re(S_{vv}S_{vh}^*) & -Im(S_{vv}S_{vh}^*) \\ |S_{hv}|^2 & |S_{hh}|^2 & Re(S_{hv}S_{hh}^*) & -Im(S_{hv}S_{hh}^*) \\ 2Re(S_{vv}S_{hv}^*) & 2Re(S_{vh}S_h h^*) & Re(S_{vv}S_{hh}^* + S_{vh}S_{hv}^*) & -Im(S_{vv}S_{hh}^* - S_{vh}S_{hv}^*) \\ 2Im(S_{vv}S_{hv}^*) & 2Im(S_{vh}S_h h^*) & Im(S_{vv}S_{hh}^* + S_{vh}S_{hv}^*) & Im(S_{vv}S_{hh}^* - S_{vh}S_{hv}^*) \end{bmatrix} \tag{6.5}$$

The Mueller matrix relates the incident and scattered Stokes vectors of a field according to Eq. (6.6) by the scattering matrix of the medium, $\bar{\bar{S}}_{pq}$.

$$\vec{I}^{s} = \frac{1}{r^2}\bar{\bar{M}}\vec{I}^{i} \tag{6.6}$$

The phase matrix of the medium, that represents the average bistatic scattered field scattered by each particle, can be calculated as the ensemble average of the Mueller matrix of all particles in the medium and their orientations, as is shown in Eq. (7).

$$P_b = n\langle\bar{\bar{M}}\rangle \tag{6.7}$$

$$\langle\bar{\bar{M}}\rangle = \begin{bmatrix} |S_{vv}|^2 & |S_{vh}|^2 & 0 & 0 \\ |S_{hv}|^2 & |S_{hh}|^2 & 0 & 0 \\ 0 & 0 & Re(S_{vv}S_{hh}^* + S_{vh}S_{hv}^*) & -Im(S_{vv}S_{hh}^* - S_{vh}S_{hv}^*) \\ 0 & 0 & Im(S_{vv}S_{hh}^* + S_{vh}S_{hv}^*) & Im(S_{vv}S_{hh}^* - S_{vh}S_{hv}^*) \end{bmatrix} \tag{6.8}$$

The ensemble average of the Mueller matrix, for a large scatterer like a semi-infinite random medium, is found to be governed by a Gaussian process [Ulaby *et al.* (1992)]. This analysis finds that the co-polarized elements of the scattering matrix are uncorrelated to the cross-polarized elements of the scattering matrix. This leads many elements of the Mueller matrix to go to zero as they are averaged. The first block of the phase matrix, related to the ensemble average of the Mueller matrix by the number density of particles in the medium n, governs the power of the incoherent field propagating in the medium. The fourth block is hereafter referred to as the polarimetric portion of the phase matrix, in that it defines the relative phase between the two measured polarizations of the field.

Many attempts to extend single scattering theory have been undertaken. Fundamentally, these methods require relaxing the assumption that all interactions between particles are incoherent. Most particularly, inter-particle coherence has been found to exist in the back-scattering direction for pairs of particles, as in [Mookerjee & Dowling (2017), McCargar & Lang (2020)]. Some field formulations, like the Quasi-Crystalline Approximation and its extensions [Tsang & Ishumaru

(1987)] are able to account for these pairwise interactions. However, higher order extensions of these methods are both challenging to apply and their direct applicability to a given problem is difficult to assess. This thesis will attempt to directly extend single scattering theory to include all orders of interaction between particles in Chapters 7 8.

6.4 Perturbation Theory Solution to Radiative Transfer Equation

The most common approach to solving the Radiative Transfer equations uses perturbation theory [Chandrasekhar, S. (1960)]. This approach can be taken to solve for the intensity propagating in a complicated random medium that includes interactions between neighboring random media. This thesis, that only solves for the field scattered by a random medium far from reflecting boundaries and other environmental factors, treats a relatively simple form of this perturbative approach. The more complex approach, for treating a random medium inside of a layered medium, can be found in [Ulaby, F.T. & Long, D.G. (2014)]. This perturbation approach is given in Eq. (9).

$$\frac{\partial\left(\vec{I}_0 + \vec{I}_1 + ...\right)}{\partial s} = -\bar{\bar{\kappa}}_e\left(\vec{I}_0 + \vec{I}_1 + ...\right) + \int_\Omega d\Omega' P_b(\Omega, \Omega')\left(0 + \vec{I}_0 + \vec{I}_1 + ...\right) \tag{6.9}$$

Here, $\vec{I}_n$ is the n^{th} order solution to the perturbation series. Here, the phase-matrix, that only adds incoherently over the entire medium, is assumed to not contribute to the zeroth-order solution to the perturbation series. Therefore, attenuation of the coherent field is assumed to be defined by a first-order (vector) partial differential equation given in Eq. (10).

$$\frac{\partial \vec{I}_0}{\partial s} = -\bar{\bar{\kappa}}_e \vec{I}_0 \Rightarrow \vec{I}_0(s) = exp(-\bar{\bar{\kappa}}_e s)\vec{I}_i \tag{6.10}$$

Here, $\vec{I}_i$ is the incident Stokes vector, $\vec{I}_0$ is the zeroth-order solution to the Radiative Transfer Equations, and this quantity is found to be attenuated by the extinction matrix, $\bar{\bar{\kappa}}_e$. The exponential function of a matrix is found in this case by diagonalizing the matrix [see: Ulaby *et al.* (1990b)]

which is possible because the extinction matrix is full-rank. This zeroth-order solution to the Radiative Transfer equations can be substituted back into the Radiative Transfer equation to solve for a higher-order solution to the perturbation series.

The first-order solution to the Radiative Transfer equation is the first that includes the effects of incoherent scattering that are governed by the phase matrix. Provided that the incident field is assumed to be a plane wave, which is true when the medium is in the far field of the source, then the zeroth-order solution to the Radiative Transfer equation is also a plane wave. Given this, the first-order Radiative Transfer equation is given in Eq. (11).

$$\frac{\partial \vec{I}_1}{\partial s} = -\bar{\bar{\kappa}}_e\left(\vec{I}_1\right) + \int_\Omega d\Omega' P_b(\Omega, \Omega')\vec{I}_0(s') \tag{6.11}$$

$$\frac{\partial \vec{I}_1}{\partial s} = -\bar{\bar{\kappa}}_e\left(\vec{I}_1\right) + P_b(\Omega, \hat{s})exp(-\bar{\bar{\kappa}}_e s)\vec{I}_i \tag{6.12}$$

Here, the zeroth-order solution to the Radiative Transfer equation is explicitly substituted into the integral in Eq. (6.11). The zeroth-order solution, being defined as a wave propagating in one direction in a lossy medium makes the integral over incident field angle trivial. Then, the phase function is seen explicitly to radiate power in every direction. This equation is most commonly solved for the backscattered intensity from a random medium, using $P_b(-\hat{s}, \hat{s})$. Higher-order solutions to the Radiative Transfer equations can be obtained, if desired. However, the first order solution is most typically used because it can be used to relate the measured intensity backscattered from a random medium to the extinction and phase matrix of the medium itself. This allows a user to solve for the extinction and phase matrices of the medium that is being interrogated.

6.5 Conclusion

This chapter reviews several methods for understanding electromagnetic propagation in a random medium composed of discrete scatterers. Several approaches for solving for propagation in such a

medium are mentioned, with one particular approach, Radiative Transfer, being explored in detail. The equations governing vector Radiative Transfer theory are given, in terms of the extinction and phase matrices. The extinction matrix is defined to govern the attenuation of the coherent power propagating in the medium, effectively absorbing it. This absorbed power is then emitted by the phase matrix. The single scattering approach to calculating these two objects is outlined, as are assumptions inherent in this approach. Lastly, the perturbative (or iterative) approach to solving for the propagating intensity is outlined and solved up to first order. This chapter primarily serves to introduce Radiative Transfer theory, as the two following chapters aim to extend the predictions made using single scattering to account for interactions between particles in the medium using Monte Carlo simulation.

CHAPTER 7

Existence and Prediction of Extinction and Phase Matrices in a Random Medium of Interacting Particles

7.1 Introduction

Wave propagation in a random medium composed of discrete scatterers is a typical problem in both acoustic and electromagnetic remote sensing. A random medium that is occupied by discrete scatterers, referred to as inclusions, placed in an infinite background of a material, referred to as a host, is typically treated as a scattering problem [Ulaby, F.T. & Long, D.G. (2014)]. One powerful method for understanding field propagation, particularly in the context of polarimetric radar, is Radiative Transfer [Chandrasekhar, S. (1960), Tsang & Ishumaru (1987)]. Radiative Transfer seeks to model random media propagation using two phenomena, coherent field attenuation and incoherent scattering, that are related by the conservation of energy. Attenuation and scattering are typically described mathematically as extinction and phase matrices, respectively [Ulaby, F.T. & Long, D.G. (2014), Tsang & Kong (1978)]. Exact analytic representations of extinction and phase matrices, postulated to arise from coherent mean field scattering and incoherent fluctuating field scattering, do not exist because of the complexity of the scattering problem [Harrington (1967), Jackson, J.D. (1999)] and therefore both functions must be approximated to make Radiative Transfer predictions. The strength of the predictions made by Radiative Transfer is governed by the

methods used to calculate the extinction and phase matrices. This chapter outlines a new method, based on Monte Carlo simulation, that can be used to calculate the extinction and phase matrices from any random medium. It demonstrates the existence of a coherent scattered (mean) field, that this mean field represents an effective medium that the wave is propagating in that can be used to understand how the field attenuates, and that this effective medium seems to be intrinsic to the form of the random medium itself and independent of choices made by the user. It also demonstrates the existence of an incoherent scattered field that governs the phase function of a random medium, and shows that this function is also intrinsic to the medium itself.

Many extant methods can be used to compute the extinction and phase matrices of a random medium for making predictions using Radiative Transfer. Generally, they can be described as theoretical, numerical, and phenomenological methods. The first methods that were published in the open literature for describing random media propagation are theoretical. Because of the insolvability of a general scattering problem, [see: Jackson, J.D. (1999)], each of these predictions is made using approximations. When inclusions in a medium are small, mixing formulas [Polder & van Santen (1946), DeLoor (1953)] predict that the extinction matrix of the medium can be understood as the existence of an effective medium based on the statistics of the medium itself. Typically, the phase matrices of such media are neglected. When particles are electrically large, but are either non- or weakly-interacting, single scattering theory [Foldy (1945), Lax (1952)] can be used to predict both the extinction and phase matrices of the medium itself. Curiously, more modern interpretations of single scattering theory [Brown & Curry (1982)] also interpret the extinction matrix as the existence of an effective medium. Several theories exist, like the Quasi-Crystalline Approximation [Tsang & Ishumaru (1987)] and its extensions, that account for interactions between particles phenomenologically. While these methods are individually powerful and can be used to accurately predict observations, they can be both complex to implement and their applicability to problems that violate their approximation is difficult to assess. The Monte Carlo simulation method outlined in this chapter is designed to help to understand what problems that these extant theoretical methods can be used to understand.

Radiative Transfer predictions can also be made phenomenologically, based on measured experimental data. Because these models are derived through examination of measured data, they do not obviously depend on any physical approximations that are made to simplify calculations. Observed data has been used to understand, among other relevant remote sensing problems, variations in soil moisture [McNairn *et al.* (2015), Han *et al.* (2014)], propagation and scattering in wheat fields [Ulaby & El-Rayes (1987)], and on roads [Li & Sarabandi (1999)]. Additionally, observed data can be used to provide larger models of propagation phenomenology [Chew & Wang (1990), Ulaby *et al.* (1990a), Huang *et al.* (2017)] that inform different problems in remote sensing. While this phenomenological approach can provide scientific insight into random media propagation that is free of mathematical assumptions, using these models to make predictions outside of the dataset that was used to make them can be challenging. Further, the process of gathering more data to expand these models can be expensive. The Monte Carlo simulation method can be used to understand how and where these models can be extrapolated and to provide predictions as to the applicability of these models in solving new problem

The methods described in this chapter are not unique in using Monte Carlo simulation to predict the extinction and phase matrices or estimate solutions to the Radiative Transfer Equations in another way in random media composed of electrically large interacting scatterers. Monte Carlo simulation has been used to successfully understand electromagnetic propagation in rice fields [Oh & Hong (2007)], forests [Zhang & Gasiewski (2020)], and in chaff [Yin & Bo (2014), Zhang & Wu (2019)]. While these methods do fundamentally use full-wave computational electromagnetics methods in conjunction with Monte Carlo simulation to understand the solution to the Radiative Transfer equations, they do not directly estimate the fields that are coherently and incoherently scattered by the random media that they are examining. The methods outlined in this chapter more closely follow [Siqueira & Sarabandi (1996), Sarabandi & Siqueira (1997)], that postulate that fields scattered by a random medium are governed by a Gaussian process [Ulaby *et al.* (1992)] in both magnitude and phase. Given this, the coherent scattered field gives direct insight into the form of the extinction matrix. These predictions were first measured in [Sarabandi & Nashishibi (1996)]

for small dielectric inclusions and were extended numerically into three dimensions in [Geroski & Sarabandi (2020)]. This method postulates that the incoherent portion of the scattered field gives insight into the phase matrix of the medium [Geroski & Sarbandi (2020)], a quantity that has never been predicted using these methods before. This chapter summarizes these findings and shows how to use them to derive the extinction coefficient and phase function of the medium, rather than the extinction and phase matrices. While there is no reason that these methods cannot be used to calculate full extinction and phase matrices, only their scalar analogues are examined here for brevity.

This chapter makes use of two powerful methods for making its predictions: the Method of Moments and inverse scattering. The Method of Moments, referred to as the Integral Equation Method in other fields, was first published in [Harrington (1967)] for solving for the Green's function of an interacting medium and is today one of the more popular computational electromagnetics routines [Jin, J. (2010)] for solving scattering problems. To facilitate both fast predictions and to make replication of these results easier, a commercial software package, FEKO [Altair Engineering (2014)], is used to calculate the fields scattered by collections of scatterers. Using these methods, the coherent and incoherent portions of the field scattered by collections of these scatterers can be isolated. Determining the extinction coefficient of a collection of scatterers from the coherent portion of the scattered field is posed as an inverse scattering problem. Inverse scattering problems [Johnson *et al.* (2008)] seek to understand the form of the medium by minimizing the difference between a field that is expected to be scattered by this medium and the field scattered by an unknown medium. Such methods have been used to understand biological tissue [Johnson *et al.* (2008), DiDonato *et al.* (2015)], and in electromagnetic remote sensing of the environment [Omar & Akhtar (2005), Zeng *et al.* (2020)]. This method poses a relatively simple version of an inverse scattering problem that matches the coherent portion of the scattered field to a field scattered by a homogeneous dielectric sphere [Bohren, C. & Huffman, D. (1983)]. The solution to this inverse problem is used to represent the extinction coefficient of the mediu

The remainder of this chapter is divided into four parts. Section 7.2 outlines the theory and

all procedures that are necessary to implement the Monte Carlo simulation method. Section 7.3 demonstrates the existence of a field that is coherently scattered by two random media composed of electrically large, metallic scatterers. It then demonstrates the conditions under which this coherent mean field can be used to solve for the extinction coefficient of the medium. Section 7.4 demonstrates the existence of an incoherent, or fluctuating, portion of the scattered field, and uses this object as the basis to understand the phase function of the medium. Section 7.5 summarizes the findings of this chapter and draws what conclusions are available.

7.2 Theory

The method outlined in this chapter is best understood from the standpoint of single scattering. Single scattering theory typically focuses on solving for the field that is scattered by a single inclusion inside of the random medium. From here, interactions between the inclusions can be accounted for using multiple scattering phenomena, and the extinction and phase matrices are expected to scale coherently and incoherently, respectively. This method proposes that the fundamental unit governing propagation is an enclosing macro-particle or scoop of the random medium that encloses many scatterers or inclusions. The form of this macro-particle and the field scattered by it is defined statistically by a Gaussian process [Ulaby *et al.* (1992)], where the first moment of this Gaussian process is postulated to define the extinction matrix of this medium and the second moment of this process is postulated to define its phase matrix. Monte Carlo simulation, then, is employed to calculate the coherent and incoherent portions of the field scattered by this enclosing macro-particle that accounts for all orders of multiple scattering and near field interaction for the inclusions contained in the enclosure. Given calculated extinction and phase matrices that represent the physically relevant portions of this field scattered by this single macro-particle, the solutions to the Radiative Transfer equations can be obtained that account for local, small-scale interactions between particles in the medium.

7.2.1 Defining the Enclosing Particle

The enclosing macro-particle of the medium that defines the extinction and phase matrices for the medium is a fictional particle that contains a single statistical configuration of the medium. For an infinite random medium, this can be thought of as removing a scoop of the medium itself. For a random medium that is very sparsely populated, most of the enclosures are expected to only contain one particle each and the predictions of the extinction and phase matrices are expected to match the predictions given by single scattering theory. For all media considered in this thesis, inclusions in a given medium are assumed to be non-overlapping. This is accomplished using a successive nomination procedure. Given an enclosing particle that contains a volume V that is occupied with inclusions that do not overlap and which contain volume $V_i \subset V$, another inclusion, that occupies volume V_i', can be added to the enclosing particle by affirming that it does not overlap with V_i. The overlap between these volumes can be evaluated by determining if their surfaces, δV_i,$\delta V_i'$ intersect. Intersection between these surfaces can be computed by discretizing the surfaces into a countable number of area elements, as in Eq. (7.1) and (7.2).

$$\begin{aligned} \left\{\delta V_{i,n}\right\} &: \cup_n \delta V_{i,n} = \delta V, \max_n \left\|\delta V_{i,n}\right\|_0 \leq \alpha \\ \left\{\delta V'_{i,n}\right\} &: \cup_n \delta V'_{i,n} = \delta V', \max_n \left\|\delta V'_{i,n}\right\|_0 \leq \alpha \end{aligned} \tag{7.1}$$

Here, $\delta V_{i,n}$, $\delta V'_{i,n}$ are elements of the surfaces δV_i,$\delta V_i'$ that enclose inclusion volumes $V_i, V_i\prime$. Each of these discrete surface elements is chosen to have a maximal area of α. Then, the new inclusion volume, V_i' is determined to not overlap with existing inclusion volume V_i if the minimum separation between area elements, Δ in Eq. (7.2), is larger than the maximal area α.

$$\Delta = \min_{m,n} \Delta_{mn} = \min_{m,n} \left\|\delta V_{i,m} - \delta V'_{i,n}\right\|_1 \tag{7.2}$$

This procedure is initialized by placing a single inclusion in the enclosing medium randomly according to the statistics that govern spatial location and orientation of inclusions in the medium.

The procedure is completed when the volume fraction or number density of inclusions inside of the medium matches that of the medium itself. This procedure can be optimized for particular inclusion geometries, such as spheres or cylinders [Geroski & Sarabandi (2020)]. This successive nomination procedure is also found to be inefficient for densely packed media, and, in this case packing algorithms [Siqueira *et al.* (1994)] can be used to more efficiently populate the medium. For all problems explored in this thesis, either successive nomination or a simplification of this procedure will be used.

7.2.2 Coherent Mean Field

Given many configurations of enclosing particles, the bistatic scattering matrices of each instantiation of the macro-particle can be solved using the Method of Moments [Jin, J. (2010)]. The Method of Moments works by calculating the currents induced on the inclusions in the medium by an incident source, that is represented as a plane wave for the entirety of this thesis. These currents are then used to compute the field scattered by this medium, as is shown in Eq. (7.3), as a summation of currents multiplied by the Dyadic Green's function of free space. The scattering matrix of this medium is defined in Eq. (7.4).

$$\vec{E}_{sc}(\vec{x}) = \int_3 d\vec{x}' \vec{J}(\vec{x}')\bar{\bar{G}}(\vec{x}, \vec{x}') \tag{7.3}$$

$$\bar{\bar{S}}_{pq}(\Omega, \Omega') = \lim_{r\to\infty}(-ikr)\ exp(-ikr)\ \vec{E}_{sc}(r, \Omega, \Omega') \tag{7.4}$$

Here, $\vec{E}_{sc}$ represents the scattered field measured at spatial location $\vec{x}$, that is given in electromagnetic theory as the sum of waves radiated by induced currents in the universe [3], $\vec{J}$, at source position $\vec{x}'$ times the Dyadic Green's Function for the medium $\bar{\bar{G}}$. The scattering matrix, $\bar{\bar{S}}$, represents the field radiated by the scattering problem. It depends on the measured and incident polarizations, p, q, as well as the solid angle that the scattered and incident field are propagating in, Ω, Ω'. Having calculated a Monte Carlo simulation of these scattering matrices, the coherent

portion of the scattering matrix can be calculated using Eq. (7.5).

$$\bar{\bar{S}}^{coh}_{pq}(\Omega, \Omega') = \left\langle \bar{\bar{S}}_{pq}(\Omega, \Omega') \right\rangle \tag{7.5}$$

The coherent portion of the scattering matrix, $\bar{\bar{S}}^{coh}_{pq}$, is expected to converge when enough Monte Carlo trials are used to calculate it, and simultaneously contains information about the enclosing particle and about the nature of the medium inside of the enclosure. Convergence of the Monte Carlo simulation will be addressed in Section 7.3. The extinction matrix should be independent of the enclosing particle, that is chosen by a user, and should only contain information about the medium itself, and must be calculated using knowledge of the enclosure.

7.2.3 Inverse Scattering: Solving for the Effective Medium

Given a convergent estimate of the coherent portion of the scattering matrix obtained by Monte Carlo simulation, the extinction matrix is postulated to depend on the existence of an effective medium that governs mean field propagation. This effective medium is postulated to be the solution to an inverse scattering problem, as in Eq. (7.6).

$$\epsilon_{eff}, \mu_{eff} = \min_{\epsilon_{eff}, \mu_{eff}} \int_{\Omega} d\Omega |S^{coh}_{vh}(\Omega) - S_{vh}(\Omega, \epsilon_{eff}, \mu_{eff})|^2 \tag{7.6}$$

Eq. (7.6) postulates that mean field propagation in a random medium should be constant everywhere, and can be represented most generally as effective permittivity and permeability, $\bar{\bar{\epsilon}}_{eff}$ and $\bar{\bar{\mu}}_{eff}$. These effective medium parameters can be determined using inverse scattering, a particular application of the equivalence principle, to minimize the difference between the coherent portion of the scattering matrix determined using Monte Carlo and the fields scattered by a homogeneous medium that occupies the same volume as the enclosing particle.

The solution to the inverse scattering problem posed in Eq. (7.6) does not necessarily exist, and can be difficult to calculate. For the scattering problems considered in this thesis, the solution to this equation is always found to exist in a simple form. This thesis focuses exclusively on random media

composed of inclusions that are randomly oriented in space, and therefore finds that the effective medium permittivity and permeability are (complex) scalars. Moreover, all problems considered herein find that the effective medium is well represented simply as an effective permittivity and has an effective permeability that matches that of free space. Given these considerations, Eq. (7.6) reduces in complexity to Eq. (7.7).

$$\epsilon_{eff} = \min_{\epsilon_{eff}} \int_{\Omega} d\Omega |S_{vh}^{coh}(\Omega) - S_{vh}(\Omega, \epsilon_{eff}, \mu_{eff} = 1)|^2 \tag{7.7}$$

Lastly, studies presented in this thesis find that only discretely many points are needed to calculate the solution to the inverse scattering problem. Therefore, rather than computing the full integral shown in Eq. (7.6), the normalized Euclidean distance between the coherent portion of the scattering matrix and the scattering matrix of the container will be minimized to compute the effective medium, as is shown in Eq. (7.8).

$$\epsilon_{eff} = \min_{\epsilon_{eff}} \frac{\sqrt{\left(\sum_n |S_{vh}^{coh}(\Omega_n) - S_{vh}(\Omega_n, \epsilon_{eff}, \mu_{eff} = 1)|^2 \right)}}{\sqrt{\sum_n |S_{vh}^{coh}(\Omega_n)|^2} + \sqrt{\sum_n |S_{vh}(\Omega_n, \epsilon_{eff}, \mu_{eff} = 1)|^2}} \tag{7.8}$$

Here, a perfect match between the scattering matrices would give a Euclidean distance of 0. If the scattering matrices are equal in magnitude and opposite in phase, the Euclidean distance between them is 2. The minimization will be calculated using either brute force or convex optimization, depending on the problem being examined at the time.

The effective permittivity of a random medium is expected to be mostly independent of the choice of the enclosing particle assuming that the enclosing particle is able to enclose relevant configurations of the random medium, meaning that the enclosing particle is much larger than the inclusions. It is also found that electrically small enclosing particles are difficult to distinguish for different permittivities, and therefore a particle larger than one free-space wavelength should be chosen as the enclosing particle. While many geometric shapes for enclosures were explored in two-dimensional scattering problems [Siqueira & Sarabandi (1996), Sarabandi & Siqueira (1997)],

three-dimensional scattering problems should use a sphere. This choice is made because an analytic solution to the field scattered by a homogeneous dielectric sphere exists. Therefore, solutions to the inverse scattering problem are derived using this Green's function, following the convention in [Bohren, C. & Huffman, D. (1983)]. The procedure for calculating the electric field scattered by a sphere made up of a homogeneous lossy dielectric material is outlined in Eq. (7.9) – (7.14).

$$\vec{E}^{\hat{\theta}}_{sc}(\Omega) = \vec{E}_0 \frac{exp(ikr)}{-ikr} cos(\phi) S_2(\theta) \tag{7.9}$$

$$\vec{E}^{\hat{\phi}}_{sc}(\Omega) = \vec{E}_0 \frac{exp(ikr)}{-ikr} sin(\phi) S_1(\theta) \tag{7.10}$$

$$S_1(\theta) = \sum_n \frac{2n+1}{n(n+1)} (a_n \pi_n + b_n \tau_n) \tag{7.11}$$

$$S_2(\theta) = \sum_n \frac{2n+1}{n(n+1)} (a_n \tau_n + b_n \pi_n) \tag{7.12}$$

$$a_n = \frac{m\psi_n(mx)\psi'_n(x) - \psi_n(x)\psi'_n(mx)}{m\psi_n(mx)\xi'_n(x) - \xi_n(x)\psi'_n(mx)} \tag{7.13}$$

$$b_n = \frac{\psi_n(mx)\psi'_n(x) - m\psi_n(x)\psi'_n(mx)}{\psi_n(mx)\xi'_n(x) - m\xi_n(x)\psi'_n(mx)} \tag{7.14}$$

Here, a_n,b_n represent the modal coefficients induced in the sphere that has index of refraction $m = \sqrt{\epsilon_r}$ by the incident field. These coefficients are solved by using the Wronskian between the relevant Riccatti-Bessel functions, ψ_n,ξ_n. Here, S_1,S_2 represent the two polarizations of the scattering matrix. These polarizations will later be defined as S_h,S_v to follow the Forward Scattering Alignment convention given in [Ulaby, F.T. & Long, D.G. (2014)]. The scattering matrix elements are calculated as a sum over modal coefficients multiplied by π_n,τ_n that represent a convenient decomposition of the vector spherical harmonic series. The scattering matrices can be used

to calculate the scattered electric fields, $\vec{E}^{\hat{\theta}}_{sc}, \vec{E}^{\hat{\phi}}_{sc}$ when multiplied by an outgoing spherical wave, but this step is not undertaken in this thesis.

7.2.4 (Incoherent) Fluctuating Field & Phase Function

The phase matrix of the random medium is postulated to be related to the second moment of the Gaussian process governing the scattered field. The full phase matrix is expected to be accessible using Monte Carlo simulation, but only some elements of the phase matrix will be computed in this thesis. Given the results of a Monte Carlo simulation and the calculated coherent portion of the scattering matrix, the incoherent portion of the scattering matrix can be calculated using Eq. (7.15).

$$\bar{\bar{S}}^{inc}_{pq}(\Omega, \Omega') = \left(\bar{\bar{S}}_{pq}(\Omega, \Omega') - \bar{\bar{S}}^{coh}_{pq}(\Omega, \Omega')\right) \tag{7.15}$$

Here, $\bar{\bar{S}}^{inc}_{pq}$ represents the incoherent portion of the p,q element of the bistatic scattering matrix with incident field propagating at solid angle Ω' and scattered field propagating at solid angle Ω for a given Monte Carlo trial. Like the coherent portion of the scattering matrix, this is intended to simultaneously convey information about the enclosure and the random medium itself. From the incoherent portion of the scattering matrix, a scattering coefficient can be computed, as in Eq. (7.16), and the phase function can be computed, as in Eq. (17).

$$\sigma^{inc}_{pq}(\Omega, \Omega') = \frac{\left(\left\langle |\bar{\bar{S}}^{inc}_{pq}(\Omega, \Omega')|^2 \right\rangle\right)}{N} \tag{7.16}$$

$$P_b(\Omega, \Omega') = n\left(\left\langle |\bar{\bar{S}}^{inc}_{pq}(\Omega, \Omega')|^2 \right\rangle\right) \tag{7.17}$$

Here, σ^{inc}_{pq} is the incoherent scattering coefficient of the medium, and it is a measure of the average amount of power scattered by each particle inside of the enclosure. This coefficient is calculated by dividing the incoherent portion of the scattering matrix by N, the number of particles

in the medium. This coefficient is calculated in this chapter because it is expected to be constant for all relevant enclosing particles. The phase function, a measure of bistatic power scattered by the entire medium, is related to the incoherent scattered power by the number density, n, of enclosing particles within the medium. The extinction and phase matrices can be used to make predictions about random media propagation using Radiative Transfer.

One additional method is employed here to calculate a convergent representation of the incoherent portion of the scattering matrix, referred to as buffer zone averaging. This step is undertaken to minimize the amount of computation that is required to estimate the incoherent portion of the scattering matrix. Here, the currents induced on all inclusions in each configuration of the medium are computed using the Method of Moments as before. Another enclosure, nested inside of the first enclosure, is proposed, and the annulus between these two particles is referred to as the buffer zone. Currents inside of the buffer zone are omitted from the computation of the scattering matrix. The size of this buffer zone can be varied to effectively produce more Monte Carlo samples. While the scattering problems used to compute these samples do not represent independent samples of the random medium, the fields scattered by these samples seem to represent independent samples of the scattered field. This postulate is demonstrated in this chapter, but proving it is beyond the scope of this thesis.

7.3 Existence of Mean Scattered Field and Effective Permittivity

To compute the effective permittivity of a random medium composed of interacting particles using Monte Carlo simulation, statistical configurations of the medium must first be generated. This chapter will demonstrate that media composed of two different kinds of conductive particles have recognizable coherent scattered mean fields and effective permittivities. For this chapter, all scattering phenomena will be computed at X-Band, and the incident plane wave will have a free-space wavelength of $\lambda = 0.03$ cm ($f \approx 10$ GHz). The two types of particles considered in this chapter are

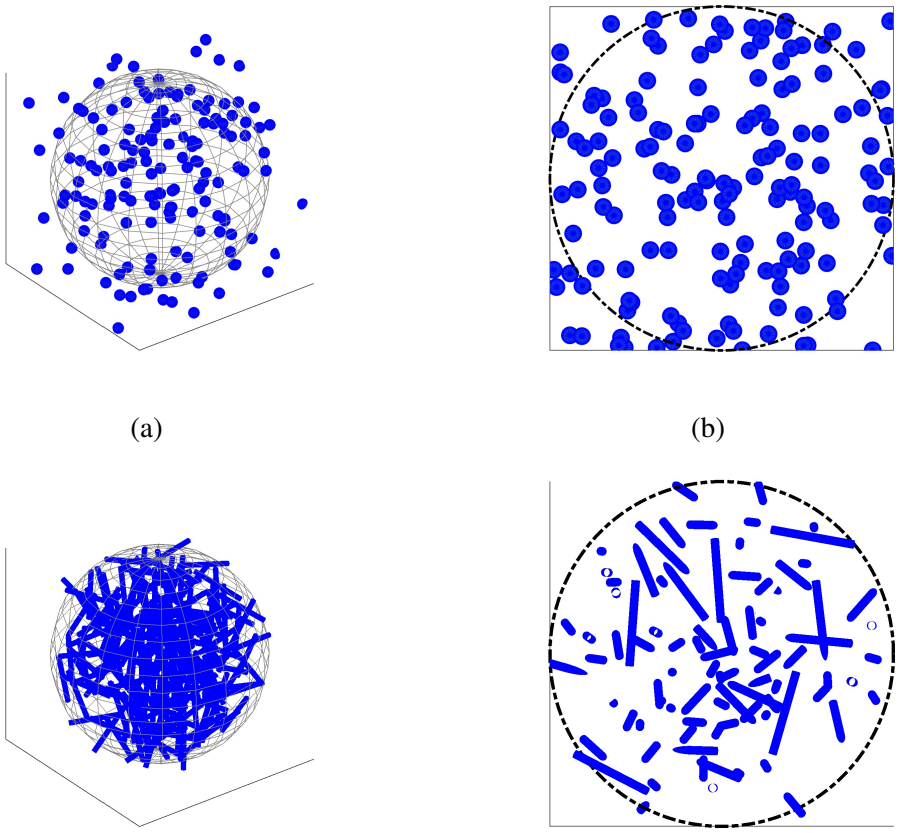

(a) (b)

(c) (d)

Figure 7.1: Example statistical configurations with (a) spherical inclusions of size $r_s = \lambda/4$ and volume fraction $\gamma = 0.05$ and (b) wire inclusions of size $r_s = \lambda/20$, length $l_s = \lambda$, and number density $n = 50$ inside of a container sphere of size $R_s = 2\lambda$, (c) two-dimensional view of subfigure (a), (d) two-dimensional view of (b)

spheres that are Perfect Electric Conductors (PEC) with a radius $r_i = \lambda/4$, and long thin wire structures with radius $r_i = \lambda/20$ and length $l = \lambda$. For spherical inclusions, the occupation density of the enclosure will be measured in volume fraction, γ, or the volume enclosed by inclusions divided by the volume of the sphere. For wire inclusions, the density of the enclosure will be measured in number density, n, or number of particles per cubic wavelength. Example configurations of the random medium are shown in Fig. 7.1, for enclosing particles of radius $R_s = 2\lambda$.

Fig. 7.1a and 7.1b show a three- and two-dimensional view of a configuration of the medium that is occupied by spherical inclusions. Fig. 7.1c and 7.1d show the same view, but for wire inclusions. All figures show the enclosing particle around the inclusions in black. Particles that

stick out of the enclosure will be fully included in computing the numerical Green's function for this scattering problem using the Method of Moments, but currents induced on the particles will be excluded formally from the calculated scattered field. Practically, this decision is not seen to have any effect on the final calculated form of the coherent scattering matrix for a sufficiently large container particle.

The scattering matrices of hundreds of these configurations was calculated using FEKO [Altair Engineering (2014)] for a Monte Carlo simulation of this scattering procedure. The incident field for this scattering problem is a single plane wave traveling at $\theta' = 0$, linearly polarized in the $\hat{x}$ direction. Bistatic scattering matrices were calculated for $-180^\circ \leq \theta \leq 180^\circ$ every one degree over two phi-cuts, $\phi = 0^\circ, 90^\circ$. For the purpose of this experiment, Forward Scattering Alignment (FSA) [Ulaby, F.T. & Long, D.G. (2014)] convention is adopted to define v,h polarization. In this case, $\bar{\bar{S}}^{vv}$ comes from the $\hat{\theta}$ component of the scattered field, and $\bar{\bar{S}}^{hv}$ comes from the $\hat{\phi}$ component of the scattered field. The result of this Monte Carlo simulation is shown in Fig. 7.2.

Fig. 7.2a and 7.2c show the co-polarized component of the calculated scattering matrices for each random medium, and Fig. 7.2b and 7.2d show the cross-polarized component of the scattering matrices. Here, the first deviation of the results given by Monte Carlo simulation from single scattering can be observed: single scattering predicts that the scattered fields should only be coherent in the forward scattering ($\theta = 0^\circ$) direction. However, each calculation is found to be coherent in an effective mainlobe around the forward scattering direction as well. The Monte Carlo simulations of wires also suggest that there are other directions, that look like scattered sidelobes, in which the field seems to be coherent as well.

Given the observation that the bistatic scattering matrices seem to be coherent in more directions than just the forward scattering direction, the coherent portion of the calculated scattering matrices was computed. The co-polarized portion of these scattering matrices is shown for both media in Fig. 7.3 in both magnitude and in phase. The cross-polarized portion of the scattering matrices is similar, but is omitted for brevity.

Fig. 7.3a shows the field scattered by a collection of long wires occupying the enclosing particle

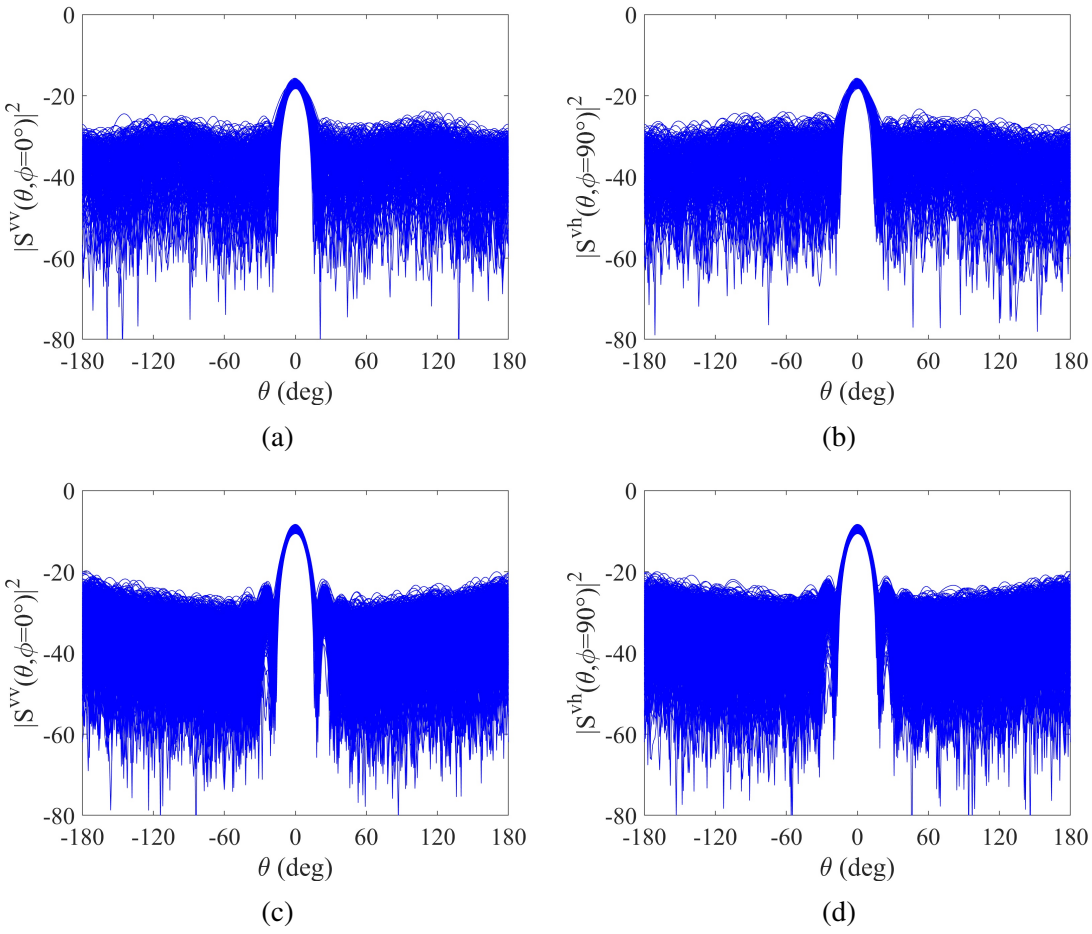

Figure 7.2: Example magnitude of (a) co-polarized, and (b) cross-polarized scattering matrices calculated using Monte Carlo analysis for spheres of size $r_s = \lambda/4$ and volume fraction $\gamma = 0.05$, with (c) co-polarized, and (d) cross-polarized component of scattering matrices for wires of size $r_s = \lambda/20$, length $l_s = \lambda$, and number density $n = 50$.

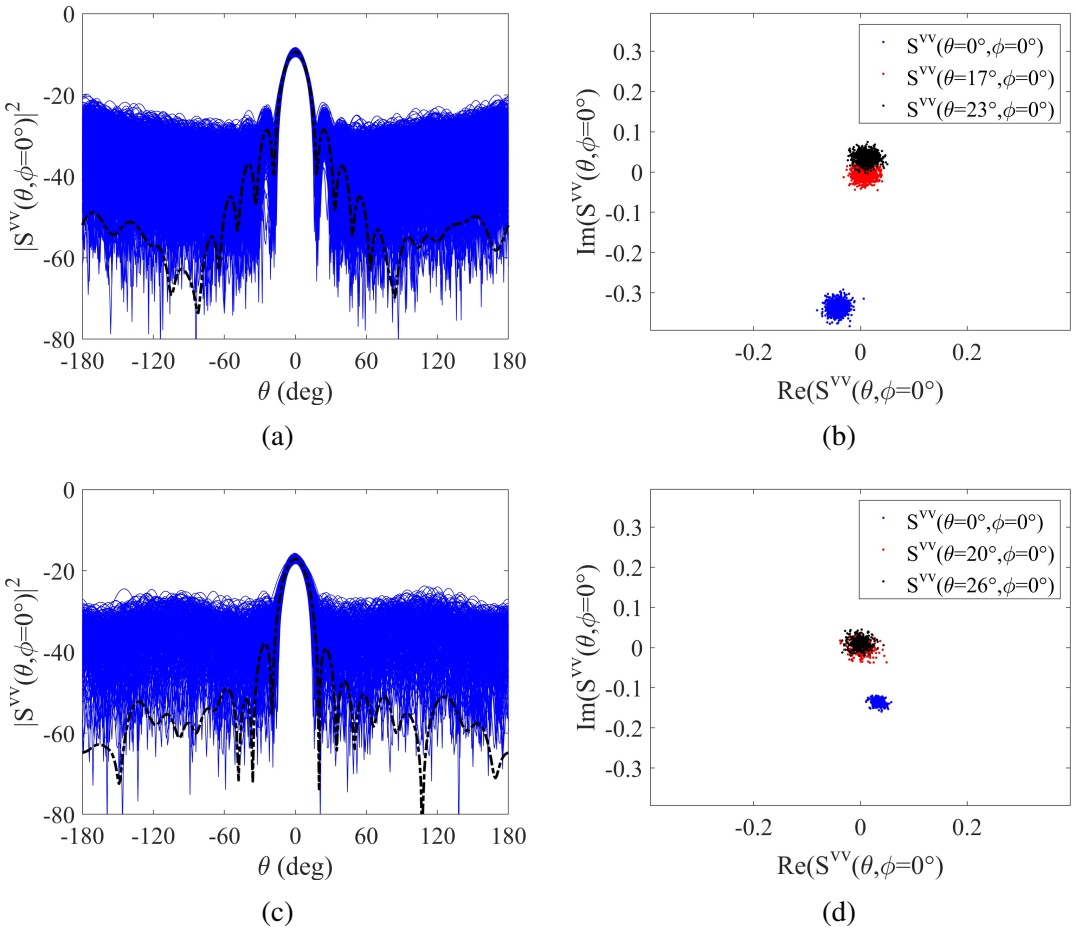

Figure 7.3: Example scattering matrices calculated using Monte Carlo simulation (a) magnitude of co-polarized scattering matrices for wire inclusions and estimated coherent scattering matrix, (b) magnitude and phase of co-polarized scattering matrices for wire inclusions at $\theta = 0°, 17°, 23°$, (c) magnitude of co-polarized scattering matrices for spherical inclusions and estimated coherent scattering matrix, (d) magnitude and phase of co-polarized scattering matrices for spherical inclusions at $\theta = 0°, 20°, 26°$

.

at number density $n = 50$ particles per cubic wavelength. The coherent portion of the scattered field is shown superimposed on top of the Monte Carlo simulation. The coherent portion of the scattering matrix is shown to have a strong coherent peak in the forward scattering direction, and to have four discernible sidelobes on each side of it, with discernible nulls between each one. Fig. 7.3b investigates the real and imaginary parts of the scattering matrices calculated in the forward scattering direction, in the first sidelobe to its left ($\theta = 23^\circ$) and at the null between them. Here, the cloud of points gives some idea of the relative contributions of the mean and fluctuating component of the scattering matrices at these angles. The center of each cloud of points represents the mean of the scattering matrix, the area covered by the points represents the fluctuating part of the scattering matrix. The fluctuations are expected to dominate most scattering angles, as is predicted by single scattering. Fig. 7.3c and 7.3d are equivalent to Fig. 7.3a and 7.3b, but are calculated using scattering data from a cloud with spherical inclusions. The coherent mean field of this data is found to have a lower forward scattering peak, and fewer discernible sidelobes and nulls than the mean field scattered by the cloud of wires. However, each of these features is still there. It will be shown that this lower amount of scattering from the same enclosing particle implies that the effective permittivity of the particle is closer to the permittivity of free space.

Given a recognizable coherent portion of the scattering matrix calculated using Monte Carlo simulation, calculating the effective permittivity is undertaken using an inverse scattering problem. The earliest studies [Siqueira & Sarabandi (1996)] on this subject postulated that the mean scattered field should match the field scattered by a homogeneous dielectric medium because these studies were examining the field scattered by electrically small, dielectric inclusions, where field prediction using a mixing formula should be accurate. This study makes two further observations: that the extinction matrix predicted using single scattering theory can also be represented as an effective permittivity [Brown & Curry (1982)], and that the mean field should be generated by an average amount of current that varies over the medium. This postulate is shown in Fig. 7.4.

Fig. 7.4a shows an example configuration of the medium, and Fig. 7.4b shows a homogeneous medium occupied by volume current. The idea that the average representation of the medium

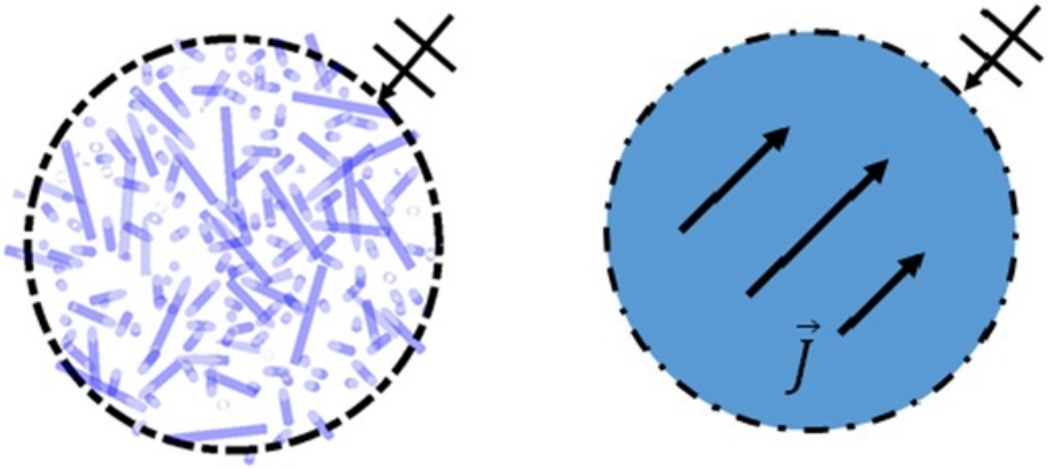

(a) (b)

Figure 7.4: Demonstration of effective medium postulate, (a) inclusions placed inside of a container sphere with an incident plane wave upon the outside, (b) homogeneous medium placed inside of a container sphere.

resembles a homogenous dielectric is not guaranteed for a medium composed of electrically large, interacting inclusions. It is only known to be true for a medium composed of inclusions that are either electrically large or interacting.

Given this observation, the solution to the inverse scattering problem was computed for the coherent portion of the scattering matrix calculated for both random media displayed in Fig. 7.1. The results for both types of media are found to be similar, and, therefore, only scattering results from random media composed of wires will be shown. Here, the minimization problem was computed using brute force instead of convex optimization because the convexity of the inverse scattering parameters was not known a priori and to examine the local matching behavior of the inverse scattering problem. The results of the inverse scattering problem are shown in Fig. 7.5.

Fig. 7.5b shows the Euclidean norm between the calculated coherent portion of the scattering matrix and the scattering matrix of a homogeneous dielectric sphere that occupies the same volume as the container particle. The best matching value is determined to be the effective permittivity $\epsilon_{eff} = 1.11 + 0.20i$ and the Euclidean norm at this point is less than 0.01, indicating a very good match between the Monte Carlo simulation and the homogeneous dielectric. Fig. 7.5a shows the

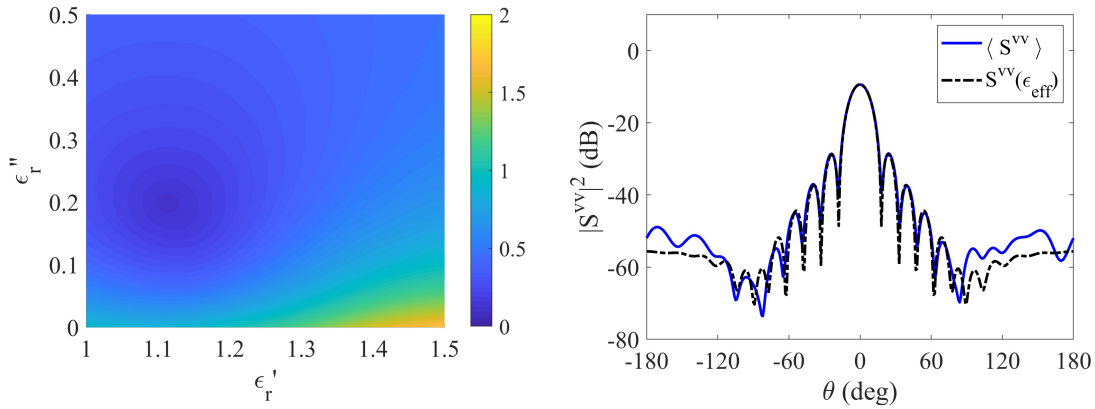

(a) (b)

Figure 7.5: Existence of solution to the inverse scattering problem. (a) Normalized Euclidean distance between calculated coherent scattering matrix and scattering matrix of homogeneous sphere of varied effective permittivity, (b) Comparison of estimated coherent scattering matrix with and scattering matrix of effective medium.

comparison between the co-polarized component of the scattering matrix calculated using Monte Carlo simulation and the same component of the scattering matrix of the effective medium. This comparison is found to be very good over the middle third of the plot.

The existence of a solution to the inverse scattering problem demonstrates that the 1000 Monte Carlo trials used to compute it are sufficient to determine the effective permittivity of the medium. The number of Monte Carlo trials needed to calculate the effective permittivity was investigated next, as the computational demands of this process are significant. This was first investigated by calculating the effective permittivity of many media composed of the same type of wire inclusion, with radius $r_i = \lambda/20$ and $lengthl = \lambda$, and different occupation numbers using 1000 Monte Carlo trials each. Next, the Euclidean norm between partial sums of the coherent scattering matrix and the scattering matrix of the effective medium were computed to determine the rate at which these quantities converged to one another. The result of this test is shown in Fig. 7.6.

Fig. 7.6 shows this trial for ten different number densities of occupying wires, from $n = 2$ to $n = 100$ particles per cubic wavelength. Here, it is seen that the Euclidean norm, used to measure how well the Monte Carlo estimate of the scattering matrix matches the scattering matrix of the effective medium, decreases rapidly for the first 100 Monte Carlo trials, and then decreases more

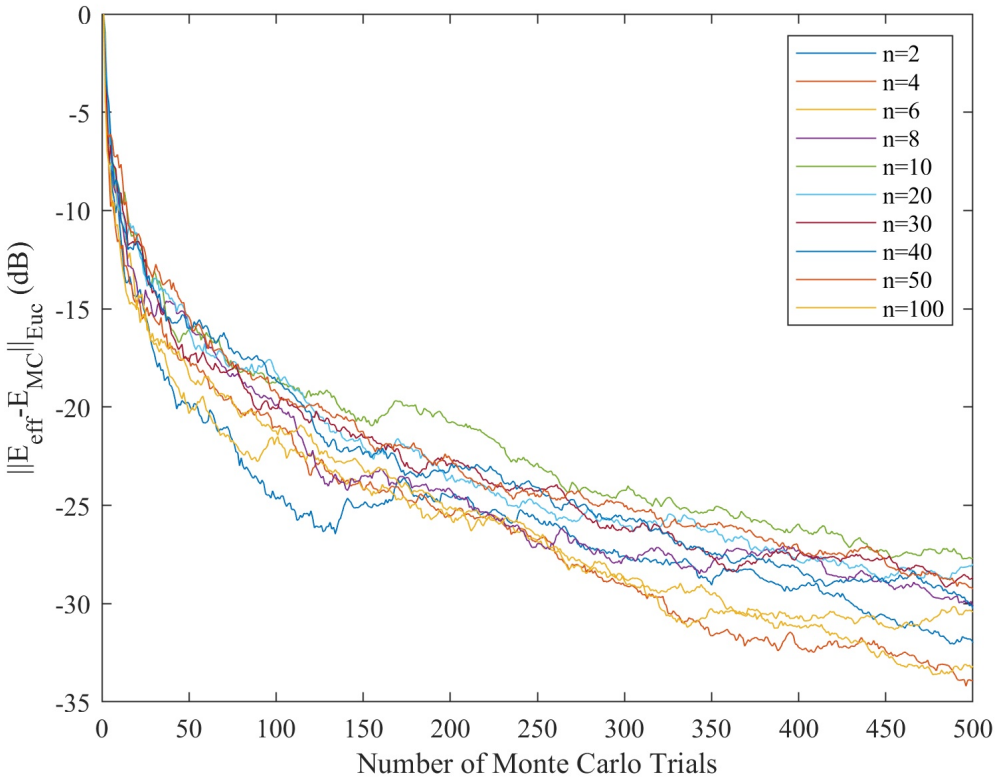

Figure 7.6: Monte Carlo convergence of the mean field to its final form for wire inclusions. All comparisons are found to have a Euclidean norm of less than 0.1 for 200 or more Monte Carlo trials.

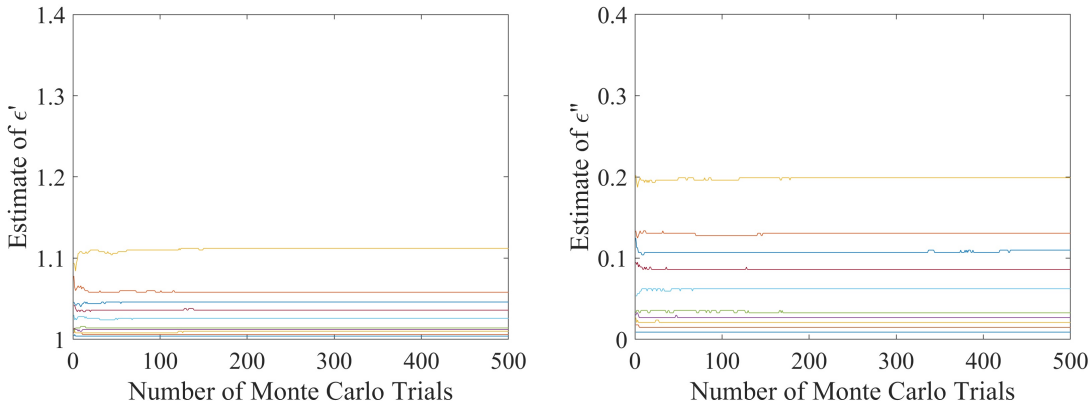

Figure 7.7: Stability and repeatability of solution to the inverse problem for varying numbers of Monte Carlo (a) real part of effective permittivity, (b) imaginary part of effective permittivity. Colored lines in each plot correspond to different occupying densities of the medium, and are the same as the colors given in Fig. 7.6.

slowly. When more than 200 trials are used to calculate the Monte Carlo simulation, this Euclidean norm is always seen to be below 0.1. While this suggests good matching between the scattering matrices, this does not say if matching is as good as this or better for another effective permittivity.

The stability of the effective permittivity estimate for varied numbers of Monte Carlo trials was investigated next. Here, rather than assessing the convergence of the Euclidean norm, that was deemed to be sufficient, the effective permittivity of each partial sum of the scattering matrix was calculated for each Monte Carlo simulation. The result of this calculation is shown in Fig. 7.7.

Fig. 7.7a shows the convergence of the real part of effective permittivity. Here, almost all of the variation of the estimate happens in the first 10 Monte Carlo trials, with only some switching (occurs because of the discrete, brute force search procedure) occurring after 50 Monte Carlo trials. Fig. 7.7b shows the same behavior. The effective permittivity converges faster than the coherent portion of the scattering matrix because calculating the effective permittivity is an integrative, rather than a pointwise, process. This integrative process tends to reduce the effect of random numerical noise that is seen in Monte Carlo simulation. Given these observations, 200 Monte Carlo trials are deemed sufficient to determine the effective medium parameter. This choice is made to make certain that convergence of the effective permittivity is achieved.

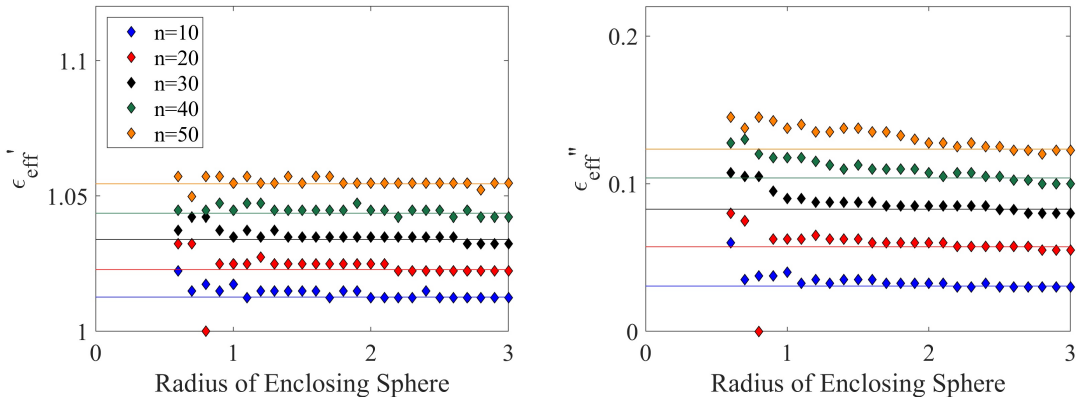

Figure 7.8: Dependence of calculated effective permittivity on size of enclosure, (a) real part of effective permittivity, (b) imaginary part of effective permittivity

The results calculated thus far have all been calculated with a non-varying enclosing particle: a sphere of radius $R_s = 2\lambda$. The effective permittivity, that is related to the extinction matrix of the random medium itself, should not depend on the user's choice of an enclosing particle, but should be a property that reflects propagation in the medium. This was initially assessed by calculating the field scattered by an enclosing particle of a different size, and the coherent portion of the scattering matrix is found to change. To assess whether or not the effective permittivity varies as a function of the size of the enclosure, Monte Carlo simulations were conducted for spheres of size $R_s = 0.6\lambda, 0.7\lambda, \ldots, 3\lambda$, the coherent portion of the scattering matrix was calculated, and the effective permittivity of each of these spheres was determined. This is shown in Fig. 7.8.

Fig. 7.8 shows how the effective permittivity of the medium varies when different enclosing particles are chosen. Here, it is seen that the effective permittivity is estimated accurately for an enclosing sphere of $R_s = 2\lambda$. One reason that a small sphere shouldn't be able to estimate an effective permittivity is the scattering matrices of electrically small spheres do not vary much with respect to permittivity. Therefore, even perfect scattering data would provide a match that is uncertain. This is found, although not shown here, to require that an enclosing sphere with $R_s \geq \lambda/2$ be used to make these computations. The other problem is that a small sphere cannot enclose many statistical configurations of a medium composed of electrically large scatterers. The

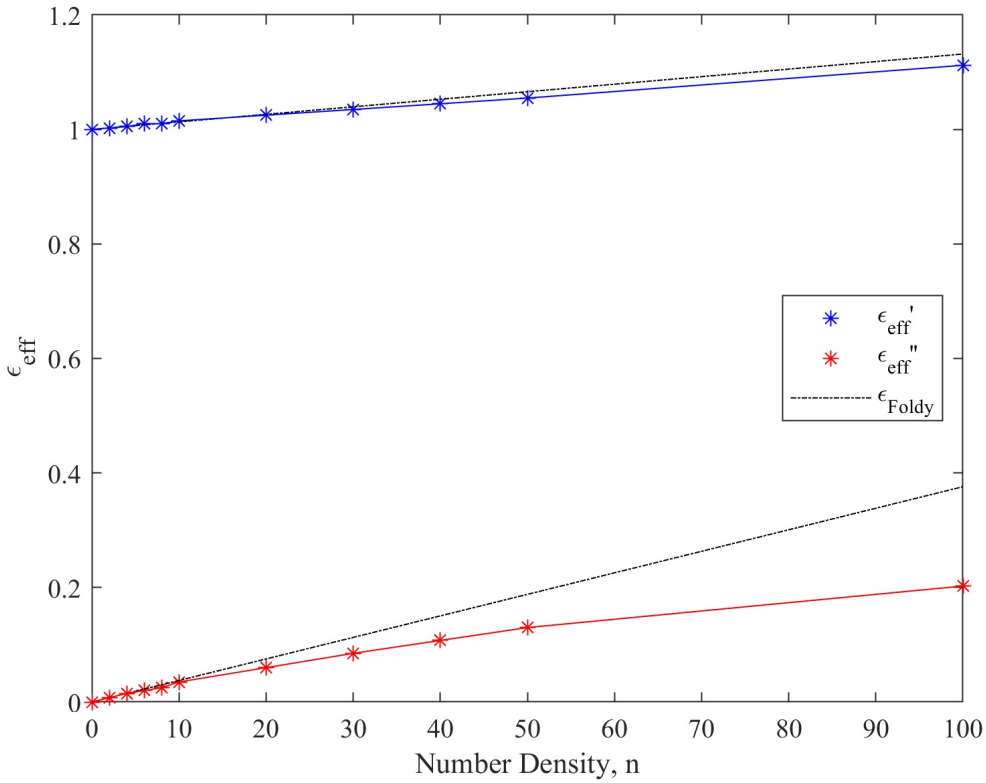

Figure 7.9: Comparison between estimated effective media parameters and the Foldy approximation for the effective medium parameter.

results in Fig. 7.8 suggest that the sphere's radius should be at least one and a half to two times as large as the inclusions to accurately estimate the effective permittivity of the medium. Above this point, the effective permittivity should not change. However, the computational complexity of calculating a Monte Carlo simulation suggests that a user would want to stay close to this bound to avoid using extra computation.

One final numerical experiment is conducted here, and that is comparing these results to the results predicted using single scattering theory. Here, all effective permittivities that were calculated for wire-like media are compared to the single scattering prediction made using the Foldy approximation [Brown & Curry (1982)]. This model predicts that the effective permittivity should increase linearly with number density of the inclusions. The comparison between single scattering and the Monte Carlo results is shown in Fig. 7.9.

Fig. 7.9 shows that single scattering very accurately represents the effective permittivity of a random medium occupied at a low number density by wires. As number density increases, single scattering overestimates both the real and imaginary parts of the effective permittivity of the medium. Of these two quantities, it is worth noting imaginary part of the effective permittivity is more important in estimating attenuation of the coherent field, since the extinction matrix, that depends on the effective permittivity of the medium, predicts the attenuation of the coherent field. The attenuation of the coherent field primarily comes from the imaginary part of the effective permittivity.

7.4 Existence of Fluctuating Field and Phase Function

The coherent portion of the scattering matrix can be calculated using Monte Carlo simulation, and demonstrates the existence of an effective permittivity that governs mean field propagation in the random medium. Based on this insight, the fluctuating component of the scattering matrix, represented by the second moment of the Monte Carlo simulation, ought to describe the phase matrix of the same medium. The fluctuating component of the scattering matrix can be calculated from the same scattering data as was the coherent component. However, one final numerical trick is used to estimate the second moment of the data: buffer zone averaging. The concept of inserting a buffer zone is illustrated in Fig. 7.10.

The buffer zone averaging step was originally undertaken to overcome two previously observed effects that hindered estimation of the phase function [Siqueira (1996)]. Without employing buffer zone averaging, the phase function estimate is hindered by the existence of a coherent reflection that comes from the interaction of the random (effective) medium and the infinite free space outside of it. Also, the phase function is supposed to represent average scattering from this particle as it is embedded in a medium of similar particles. It was originally thought that this would have to be overcome by calculating scattering from particles placed inside of a hollow sphere embedded in a background of the (lossy) effective medium, and then averaging over the phase functions calculated

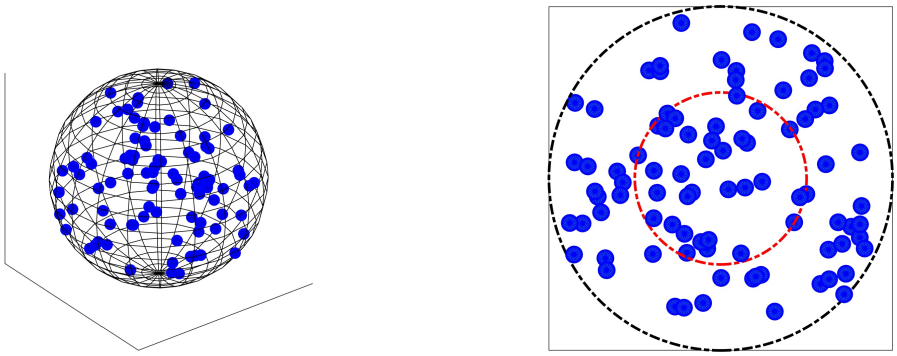

(a) (b)

Figure 7.10: Illustration of buffer zone concept used to compute the incoherent scattered field using Monte Carlo simulation, (a) 3D view of inclusions (blue spheres) and enclosure (black mesh) with radius R_s, this part of the process matches the process used to compute the effective permittivity. (b) Buffer zone illustration. Black dashed line is two-dimensional projection of enclosure, the Method of Moments will be used to calculate current induced on all inclusions. Red dashed line represents a second particle inside of a buffer zone, and calculated currents inside of this line will be used to calculate the scattered field.

by several of these spheres. Calculating a Green's function for such a medium, where the Green's function is represented by a modal sum, is sufficiently challenging [see: Tan & Tsang (2017), Tsang *et al.* (2018), Tan & Tsang (2019)] as to have been a primary topic in another doctoral thesis within the past few years. The buffer zone averaging idea is a convenient way to circumvent this problem, it seems to smooth out any coherent reflections from the boundary of the random medium and free space and to remove the presence of numerical noise. Buffer zone averaging in this thesis is undertaken by fixing an enclosing particle size and then removing current basis functions from the scattered field computation when those basis functions are in the buffer zone. This could create a coherent effect from the boundary of the enclosure. However, as the incoherent scattering coefficient estimates that are made with different sized enclosing partices agree with one another, this coherent effect is deemed to be negligible at best.

The incoherent portion of the scattering matrix is first investigated for conducting spheres of size $r_i = \lambda/4$ inside of a container sphere of size $R_s = 3\lambda$ with a volume fraction of $\gamma = 0.05$. Induced current on all inclusions in the medium were calculated for 1000 Monte Carlo trials of

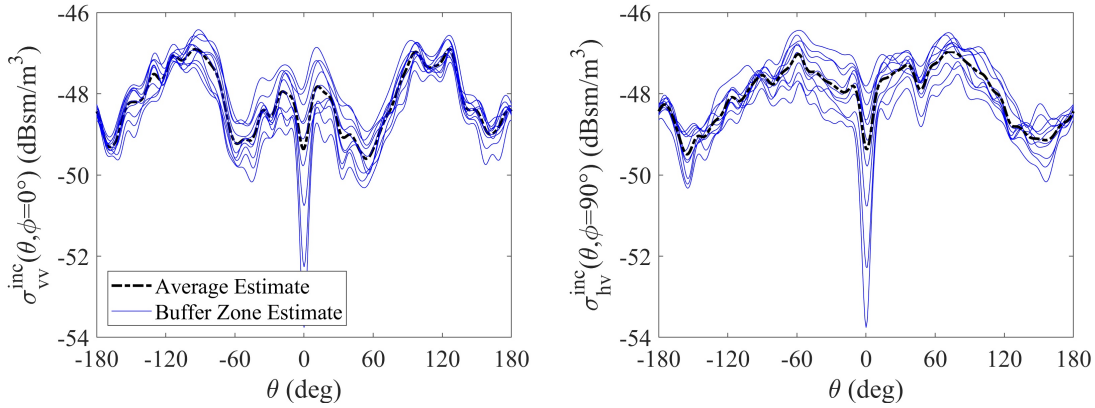

(a) (b)

Figure 7.11: Estimated incoherent scattering coefficient of cloud of spherical particles of size $r_s = \lambda/4$ and volume fraction $\gamma = 0.05$ for multiple buffer sizes inside container sphere of size $R_s = 3\lambda$. Estimates seem to mostly agree with one another outside of a small region near to $\theta = 0°$.

different configurations of the medium. With this calculated current data, 25 buffer zones of size $0 \leq r_b \leq 2.5\lambda$ were inserted, and the scattering matrix of particles inside of the buffers were calculated. For this trial, scattering from a single enclosing particle is calculated, and buffer zones are inserted by removing particles near the boundary of the enclosure. These estimates are expected to provide the same estimate of the scattering coefficient provided that the estimate is convergent. Note that here a buffer zone of size $r_b = 0$ includes all currents in computing the bistatic scattering matrix of this configuration of the medium. The maximum buffer size $r_b = 2.5\lambda$ is the maximum allowable buffer size found in Section 7.3 for inclusions of this size. For a sufficiently large buffer zone, the bistatic scattering cross section per unit volume ought to be the same. The estimated bistatic scattering cross section per unit volume for each of these buffer zones is calculated, and is shown in Fig. 7.11.

Each estimate of the scattering coefficient is found to mostly agree in a pointwise sense outside of a small region near $\theta = 0$. This deviation will be explored later. The average incoherent portion of the scattered field is superimposed on top of each estimate and is generally found to be smoother than any of the individual samples. Lastly, there is no observable ordered dependence of the scattering coefficient on the buffer size. This is to say that the scattering coefficient is not found to increase or decrease with buffer zone size.

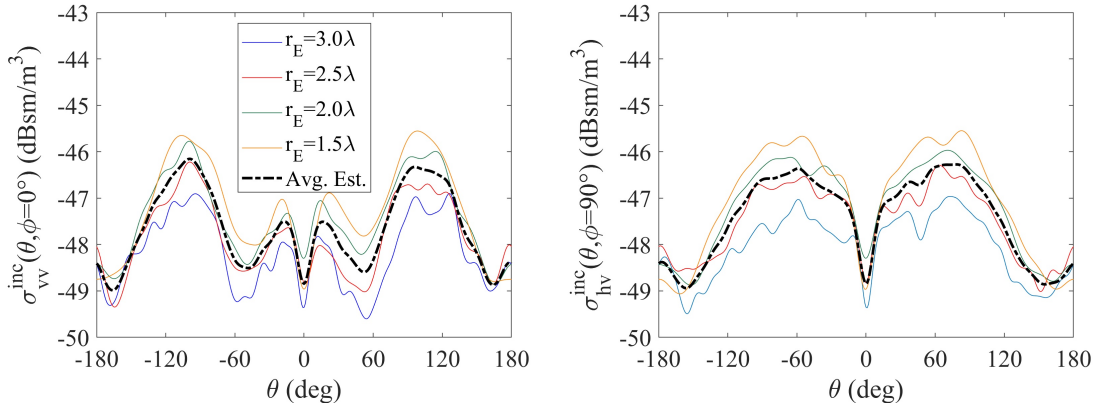

(a) (b)

Figure 7.12: Estimated (a) co-polarized and (b) cross-polarized components of the incoherent scattering coefficient of the medium for cloud of spherical particles of size $r_s = \lambda/4$, volume fraction $\gamma = 0.05$ for multiple enclosure sizes. All estimates seem to agree with one another.

Given that the incoherent scattering coefficients of the medium that are made with different buffer zones are found to agree, the dependence of the scattering coefficient on the size of the enclosing particle was next investigated. Here, scattering from four different enclosing particles, $R_s = 1.5\lambda, 2\lambda, 2.5\lambda, 3\lambda$, was calculated to make certain that estimates of the incoherent scattered power per unit volume are the same. Each estimate uses buffer zone averaging ranging from no buffer zone ($r_b = 0$, to a buffer zone of size $R_s - r_b = 0.5\lambda$. The largest buffer zone is chosen based on convergence criteria given in Section 7.3. The resulting estimates are shown in Fig. 7.12.

Estimates of the co-polarized, shown in Fig. 7.12a, and cross-polarized, shown in Fig. 7.12b, scattering coefficients made with different sized enclosing particles are generally seen to agree with one another. The repeatability of the estimate of the scattering coefficient suggests that the Monte Carlo simulation and the associated buffer zone averaging is doing a good job estimating the fluctuating component of the scattering matrix.

The dependence of the scattering coefficient on the number of Monte Carlo trials used to estimate it is investigated next. Here, the desired final result of the method is the pointwise convergence of the scattering coefficient, that is directly (linearly) related to the phase function for the random medium. Therefore, convergence of this quantity is judged in a pointwise sense: the percent error between the final estimate of the scattering coefficient and the partial estimate of the

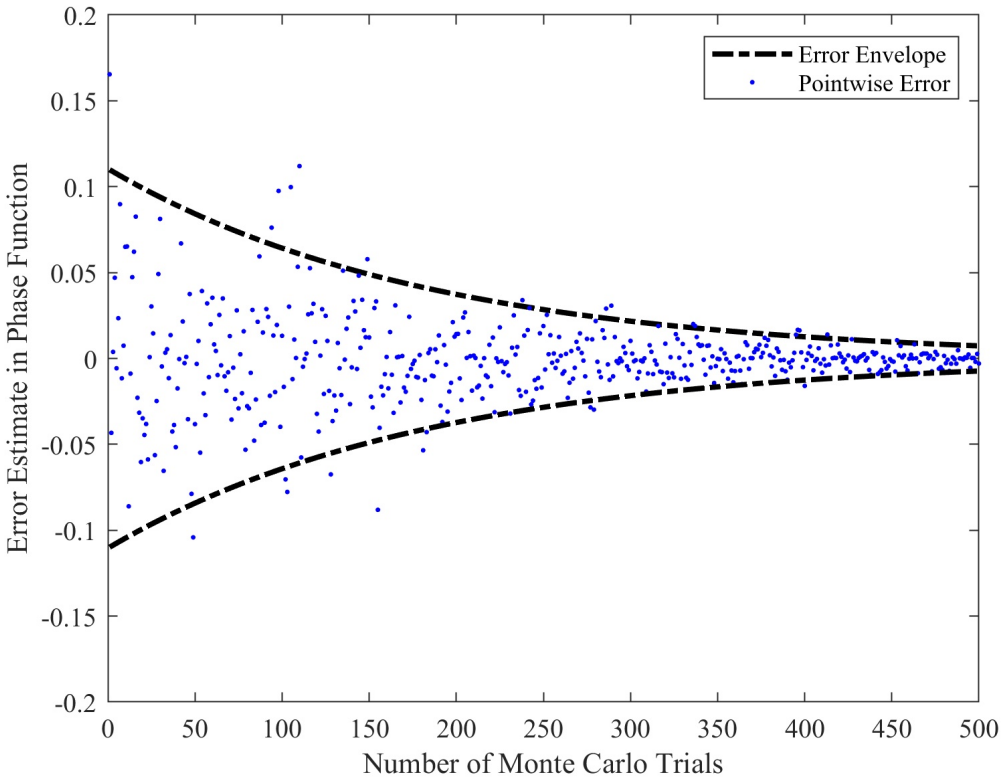

Figure 7.13: Error metric of phase function, which is average pointwise difference between the estimated and final phase function, made using a certain number of Monte Carlo trials. Black lines are fitted envelopes of twice the standard deviation of the average pointwise error, showing 95% of estimated values for the phase function are inside of this envelope.

scattering coefficient is calculated for each point in the bistatic scattering matrix. The average and envelope of this percent error is shown in Fig. 7.13.

Fig. 7.13 shows the average and fitted envelope of the percent error of the Monte Carlo simulation. Here, 95% of all estimates of the phase function are found to have an error rate that is less than that indicated by the black dashed line. This envelope decreases below ±0.05, 5% error, when 300 or more Monte Carlo trials are used to estimate the phase function. This means that accurately estimating a phase function requires more Monte Carlo trials than estimating the effective permittivity. This makes sense for two reasons: firstly, that the scattering coefficient estimate requires a convergent representation of the coherent portion of the scattering matrix to converge, and, secondly, that this estimate depends on pointwise, rather than average, convergence, unlike

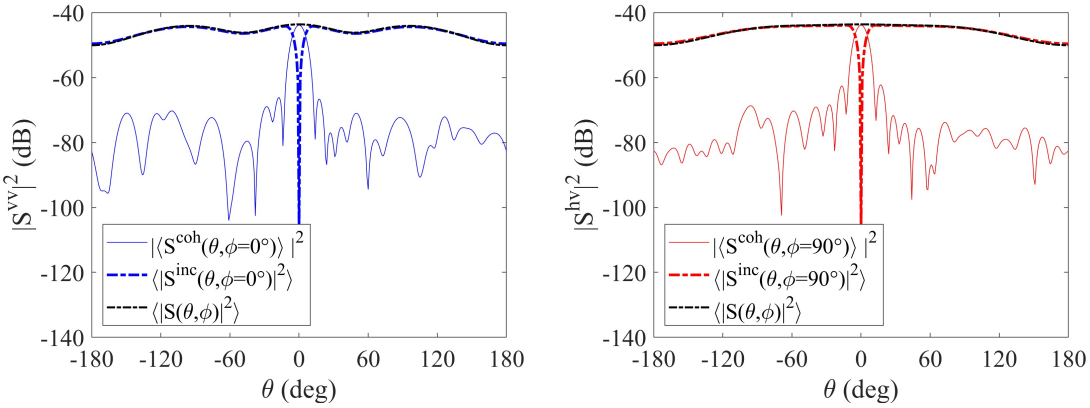

Figure 7.14: Comparison of coherent and incoherent portion of the scattering matrices estimated using Monte Carlo simulation and single scattering theory (a) co-polarized component of the scattering matrix in the $\phi = 0°$ plane and (b) cross-polarized component of the scattering matrix in the $\phi = 90°$ plane. Deviations are shown here to be contained within the mainlobe of the coherent portion of the scattering matrix.

the estimate of the effective permittivity. Therefore, we do not expect to require fewer Monte Carlo trials to estimate the incoherent scattering coefficient.

The scattering coefficient of a very sparsely occupied cloud was next investigated to determine that it gives the same estimate as single scattering theory. For this investigation, a single sphere of radius $r_i = \lambda/4$ is randomly placed inside of a container sphere of size $R_s = 3\lambda$. The scattering matrix of this sphere is calculated. This procedure is repeated 300 times to attempt to estimate the scattering coefficient of the random medium. This result is compared to the prediction made by single scattering theory in Fig. 7.14.

Both the co-polarized and cross-polarized elements of the incoherent part of the scattering matrix match the prediction given by single scattering very well when the coherent portion of the scattering matrix is small. The agreement between these estimates deviate near the forward scattering ($\theta = 0°$) direction. Single scattering predicts that the scattered fields should only be coherent exactly in the forward direction. The dependence of this deviation on the size of the container sphere is investigated next for spheres of size $R_s = \lambda, 2\lambda, 3\lambda$, and the result of this is

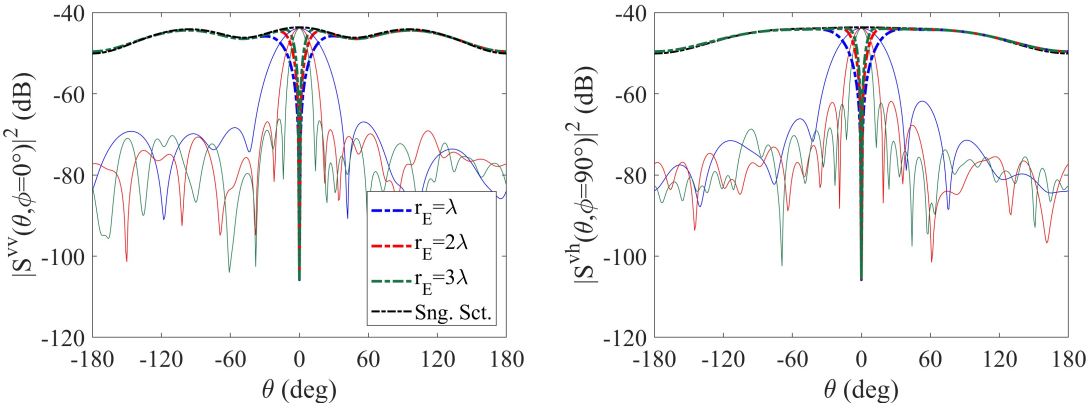

Figure 7.15: Comparison of the incoherent portion of the scattering matrices predicted using single scattering theory and Monte Carlo simulation with varied size of an enclosing particle. (a) Co-polarized component of the scattering matrix in the $\phi = 0°$ plane, (b) cross-polarized component of the scattering matrix in the $\phi = 90°$ plane. Deviations are shown here to remain contained within the mainlobe of the coherent portion of the scattering matrix, which depends on the size of the container sphere.

shown in Fig. 7.15.

As the size of the container is increased, the deviation is seen to concentrate more in the forward scattering direction. Logically, it would make sense that this deviation would shrink to being a Dirac δ-function at $\theta = 0°$ for an infinite sphere. In this case, the two predictions would converge to one another perfectly. Therefore, it seems that the incoherent scattering coefficient is correctly estimated outside of a region near $\theta = 0°$ that can be made as small as a user desires by increasing the size of the enclosing particle.

Lastly, the dependence of the scattering coefficient on the volume fraction of the medium is investigated for relatively sparsely occupied container particles. For low volume fraction, the particles are expected to behave similar to single scattering, as was confirmed in Fig. 7.14 and 7.15. As the volume fraction is increased, the (per-particle) incoherent scattering coefficient is expected to decrease because of the presence of shadowing. The results of this investigation are shown in Fig. 7.16, for volume fractions $\gamma = 0, 0.01, \ldots, 0.05$ inside of a container sphere of size $R_s = 3\lambda$.

Here, it is seen that both polarization components of the scattering coefficient decrease with increasing volume fraction in almost every direction. One noticeable place where the scattering

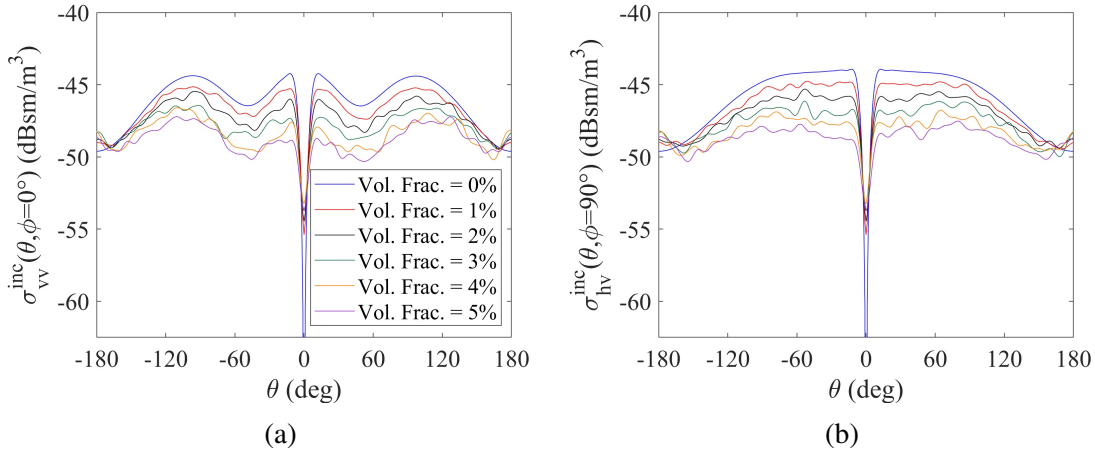

Figure 7.16: Comparison between estimated (number density normalized) phase functions for spherical inclusions with volume fractions $\gamma \in \{0, 5\%\}$ compared to the single scattering prediction. Shows noticeable shadowing effects.

coefficient increases is near the forward scattering direction, which is not expected to be valid for enclosing particles of this size. Curiously, the incoherent scattering coefficient also increases on average in the back-scattering direction. This occurs because of the coherence of two-path interactions between the particles and has been observed before in [Mookerjee & Dowling (2017)].

7.5 Conclusion

This chapter uses Monte Carlo simulation in conjunction with the Method of Moments to estimate the effective permittivity and incoherent scattering coefficient, related to the extinction coefficient and phase function, of several random media composed of differing kinds of conducting scatterers. The results here lend themselves to several positive conclusions. First, it seems that the coherent and incoherent portions of a scattering matrix can be estimated by way of the first two statistical moments of a universe of scattering matrices calculated using Monte Carlo simulation. While higher order moments of this data exist, they are not currently postulated to carry the same physical meaning that the first two moments do and ought to vanish as the number of Monte Carlo trials used to estimate them increases. Second, it seems that the coherent portion of the scattering matrix suggests that the average field propagating in the random medium sees an effectively homogeneous,

lossy dielectric medium. This effective permittivity is expected to be useful in predicting the attenuation of a field propagating through a random medium, represented by the extinction matrix in Radiative Transfer. Thirdly, the incoherent portion of the estimated scattering matrix can be used to estimate an incoherent scattering coefficient for the particles occupying the medium. This incoherent scattering coefficient is found to depend on the random medium, and is postulated to be directly related to the phase function for the medium. Overall, this method is thought to provide a way for accounting for inter-particle interactions inside of a random medium composed of electrically large wires for use in remote sensing.

CHAPTER 8

Using Monte Carlo to Compute Extinction and Phase Matrices for Multiple Random Media

8.1 Introduction

Monte Carlo simulation can be used to provide insight into random media propagation in media composed of discrete scatterers, to test and extend predictions made using theoretical or empirical phenomenology, and can be used to model wave propagation phenomena in an interacting medium composed of electrically large scatterers. This technique, as implemented and demonstrated in Chapter 7, has so far been used only to predict the extinction coefficient and phase function of very particular media to extend the predictions provided by Radiative Transfer, but there is no reason to believe that it cannot be extended to model all elements of the extinction and phase matrices. This method is best understood as an extension of single scattering theory, where the scatterer is a particle that encloses many inclusions in the medium, rather than a single inclusion, and scattering from these macro-particles (or enclosures) is solved for using the Method of Moments [Jin, J. (2010)]. The extinction coefficient is understood as the existence of an effective (lossy) dielectric medium that governs mean field propagation and attenuates the coherent portion of a wave that is propagating through the random medium. The phase function is understood as the fluctuating portion of the field scattered by the medium. This chapter uses this Monte Carlo methodology to study problems in random media propagation, including designing a random media for a particular application and to construct a model for random media propagation in chaff. The designed

random medium demonstrates that some heterogeny in the inclusions of a random medium can be understood by examining the constituents separately and combining them using a mixing formula, and shows how to design a random medium to attenuate a coherent field faster than tradition chaff designs. The macro-model for chaff proposes a model for a chaff-like random medium, and then constructs a macromodel for mean- and fluctuating-field propagation in chaff clouds made up of wires of many sizes and occupation densities. These applications provide evidence of two kinds of utility that Monte Carlo simulation of random media provides.

Chaff is a form of counter-measure that can be employed in defense applications to block the operation of remote sensing systems. Chaff, or an equivalent counter-measure, has been employed against radar and sonar, in the form of air bubbles, since the Second World War [Skolnik, M.I. (1980), Urick, R.J. (1996)]. Chaff is typically deployed in radar remote sensing applications as pieces of highly conducting foil blowing in air. The first paper to model field propagation in chaff is [Foldy (1945)], that leads to the famous Foldy approximation, and models chaff as a collection of many electric monopoles or dipoles that are spatially distributed and randomly oriented. For radars that existed at this time, which typically transmitted in the tens of Megahertz, this is a good model as all pieces of chaff are electrically small. Given the modern advent of millimeter wave radar and radiometric remote sensing that is employed in both civilian and defense applications, improved models based on electrically large scatterers [Yin & Bo (2014), Zhang & Wu (2019)] are studied using Monte Carlo simulation. This chapter studies field propagation in a chaff-like random medium because of its simplicity from an electromagnetic standpoint: chaff clouds are typically found in free-space far from reflecting boundaries, and the conductivity of the inclusions in the random medium eases the computational burden of using the Method of Moments [Altair Engineering (2014)]. This method could be extended to help understand field propagation in other random media that are densely populated with electrically large scatterers [Tsang & Kong (1978), Ulaby & El-Rayes (1987)], but these problems represent far greater computational complexity for this method because of their proximity to layered media and because the inclusions are both dispersive and dielectric. Because of these concerns, and for the sake of brevity, this chapter

will focus on solving for the extinction coefficient and phase function of chaff-like random media.

A very simple model for chaff-like random media is studied throughout this chapter to further simplify the problem from a computational standpoint. Inclusions in this medium are generally treated using the long, thin wire Green's function [Altair Engineering (2014)] rather than as two- or three-dimensional scatterers. Further, because this method uses a simple formulation of the Method of Moments, inclusions are treated as static when the scattering matrix of a given enclosing particle is calculated. Generally, particles are moving slowly enough with respect to the speed of light that time-evolution of the configuration is unimportant. However, this approximation neglects Doppler broadening [Skolnik, M.I. (1980)] that can occur in field propagation for random media of this type. Thirdly, the successive nomination procedure used to generate configurations of inclusions within the enclosing particle assumes that the inclusions are uniformly distributed in spatial and inclusion orientation space provided that the inclusions do not overlap. None of these approximations are required to implement this method. The thin-wire approximation could be relaxed when solving for scatterers that are not well modeled using this Green's function. Indeed, this assumption is relaxed when solving for field propagation in electrically small wires in Sections 8.3 and 8.4. Doppler broadening could possibly be solved for using a time-domain method, rather than the frequency-domain version of the Method of Moments. It is worth noting that a time-domain version of the Method of Moments exists [see: Wang *et al.* (2000)], but this step is beyond the scope of the work contained in this thesis. A structure factor could also be imposed on the medium to impose a particular distribution of inclusions, as in [Siqueira *et al.* (1994)]. These steps could represent important future applications to the work presented herein, depending on the scientific interest in solving them.

Chaff tends to present as a lossy medium across a broad range of operational frequencies. For a medium composed of electrically small inclusions, as in [Foldy (1945)] such a response can be directly calculated. For media composed of larger scatterers, like those explored in Section 8.3 and 8.4 [Geroski & Sarbandi (2020), Yin & Bo (2014)], the response is still found to be broadband for clouds of randomly oriented inclusions because some modes will be excited on these scatterers.

The random medium designed in this chapter attempts to use resonance phenomena to sharply attenuate propagating fields even in very sparsely occupied media. For this purpose, a design is proposed for a chaff cloud that is composed of subwavelength resonators [Svigelj *et al.* (1992)]. These inclusions give the desired powerful response to an incident wave, that leads to a high extinction coefficient, but also confines this extinction to a narrow bandwidth.

The remainder of this chapter is divided into four sections. Section 8.2 focuses on designing a random medium that has a narrowband response. It also demonstrates the utility that is available from using single scattering theory to understand mean field propagation in clouds of electrically small scatterers, and of using mixing formulae to understand mean field propagation in clouds of heterogenous scatterers. Section 8.3 solves for mean field propagation in clouds of conductive wires of varying lengths, and occupying densities. It proposes a new macromodel that extends the Foldy approximation to account for field attenuation in chaff, and examines the dependence of this model on inclusion size, number density, and for partially bent inclusions. Section 8.4 solves for the fluctuating component of the scattered field observed for propagation in chaff-like media with inclusions of varying lengths and occupying densities. Two models are given for the observed scattering coefficients for several inclusion lengths and densities for use in first-order Radiative Transfer modeling. Methods for extending this model to solve for the three-dimensional phase function are discussed. Section 8.5 draws what conclusions are available from the work contained in this chapter, and proposes follow-on work to extend the scientific utility of these results.

8.2 Designing a Random Medium for a Mean Field Response

The first application laid out in this thesis demonstrates how to design a random medium to provide significant attenuation to a propagating wave even in a sparsely occupied random medium. This medium is designed here to provide attenuation to a propagating wave from 2.7–2.9 GHz. To make certain that this medium only has a significant coherent scattering matrix in this, and potentially other, small bands, inclusions are designed to be resonant particles much smaller than a wavelength

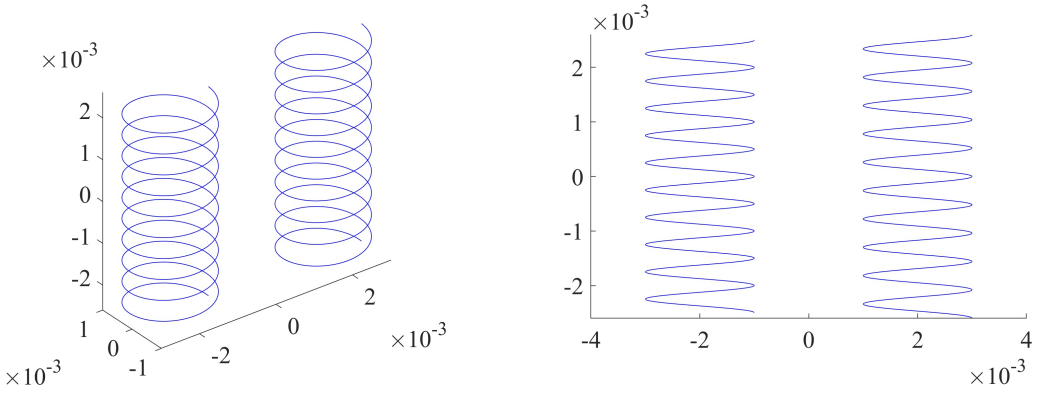

(a) (b)

Figure 8.1: Side by side comparison of Helix # 1 and Helix # 2 that will be examined in this study.

of the light propagating in free space. In this study, multiple types of resonant particles were explored, and the most convenient of these particles from a calculation standpoint was found to be helices. Also of interest in this study is whether two types of particles have a measurable coherent, mean field interaction, or if the scattered mean field is better understood as being a mix of the field coherently scattered by each type of particle, and whether or not modeling the particles as perfect conductors is valid at these frequencies.

To cover the 2.7 – 2.9 GHz bandwidth, two helices of slightly differing geometries are designed. The first helix, labelled Helix #1, is designed to resonate just below 2.8 GHz, and the second, labelled Helix #2, is designed to resonate just above 2.8 GHz. The helices have the same radii, $r_1 = r_2 = 1$ mm, the same number of turns, $N_1 = N_2 = 10$, and slightly differ in length, $h_1 = 5$ mm, $h_2 = 5.2$ mm. Each particle is modeled as a helical wire in FEKO, with a wire radius of 0.1 mm. The two scattering geometries are shown in Fig. 8.1.

The two particles shown in Fig. 8.1, that represent Helix #1 and #2, seem to barely differ by eye. The side-view in Fig. 8.1b shows that the two particles have slightly differing heights. For the given resonant bandwidth around 2.8 GHz, that has a free-space wavelength of 100 mm, all dimensions of the scatterers are electrically small.

The average forward scattered fields are calculated using dual-polarized incident plane waves of frequencies from 1 – 3 GHz at incident elevation angles from above to below the scatterers.

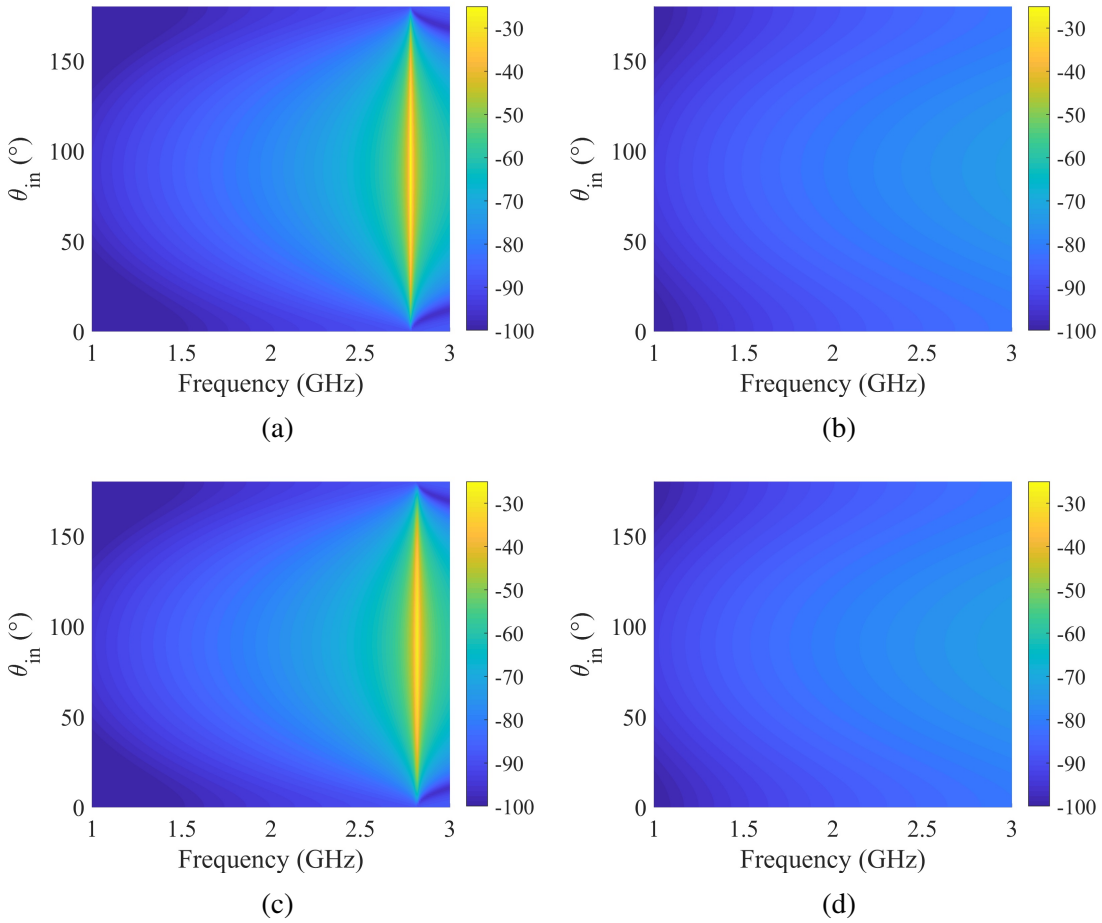

Figure 8.2: Wide-band, multi-angular prediction of total power forward scattered by (a) Helix 1 (b) cylinder occupying same volume as Helix 1 (c) Helix 2 (d) cylinder occupying same volume as Helix 2.

Multiple different incident azimuthal angles of the plane waves are also calculated, but the forward scattered field is not found to change much at this frequency. The results of this scattering calculation are shown in Fig. 8.2, compared to an equivalent calculation that is made on cylinders that occupy the same volume as each helix.

The power that is forward scattered by the helices is shown to be sharply concentrated in the 2.7 – 2.9 GHz band, as desired, with > 40 dB lower forward scattering cross section being observed 100 MHz away from the affected band (2.7 – 2.9 GHz). This resonant response contrasts with the gently increasing behavior of the cylindrical scatterers. While this narrowband behavior is not specifically desired, the more than two orders of magnitude increase in forward scattered power

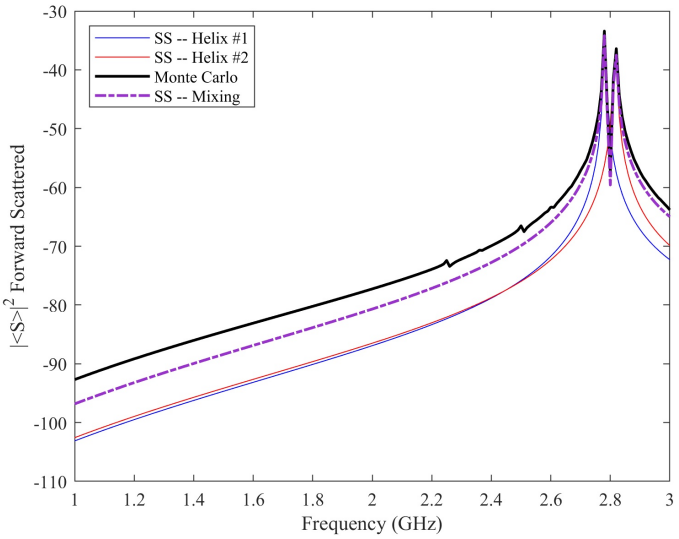

Figure 8.3: Coherent average field scattered by a cloud composed of these two types of helices occupying the cloud at $n = 700$ particles per cubic meter, compared to single scattering prediction of adding the field scattered by two clouds of each type of helix occupying $n = 350$ particles per cubic meter.

is useful for blocking propagating signals. Seeing this response, single scattering theory would predict this medium would only scatter and attenuate coherent field propagation in the $2.7 - 2.9$ GHz frequency band.

The applicability of single scattering in this problem was tested using Monte Carlo simulation. Field propagation through an interacting cloud of these helices was calculated with 700 helices per cubic meter, or 10 helices inside of each container of radius $R_s = 150$ mm. The helices are assumed to occupy the cloud with equal likelihood, giving an expected number density of 350 helices per cubic meter for each type of helix. The size of the container sphere was chosen to be large enough to make a reasonable prediction of effective permittivity for 200 MHz below the relevant bandwidth. 500 Monte Carlo trials were calculated for helices placed and oriented randomly within the container. The coherent forward scattered field calculated using this method is shown in Fig. 8.3, compared to equivalent single scattering predictions.

Here, the scattered field predicted using Monte Carlo agrees very well at resonance with the single scattering results of the individual scatterers. The mixing formula version of the single

scattering prediction agrees even better with the Monte Carlo results in a wider band around the resonant peaks. Single scattering underestimates the field response far from the peaks, this is thought to be occurring because there is very little signal out here, and so the coherent scattered field predicted using Monte Carlo simulation is still dominated by numerical noise. This is not investigated further because the low scattering coefficient is unlikely to have an effect on field propagation at these frequencies.

Having ascertained that single scattering theory applies in the forward scattering direction, the coherent portion of the bistatic scattering matrix was calculated to solve for the effective permittivity of the medium. At the same time, the ensemble average of the forward scattered field from each single helix was calculated to determine the single scattering prediction of the effective permittivity following [Brown & Curry (1982)], that is given in Eq. (8.1).

$$\epsilon_{eff}(n) = 1 + \frac{4\pi F}{k_0^2} n \tag{8.1}$$

When the medium is unoccupied ($n = 0$) the medium should resemble free space, F represents the average field forward scattered from a single scatterer, and k_0 is the free-space wavenumber of the incident field. The solution to the inverse scattering problem, that gives the Monte Carlo prediction of the effective permittivity, and the effective permittivity predicted from single scattering theory are displayed in Fig. 8.4.

Fig. 8.4a shows the real part of the effective permittivity and Fig. 8.4b shows the imaginary part of the effective permittivity. While both predictions of effective permittivity are small, they do show the desired behavior: the effective permittivity of the random medium only differs from the permittivity of free space over a narrow bandwidth from approximately 2.7 – 2.9 GHz. Also, for these sparsely populated clouds ($n = 350$ particles per cubic meter or five of each type of helix in each configuration), the single scattering prediction accurately describes the effective permittivity of the medium. Lastly, because these particles don't appear to be coherently interacting with one another in the mean field, the mean scattered field should be able to be calculated for clouds composed of either one type of helix or the other.

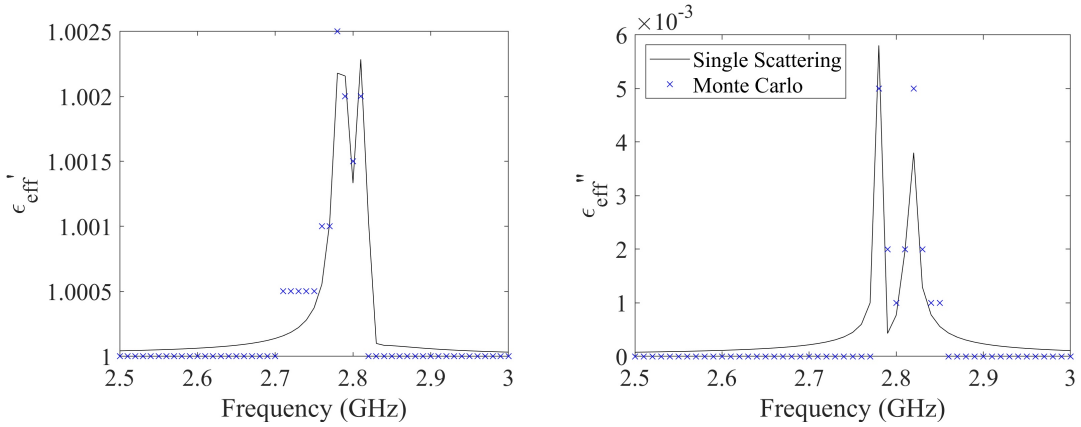

(a) (b)

Figure 8.4: Solution to the inverse problem of the field scattered by a chaff-like random medium composed of these two types of helices occupying air at number density $n = 700$ particles per cubic meter compared to the single scattering prediction (a) ϵ'_{eff}, (b) ϵ''_{eff}. Good agreement is shown between the two predictions near resonance, with some small disagreement likely arising due to quantization of the brute force inverse problem calculation.

To increase the difference between the effective permittivity and the permittivity of free space, denser clouds populated by only one type of helix, Helix #1, were studied. Single scattering theory predicts that increasing the number density of these helices by a factor of 10 ought to increase the effective permittivity's deviation from that of free space ($\epsilon_{eff} - 1$) by a factor of 10, as well. For this purpose, the fields scattered by 500 configurations of helices at number density of 3500 particles per cubic meter were calculated over a band from 2.5 to 3 GHz. The forward scattered field of these particles is shown in Fig. 8.5.

The forward scattered field magnitude is found to increase by two orders of magnitude here, suggesting that the forward scattered fields are still entirely coherent as they are predicted to be in single scattering theory and are not interfering with one another due to shadowing. The effective permittivity of these clouds is also solved for, as shown in Fig. 8.6, compared to the predictions offered by single scattering theory.

Fig. 8.6 shows that the single scattering predictions are mostly accurate for predicting the effective permittivity. At resonance, the effective permittivity is found to have an imaginary part of $\epsilon''_{eff} > 0.1$, indicating significant attenuation will be experienced by a wave propagating in this

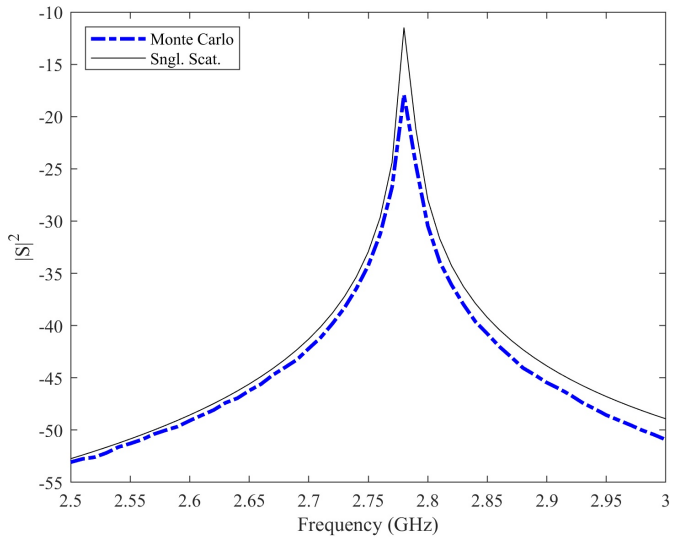

Figure 8.5: Coherent and Incoherent portions of the field scattered by a cloud of helices at number density $n = 3500$ particles per cubic meter over a wide frequency band. Single scattering predicts slightly more scattering than Monte Carlo simulation.

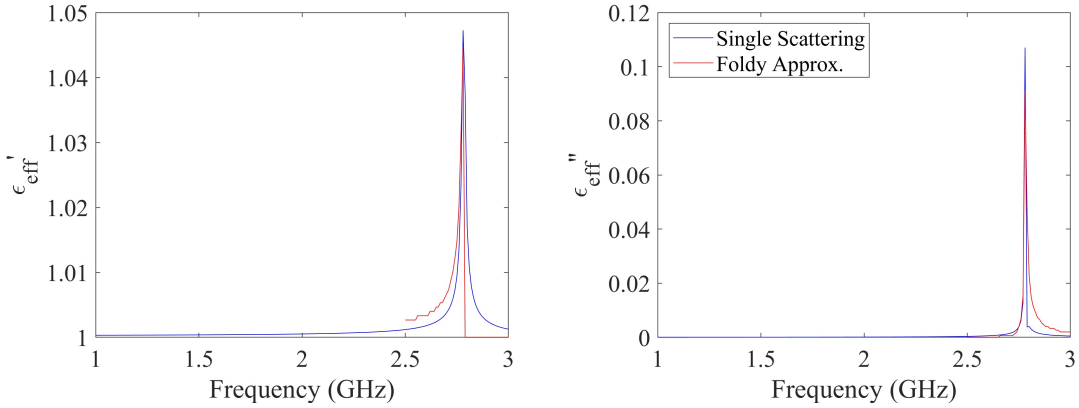

(a) (b)

Figure 8.6: Effective Medium parameters for cloud of helices at number density $n = 3500$ particles per cubic meter over a wide frequency band, compared to the single scattering prediction made herein.

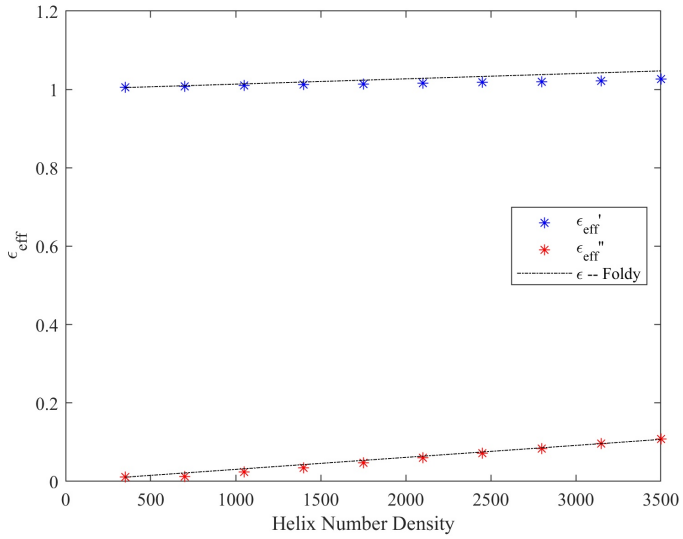

Figure 8.7: Effective medium parameters for cloud of helices at resonance and over varied number density. For occupation densities explored, they seem to be obeying single scattering.

medium. The value of the effective permittivity at this resonance predicted using Monte Carlo simulation is compared to the prediction made using single scattering for varied number density in Fig. 8.7.

The last effect explored in this model was to look at the effect of modeling scatterers, that would be constructed of metallic material in real life, as perfectly conducting. This question could represent a noticeable computational burden from a Method of Moments standpoint [Jin, J. (2010)], because penetrable scatterers, or any scatterer that is not perfectly conducting, require solving a larger system of unknowns than perfectly conducting scatterers. Because single scattering seems to accurately model the behavior of the field scattering, this question is also assessed using single scattering. The scattered fields predicted using the Method of Moments for perfectly conducting particles, as well as copper and silver particles, are shown in Fig. 8.8.

The permittivities of these materials are given by the Drude model [Jackson, J.D. (1999)], and numerically are $\epsilon_{PEC} = 1 + i\infty$, $\sigma_{Cu} = 5.8 * 10^7$ S/m, $\sigma_{Au} = 6.2 * 10^7$ S/m. The fields scattered by each of these media agree well with one another at this frequency, because of the high conductivity of the metals examined.

Given these results, it seems that sparsely populated random media with a significant scattered

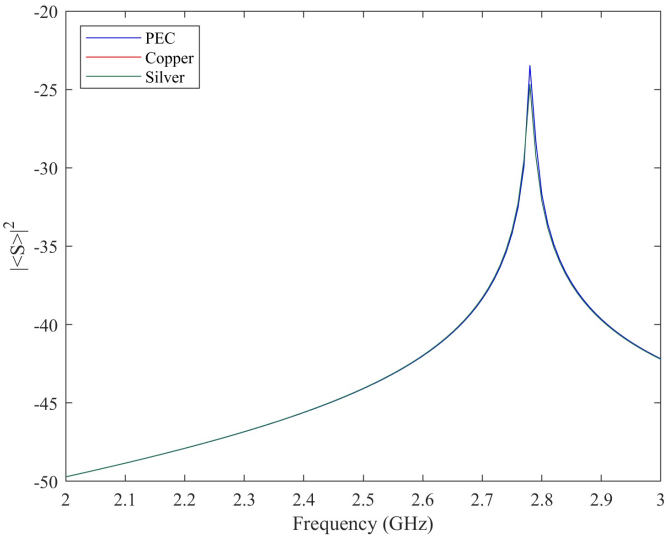

Figure 8.8: Comparisons of fields scattered by perfectly conducting helices, and helices made of silver or copper. Calculated using the Method of Moments.

field response can be designed within a narrow bandwidth. This particular random medium is designed by taking advantage of the physical intuition that is given by single scattering. Here, it is seen that the mean fields of media composed of more than one kind of scatterer can be understood by modeling mean fields scattered by only one type of scatterer and then combined in a way that is similar to a mixing formula. Here, a scatterer with a higher Q-factor that covers the relevant bandwidth could be desired, so that the medium could be designed using only one type of scatterer, but this secondary design step is omitted from this thesis for brevity. Lastly, it is seen that, at these low frequencies, metallic inclusions are very similar to perfectly conducting inclusions, suggesting that the effects of particle interaction can be understood using conducting particles as an acceptable substitute for particles which are highly, but not infinitely, conductive.

8.3 Effective Permittivity of a Chaff-like Random Medium

Chaff clouds tend to be composed of electrically large, conductive scatterers that are here assumed to be uniformly distributed in space and uniformly oriented. The media under study here are assumed to be manufactured to be identical prior to packaging and deployment. It is assumed that

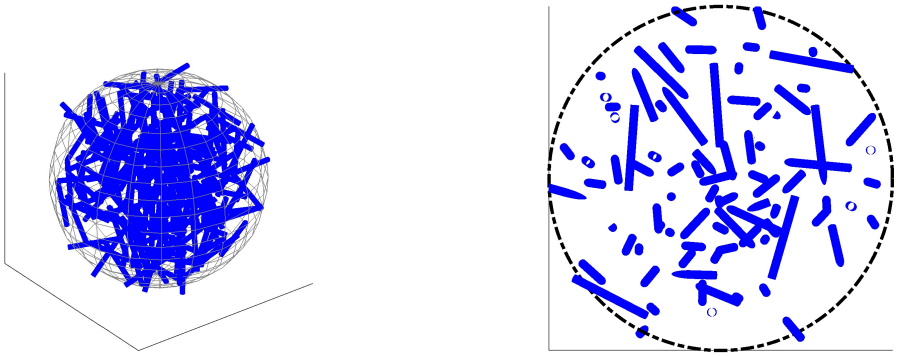

(a) (b)

Figure 8.9: (a) Three- and (b) two-dimensional view of enclosing particle of size $R_s = 2\lambda$ enclosing cylindrical inclusions with length $l = \lambda$, and radius $r_i = \lambda/20$ at $n = 50$ particles per cubic wavelength.

packing and deployment may cause inclusions to bend somewhat. Therefore, the parameters that are considered important to understand for the purpose of this macromodel is how the effective permittivity of a chaff-like random medium varies with respect to particle size (length), number density within the medium, and in the presence of some bending of the particles. Here, particle number density is chosen instead of volume fraction because each particle is essentially represented one-dimensionally. For relatively sparsely populated media of this type, such as those examined in Chapter 7, single scattering was found to provide a good estimate for the effective permittivity of this medium. Therefore, this model will be presented as an extension to the Foldy approximation [Brown & Curry (1982)] that solves for the effective permittivity of chaff-like random media for particles of any size and varying number density.

Studying this random medium starts by ascertaining that the effective permittivity of a medium can be solved for accurately for the densest clouds included in this study. This first step was undertaken by calculating the coherent portion of the scattering matrix for wire particles of length $l = \lambda$ and radius $r_i = \lambda/20$, placed inside of an enclosing sphere of size $R_s = 2\lambda$, at occupying number densities of up to $n = 100$ particles per cubic wavelength. Bistatic scattering from each of these clouds was calculated for 200 Monte Carlo trials, for scattered angles $\theta = -180^\circ, -179^\circ, \ldots, 180^\circ$ and $\phi = 0^\circ, 90^\circ$. Scattering from the densest clouds was calculated using a computing cluster. Of

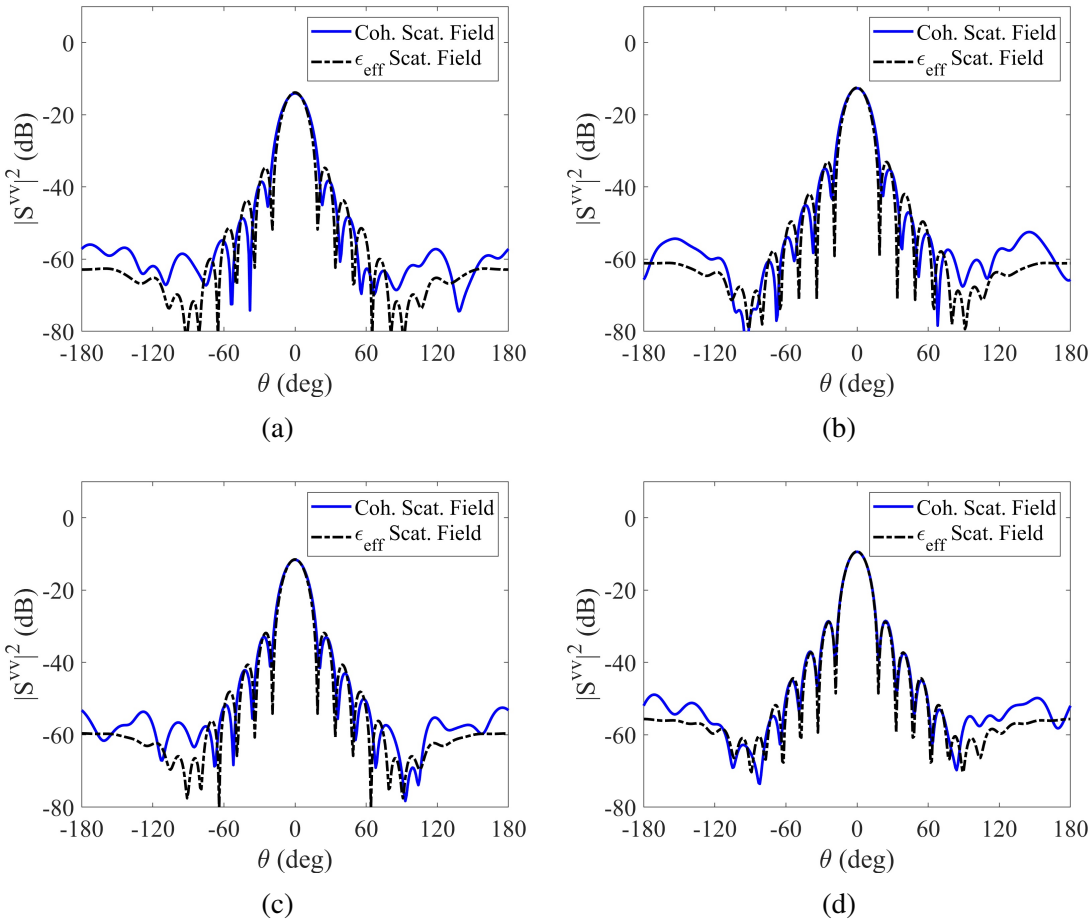

Figure 8.10: Comparison of fields scattered by wire particles with nominal radius $r = \lambda/20$, and length $l = \lambda$, placed in a container sphere with radius $R_s = 2\lambda$ at (a) $n = 30$ particles per cubic wavelength, (b) $n = 40$ particles per cubic wavelength, (c) $n = 50$ particles per cubic wavelength, and (d) $n = 100$ particles per cubic wavelength.

these calculations, the coherent portion of the scattering matrices for the four densest clouds are shown in Fig. 8.10, along with the solution to the inverse scattering problem. The matching between the coherent portion of the scattering matrix and the field scattered by the effective medium is shown in Fig. 8.11.

Of the trials shown, all are seen to have recognizable coherent fields that match well to the scattering matrix of their counterpart scattered by the homogeneous effective medium. The matching surfaces, shown in Fig. 8.11, are each shown to have single minima that are locally convex. Media that are more densely occupied by wires are found to have a higher effective permittivity. This makes sense, as these media ought to have more scattering in them and attenuate the coherent

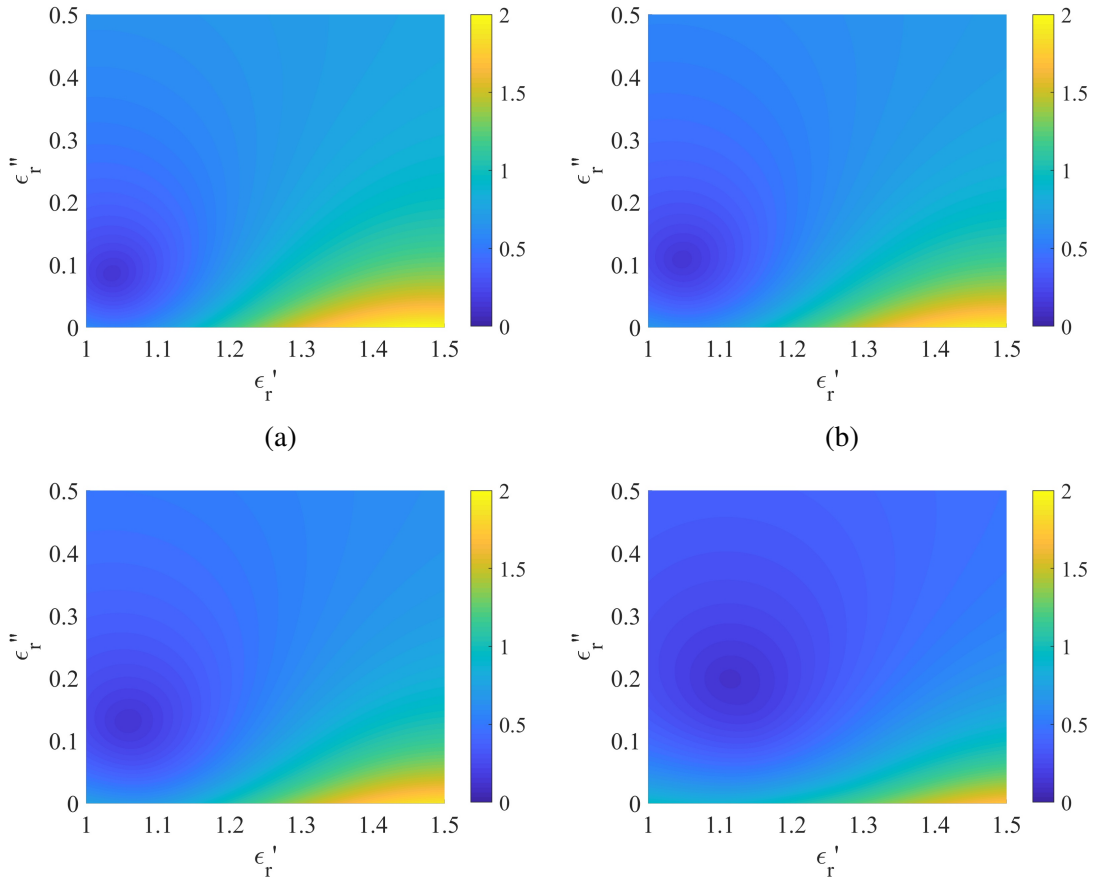

Figure 8.11: Euclidean norm between the coherent portion of the scattering matrix estimated using Monte Carlo simulation and the scattering matrix of a homogeneous sphere for (a) $n = 30$ particles per cubic wavelength, (b) $n = 40$ particles per cubic wavelength, (c) $n = 50$ particles per cubic wavelength, (d) $n = 100$ particles per cubic wavelength.

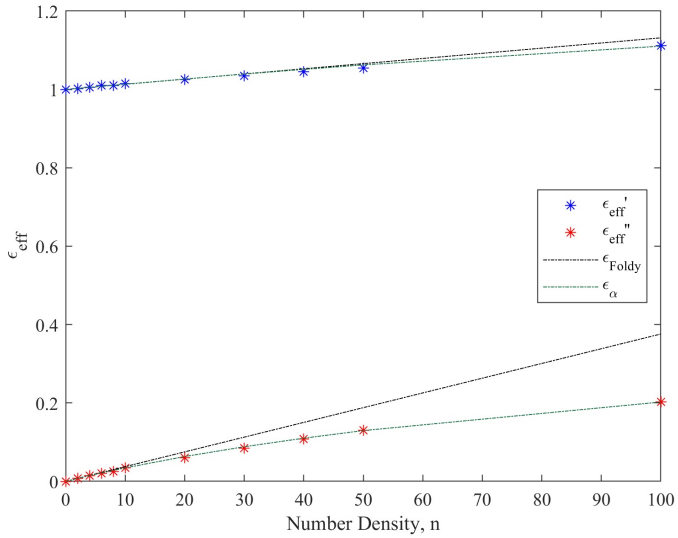

Figure 8.12: Variation of effective permittivity for particles of radius $\lambda/20$, length $l = \lambda$, inside a sphere of radius 2λ at varied number density compared to single scattering prediction and expanded macromodel prediction.

propagating field more quickly. The dependence of the effective medium parameter on number density is investigated next.

The effective permittivity of the medium ought to increase as the medium becomes more densely occupied. Single scattering theory, given in [Brown & Curry (1982)], states that this increase ought to be linear for sparsely occupied media because the forward scattered field from each particle ought to add constructively. This dependence is given in Eq. (8.1). Here, ϵ_{eff} is the relative effective permittivity of the medium and it is explicitly dependent on the number density, n, of the inclusions that is measured in particles per cubic wavelength. When the occupation of the medium is no longer sparse and particles begin to interact, it is thought that the increase should taper off due to particles being in one another's shadow. This is confirmed in Fig. 8.12, by comparing single scattering prediction to predictions given by Monte Carlo simulation.

In Fig. 8.12, the blue (red) asterisks indicate the real (imaginary) part of the effective permittivity calculated using Monte Carlo simulation. The black dashed line represents the single scattering prediction, and the green line represents an updated model proposed in Eq. (8.2).

$$\epsilon_{eff}(n, \alpha) = 1 + \frac{4\pi F \alpha}{k_0^2} \log\left(1 + \frac{n}{\alpha}\right) \tag{8.2}$$

This model is proposed because it offers the correct solution in limiting cases in that it reduces to the single scattering model when $n \ll \alpha$, and represents infinite permittivity as $n \to \infty$. Fitting the model to the results given by Monte Carlo simulation gives a value of $\alpha = 48.6$. This model ought to deviate from the prediction offered by single scattering when $n \approx \sqrt{\alpha} \approx 7$ for the observed data. This correction can be derived by considering the small argument expansion for $\log(1 + x)$, and the deviation near $n = 10$ is also observed in Fig. 8.12. This model appears to fit the imaginary part of the effective permittivity better than the real part. This observation generally describes all of the results fitted to this model in this section. Here, it is important to note that fitting the deviation in the imaginary part of the effective permittivity is desired as this number both deviates more from the single scattering prediction and is more important in calculating the loss factor of the medium. This model could be made to fit even better if α were allowed to be complex, but estimating two numbers (the real and imaginary part of α) is more complex than estimating one.

The model proposed in Eq. (8.2) can be extended to understand the dependence of α on chaff clouds that contain inclusions of lengths other than $l = \lambda$. In this way, the utility of single scattering as a model can be understood for particles of differing sizes. It is expected that α, that effectively can be understood as the point at which the effective permittivity 'saturates' and single scattering stops being a good model, will decrease as particles get larger and have larger near field interactions and more multiple scattering interactions. Monte Carlo simulations for particles of size $0.1 \leq l/\lambda \leq 3$, and radii $r_i = \lambda/20$ are conducted for chaff clouds of varying density $0 < n < 100$ to determine α for each inclusion length. The results of this calculation are shown in Fig. 8.13.

Fig. 8.13 shows $\alpha(l/\lambda)$. To calculate these results particles of lengths $l \leq \lambda$ are calculated for number densities up to $n = 50$, and the smallest particle lengths ($l < \lambda/3$) are calculated until a deviation is observed ($n = 100$ for $l = \lambda/10$). For particles longer than this length, deviation is always observed for clouds with number density $n = 20$ particles per cubic wavelength, and these represent the densest clouds used to calculate α. Despite this simplification, clouds of the longest

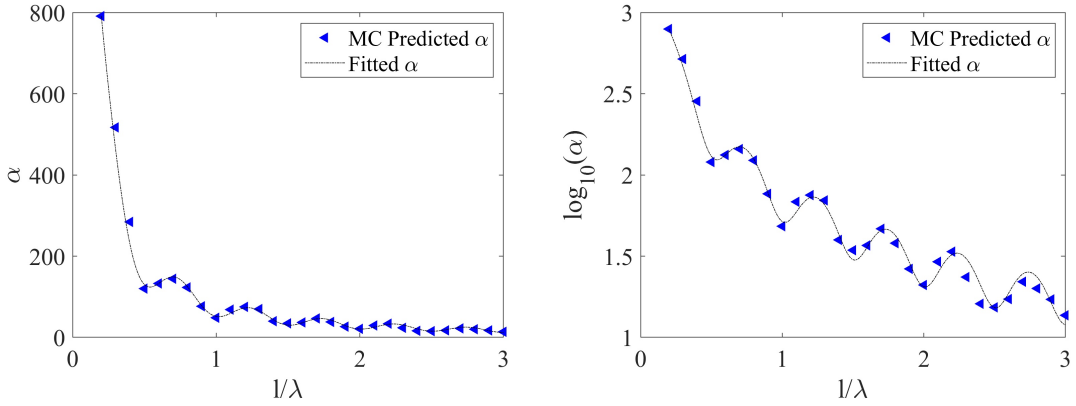

Figure 8.13: (a) Linear, and (b) logarithmic dependence of α in length of a wire for wires of length $l = \lambda/10$ to $l = 3\lambda$.

particles still represent considerable computational complexity. The correction factor, α, is seen to have two primary factors governing its dependence on wire length: a periodic dependence and an inverse-power dependence. These calculated coefficients are fitted to Eq. (8.3), and show relative contributions of $\alpha' = 74.3$ and $\alpha'' = -22.6$.

$$\alpha(l/\lambda) = \frac{\alpha' + \alpha'' cos(4\pi(l/\lambda))}{(l/\lambda)^{4/3}} \tag{8.3}$$

This fitting procedure seems to do a good job describing the calculated correction factor, and mostly agrees with the previously calculated value $\alpha(l/\lambda = 1) = 48.6$. The periodic dependence of the coefficient also suggests that anti-resonant particles obey single scattering in denser clouds than do particles that are resonant.

The dependence of the correction factor α was next investigated in the face of particle bending. In this model, particle bending is thought to arise incidentally during the process of packing wires into a contained area or of deploying the particles into a cloud. Bent particles are modeled as subtending a piece of a circular arc. Particles that aren't bent subtend 0° of this arc. Bending was also modeled by modeling the wires as parabolas, this is seen to not affect the calculated correction factor for the particles investigated herein. Clouds of bent particles of length $l = \lambda$ are generated, and the dependence of the correction factor α on this bending is shown in Fig. 8.14.

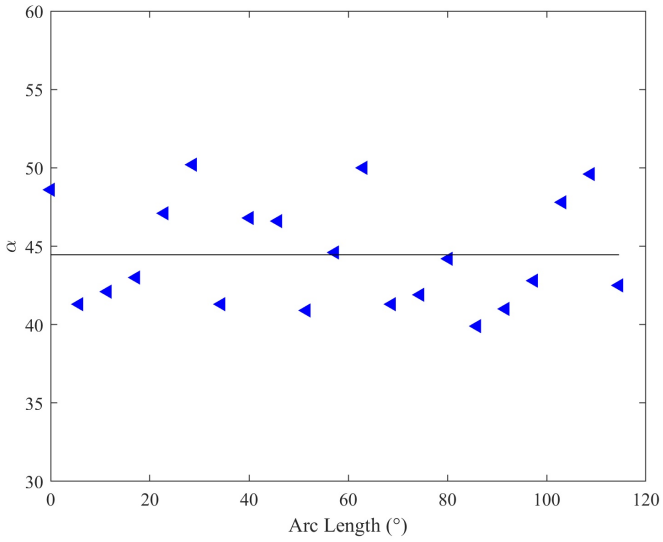

Figure 8.14: Dependence of α on wire curvature.

For the amount of bending explored, it seems that the correction factor is independent of particle bending. One important result of this study is that the precision of the correction factor can be assessed from it using the standard deviation of the predictions. The calculated correction factors have a value of $\alpha = \alpha_1 \pm \alpha_2 = 44.8 \pm 3.6$, where α_2 represents the uncertainty of each prediction given herein.

$$\epsilon_{eff}(n, l, R, \lambda) = 1 + \frac{4\pi\alpha(l/\lambda)}{k_0^2} F(\lambda, l, R) \log\left(1 + \frac{n}{\alpha(l/\lambda)}\right) \tag{8.4}$$

These independent effects can be composed to give a macromodel for field propagation in chaff. This macromodel is given in Eq. (8.4). Each result shown in this section is found to agree well with the macromodel. This model is given in terms of α, the correction factor to the single scattering model in Eq. (8.2). To use this factor to predict the effective permittivity of a chaff cloud, the single scattering prediction should be computed by ensemble averaging the forward scattered field over the probability density function of orientations of the particle in space. This predicted forward scattered field can then be multiplied by the logarithmic function that depends on the correction factor α that can be determined using interpolation to predict the attenuation rate of a wave propagating in this medium. It is expected that this method could be used to assess and

extend the predictions offered by other theoretical models.

8.4 Modeling Phase Function of a Chaff-like Random Medium

The mean field model in Section 8.3 is extended to model the fluctuating component of the field scattered by a chaff-like random medium. Like the model in Section 8.3, this model is intended to extend the single scattering prediction of the phase function for use in Radiative Transfer modeling of wave propagation in these media. The model presented here models only the co- and cross-polarized elements of the phase matrix for this medium in two scattering ϕ-planes. These elements of the phase function represent four of the eight nonzero elements of the phase matrix. The remaining four elements of the phase matrix, that are not calculated in this chapter, represent the polarimetric part of the phase function. The form of these elements is not explored further here for brevity. Methods for analytically extending this model to give a three-dimensional prediction of the phase function are discussed, as well as the procedure that should be undertaken to calculate such a model using Monte Carlo simulation. Because particle bending was found to have no effect in the mean field model, it is not assessed in this model.

The scattering coefficient is first predicted for inclusions of length $l = \lambda$ and radius $r_i = \lambda/20$ using single scattering. The scattering coefficients here are calculated because they are expected to agree for enclosing particles of differing sizes and for differing buffer zones. The scatternig coefficient of configurations occupying multiple enclosing particles are calculated to find agreement between them and to remove some of the numerical noise that seems to be plaguing this process. Scattering matrices are calculated for $-180 \leq \theta \leq 180$ in the two principal ϕ-planes, $\phi = 0°, 90°$. The co-polarized and cross-polarized elements of the scattering matrix are shown in Fig. 8.15, calculated using two different spherical container particles of size $R_s = 2\lambda, 3\lambda$.

The scattering coefficients are fit in their principal ϕ-plane to a sum of Associated Legendre Functions, $P_l^m(\theta)$ [Jackson, J.D. (1999)] for fixed $m = 0$. These functions represent a computationally convenient decomposition of angular space, and this set of special functions is chosen

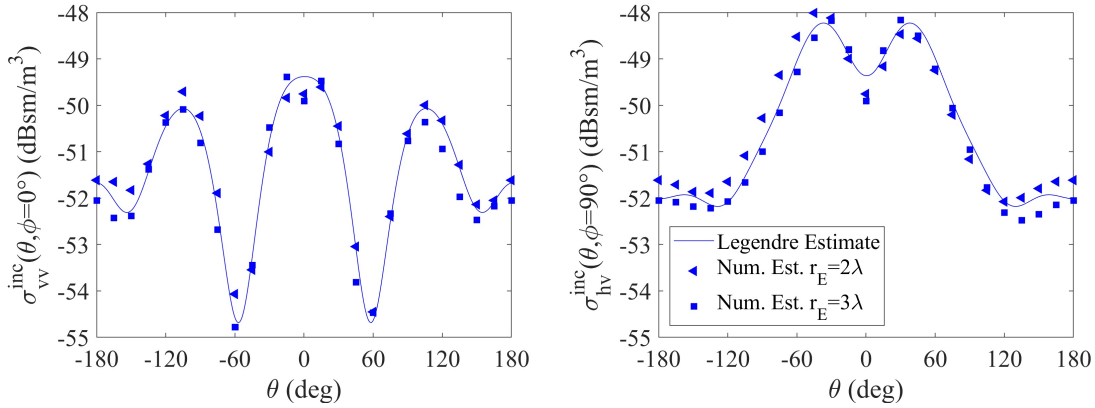

Figure 8.15: (a) Co-polarized and (b) cross-polarized incoherent scattering coefficient predicted using Monte Carlo simulation for enclosing particles of size $R_s = 2\lambda, 3\lambda$ containing a single wire of length $l = \lambda, r_i = \lambda/20$.

for their relation to the spherical harmonic set, $Y_{lm}(\Omega)$ that can be used to analytically extend the predictions into three dimensions. While the spherical harmonics form a complete, orthogonal decomposition of three-space, see Eq. (8.5), and are the minimal tensor space for representing the two-dimensional special rotation group, the Associated Legendre Functions themselves are not orthogonal to one another for simultaneously varied l and m, as is shown in Eq. (8.6).

$$\int_{\Omega} d\Omega Y_{lm}^{*}(\Omega) Y_{l',m'}(\Omega) = c_{lm}\delta_{l,l'}\delta_{m,m'} \tag{8.5}$$

$$\int_{1}^{1} d(\cos(\theta)) P_{l}^{m}(\cos(\theta)) P_{l'}^{m}(\cos(\theta)) = c_{l}\delta_{l,l'} \tag{8.6}$$

In Eq. (8.5) and (8.6), δ represents the Kronecker-delta function, that is zero when its arguments are not equal and unity when they are equal. This function is used to indicate the orthogonality of the special functions. Calculating a full spherical harmonic expansion is not possible with this data, and would require calculating the bistatic scattering matrix along more ϕ-planes. This step is not undertaken in this thesis because of the computational complexity and memory demands of making it.

Given the successful fitting of the single scattering results, results in an interacting medium

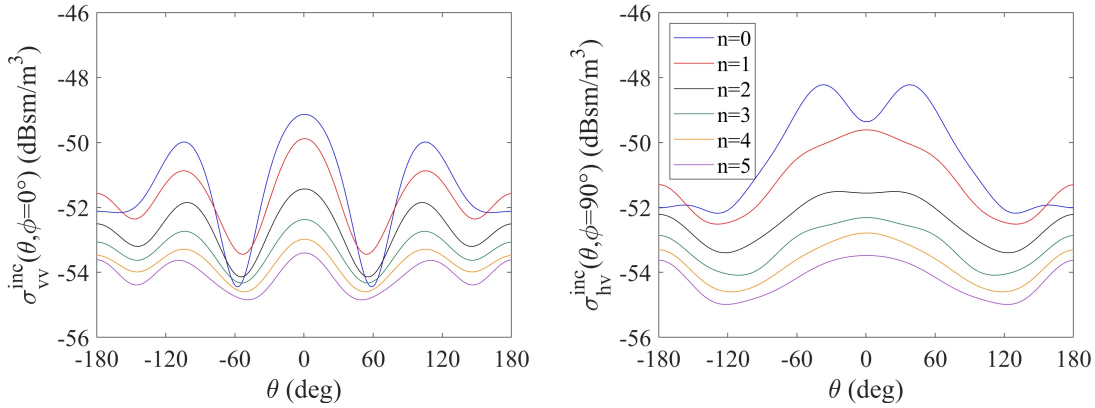

Figure 8.16: (a) Co-polarized and (b) cross-polarized incoherent scattering coefficient predicted using Monte Carlo simulation for enclosing particles of size $R_s = 2\lambda, 3\lambda$ occupied at varying number densities of wire particles of length $l = \lambda, r_i = \lambda/20$. These fits are made for chaff inclusions of many lengths and are included in Table 8.1.

were calculated next. Here, slightly denser media, with $0 < n \leq 5$ particles per cubic wavelength were studied using Monte Carlo simulation. The particles are chosen to have a length of $l = \lambda$ and a radius of $r_i = \lambda/20$, and were placed inside of two enclosing spheres of size $R_s = 2\lambda, 3\lambda$. Buffer zone averaging was employed to stabilize the numerical noise of this process, with buffers implemented for $0 \leq r_b \leq (R_s - l)$. The scattering coefficients calculated are found to be remarkably consistent across the buffer zones examined and for the different sized enclosures used, with observed differences being explained as arising from numerical noise. The scattering coefficients are again fitted to Associated Legendre Functions with $m = 0$, the fitted results are shown in Fig. 8.16.

The numerical estimates of the scattering coefficients obtained using fitting obey physical intuition. The estimates made for the single scattering cloud scatter the most power per inclusion, and the scattering coefficient decreases in most directions as the cloud becomes denser. One place where relatively more power is scattered is backwards, which can be thought of as arising from the coherence of pairwise interactions in the cloud, and was observed in [Lax (1952), Mookerjee & Dowling (2017)]. The fitted scattering coefficient of the three densest clouds explored is consistent, and only changes due to shadowing phenomena. So, it seems as though this model could be

	$c_{00} \times 10^6$	$c_{10} \times 10^6$	$c_{20} \times 10^6$	$c_{30} \times 10^6$	$c_{40} \times 10^6$
$\sigma_{vv}^{inc}(n=0)$	7.23	-0.90	-0.54	4.78	3.01
$\sigma_{vv}^{inc}(n=1)$	6.57	-0.55	-0.45	2.49	2.19
$\sigma_{vv}^{inc}(n=2)$	5.31	-0.40	-0.46	1.57	1.63
$\sigma_{vv}^{inc}(n=3)$	4.59	-0.33	-0.23	0.98	0.94
$\sigma_{vv}^{inc}(n=4)$	4.15	-0.29	-0.19	0.69	0.70
$\sigma_{vv}^{inc}(n=5)$	3.83	-0.30	-0.16	0.58	0.53
$\sigma_{hv}^{inc}(n=0)$	9.36	5.14	1.55	-1.50	-1.30
$\sigma_{hv}^{inc}(n=1)$	7.38	2.58	1.35	-0.76	0.12
$\sigma_{hv}^{inc}(n=2)$	5.55	1.22	0.89	-0.53	0.08
$\sigma_{hv}^{inc}(n=3)$	4.59	0.82	0.79	0.00	0.00
$\sigma_{hv}^{inc}(n=4)$	4.03	0.65	0.72	0.00	0.00
$\sigma_{hv}^{inc}(n=5)$	3.61	0.46	0.59	0.00	0.00

Table 8.1: Fitted Associated Legendre Function expansion coefficients for Fig. 16.

extended to denser clouds only as a shadowing phenomenon.

Given the successful results, equivalent results for particles of other lengths were derived. Here, the same enclosing particle parameters and number densities were calculated for inclusions of $0.1 \leq l/\lambda \leq 2$. For the two smallest particles: $l/\lambda = 0.1, 0.2$, that have to be modeled as cylinders rather than wire structures, only the smaller of the enclosing particles is used to limit the computational burden of this exercise. This is not thought to affect the results because of the amount of buffer zone averaging available in these clouds. The largest particles, that have $\frac{l}{\lambda} > 1.5$, only use the larger of the enclosing particles because of the convergence criteria observed in Chapter 7. While less averaging is undertaken on these trials to remove the numerical noise, their results still appear to follow the physical intuition that comes from shadowing. The fitted Associated Legendre Function coefficients that are the output of this study are given in the Appendix A in table form. This table is not included in the text of the chapter because it does not illuminate the results of the chapter very much, although it could be useful in calculating Radiative Transfer predictions for random media propagation. These coefficients, such as they are, are sufficient to provide a first-order Radiative Transfer solution. They could be analytically extended using spherical harmonics to solve the Radiative Transfer equations at higher order or in a matrix method, but spherical harmonic expansion coefficients are not calculated here.

8.5 Conclusion

The work shown in this chapter shows two ways to use Monte Carlo simulation in random media propagation. One way that Monte Carlo simulation can be used here is in the design of inclusions to have a desirable effective permittivity for a particular application. This is shown here by designing a random medium that should provide significant attenuation to propagating waves in sparsely occupied media over a narrow (200 MHz) frequency band. In this study, several assumptions of Monte Carlo simulation are also tested and show the validity of the approach. Monte Carlo simulation is also used to construct a macro-model of propagation in a chaff-like random medium to verify and extend the applicability of the Foldy approximation. This model greatly simplifies the process of calculating the extinction coefficient and phase function for these media, and can be used to estimate first-order solutions to the Radiative Transfer equations for a large number of random media. Three-dimensional analytic extensions of the process used to estimate the phase function are also proposed to give higher-order estimates of the solution to the Radiative Transfer equations, but this step is not undertaken in this portion of the thesis for brevity.

CHAPTER 9

Autoproduct Processing Using Electromagnetic Waves

9.1 Introduction

The development of autoproduct-processing algorithms, both those used for beamforming [Abadi *et al.* (2011), Douglass *et al.* (2017)] and those used for source localization [Worthmann *et al.* (2015), Geroski & Dowling (2019)], has focused on solving problems in passive remote sensing using acoustic pressure waves propagating in waveguiding ocean environments. These algorithms, particularly those using the frequency-difference autoproduct, have been successfully used to mitigate problems associated with environmental mismatch and wave scintillation to increase the robustness of nonlinear signal processing algorithms that are used in underwater acoustics. Further, these algorithms have demonstrated that frequency-differencing can also be used to increase the robustness of beamforming algorithms in random scattering media [Douglass & Dowling (2019), Worthmann & Dowling (2020a)]. Problems related to a loss of frequency-domain stability due to wave scintillation and scattering in a random medium are seen in other remote sensing disciplines, such as radar and radiometric remote sensing [Skolnik, M.I. (1980), Ulaby, F.T. & Long, D.G. (2014)]. As such, it is possible that autoproduct-processing algorithms could be applied to increase the robustness of existing signal processing techniques in these systems as well. While both active and passive electromagnetic remote sensing systems exist, frequency-differencing algorithms are expected to have greater utility in passive electromagnetic remote sensing. This is

because active remote sensing systems tend to operate over narrower bandwidths than passive systems. This chapter extends the current definition of the frequency-difference autoproduct, which has always previously treated scalar waves, to account for polarization. While propagating electromagnetic waves do not carry a compressional component, extending this definition to account for waves that carry both transverse and compressional components [Maurice, E.W. *et al.* (1957)] is given. This chapter then evaluates the utility of using autoproduct processing by simulating models of scintillating and scattering electromagnetic random media using a two-dimensional Method of Moments-based scattering code [Jin, J. (2010)], and evaluating the effect that these models have on passive beamforming.

This chapter uses simple models of both scintillating and scattering random media in electromagnetics. The first of these models, the random phase screen, is a scintillating random medium that is often used to model signal distortion in atmospheric propagation [Andrews *et al.* (1994), Lane *et al.* (1992)]. The medium is designed to cause random scattering, to lack both spatial coherence and frequency coherence, and to cause a signal to lose its stability without attenuating the signal. In this way, the phase screen is expected to behave similarly to the time-front mismatch model that was employed in Chapters 3 and 5, that modeled environmental mismatch primarily by corrupting the phase measured from a signal without directly modifying the magnitude of the propagating field. This model is analyzed in this chapter with the goal of demonstrating the utility that autoproduct-processing might have in passive remote sensing where a loss of field stability is the primary concern. This analysis is then extended to investigate media that have some level of coherence by employing the Method of Moments [Jin, J. (2010)] to calculate the field scattered by random media. This chapter imposes this partial coherence in two ways: first, it models a phase screen as randomly placed discrete conducting cylinders, and, second, it randomly places cylinders across an area to determine the effect that this has on degrading the performance of beamforming algorithms. These models are expected to lend insight into the utility of employing autoproduct-processing techniques for studying problems in electromagnetic remote sensing in a setting that requires only minimal computational power. Given success in these investigations, this analysis

could be extended to provide greater insight into three-dimensional remote sensing problems or into analyzing problems with more realistic propagation modeling.

This is not the first time that autoproduct processing algorithms have been applied to study the performance of nonlinear signal processing algorithms in environments composed of discrete scatterers. The autoproduct field in environments that contain a single scatterer was first investigated analytically in [Worthmann & Dowling (2020a)]. This study examined the pressure field, and related autoproduct, that is scattered by a sphere using a Mie series calculation. The frequency-difference autoproduct is found to mimic the pressure field at the difference frequency for this calculation outside of a shadow zone. This study finds a similar result (in the two-dimensional scattering from an infinite cylinder case) using a full-wave solver to calculate the scattered field. This perspective, drawn from the Method of Moments, lends itself to generalization in a medium composed of many interacting scatterers or scatterers of varied geometry. The autoproduct has also been investigated in a multiple scattering environment in [Douglass & Dowling (2019)], where the autoproduct is found to offer increased robustness for beamforming through a medium composed of soft scatterers. These soft scatterers, ping pong balls in the experiment, are meant to mimic a bubbly fluid in a controlled environment. In this study, the Born approximation is used to argue that high-order, multiple scattering phenomena should be suppressed by the bandwidth-averaging step of frequency-difference beamforming, and this observation is supported by the successful experimental results contained in the study. This chapter aims to extend this study by analyzing an electromagnetic analogue to bubbly fluid, which is a medium occupied by perfectly conducting scatterers. Here, the bubbles, that approximately represent pressure release boundaries in underwater acoustics [Urick, R.J. (1996)], have the same reflection coefficient as do perfect electrical conductors (for the appropriate incident polarization) in electromagnetics. This study also uses the Method of Moments to determine where bandwidth-averaging is sufficient to suppress cross-terms that arise from multiple scattering in a medium of interacting scatterers.

This study makes use of a two-dimensional Method of Moments code for numerically solving electromagnetic scattering problems. This code is developed following [Jin, J. (2010)], and the

information contained therein is used to verify the results calculated using this code. The Method of Moments, first published in [Harrington (1967)], solves scattering problems numerically by discretizing the scatterers in question. This chapter, that only solves for the field scattered by homogeneous scatterers, only discretizes the surface area of the scatterers in question, but generalizations of this method, for solving the field scattered by bodies that are both penetrable and inhomogeneous, for solving for volumetric current exist as well. The surface area of all scatterers is decomposed into small enough basis functions that the current on the basis functions can be approximated as a Dirac δ-function. Then, the interactions between each basis function is solved for and represented as an impedance matrix, referred to as an interaction matrix outside of the computational electromagnetics community, that represents the current induced on all basis functions by a source current placed on any basis function. The current induced on each basis function by a general incident field can be solved for, and the impedance matrix can be used to compute the scattered field. This method is found to exactly represent the field scattered by any scatterer to within specified numerical tolerances. This method is found to be more efficient at calculating scattering problems than methods that rely on finite differencing when the scatterers are homogeneous or when there is a significant amount of space between sources and scatterers.

The remainder of this chapter is divided into four sections. Section 9.2 lays out the theory that governs the autoproduct for polarized waves, as well as the expected form of the autoproduct field in a scattering environment. Section 9.3 proposes and analyzes two models of the random phase screen, chosen to demonstrate the utility of autoproduct-processing in understanding propagation through a random medium that entirely lacks coherence and propagation through a random medium that has some coherence. Section 9.4 extends this analysis to beamforming in an electromagnetic random medium that is occupied by many cylinders. Section 9.5 draws what conclusions are available from this chapter.

9.2 Theory

The frequency-difference autoproduct can be defined for any field quantity that has some bandwidth and which can be coherently measured in the frequency domain. An electric field, $\vec{E}(\vec{x},\omega)$, propagating in an isotropic medium is most easily represented in the frequency-domain as the solution to the vector Helmholtz equation [Jackson, J.D. (1999)], given in Eq. (9.1).

$$\nabla^2\vec{E}(\vec{x},\omega) + \frac{\omega^2}{c^2}\vec{E}(\vec{x},\omega) = \vec{J}(\vec{x},\omega) \tag{9.1}$$

Here, $\vec{E}$ is the electric field, a vector quantity in free space measured at spatial location $\vec{x}$ and frequency ω. The electric field is understood in the frequency domain as being the solution to the vector Helmholtz equation with (vector) Laplacian $\nabla^2 = \frac{\partial^2}{\partial x^2}\hat{x} + \frac{\partial^2}{\partial y^2}\hat{y} + \frac{\partial^2}{\partial z^2}\hat{z}$, wave speed c being the speed of light in the local medium, and with current source $\vec{J}$. The electric field is found to propagate in a source-free medium as a plane wave, as is shown in Eq. (9.2).

$$\vec{E}(\vec{x},\omega) = \begin{bmatrix} 0 \\ E_h \\ E_v \end{bmatrix} exp\Big(i\big(\vec{k}\circ\vec{x} \pm \omega t\big)\Big) \tag{9.2}$$

The plane-wave solution to the vector Helmholtz equation, that is fundamentally derived from Maxwell's equations, finds that a plane wave propagating in direction $\hat{k} = \vec{k}/|k|$ has no compressional component to the wave $E_k = 0$ and instead carries transverse components, E_v, E_h. The polarizations, h, v are defined by a user based on the propagation problem. In this chapter, that focuses on propagation in a medium that is uniform in $\hat{z}$, polarization is defined by what field quantity, electric field or magnetic field, is transverse to the plane of propagation $(\hat{x},\hat{y})$.

Given an electric field, $\vec{E}$, that is the solution to the vector Helmholtz equation, the bandwidth-averaged frequency difference autoproduct is defined as a dyadic quantity constructed from the electric field [Tai, C.T. (1993)]. This dyadic quantity is a vector outer-product between the electric field and itself, and is represented as a rank-2 tensor, as in Eq. (9.3) and (9.4).

$$\bar{\bar{AP}}(\vec{x}, \Delta\omega) = \left\langle \vec{E}^{*,T}\left(\vec{x}, \omega_{-}\right)\vec{E}\left(\vec{x}, \omega_{+}\right)\right\rangle \tag{9.3}$$

$$\bar{\bar{AP}}(\vec{x}, \Delta\omega) = \begin{bmatrix} 0 & 0 & 0 \\ 0 & \langle AP_{hh}\rangle & \langle AP_{hv}\rangle \\ 0 & \langle AP_{vh}\rangle & \langle AP_{vv}\rangle \end{bmatrix} \tag{9.4}$$

Here, $\bar{\bar{AP}}$ is the frequency-difference autoproduct at difference frequency $\Delta\omega$. It is constructed from a bandwidth average of the product of the Hermitian transpose of the electric field with itself. This can be represented, after the bandwidth average, as a three-by-three matrix with four different elements, $AP_{hh}, AP_{hv}, AP_{vh}, AP_{vv}$. For a wave propagating in a medium that admits both compressional and transverse waves, such as vibrational waves propagating in an elastic structure, the elements in Eq. (9.4) that are zero would be nonzero. Here, it is worth noting that the four non-zero elements are represented in a way that makes them similar to scattering matrix elements. However, in a scattering matrix, these elements represent incident and scattered polarizations, rather than a dyadic product of measured polarizations. The equivalent scattering matrix for an autoproduct would have four times as many elements. Because of the complexity of this formulation, this chapter focuses on solving for field propagation in random media for which the cross-polarized elements of the autoproduct are zero.

This analysis can be applied to understand the autoproduct as it propagates through a region of discrete scatterers. Here, it is expected that a measurement device will see the total field, or the summation of the incident and scattered field, that is propagating in such a medium. Here, it is assumed that all scattered fields and cross-terms that are related to scattered fields will degrade the performance of beamforming algorithms. Therefore, all of these terms are considered undesirable. The total electric field, as it would be calculated in a Method of Moments code, is given in Eq. (9.5).

$$\vec{E}_{tt}(\vec{x},\omega) = \vec{E}_i(\vec{x},\omega) + \vec{E}_{sc}(\vec{x},\omega) = \vec{J}_0 G(\omega,\vec{x},\vec{x}_s) + \sum_n \vec{J}_n(\omega) G(\omega,\vec{x},\vec{x}_n) \tag{9.5}$$

Here, $\vec{E}_{tt}$ is the total field measured at location $\vec{x}$, that is the sum of the incident field, $\vec{E}_i$, and the scattered field, $\vec{E}_{sc}$. The incident field can be computed as the product of the source current, $\vec{J}_0$, that is assumed to be impulsive for all scattering problems considered herein, and the Green's function for the medium G. In two-dimensional scattering problems, the Green's function is an outward-traveling Hankel function, H_0^2 in the time-convention of [Jin, J. (2010)]. This function becomes a plane wave when the source is in the extreme far-field of the receiver. The scattered field is a sum over the current, $\vec{J}_n$ induced on each basis function located at $\vec{x}_n$ that represents the scatterers in a medium which is calculated using the Method of Moments, multiplied by the Green's function of the medium. The polarization of the incident and scattered waves, v, h, is important in computing both the induced current and the Green's function. The autoproduct related to this electric field is given in Eq. (9.6).

$$\begin{aligned} \bar{\bar{A}}P(\vec{x},\Delta\omega) &= \left|\vec{J}_0\right|^2 \left\langle G^*(\omega_-,\vec{x},\vec{x}_s) G(\omega_+,\vec{x},\vec{x}_s)\right\rangle \\ &+ \sum_n \left\langle J_n^*(\omega_-) J_n(\omega_+) G^*(\omega_-,\vec{x},\vec{x}_n) G(\omega_+,\vec{x},\vec{x}_n)\right\rangle \\ &+ \sum_{m\neq n} \left\langle J_m^*(\omega_-) J_n(\omega_+) G^*(\omega_-,\vec{x},\vec{x}_m) G(\omega_+,\vec{x},\vec{x}_n)\right\rangle \end{aligned} \tag{9.6}$$

The autoproduct given in Eq. (9.6) is directly comparable to Eq. (9) and Eq. (10) in [Douglass & Dowling (2019)] that was derived using the Born approximation. For the purpose of frequency-difference beamforming, only the first term, that arises from multiplying the incident (or source) field with itself is thought to be useful because all other terms arise from interference. This implies that, for autoproduct-processing to perform as well as or better than in-band beamforming in a scattering random medium, all other terms must average to zero in the bandwidth averaging process.

For the bandwidth-average to cancel the induced cross-terms in the scattered field, it is noted

that two things must be true: firstly, that all of the terms in question must be incoherent over the averaging bandwidth, and, secondly, that the amount of averaging bandwidth must be sufficient to cancel the term. The first of these criteria suggests that either the currents must be incoherent in space or in frequency, or that the product of the Green's functions, that represents the response of the medium to each current, must be incoherent. These criteria are given in Eq. (9.7) and (9.8).

$$\left\langle J_m^*(\omega_-) J_n(\omega_+) \right\rangle = \frac{1}{|\Omega|} \int_\Omega d\omega J_m^*(\omega_-) J_n(\omega_+) \to 0; \Omega \to \infty \tag{9.7}$$

$$\left\langle G^*(\omega_-, \vec{x}, \vec{x}_m) G(\omega_+, \vec{x}, \vec{x}_n) \right\rangle = \frac{1}{|\Omega|} \int_\Omega d\omega G^*(\omega_-, \vec{x}, \vec{x}_m) G(\omega_+, \vec{x}, \vec{x}_n) \to 0; \Omega \to \infty \tag{9.8}$$

The first condition, that currents are incoherent in space and frequency, can be satisfied in two ways. Firstly, if the currents are excited on different basis functions, (for $m \neq n$) they can be spatially incoherent with one another. Secondly, if the difference frequency, $\Delta\omega$, is non-zero, then this quantity can integrate to zero because of a lack of frequency coherence. It is this idea that can cause the cross-cross term of the scattered field to go to zero, allowing autoproduct-processing to outperform field-processing algorithms. The second condition, that the Green's functions might be incoherent, can be understood in much the same way. In both cases, these observations also require that sufficient bandwidth averaging be employed to adequately cancel these signals.

The incoherence of the cross-terms, that is required to cancel the scattering cross-terms analytically, can be analyzed further using the known Green's function for two-dimensional random media propagation. This Green's function is an outgoing cylindrical wave, referred to as a Hankel function of the second kind, that can be directly analyzed in the far field. The far-field approximation is given by the large argument expansion for the Hankel function, given in Eq. (9.9) [DLMF (2021) 10.2.6].

$$G(\omega,\vec{x},\vec{x}_n) = \frac{i}{4}H_0^2\left(\frac{\omega}{c}|\vec{x}-\vec{x}_n|\right) \approx \frac{exp\left(i\left(\frac{\omega}{c}|\vec{x}-\vec{x}_n| + \frac{3\pi}{4}\right)\right)}{\sqrt{\frac{\pi\omega|\vec{x}-\vec{x}_n|}{2c}}} \tag{9.9}$$

Here, the Hankel function is seen to approximate a plane wave in the far field. The bandwidth-average of a frequency-interferometric product of the Green's function is given in Eq. (9.10).

$$\begin{aligned}\left\langle G^*(\omega_-,\vec{x},\vec{x}_m)G(\omega_+,\vec{x},\vec{x}_n)\right\rangle &= \frac{1}{|\Omega|}\int_\Omega d\omega G^*(\omega_-,\vec{x},\vec{x}_m)G(\omega_+,\vec{x},\vec{x}_n)\\ &\approx \frac{2c}{\pi|\Omega|\sqrt{|\vec{x}-\vec{x}_m||\vec{x}-\vec{x}_n|}}\int_\Omega d\omega\frac{exp\left(\frac{i}{c}\left(\omega_-|\vec{x}-\vec{x}_m| - \omega_+|\vec{x}-\vec{x}_n|\right)\right)}{\omega\sqrt{1-\frac{\Delta\omega^2}{\omega^2}}}\\ = \frac{2cexp\left(\frac{i\Delta\omega}{2c}(|\vec{x}-\vec{x}_n| + |\vec{x}-\vec{x}_m|)\right)}{\pi|\Omega|\sqrt{|\vec{x}-\vec{x}_m||\vec{x}-\vec{x}_n|}}&\int_\Omega d\omega\frac{exp\left(\frac{i\omega}{c}\left(|\vec{x}-\vec{x}_m| - |\vec{x}-\vec{x}_n|\right)\right)}{\omega\sqrt{1-\frac{\Delta\omega^2}{\omega^2}}}\end{aligned} \tag{9.10}$$

This equation can be represented as a product of two types of quantities: quantities that are expected to be constant with respect to the bandwidth-average, and quantities that will not change over the bandwidth average. Of these quantities, only the second quantity can cancel an undesirable term. This decomposition of Eq. (9.10) is given in Eq. (9.11).

$$\left\langle G^*(\omega_-,\vec{x},\vec{x}_m)G(\omega_+,\vec{x},\vec{x}_n)\right\rangle = C_{mn}\int_\Omega d\omega\frac{exp\left(\frac{i\omega}{c}\left(|\vec{x}-\vec{x}_m| - |\vec{x}-\vec{x}_n|\right)\right)}{\omega\sqrt{1-\frac{\Delta\omega^2}{\omega^2}}} \tag{9.11}$$

When the difference frequency is much smaller than all in-band frequencies, as is often the case in autoproduct processing, this equation can be understood as an exponential integral Ei [DLMF (2021) 6.12.2], that can be approximated using the method of stationary phase. In this case, it is seen that this term will go to zero with sufficient bandwidth averaging provided that the basis functions at $\vec{x}_m$,and $\vec{x}_n$ are at least one wavelength from one another at the in-band frequency.

However, the Method of Moments represents scatterers as basis functions that are, at most, a

fraction of a wavelength in size. Therefore, this criterion is expected to be violated for many basis functions, and that cross-terms in the frequency-difference autoproduct are expected to be non-zero for any amount of bandwidth averaging. Further, the spatial and frequency coherence that exists between currents, as defined in Eq. (9.7), is expected to be greatest when the basis functions are nearby one another. This consideration poses a natural question with respect to the performance of autoproduct beamforming vs. field beamforming: which process is more susceptible to the cross-terms in the scattering equations. This question will be addressed using simulated environments in Sections 9.3 and 9.4.

Source localization calculations in this chapter will be undertaken using cylindrical wave beamforming. This decision is made in an attempt to make the results more comparable to [Douglass & Dowling (2019)] that used spherical wave beamforming. Beamforming is similar to the Matched Field Processing techniques that are described in Chapter 5, but the weight (replica) vector is computed from a normalized Green's function. This is given in Eq. (9.12).

$$B(\omega, \vec{x}_t) = \frac{|w^*(\omega, \vec{x}_t, \vec{x}_n) E_{v,h}(\omega, \vec{x}_n)|}{\sqrt{|w^*(\omega, \vec{x}_t, \vec{x}_n) w(\omega, \vec{x}_t, \vec{x}_n)|^2} \sqrt{|E^*_{v,h}(\omega, \vec{x}_n) E_{v,h}(\omega, \vec{x}_n)|^2}} \tag{9.12}$$

Here, B is the ambiguity surface, that indicates the level of matching between the calculated weight vector w and (simulated) measured field quantity E with a given polarization. This matching is computed over an indexed array of receivers that measure at spatial locations $\vec{x}_n$, and is varied over test source locations $\vec{x}_t$. The replica vector w is a free-space Green's function for the medium. Given that two-dimensional propagation is analyzed in this chapter, this will be represented by a two-dimensional Green's function, given in Eq. (9.13).

$$w(\omega, \vec{x}_t, \vec{x}_n) = \frac{-i}{4} H_0^2\left(\frac{\omega}{c}\left|\vec{x}_t - \vec{x}_n\right|\right) \tag{9.13}$$

Notably, this cylindrical wave function is the same for both polarizations. Frequency-difference beamforming will utilize the exact same formulation as spherical wave beamforming, with the autoproduct replacing the electric field and all matching computed at the difference frequency.

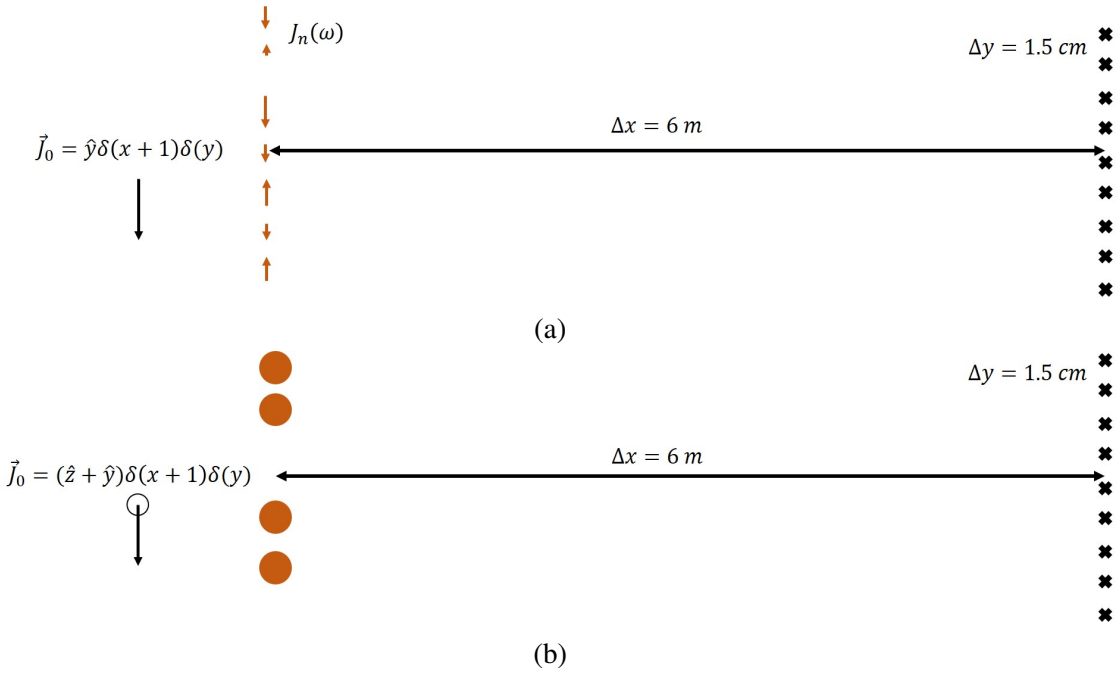

Figure 9.1: Two-dimensional rendering of phase screen for (a) no coherence in current basis functions (b) coherence is defined by the Method of Moments

9.3 Effect of a Phase Screen on Autoproduct Propagation

The field and autoproduct scattered by a scintillating random medium is explored first using a very basic model for a random phase screen. The random phase screen model starts by assuming that a source sits on one side of a collection of scatterers and emits an impulsive signal. This signal, as well as the field scattered by the phase screen, is measured in the microwave frequencies on the other side of the screen. For the purpose of this experiment frequencies $8 \leq f \leq 16$ GHz, will be investigated. The two phase screen experiments that will be analyzed here are shown in Fig. 9.1.

Fig. 9.1 shows two different phase screen models that will be analyzed here. The first, shown in Fig. 9.1a, assumes that all of the currents that are induced on the phase screen will completely lack spatial and frequency coherence. The second, shown in Fig. 9.1b, assumes that scatterers are infinite cylinders, and currents that are induced on these scatterers will have some coherence in space and frequency that are defined by physics. The first of these models is expected to show significant utility for autoproduct-processing, where the bandwidth-averaging step can be used to

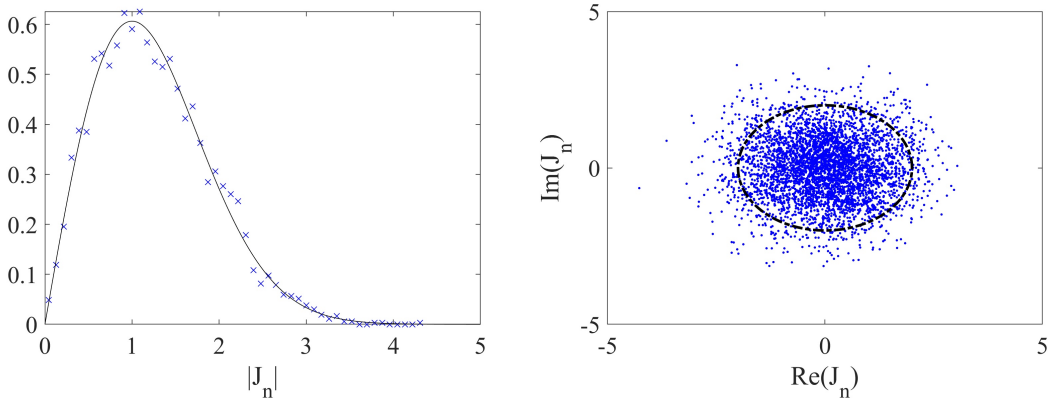

Figure 9.2: Example random currents placed on the phase screen for distortion of the signal, (a) probability density function of current magnitude that has the same expected power as the source, (b) magnitude and phase of random currents.

cancel all cross-terms in the scattered field as the condition given in Eq. (9.7) will be explicitly satisfied for all currents in the experiment except the source current. The second of these models works by relaxing the random induced current model, to determine the extent to which coherence of the scattered field is expected to affect autoproduct-processing.

To investigate the first model, the induced currents are generated to have zero-mean Gaussian random real and imaginary parts at every frequency. The standard deviation of these currents will be defined relative to the source current, and will be varied to determine the extent to which these random currents distort the autoproduct and electric field. Example randomly generated currents are shown, in magnitude and phase plots, in Fig. 9.2.

The randomly generated currents are placed at 121 random points in y in the scattering plane at $x = 0$, for frequencies $f = 8, 8.1, \ldots, 16$ GHz. Fig. 9.2a shows a probability-density-function of the magnitudes of these currents generated with a standard deviation of unity, fitted to a Rayleigh distribution [Jackson, J.D. (1999)]. Here, it is seen that the standard deviation of the real and imaginary parts of the currents is equal to the mode of the induced magnitude. Fig. 9.2b shows the real and imaginary parts of the currents, and demonstrates that the generated currents are uniformly distributed in phase.

The autoproduct and electric field for this model are explicitly calculated first to determine

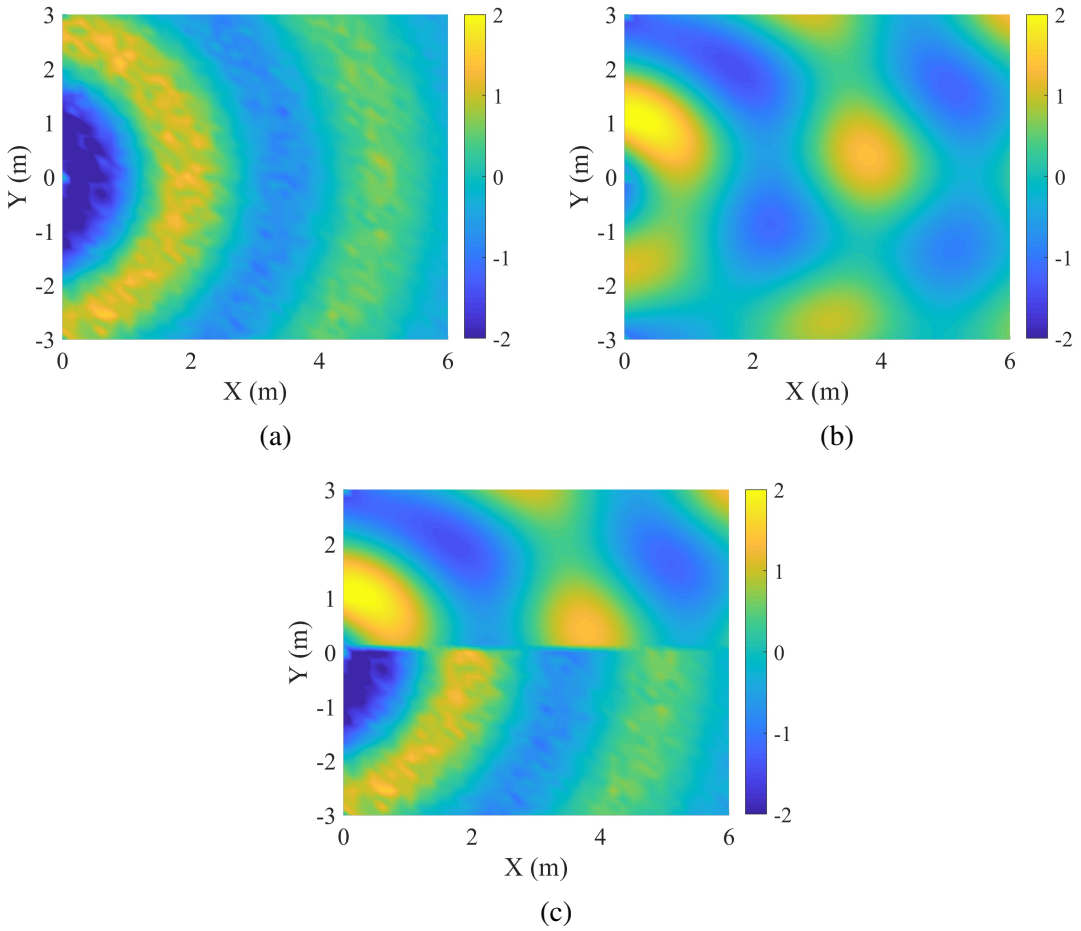

Figure 9.3: Real part of the (a) autoproduct (b) out-of-band field (c) compared autoproduct and out-of-band field for phase screen (at x=0 plane) current basis functions with no coherence

the extent to which the autoproduct emulates an out-of-band electric field. In the absence of the phase screen, the correspondence between an autoproduct and an electric field at $\Delta\omega$ is seen to be extremely good for many difference frequencies, with the exception of a constant phase shift of $\frac{3\pi}{4}$ radians. This phase shift is understood to arise from the autoproduct processing, and can be seen in Eq. (9.9) and Eq. (9.10). Given that preliminary success, the autoproduct and the out-of-band field are next calculated at a (difference) frequency of 1 GHz. To calculate the autoproduct, the electric field is calculated for all frequencies $f = 8, 8.1, \ldots, 12$ GHz with an impulsive source current $J_0(\omega) = 1$ for all frequencies. Currents in the phase screen with smaller magnitudes, $\langle |J_n| \rangle = 0.1 J_0$, are generated to distort the signal at all in-band frequencies and at the difference frequency. The result of this simulation is shown in Fig. 9.3.

Multiple things can be seen from these results. Firstly, it is seen that the bandwidth-averaged frequency-difference autoproduct of an electric field, shown in Fig. 9.3a, is more symmetric than the out-of-band electric field shown in Fig. 9.3b. This can be understood as the "speckle" of the autoproduct is occurring on a much smaller scale than that of the out-of-band field. These two quantities are compared in Fig. 9.3c, where the $\frac{3\pi}{4}$ radian shift between the autoproduct and the out-of-band field is evident, and will be removed in future comparisons. To make the comparison between these two field quantities more evident, they are both normalized to have an RMS magnitude of 2. This result, generated from a model that is explicitly defined to have no coherence, shows that the autoproduct is expected to cancel a distorting scattered field better than a time-harmonic out-of-band field.

This model was further interrogated to determine whether or not autoproduct-processing is expected to improve beamforming results in this phase screen experiment. In particular, this improvement is quantified by cross-correlating calculated autoproducts and time-harmonic electric fields with analogous field quantities calculated without the presence of scatterers, similar to the cross-correlation in Chapter 3. Here, the cross-correlation is calculated for in-band frequency set $f = 8, 8.1, \ldots, 16$ GHz and the autoproduct is calculated for all admissible difference frequencies, $\Delta f = 0.1, 0.2, \ldots, 8$ GHz. The results of this cross-correlation simulation are shown in Fig. 9.4, for phase screen currents with two different magnitude expectations.

Fig. 9.4 shows that the autoproduct has higher cross-correlation than the in-band electric field provided that sufficient bandwidth averaging is available. When little bandwidth averaging is available, as is seen for $\Delta f > 7$ GHz, this cross-correlation decreases. Further, the bandwidth-average leads to more consistent cross-correlation behavior for all computed difference frequencies. This result demonstrates that autoproduct-processing is expected to improve upon in-band processing techniques when the measurements are corrupted by truly incoherent scattered fields. This is further investigated for several more relative magnitudes in Fig. 9.5.

The average cross-correlation between the frequency-difference autoproduct at all difference frequencies and the electric field at all measured frequencies is explored for varying expected

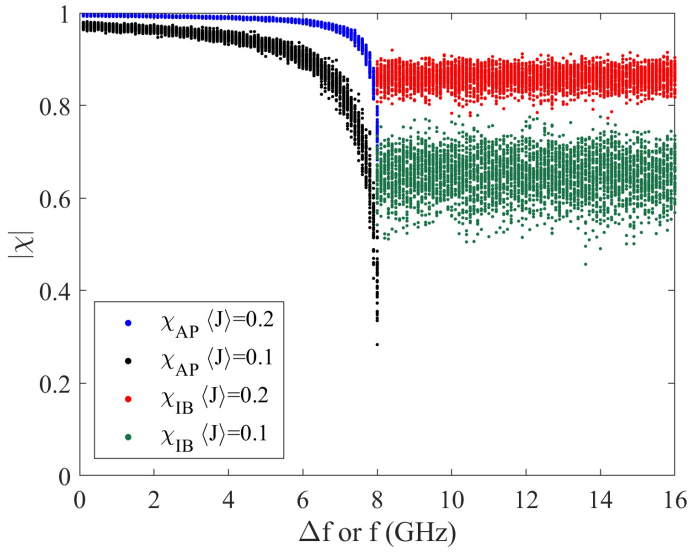

Figure 9.4: Cross-correlation between autoproducts and electric fields at the difference frequency and electric fields at in-band frequencies in the presence of a phase screen of currents that are incoherent in space and frequency.

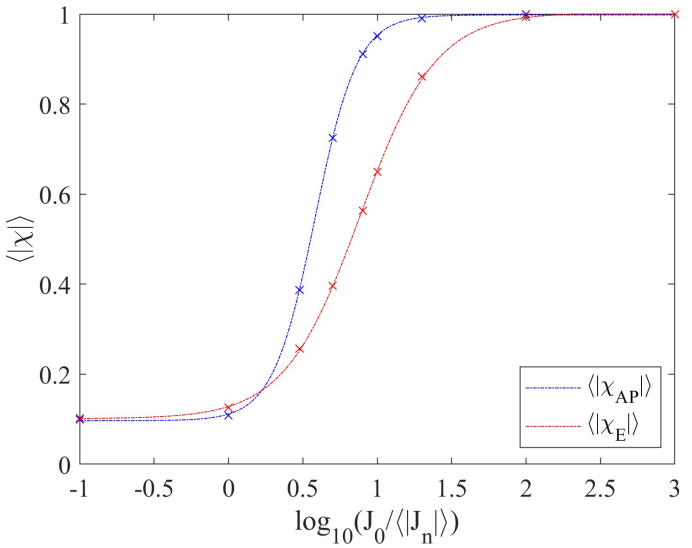

Figure 9.5: Average autoproduct to out-of-band electric field and in-band electric field cross correlation in the presence of a phase screen made up of incoherent current basis functions of varying magnitude. Results fitted to sigmoids, each curve runs from 1 to 0.1, autoproduct attains average cross-correlation of 0.5 at $\langle |J_n| \rangle = 0.58 J_0$ and has fall-off rate of 0.14 in the same (relative current) metric, electric field attains average cross-correlation of 0.5 at $\langle |J_n| \rangle = 0.89$ and has fall-off rate of 0.26 in the same metric.

scattering currents. For small amounts of induced current, $J_n << J_0$, the cross-correlation of both electric fields and autoproducts is found to be high, and the cross-correlation is found to decrease significantly for large amounts of induced current, $J_0 << \langle|J_n|\rangle$, as expected. Between these two regimes, the electric field cross-correlation, shown in red, is seen to fall off sooner $J_0 = 20\langle|J_n|\rangle$ than the autoproduct cross-correlation. This result suggests that frequency-difference beamforming in scattering random media may be superior to beamforming using an electric field, provided that the sources of the scattered field are sufficiently incoherent.

The expected lack of coherence of the field scattered by the random phase screen is evaluated next. The coherence of the scattered field will be enforced here using the Method of Moments, which ought to mimic the coherence imposed by physics in a scattering problem. The Method of Moments code here is a two-dimensional code based on [Jin, J. (2010)]. First, the operation of the code is validated, for both electrically large and electrically small conducting cylinders in Fig. 9.6.

Here, the currents induced on a conducting cylinder by incident plane waves are computed. Fig. 9.6a shows the field induced on a cylinder at resonance, $r = \lambda$, by a Transverse Electric (TE) polarized plane wave. Fig. 9.6b shows current induced on a cylinder of the same size by a Transverse Magnetic (TM) polarized plane wave, Fig. 9.6c and 9.6d show the equivalent currents induced when the cylinder is much smaller than the wavelength of the incident field, $r = \lambda/10$. These plots are shown to validate the operation of the code, as they resemble equivalent plots shown in [Jin, J. (2010)]. Currents induced on these cylinders, particularly the currents in Fig. 9.6a, are seen to have significant spatial coherence over the scatterer, violating the assumption in Eq. (9.7).

The scattered electric field at the difference frequency and the frequency-difference autoproduct of these scatterers is investigated next, to determine how spatial coherence of induced currents affects each field quantity. For this purpose, a difference frequency of $\Delta f = 1$ GHz is chosen for a scatterer with a radius $r = 0.03 \approx \Delta\lambda/10$. The in-band electric field is computed for frequencies $f = 8, 8.1, \ldots, 16$ GHz. The total electric field and total autoproduct for TE and TM polarized incident fields are shown in Fig. 9.7, also compared to a time-harmonic in-band electric field.

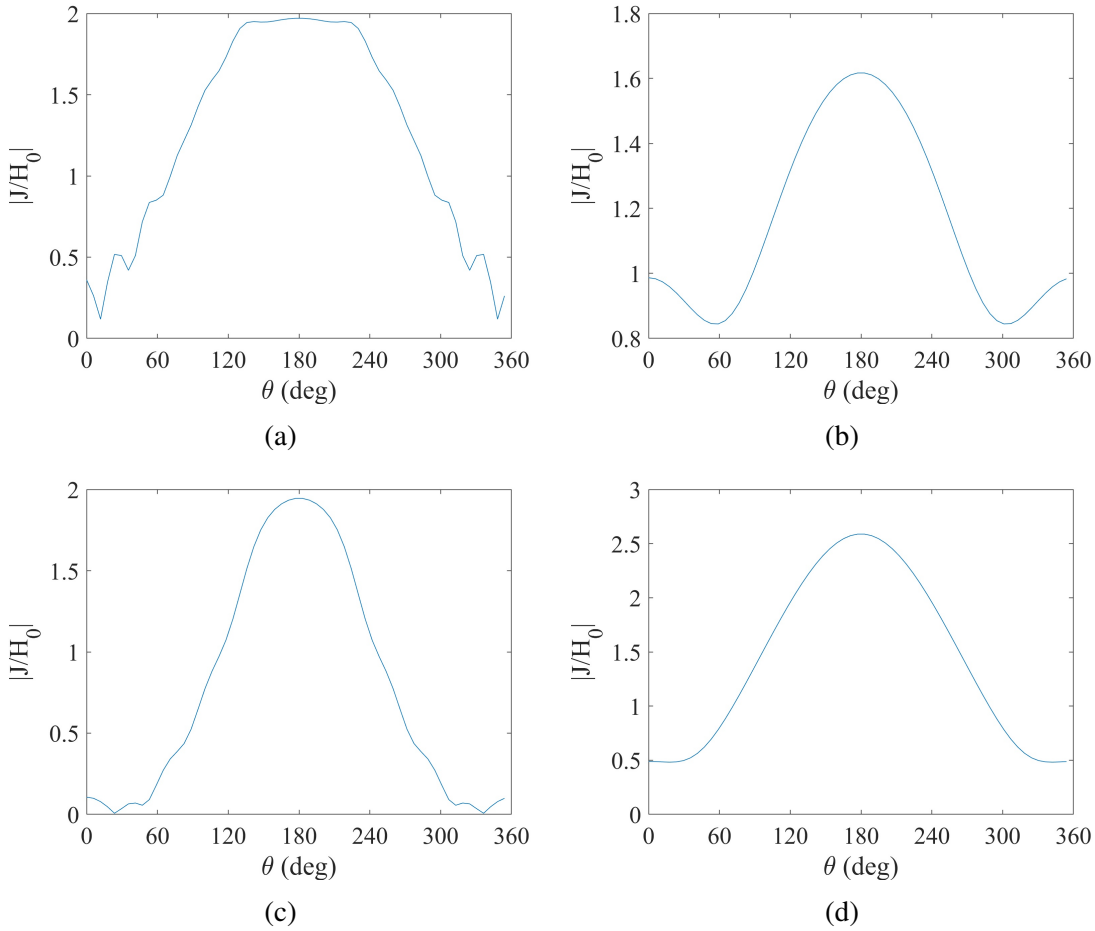

Figure 9.6: (a)TE and (b) TM currents excited on a conducting cylinder at resonance, (c) TE and (d) TM currents induced on an electrically small cylinder ($r = \lambda/10$).

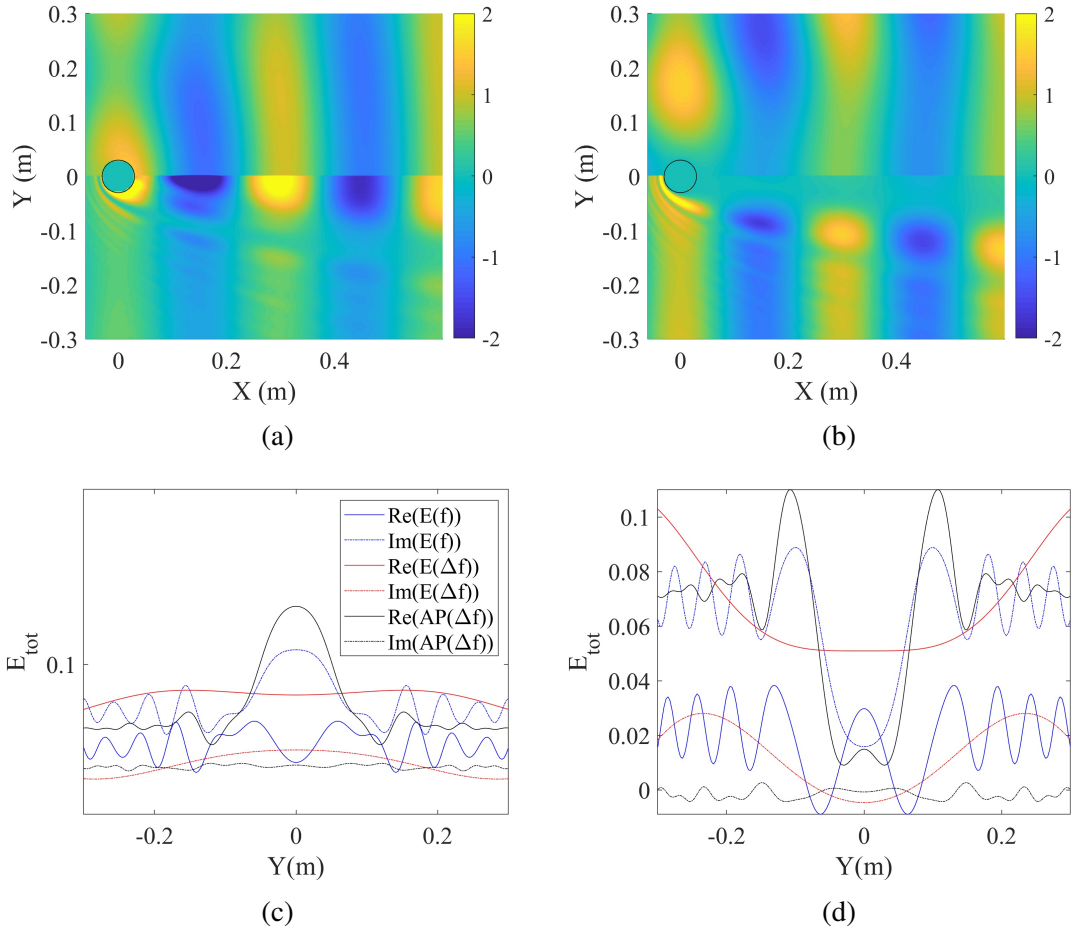

Figure 9.7: Comparison of total autoproduct (bottom half) and electric field (top half) at (difference) frequency 1 GHz for incident (a) TE and (b) TM polarized incident fields over a nearby area. Comparison of total autoproduct, out-of-band electric fields, and in-band electric field at x=0.6 m plane for (c) TE and (d) TM polarized incident fields. Out-of-band field quantities are shown at Δf = 1 GHz, in-band fields shown at f = 12 GHz.

The total field and autoproduct for both a TE, shown in Fig. 9.7a, and a TM, shown in Fig. 9.7b, are shown to have excellent correspondence overall. The difference between the autoproduct and field is most pronounced in the shadowed region of the cylinder, seen just below the cylinder in each plot where the field scattered by an electrically large cylinder is similar in magnitude to the incident field. Additionally, striations are seen in the autoproduct of both plots that are not replicated in the electric field. These striations almost certainly arise from cross-terms in the scattered field that are imperfectly cancelled at these points. These striations are seen to generally decrease in magnitude relative to the incident field far from the cylinder. Normalized versions of these field quantities are compared in Fig. 9.7c and 9.7d, that further bears out that the largest difference between the autoproduct and the out-of-band field is seen in the shadowed region of the cylinder.

The effect that these coherences have on cross-correlation in the presence of a distorting, random phase screen is next investigated. Here, a phase screen that is randomly populated with 5 cylinders of size $r = 0.3$ m is placed in the $x = 0$ plane. Cylinders are generated to be placed within 20 meters of the center of the phase screen, that is defined as the origin of the scattering problem. An impulsive source current with unity magnitude is placed one meter from the center of the screen, at $\{x, y\} = 0, -1$. The total field for this scattering problem is computed for frequencies $f = 8, 8.1, \ldots, 16$ GHz in the $y = 20$ cm plane. The cross-correlation between the (undistorted) incident field and the (distorted) total field is computed for all relevant in-band and difference frequencies, and is shown in Fig. 9.8.

The average cross-correlation is shown in Fig. 9.8 for TE and TM source currents in the presence of 50 randomly generated phase screens. Two observable features come from this plot: first, that scattering more significantly effects TE polarized waves, and, second, that autoproduct cross-correlation remains better than (in-band) electric field cross correlation given sufficient difference frequency averaging. This suggests that frequency-differencing may offer useful insight into electromagnetic scattering in random media that is not available from in-band processing.

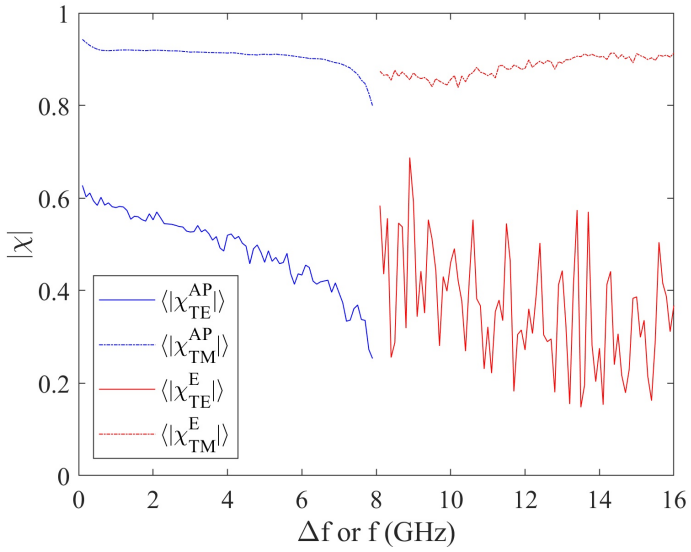

Figure 9.8: Autoproduct and electric field cross correlation in the presence of a random phase screen composed entirely of conducting cylinders.

9.4 Autoproduct and Field Propagation in a Collection of Metallic Scatterers

The utility of autoproduct-processing in electromagnetic remote sensing of scattering random media is assessed using spherical wave beamforming. This algorithm is chosen to mimic the study given in underwater acoustics in [Douglass & Dowling (2019)] and to assess whether or not the results of this study are also available in electromagnetic remote sensing. To assess the effect that this type of scattering will have on beamforming, an impulsive current source $J = 1$, will be placed at spatial location $(x, y) = (0, -1)$. Varying numbers of cylinders of radius $r = 0.03$ m, chosen to be electrically large at transmitting frequencies, will randomly populate the local area $0 \leq x \leq 5$, $-4.5 \leq y \leq 4.5$, and the total electric field will be measured in the $x = 7$ plane. An example schematic of this environment, with 9 cylinders, is shown in Fig. 9.9.

The total field will be calculated in this environment to assess the effect that these scatterers have on in-band and frequency-difference beamforming.

The initial simulation of beamforming is undertaken in an ideal environment with no scatterers

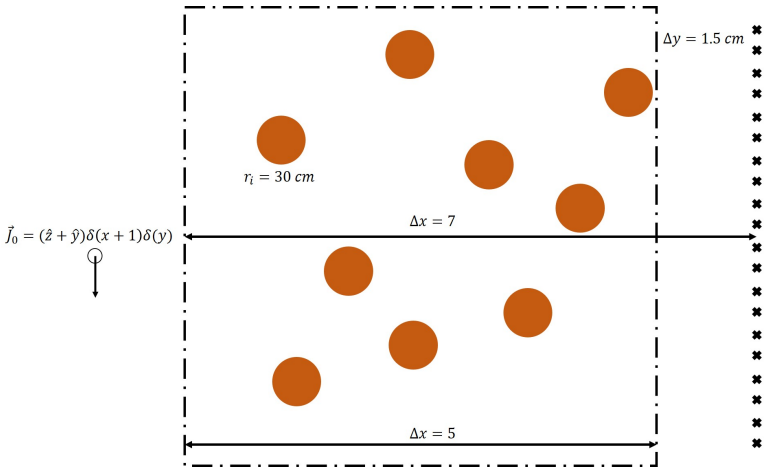

Figure 9.9: Artistic rendering of a random, volume scattering environment with 9 cylinders of size $r_i = 30$ cm placed inside a box of size $6 \times 5\ m^2$. Source current (doubly polarized) is placed at $\{x, y\} = \{-1, 0\}$. The total field of this environment will be calculated at the observer points (shown with crosses) on at $x = 7$. Will be solved at frequency $8 \leq f \leq 16$ GHz

present. This step is undertaken to ascertain that both forms of beamforming are working using polarized waves. Here, electric fields are computed at all relevant frequencies, $f = 8, 8.1, \ldots 16$ GHz, and the autoproduct is computed for difference frequencies $\Delta f = 0.1, 0.2, \ldots, 8GHz$. Beamforming calculations are undertaken to localize the scatterer within the plane defined by $-3 \leq y \leq 3$ and $-6 \leq x \leq 6$ meters for source currents of both TE and TM polarizations. The resulting ambiguity surfaces are shown in Fig. 9.10.

These results show success for both in-band and frequency-difference beamforming. All results show a strong peak at the correction location, and no other coherent peak is seen in any ambiguity surface. The peak seen in the in-band results, shown in Fig. 9.10b and 9.10d, is much smaller than the peak given by frequency-differencing results. This difference is expected, as the autoproduct has a lower frequency, and therefore has lower spatial resolution.

Given that the performance of both in-band and frequency-difference beamforming is confirmed in the ideal case, a similar simulation is undertaken using 5 randomly placed conducting cylinders to distort the field for both polarizations. This number of cylinders is chosen because this is found to cause in-band beamforming results to fail for TM polarization. The result of this beamforming simulation is shown in Fig. 9.11.

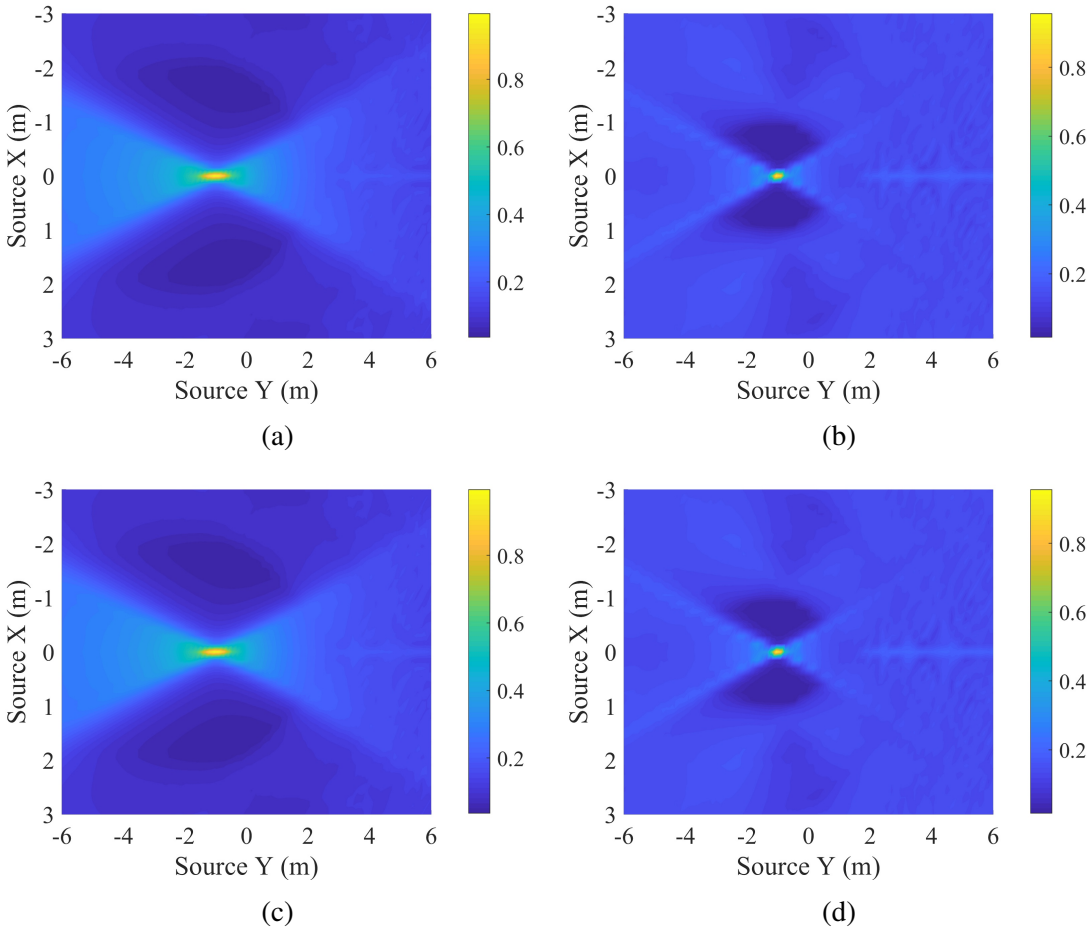

Figure 9.10: Result of ideal cylindrical wave beamforming simulation using (a) TE autoproduct, (b) TE in-band field, (c) TM autoproduct, (d) TM in-band field.

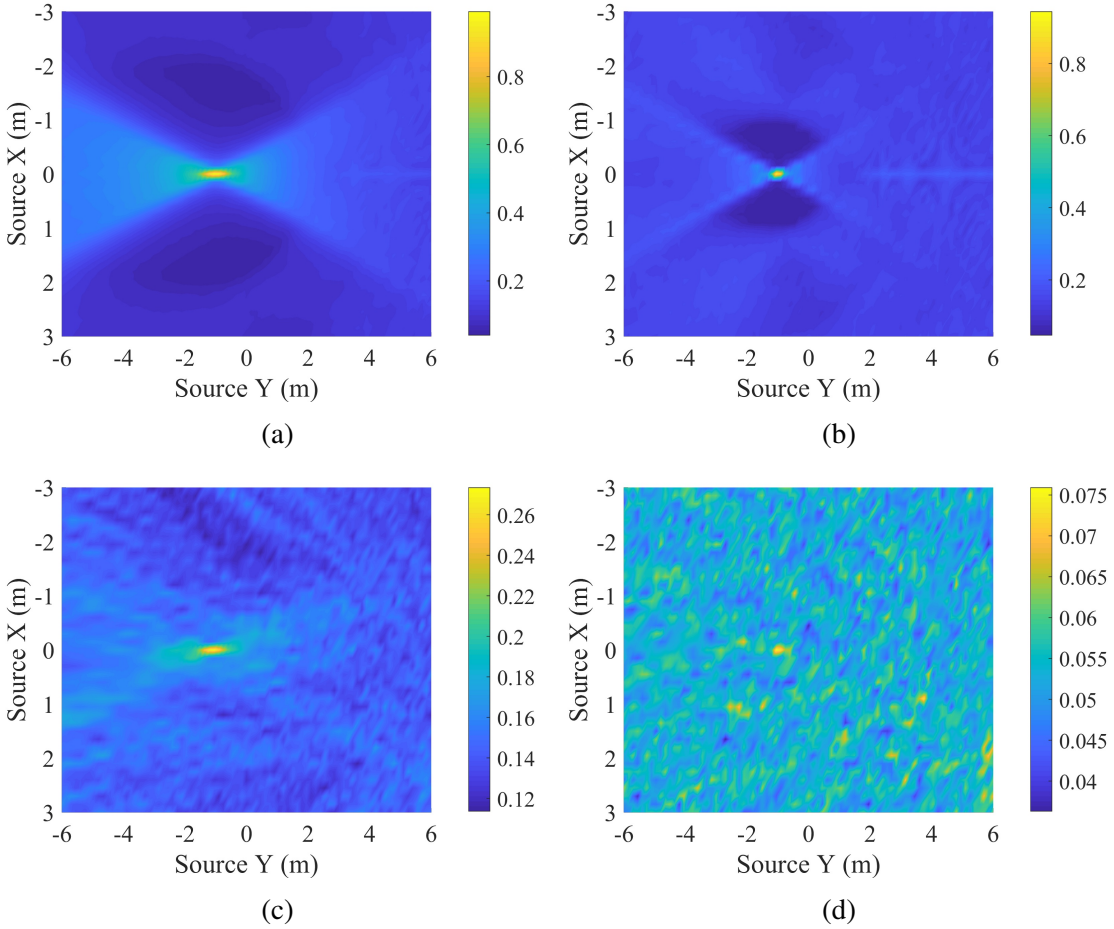

Figure 9.11: Result of cylindrical wave beamforming simulation with 5 scatterers corrupting the forward signal for (a) TE frequency-difference beamforming, (b) TE in-band beamforming,(c) TM frequency-difference beamforming,(d) TM in-band beamforming.

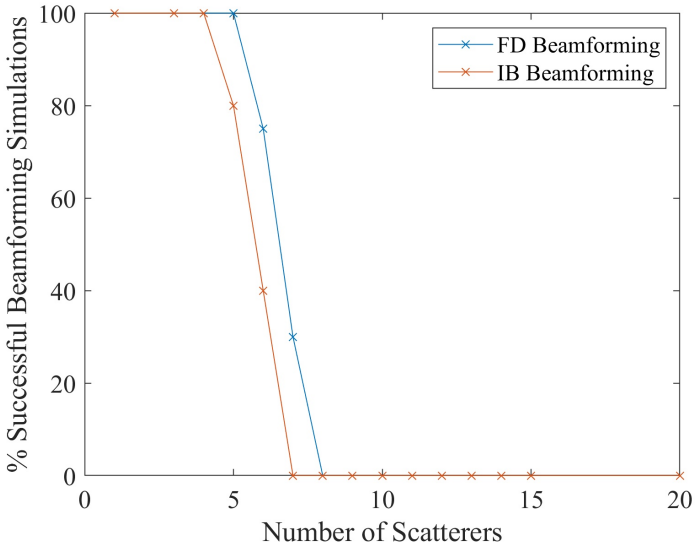

Figure 9.12: Success rate for simulated cylindrical wave beamforming for TM polarized incident wave with varied numbers of scatterers in the medium

Here, it is seen that frequency-difference beamforming, shown in Fig. 9.11c, actually outperforms in-band beamforming, shown in Fig. 9.11d, for a TM polarized source. This number of scatterers in the medium is not found to significantly affect the performance of spherical wave beamforming for a TE polarized source, shown in Fig. 9.11a and 9.11b. The difference between the different polarizations likely arises because the electric field vector runs along the infinite dimension in the TM case. While the in-band results for a TM polarized source do show a relatively strong peak in approximately the location of the source, several other peaks are observed in other parts of the matching surface that are larger than this one. The frequency-differencing results, meanwhile, show no such competing peaks. The performance of spherical wave beamforming, for TM polarized sources, is further investigated for varying numbers of cylinders included to distort the field. The result of this is shown in Fig. 9.12.

Here, it is seen that the improvement offered by frequency-differencing is marginal. However, this result demonstrates that there is utility to be offered to the field of passive electromagnetic remote sensing by autoproduct-processing algorithms.

9.5 Conclusion

This chapter offers three conclusions that are unique to this thesis. Firstly, this chapter defines the autoproduct that can be calculated from a measured wave with some polarization as a dyadic product of all elements of the wave. While the cross-polarized terms of this tensor are not investigated in this chapter, it is possible that they will lend scientific insight to frequency-differencing that isn't available in scalar field processing. Secondly, this thesis extends previous analyses of the existence of cross-terms in scattering environments. Previous analyses of this subject focused on analyzing Mie series solutions and accounted for inter-particle interaction using the Born approximation. This analysis explicitly focuses on the coherence of currents induced on the surface of a scatterer to better understand the way in which autoproduct cross-terms arise in frequency-differencing. These cross-terms are found to not average to zero in the face of bandwidth-averaging when the currents are within one another's near field. Secondly, the effect that scattered fields have on distorting an autoproduct in scattering environments is investigated in three different environments: a random phase screen where induced currents are completely incoherent, a random phase screen where induced currents have coherence defined by the Method of Moments, and a random medium with cylinders distributed over a small area. In all three of these environments, frequency-differencing methods are found to give results that are equal to or better than those offered by in-band methods.

CHAPTER 10

Conclusions and Future Work

10.1 Conclusions

1. The studies on the frequency-difference autoproduct conclude that this quantity exists and can be measured and computed from any field quantity that has some bandwidth. The definitions of the autoproduct formed from scalar, given in Chapter 2, and vector, given in Chapter 9, waves are applied in Chapters 3,4,5,9 to determine their applicability in both acoustic and electromagnetic remote sensing. The cross-domain applicability of autoproduct-processing suggests that these techniques may be useful in remote sensing systems that operate using waves that arise from other physical phenomena. These methods, unfortunately, cannot be applied if a Fourier transform of a measured wave quantity cannot be calculated. Therefore, these methods are not expected to have any significant utility at frequencies where the phase of a measurement cannot be accurately determined.

2. Prior to the work outlined in this thesis, the frequency-difference autoproduct formed from an acoustic pressure field was always thought of as resembling a pressure field at the difference frequency used to calculate the autoproduct. The results contained in Chapters 3-5 demonstrate that an autoproduct always fundamentally differs from a pressure field at the difference frequency, and that this difference is significant when investigating the autoproduct propagating in a refracting waveguide. While the difference between an autoproduct and a pressure field propagating in a refracting waveguide has been investigated before this thesis,

these differences were first measured in this thesis.

This study is the first of its kind to quantify the differences between an autoproduct and an out-of-band pressure field and to demonstrate that the comparison (or cross-correlation) between a measured autoproduct and out-of-band pressure field is both spatially unstable and unstable with respect to difference frequency even in the absence of environmental mismatch. This lack of stability in the absence of environmental mismatch limits the utility of frequency-difference field processing over long ranges in refracting waveguides.

3. The results contained in Chapters 3 and 5 of this thesis contain the most complete documentation to date of the stability of the frequency-difference autoproduct in the face of environmental mismatch. Further, despite the fundamental differences between an autoproduct and an out-of-band pressure field, the autoproduct is seen to lose coherence and stability in the face of environmental mismatch in the same way as does an out-of-band pressure field. This observation demonstrates the utility of using autoproduct-processing to investigate field quantities that are propagating in random media that are uncertainly known, scintillating, or both. In particular, autoproduct cross-correlation is found to have significant spatiotemporal- and difference-frequency-coherence when propagating over long (hundreds of kilometer) distances in the deep ocean. The cross-correlation study results, given in Chapter 3, show that both the magnitude and phase of cross-correlation can be computed consistently for many measurements of a field quantity that was previously thought to have little or no coherence in the frequency domain.

   Further, this study is the first of its kind to successfully localize sources transmitting at high (hundreds of Hz) frequencies over long (hundreds of km) ranges in the deep ocean using frequency-domain methods. These results are shown in Chapter 5 to be robust and predictable across a wide difference frequency bandwidth.

4. This document also investigates the existence and form of two types of autoproduct cross-terms, those related to a signal and those related to the presence of a strong interfering source,

that arise incidentally as a part of autoproduct-processing algorithms. These cross-terms are generally considered undesirable in autoproduct-processing, and removing them coherently is found to be challenging when operating in an uncertain propagation environment. Despite this complication, signal-cross-terms are found to lack coherence and, therefore, to be removable using noise rejection techniques. Further, the effect that signal-cross-terms have on nonlinear signal processing algorithms are found to be minimal. Interferer-cross-terms are found to be more challenging to remove and to degrade performance of autoproduct-processors. This thesis determines that this performance degradation is minimal when using a large array.

5. This study also determines that Monte Carlo simulation can be used in conjunction with the Method of Moments to solve for the coherent portion of a scattering matrix of a collection of electrically large, interacting metallic particles. The coherent portion of the scattering matrices are shown, in Chapters 7 and 8, to be related to the extinction matrix, that governs coherent field quantity absorption, of such a random medium. While similar methods have been investigated before, this is the first study that demonstrates the existence of an effective homogeneous dielectric medium in three-dimensional propagation through a random medium composed of electrically large, interacting scatterers. The existence of this effective medium is proven using an inverse scattering technique. This inverse scattering problem is shown to be well posed for random media composed of many types of scatterers filling the media at varying densities.

6. Propagation in a medium composed of discrete scatterers is further investigated using Monte Carlo simulation in conjunction with the Method of Moments to determine the incoherent portion of a scattering matrix of a medium composed of electrically large, interacting scatterers. The incoherent portion of the scattering matrix is postulated to be related to the phase function of the medium, that governs incoherent emission of absorbed power in Radiative Transfer. The incoherent scattering matrix is shown to converge, in a pointwise sense, to the

prediction of a phase matrix that is made using single scattering theory. This document represents the first time that a phase function has been predicted using Monte Carlo simulation for a random medium of this type.

7. Given the capacity of Monte Carlo simulation to calculate the extinction and phase matrices of a random medium, this technique can be used to understand the applicability of existing theoretical, empirical, and phenomenological models to varying problems in random media propagation. In particular, the applicability of single scattering models in interacting random media is assessed in Chapter 8. Further, Monte Carlo simulation is used as the basis for predicting new macro-models that quantify extinction and emission in interacting, chaff-like random media.

10.2 Future Work

The nonlinear signal processing algorithms provided in Chapters 2,3,4,5 and 9 of this thesis demonstrate the validity of using autoproduct-processing for solving problems in acoustic and electromagnetic remote sensing. However, predicting (and therefore matching) the magnitude of an autoproduct that has propagated over long distances or through an uncertain environment is demonstrated to be a shortcoming of current autoproduct theory. Therefore, a probabilistic investigation of autoproduct magnitude in an uncertain environment is an obvious extension of the work contained herein. Another follow-on to this work would be to investigate whether autoproduct-processing techniques can be used for source localization in the Arctic Ocean, or whether other environmental information can be inferred using autoproduct-processing. The effect that several phenomena, such as frequency dispersion and reflection from a layered random medium, has on the frequency-difference autoproduct has not been investigated as of the writing of this thesis, and could offer useful insight into other applications of this method. Further, the autoproduct may be of some use in solving other signal processing problems, such as detection or classification.

While the utility of Monte Carlo simulation as it relates to studying the extinction and phase matrices of complex random media is investigated in Chapters 6,7 and 8, these predictions currently rest only on numerical analysis. Therefore, measuring the predictions offered by Monte Carlo simulation would be useful. Further, while this thesis proposes and uses buffer zone averaging to compute the phase function for a random medium to remove several sources of numerical noise, these predictions are only shown to be self-consistent and repeatable. The validity of using this method to predict a phase function has not been investigated from either a theoretical or an experimental standpoint. On top of this, the full vector formulation of Radiative Transfer has not yet been computed using Monte Carlo simulation. While this method ought to be able to calculate the full polarimetric response of a random medium, this calculation has not yet been completed. In addition to calculating the full polarimetric response of the medium, a full three-dimensional prediction of the phase function scattered by a random medium would be of interest in solving higher-order Radiative Transfer theory.

Appendices

Appendix A

Fitting Coefficients for Incoherent Scattering Coefficient of Chaff

This appendix contains the Associated Legendre Function coefficients for fitting the incoherent scattering coefficient of a chaff-like random medium. These coefficients are related to the content given in Chapter 8. The incoherent scattering coefficient is computed using Monte Carlo simulation in conjunction with the Method of Moments. The media that are considered have wire constituent particles of length $0.5\lambda \leq l \leq 2\lambda$ and radius $r_i = 0.05\lambda$ and are calculated at X-Band ($\lambda = 3$ cm). The wires occupy the media in question at number densities $0 < n \leq 5$ particles per cubic wavelength. The incoherent scattering coefficient is then fit to Associated Legendre Functions [Jackson, J.D. (1999)] with $m = 0$ in the principal $\phi-$plane of each scattered polarization. The polarization convention of the scattering coefficient is defined using the Forward Scattering Alignment convention [Ulaby, F.T. & Long, D.G. (2014)]. For all media, five Associated Legendre coefficients are found to represent the calculated scattering coefficient. This convergence of the fitting function is judged in two ways: first, higher coefficients are found to be smaller than $5 * 10^{-9}$, which gives an error that is at most one part in one thousand for the fit, second, that the Euclidean difference between the calculated incoherent scattering coefficient and the function calculated using the Associated Legendre function coefficients is less than 0.01. Each of these coefficients is given in Tables A.1 - A.16.

	$c_{00} \times 10^6$	$c_{10} \times 10^6$	$c_{20} \times 10^6$	$c_{30} \times 10^6$	$c_{40} \times 10^6$
$\sigma_{vv}^{inc}(n=0)$	3.65	-0.40	2.58	-0.60	0.00
$\sigma_{vv}^{inc}(n=1)$	6.55	-0.79	2.88	0.00	0.00
$\sigma_{vv}^{inc}(n=2)$	5.24	-0.59	1.57	0.00	0.00
$\sigma_{vv}^{inc}(n=3)$	4.49	-0.39	0.95	0.00	0.00
$\sigma_{vv}^{inc}(n=4)$	4.16	-0.30	0.57	0.00	0.00
$\sigma_{vv}^{inc}(n=5)$	3.80	-0.22	0.38	0.00	0.00
$\sigma_{hv}^{inc}(n=0)$	6.72	-0.55	-0.53	0.00	0.00
$\sigma_{hv}^{inc}(n=1)$	9.75	-1.10	0.00	0.00	0.00
$\sigma_{hv}^{inc}(n=2)$	6.89	-0.85	0.00	0.00	0.00
$\sigma_{hv}^{inc}(n=3)$	5.54	-0.59	0.00	0.00	0.00
$\sigma_{hv}^{inc}(n=4)$	4.78	-0.52	0.00	0.00	0.00
$\sigma_{hv}^{inc}(n=5)$	0.33	-0.02	0.00	0.00	0.00

Table A.1: Fitted Associated Legendre Function expansion coefficients for chaff cloud with wire particles of length $l = 0.5\lambda$.

	$c_{00} \times 10^6$	$c_{10} \times 10^6$	$c_{20} \times 10^6$	$c_{30} \times 10^6$	$c_{40} \times 10^6$
$\sigma_{vv}^{inc}(n=0)$	2.05	-0.22	1.57	-0.53	0.00
$\sigma_{vv}^{inc}(n=1)$	4.45	-0.49	2.55	-0.64	0.00
$\sigma_{vv}^{inc}(n=2)$	3.67	-0.43	1.69	-0.36	0.00
$\sigma_{vv}^{inc}(n=3)$	3.27	-0.32	1.15	-0.47	0.00
$\sigma_{vv}^{inc}(n=4)$	3.07	-0.35	0.82	0.00	0.00
$\sigma_{vv}^{inc}(n=5)$	2.88	-0.17	0.56	0.00	0.00
$\sigma_{hv}^{inc}(n=0)$	3.82	-0.56	0.00	0.00	0.00
$\sigma_{hv}^{inc}(n=1)$	7.46	-1.12	0.00	0.00	0.00
$\sigma_{hv}^{inc}(n=2)$	5.49	-0.88	0.00	0.00	0.00
$\sigma_{hv}^{inc}(n=3)$	4.40	-0.68	0.00	0.00	0.00
$\sigma_{hv}^{inc}(n=4)$	3.90	-0.48	0.00	0.00	0.00
$\sigma_{hv}^{inc}(n=5)$	0.28	-0.04	0.00	0.00	0.00

Table A.2: Fitted Associated Legendre Function expansion coefficients for chaff cloud with wire particles of length $l = 0.6\lambda$.

	$c_{00} \times 10^6$	$c_{10} \times 10^6$	$c_{20} \times 10^6$	$c_{30} \times 10^6$	$c_{40} \times 10^6$
$\sigma_{vv}^{inc}(n=0)$	1.84	-0.22	1.40	-0.80	0.00
$\sigma_{vv}^{inc}(n=1)$	3.26	-0.26	1.97	-0.91	0.00
$\sigma_{vv}^{inc}(n=2)$	2.72	-0.38	1.34	-0.72	0.00
$\sigma_{vv}^{inc}(n=3)$	2.43	-0.23	0.99	-0.63	0.00
$\sigma_{vv}^{inc}(n=4)$	2.25	-0.29	0.71	-0.44	0.00
$\sigma_{vv}^{inc}(n=5)$	2.17	-0.20	0.56	-0.41	0.00
$\sigma_{hv}^{inc}(n=0)$	3.41	-0.87	0.00	0.00	0.00
$\sigma_{hv}^{inc}(n=1)$	5.44	-1.34	0.00	0.00	0.00
$\sigma_{hv}^{inc}(n=2)$	4.24	-1.02	0.00	0.00	0.00
$\sigma_{hv}^{inc}(n=3)$	3.54	-0.88	0.00	0.00	0.00
$\sigma_{hv}^{inc}(n=4)$	3.06	-0.68	0.00	0.00	0.00
$\sigma_{hv}^{inc}(n=5)$	0.22	-0.05	0.00	0.00	0.00

Table A.3: Fitted Associated Legendre Function expansion coefficients for chaff cloud with wire particles of length $l = 0.7\lambda$.

	$c_{00} \times 10^6$	$c_{10} \times 10^6$	$c_{20} \times 10^6$	$c_{30} \times 10^6$	$c_{40} \times 10^6$
$\sigma_{vv}^{inc}(n=0)$	2.55	-0.21	1.26	-1.14	0.81
$\sigma_{vv}^{inc}(n=1)$	4.43	-0.39	1.10	-1.22	1.35
$\sigma_{vv}^{inc}(n=2)$	3.65	-0.39	0.90	-0.75	0.93
$\sigma_{vv}^{inc}(n=3)$	3.28	-0.28	0.66	-0.65	0.73
$\sigma_{vv}^{inc}(n=4)$	3.09	-0.30	0.42	-0.44	0.57
$\sigma_{vv}^{inc}(n=5)$	2.88	-0.19	0.32	-0.31	0.45
$\sigma_{hv}^{inc}(n=0)$	4.27	-1.20	0.00	0.00	0.00
$\sigma_{hv}^{inc}(n=1)$	6.21	-1.55	0.00	0.00	0.00
$\sigma_{hv}^{inc}(n=2)$	4.84	-1.27	0.72	0.00	0.00
$\sigma_{hv}^{inc}(n=3)$	4.08	-0.95	0.51	0.00	0.00
$\sigma_{hv}^{inc}(n=4)$	3.58	-0.74	0.42	0.00	0.00
$\sigma_{hv}^{inc}(n=5)$	0.25	-0.06	0.03	0.00	0.00

Table A.4: Fitted Associated Legendre Function expansion coefficients for chaff cloud with wire particles of length $l = 0.8\lambda$.

	$c_{00} \times 10^6$	$c_{10} \times 10^6$	$c_{20} \times 10^6$	$c_{30} \times 10^6$	$c_{40} \times 10^6$
$\sigma_{vv}^{inc}(n=0)$	7.49	-0.48	-0.93	0.73	3.82
$\sigma_{vv}^{inc}(n=1)$	7.11	-0.14	-0.29	0.44	2.93
$\sigma_{vv}^{inc}(n=2)$	5.61	-0.33	-0.25	0.21	1.59
$\sigma_{vv}^{inc}(n=3)$	4.81	-0.30	-0.15	0.05	1.14
$\sigma_{vv}^{inc}(n=4)$	4.29	-0.12	-0.23	0.01	0.67
$\sigma_{vv}^{inc}(n=5)$	3.95	0.00	0.00	0.00	0.00
$\sigma_{hv}^{inc}(n=0)$	8.98	1.12	2.13	-1.14	-0.91
$\sigma_{hv}^{inc}(n=1)$	7.83	0.44	1.52	0.00	0.00
$\sigma_{hv}^{inc}(n=2)$	5.67	0.08	1.19	0.00	0.00
$\sigma_{hv}^{inc}(n=3)$	4.64	-0.08	1.00	0.00	0.00
$\sigma_{hv}^{inc}(n=4)$	4.02	-0.04	0.69	0.00	0.00
$\sigma_{hv}^{inc}(n=5)$	0.28	-0.00	0.05	0.00	0.00

Table A.5: Fitted Associated Legendre Function expansion coefficients for chaff cloud with wire particles of length $l = 0.9\lambda$.

	$c_{00} \times 10^6$	$c_{10} \times 10^6$	$c_{20} \times 10^6$	$c_{30} \times 10^6$	$c_{40} \times 10^6$
$\sigma_{vv}^{inc}(n=0)$	7.23	-0.90	-0.54	4.78	3.01
$\sigma_{vv}^{inc}(n=1)$	6.57	-0.55	-0.44	2.49	2.19
$\sigma_{vv}^{inc}(n=2)$	5.31	-0.40	-0.46	1.57	1.63
$\sigma_{vv}^{inc}(n=3)$	4.59	-0.33	-0.22	0.98	0.95
$\sigma_{vv}^{inc}(n=4)$	4.15	-0.29	-0.19	0.69	0.70
$\sigma_{vv}^{inc}(n=5)$	3.83	-0.30	-0.16	0.58	0.53
$\sigma_{hv}^{inc}(n=0)$	9.36	5.14	1.55	-1.50	-1.30
$\sigma_{hv}^{inc}(n=1)$	7.38	2.58	1.35	-0.76	0.00
$\sigma_{hv}^{inc}(n=2)$	5.55	1.22	0.89	0.00	0.00
$\sigma_{hv}^{inc}(n=3)$	4.59	0.82	0.79	0.00	0.00
$\sigma_{hv}^{inc}(n=4)$	4.03	0.65	0.72	0.00	0.00
$\sigma_{hv}^{inc}(n=5)$	0.29	0.04	0.05	0.00	0.00

Table A.6: Fitted Associated Legendre Function expansion coefficients for chaff cloud with wire particles of length $l = 1.0\lambda$.

	$c_{00} \times 10^6$	$c_{10} \times 10^6$	$c_{20} \times 10^6$	$c_{30} \times 10^6$	$c_{40} \times 10^6$
$\sigma_{vv}^{inc}(n=0)$	4.64	-0.91	0.04	3.69	1.63
$\sigma_{vv}^{inc}(n=1)$	4.61	-0.67	0.28	2.56	1.43
$\sigma_{vv}^{inc}(n=2)$	3.92	-0.45	0.10	1.80	1.80
$\sigma_{vv}^{inc}(n=3)$	3.33	-0.45	0.03	1.39	0.57
$\sigma_{vv}^{inc}(n=4)$	3.04	-0.38	-0.02	1.07	0.47
$\sigma_{vv}^{inc}(n=5)$	2.86	-0.30	0.07	0.69	0.35
$\sigma_{hv}^{inc}(n=0)$	6.26	3.20	0.50	-0.78	-0.65
$\sigma_{hv}^{inc}(n=1)$	5.63	2.14	0.78	0.00	0.00
$\sigma_{hv}^{inc}(n=2)$	4.41	1.46	0.45	0.00	0.00
$\sigma_{hv}^{inc}(n=3)$	3.64	0.97	0.46	0.00	0.00
$\sigma_{hv}^{inc}(n=4)$	3.24	0.69	0.35	0.00	0.00
$\sigma_{hv}^{inc}(n=5)$	0.23	0.04	0.02	0.00	0.00

Table A.7: Fitted Associated Legendre Function expansion coefficients for chaff cloud with wire particles of length $l = 1.1\lambda$.

	$c_{00} \times 10^6$	$c_{10} \times 10^6$	$c_{20} \times 10^6$	$c_{30} \times 10^6$	$c_{40} \times 10^6$
$\sigma_{vv}^{inc}(n=0)$	4.01	-1.07	0.25	3.38	0.98
$\sigma_{vv}^{inc}(n=1)$	4.20	-0.79	0.75	2.70	0.95
$\sigma_{vv}^{inc}(n=2)$	3.57	-0.58	0.49	1.80	0.58
$\sigma_{vv}^{inc}(n=3)$	3.13	-0.64	0.28	1.39	0.42
$\sigma_{vv}^{inc}(n=4)$	2.85	-0.50	0.20	0.97	0.27
$\sigma_{vv}^{inc}(n=5)$	2.64	-0.45	0.13	0.78	0.20
$\sigma_{hv}^{inc}(n=0)$	5.39	2.40	0.52	-0.66	0.00
$\sigma_{hv}^{inc}(n=1)$	5.28	1.89	0.62	0.00	0.00
$\sigma_{hv}^{inc}(n=2)$	4.26	1.16	0.41	0.00	0.00
$\sigma_{hv}^{inc}(n=3)$	3.59	0.86	0.41	0.00	0.00
$\sigma_{hv}^{inc}(n=4)$	3.15	0.50	0.30	0.00	0.00
$\sigma_{hv}^{inc}(n=5)$	0.22	0.03	0.02	0.00	0.00

Table A.8: Fitted Associated Legendre Function expansion coefficients for chaff cloud with wire particles of length $l = 1.2\lambda$.

	$c_{00} \times 10^6$	$c_{10} \times 10^6$	$c_{20} \times 10^6$	$c_{30} \times 10^6$	$c_{40} \times 10^6$
$\sigma_{vv}^{inc}(n=0)$	5.02	-1.27	0.82	3.11	0.27
$\sigma_{vv}^{inc}(n=1)$	4.52	-0.81	0.49	1.93	0.66
$\sigma_{vv}^{inc}(n=2)$	3.71	-0.67	0.32	1.08	0.48
$\sigma_{vv}^{inc}(n=3)$	3.27	-0.58	0.15	0.83	0.35
$\sigma_{vv}^{inc}(n=4)$	2.89	-0.54	0.19	0.66	0.21
$\sigma_{vv}^{inc}(n=5)$	2.68	-0.46	0.12	0.41	0.18
$\sigma_{hv}^{inc}(n=0)$	6.57	2.17	0.82	-0.59	0.00
$\sigma_{hv}^{inc}(n=1)$	5.16	1.26	0.82	-0.50	0.00
$\sigma_{hv}^{inc}(n=2)$	4.09	0.72	0.76	-0.36	0.00
$\sigma_{hv}^{inc}(n=3)$	3.45	0.36	0.60	-0.21	0.00
$\sigma_{hv}^{inc}(n=4)$	2.97	0.19	0.52	0.00	0.00
$\sigma_{hv}^{inc}(n=5)$	0.21	0.01	0.04	-0.02	0.00

Table A.9: Fitted Associated Legendre Function expansion coefficients for chaff cloud with wire particles of length $l = 1.3\lambda$.

	$c_{00} \times 10^6$	$c_{10} \times 10^6$	$c_{20} \times 10^6$	$c_{30} \times 10^6$	$c_{40} \times 10^6$
$\sigma_{vv}^{inc}(n=0)$	9.28	0.00	-1.33	2.08	2.85
$\sigma_{vv}^{inc}(n=1)$	6.60	-0.20	-0.38	0.98	1.96
$\sigma_{vv}^{inc}(n=2)$	5.03	-0.27	-0.14	0.34	1.11
$\sigma_{vv}^{inc}(n=3)$	4.26	-0.38	-0.13	0.31	0.73
$\sigma_{vv}^{inc}(n=4)$	3.73	-0.34	-0.08	0.08	0.63
$\sigma_{vv}^{inc}(n=5)$	3.30	-0.39	-0.01	0.07	0.40
$\sigma_{hv}^{inc}(n=0)$	10.07	4.02	4.71	-0.94	0.32
$\sigma_{hv}^{inc}(n=1)$	6.89	1.91	2.45	-0.29	0.61
$\sigma_{hv}^{inc}(n=2)$	5.12	0.87	1.61	-0.30	0.00
$\sigma_{hv}^{inc}(n=3)$	4.15	0.32	1.17	0.00	0.00
$\sigma_{hv}^{inc}(n=4)$	3.54	0.16	0.85	-0.01	0.00
$\sigma_{hv}^{inc}(n=5)$	0.25	0.00	0.06	-0.02	0.00

Table A.10: Fitted Associated Legendre Function expansion coefficients for chaff cloud with wire particles of length $l = 1.4\lambda$.

	$c_{00} \times 10^6$	$c_{10} \times 10^6$	$c_{20} \times 10^6$	$c_{30} \times 10^6$	$c_{40} \times 10^6$
$\sigma_{vv}^{inc}(n=0)$	8.76	0.38	-1.56	2.4548	4.2746
$\sigma_{vv}^{inc}(n=1)$	6.52	-0.10	-0.38	1.0009	2.2819
$\sigma_{vv}^{inc}(n=2)$	5.13	-0.12	-0.33	0.4293	1.3181
$\sigma_{vv}^{inc}(n=3)$	4.44	-0.18	-0.25	0.33647	0.73279
$\sigma_{vv}^{inc}(n=4)$	3.97	-0.07	-0.28	0.082881	0.66907
$\sigma_{vv}^{inc}(n=5)$	3.59	-0.04	-0.12	0.1175	0.38568
$\sigma_{hv}^{inc}(n=0)$	10.17	5.54	4.83	-0.81534	-0.36403
$\sigma_{hv}^{inc}(n=1)$	7.17	2.30	2.69	-0.19557	0
$\sigma_{hv}^{inc}(n=2)$	5.10	1.02	1.56	-0.32908	0
$\sigma_{hv}^{inc}(n=3)$	4.20	0.47	1.06	0	0
$\sigma_{hv}^{inc}(n=4)$	3.59	0.37	0.87	0	0
$\sigma_{hv}^{inc}(n=5)$	0.25	0.02	0.07	0	0

Table A.11: Fitted Associated Legendre Function expansion coefficients for chaff cloud with wire particles of length $l = 1.5\lambda$.

	$c_{00} \times 10^6$	$c_{10} \times 10^6$	$c_{20} \times 10^6$	$c_{30} \times 10^6$	$c_{40} \times 10^6$
$\sigma_{vv}^{inc}(n=0)$	8.40	0.19	-1.96	2.95	4.73
$\sigma_{vv}^{inc}(n=1)$	6.07	-0.08	-0.25	1.30	2.44
$\sigma_{vv}^{inc}(n=2)$	4.80	-0.14	-0.31	0.57	1.33
$\sigma_{vv}^{inc}(n=3)$	4.11	-0.17	-0.19	0.36	0.88
$\sigma_{vv}^{inc}(n=4)$	3.71	-0.15	-0.21	0.17	0.68
$\sigma_{vv}^{inc}(n=5)$	3.13	-0.16	-0.24	0.15	2.56
$\sigma_{hv}^{inc}(n=0)$	9.34	5.37	5.17	-0.58	-0.29
$\sigma_{hv}^{inc}(n=1)$	6.90	2.48	2.37	-0.16	0.00
$\sigma_{hv}^{inc}(n=2)$	5.00	1.07	1.42	0.00	0.00
$\sigma_{hv}^{inc}(n=3)$	4.09	0.66	1.09	0.00	0.00
$\sigma_{hv}^{inc}(n=4)$	3.49	0.39	0.82	0.00	0.00
$\sigma_{hv}^{inc}(n=5)$	0.23	0.09	0.17	0.00	0.00

Table A.12: Fitted Associated Legendre Function expansion coefficients for chaff cloud with wire particles of length $l = 1.6\lambda$.

	$c_{00} \times 10^6$	$c_{10} \times 10^6$	$c_{20} \times 10^6$	$c_{30} \times 10^6$	$c_{40} \times 10^6$
$\sigma_{vv}^{inc}(n=0)$	8.26	-0.22	-1.50	3.03	4.34
$\sigma_{vv}^{inc}(n=1)$	5.82	-0.27	-0.29	1.41	2.28
$\sigma_{vv}^{inc}(n=2)$	4.52	-0.28	-0.17	0.63	1.24
$\sigma_{vv}^{inc}(n=3)$	3.89	-0.25	-0.13	0.42	0.85
$\sigma_{vv}^{inc}(n=4)$	3.50	-0.24	-0.17	0.24	0.65
$\sigma_{vv}^{inc}(n=5)$	3.15	-0.21	-0.06	0.20	0.38
$\sigma_{hv}^{inc}(n=0)$	10.03	4.81	5.41	-0.78	-0.23
$\sigma_{hv}^{inc}(n=1)$	6.67	2.23	2.30	0.00	0.00
$\sigma_{hv}^{inc}(n=2)$	4.80	1.01	1.44	0.00	0.00
$\sigma_{hv}^{inc}(n=3)$	3.87	0.55	1.02	0.00	0.00
$\sigma_{hv}^{inc}(n=4)$	3.35	0.32	0.78	0.00	0.00
$\sigma_{hv}^{inc}(n=5)$	0.23	0.02	0.05	0.00	0.00

Table A.13: Fitted Associated Legendre Function expansion coefficients for chaff cloud with wire particles of length $l = 1.7\lambda$.

	$c_{00} \times 10^6$	$c_{10} \times 10^6$	$c_{20} \times 10^6$	$c_{30} \times 10^6$	$c_{40} \times 10^6$
$\sigma_{vv}^{inc}(n=0)$	8.91	-0.27	-1.51	3.09	3.47
$\sigma_{vv}^{inc}(n=1)$	6.10	-0.25	-0.10	1.23	2.03
$\sigma_{vv}^{inc}(n=2)$	4.78	-0.42	-0.12	0.58	1.08
$\sigma_{vv}^{inc}(n=3)$	4.05	-0.38	-0.05	0.35	0.71
$\sigma_{vv}^{inc}(n=4)$	3.57	-0.33	-0.10	0.18	0.54
$\sigma_{vv}^{inc}(n=5)$	3.21	-0.29	-0.05	0.17	0.31
$\sigma_{hv}^{inc}(n=0)$	9.60	4.59	5.25	-0.87	0.05
$\sigma_{hv}^{inc}(n=1)$	6.83	1.94	2.45	-0.61	0.00
$\sigma_{hv}^{inc}(n=2)$	4.90	0.81	1.46	-0.35	0.00
$\sigma_{hv}^{inc}(n=3)$	3.99	0.31	1.03	-0.26	0.00
$\sigma_{hv}^{inc}(n=4)$	3.38	0.07	0.86	-0.34	0.00
$\sigma_{hv}^{inc}(n=5)$	0.24	0.00	0.06	-0.02	0.00

Table A.14: Fitted Associated Legendre Function expansion coefficients for chaff cloud with wire particles of length $l = 1.8\lambda$.

	$c_{00} \times 10^6$	$c_{10} \times 10^6$	$c_{20} \times 10^6$	$c_{30} \times 10^6$	$c_{40} \times 10^6$
$\sigma_{vv}^{inc}(n=0)$	11.20	0.48	-1.54	1.83	3.38
$\sigma_{vv}^{inc}(n=1)$	6.70	-0.01	-0.04	0.64	1.71
$\sigma_{vv}^{inc}(n=2)$	5.01	-0.38	-0.16	0.32	0.88
$\sigma_{vv}^{inc}(n=3)$	4.13	-0.39	-0.02	0.06	0.57
$\sigma_{vv}^{inc}(n=4)$	3.64	-0.35	-0.10	0.00	0.48
$\sigma_{vv}^{inc}(n=5)$	3.24	-0.32	0.00	0.06	0.22
$\sigma_{hv}^{inc}(n=0)$	12.33	6.48	7.17	-0.23	0.41
$\sigma_{hv}^{inc}(n=1)$	7.01	2.08	2.78	0.00	0.00
$\sigma_{hv}^{inc}(n=2)$	5.00	0.74	1.45	0.00	0.00
$\sigma_{hv}^{inc}(n=3)$	3.97	0.25	1.09	-0.28	0.00
$\sigma_{hv}^{inc}(n=4)$	3.36	0.06	0.83	-0.19	0.00
$\sigma_{hv}^{inc}(n=5)$	0.23	0.00	0.05	-0.01	0.00

Table A.15: Fitted Associated Legendre Function expansion coefficients for chaff cloud with wire particles of length $l = 1.9\lambda$.

	$c_{00} \times 10^6$	$c_{10} \times 10^6$	$c_{20} \times 10^6$	$c_{30} \times 10^6$	$c_{40} \times 10^6$
$\sigma_{vv}^{inc}(n=0)$	11.02	0.83	-1.94	1.07	4.26
$\sigma_{vv}^{inc}(n=1)$	6.34	0.08	-0.18	0.57	2.17
$\sigma_{vv}^{inc}(n=2)$	4.69	-0.30	-0.02	0.15	1.02
$\sigma_{vv}^{inc}(n=3)$	3.86	1.01	2.18	3.11	4.23
$\sigma_{vv}^{inc}(n=4)$	3.34	-0.41	-0.00	-0.10	0.49
$\sigma_{vv}^{inc}(n=5)$	2.93	-0.40	0.01	0.03	0.33
$\sigma_{hv}^{inc}(n=0)$	13.00	8.15	7.08	0.33	-0.35
$\sigma_{hv}^{inc}(n=1)$	6.88	2.42	2.57	0.22	0.76
$\sigma_{hv}^{inc}(n=2)$	4.85	0.87	1.47	-0.08	0.44
$\sigma_{hv}^{inc}(n=3)$	3.84	1.79	3.42	3.37	4.48
$\sigma_{hv}^{inc}(n=4)$	3.21	-0.02	0.67	-0.26	0.00
$\sigma_{hv}^{inc}(n=5)$	0.22	-0.01	0.04	-0.02	0.00

Table A.16: Fitted Associated Legendre Function expansion coefficients for chaff cloud with wire particles of length $l = 2.0\lambda$.

BIBLIOGRAPHY

Abadi, S.H., Song, H.C., & Dowling, D.R. 2011. Broadband sparse-array blind deconvolution using frequency-difference beamforming. *The Journal of the Acoustical Society of America*, **132**, 3018–3029.

Abadi, S.H., Rousseff, D., & Dowling, D.R. 2012. Blind deconvolution for robust signal extimation and approximate source localization. *The Journal of the Acoustical Society of America*, **131**, 2599.

Abadi, S.H., Van Overloop, M.J., & Dowling, D.R. 2013. Frequency-sum beamforming in an inhomogeneous environment. *The Journal of the Acoustical Society of America*, **133**, 3524.

Abadi, S.H., Leckta, D.C., Mercado, K., Haworth, K.J., & Dowling, D.R. 2015. Frequency-sum beamforming in a random scattering environment. *The Journal of the Acoustical Society of America*, **138**, 1925.

Altair Engineering, Inc. 2014. FEKO.

Andrews, L.C., Phillips, R.L., & Weeks, A.R. 1994. Propagation of a Gaussian-beam wave through a random phase screen. *Waves in Random and Complex Media*, **7**, 229–244.

Aravkin, A., Becker, S., Cevher, V., & Olsen, P. 2014. A variational approach to stable principal component pursuit. *UAI Proceedings*.

Baggeroer, A.B., Kuperman, W.A., & Michalevsky, P.N. 1993. An overview of matched field methods in ocean acoustics. *IEEE Journal of Ocean Engineering*, **18**, 401–424.

Bianco, M.J., Gerstoft, P., Traer, J., Ozanich, E., Roch, M.A., Gannot, S., & Deledalle, C. 2019. Machine learning in acoustics: Theory and applications. *The Journal of the Acoustical Society of America*, **146**, 3590–3628.

Birdsall, T.G., & Metzger, K. 1986. Factor inverse matched filtering. *The Journal of the Acoustical Society of America*, **79**, 91–99.

Bishop, R.L., & Goldberg, S.I. 1968. *Tensor Analysis on Manifolds*. Dover.

Blae, W.K., & Chase, D.M. 1971. Wavenumber-frequency spectra of turbulent boundary-later pressure mounted by microphone arrays. *The Journal of the Acoustical Society of America*, **49**, 862–877.

Bohren, C. , & Huffman, D. 1983. *Absorption and Scattering of Light by Small Particles*. Wiley.

Bracewell, R. 1965. *The Fourier Transform and Its Applications*. McGraw-Hill.

Brekhovskikh, L.M., & Lysanov, Y.P. 2003. *Fundamentals of Ocean Acoustics*. Springer-Verlag.

Brown, G.S., & Curry, W.J. 1982. A theory and model for wave propagation through foliage. *Radio Science*, **17**, 1027–1036.

Bucker, H.P. 1976. Use of calculated sound fields and matched-field detection to locate sound sources in shallow water. *The Journal of the Acoustical Society of America*, **59**, 368.

Byun, G., Song, H.C., Kim, J.S., & Park, J.S. 2018. Real-time tracking of a surface ship using a bottom-mounted horizontal array. *The Journal of the Acoustical Society of America*, **144**, 2375–2382.

Cao, R., Yang, K., Ma, Y., Yang, Q., & Shi, Y. 2019. Passive broadband source localization based on a Riemannian distance with a short vertical array in the deep ocean. *The Journal of the Acoustical Society of America*, **145**, EL567–EL573.

Carriere, O., Gerstoft, P., & Hodgkiss, W.S. 2014. Spatial filtering in ambient noise interferometry. *The Journal of the Acoustical Society of America*, **135**, 1186.

Carroll, B.W., Ostlie, D.A. 1996. *An Introduction to Modern Astrophysics*. Addison-Westley.

Chandrasekhar, S. 1960. *Radiative Transfer*. Dover Publications.

Chew, W.C., & Wang, Y.M. 1990. A fast algorithm for solution of a scattering problem using a recursive aggregate T matrix method. *Microwave and Optical Technical Letters*, **3**, 164–169.

Cho, C., & Song, H.C. 2017. Iterative range estimation in a slopingbottom shallow-water waveguide using the generalized array invariant. *The Journal of the Acoustical Society of America*, **142**, 55–60.

Colosi, J., van Uffelen, L.J., Cornuelle, B.D., Dzieciuch, M.A., Worcester, P.F., Dushaw, B.D., & Ramp, S.R. 2013. Observations of sound-speed fluctuations in the western Philippine Sea in the spring of 2009. *The Journal of the Acoustical Society of America*, **54**, 1743–1746.

Colosi, J., Cornuelle, B.D., Dzieciuch, M.A., Worcester, P.F., & Chandrayadula, T.K. 2019. Observations of phase and intensity fluctuations for low-frequency, long-range transmissions in the Philippine Sea and comparisons to path-integral theory. *The Journal of the Acoustical Society of America*, **146**, 567–585.

Cox, H. 1973. Line array performance when the signal coherence is spatially dependent. *The Journal of the Acoustical Society of America*, **54**, 1743–1746.

DeLoor, G. 1953. Method of obtaining information on the internal dielectric constant of mixtures. *Applied Science Res.*, **3**, 479–482.

DiDonato, L., Bevacqua, M.T., Crocco, L., & Isernia, T. 2015. Inverse scattering via virtual experiments and contrast source regularization. *IEEE Transactions on Antennas and Propagation*, **63**, 1667–1677.

Dinsenmeyer, A., Antoni, J., Leclere, Q., & Pereira, A. 2018. On the denoising of cross-spectral matrices for (aero)acoustic applications. *Proceedings of the Berlin Beamforming Conference*.

DLMF. 2021. NIST Digital Library of Mathematical Functions. *National Institute of Standards and Technology*, **1.1.1**.

Dong, H., Chapman, N.R., Hannay, D.E., & Dosso, S.E. 2010. Estimation of seismic velocities of upper oceanic crust from ocean bottom reflection loss data. *The Journal of the Acoustical Society of America*, **127**, 2182.

Dosso, S.E., & Wilmut, M.J. 2012. Maximum-likelihood and other processors for incoherent and coherent matched-field localization. *The Journal of the Acoustical Society of America*, **132**, 2273.

Douglass, A.S., & Dowling, D.R. 2019. Frequency-difference beamforming in the presence of strong random scattering. *The Journal of the Acoustical Society of America*, **146**, 122.

Douglass, A.S., Song, H.C., & Dowling, D.R. 2017. Performance comparisons of frequency-difference and conventional beamforming. *The Journal of the Acoustical Society of America*, **142**, 55–60.

Dowling, D.R., & Sabra, K. 2015. Acoustic remote sensing. *Annual Review of Fluid Mechanics*, **47**, 221–243.

D'Spain, G.L., Williams, D. P., Rovner, G., Kuperman, W. A., & Team, S. 2002. Energy Flow in Interference Fields. *Ocean Acoustic Interference Phenomena and Signal Processing*, **621**, 171–203.

Duda, T. F., Collis, J. M., Lin, Y.T., Newhall, A. E., Lynch, J. F., & DeFerrari, H. A. 2012. Horizontal coherence of low-frequency fixed-path sound in a continental shelf region with internal-wave activity. *The Journal of the Acoustical Society of America*, **131**, 1782–1797.

Dzieciuch, M.A., Skarsoulis, E.K., & Cornuelle, B.D. 2013. Structure and stability of wave-theoretic kernels in the ocean. *The Journal of the Acoustical Society of America*, **134**, 3318.

Fante, R.L. 1975. Electromagnetic Beam Propagation in Turbulent Media. *Proceedings of the IEEE*, **63**, 1669–1692.

Fialkowski, L.T., Perkins, J.S., Collins, M.D., Nicholas, M., Fawcett, J.A., & Kuperman, W.A. 2001. Matched-field source tracking by ambiguity surface averaging. *The Journal of the Acoustical Society of America*, **110**, 739.

Finette, S. 2006. A stochastic representation of environmental uncertainty and its coupling to acoustic wave propagation in ocean waveguides. *The Journal of the Acoustical Society of America*, **120**, 2567.

Finette, S., & Mignerey, P.C. 2018. Stochastic matched-field localization of an acoustic source based on principles of Riemannian geometry. *The Journal of the Acoustical Society of America*, **146**, 3628–3638.

Flatte, S.M., Bernstein, D.R., & Dashen, R. 1983. Intensity moments by path integral techniques for wave propagation through random media, with application to sound in the ocean. *The Journal of Physical Fluids*, **26**, 1701–1713.

Flatte, S.M. 1979. *Sound Transmission through a Fluctuating Ocean*. Cambridge University Press.

Foldy, L.L. 1945. The multiple scattering of waves. *Physical Review*, **67**, 621.

GEBCO, Compilation Group. 2021. Philippine Sea. *GEBCO 2020 Grid*.

Geroski, D.J., & Dowling, D.R. 2019. Long range frequency-difference source localization in the Philippine Sea. *The Journal of the Acoustical Society of America*, **146**, 4727–4739.

Geroski, D.J., & Dowling, D.R. 2021. Robust Long-Range Source Localization in the Deep Ocean Using Phase-Only Matched Autoproduct Processing. *The Journal of the Acoustical Society of America*, **Submitted: 1 February 2021**.

Geroski, D.J., & Sarabandi, K. 2020. Full-wave calculation of complex propagation constant for a medium of conducting wires. *IEEE Transactions on Antennas and Propagation*, **N**, 1–9.

Geroski, D.J., & Sarbandi, K. 2020. Full-wave estimate of the extinction and phase matrices of collections of metallic particles. *IEEE International Symposium on Antennas and Propagation and USNC-URSI Radio Science Meeting*.

Geroski, D.J., & Worthmann, B.M. 2021. Cross-Term Analysis for Improved Dynamic Range of Autoproduct Based Ambiguity Surfaces . *The Journal of the Acoustical Society of America*.

Geroski, D.J., Worthmann, B.M., & Dowling, D.R. 2021a. Localization of a Distant Source in a Noisy Deep Ocean Sound Channel Using Phase-Only Matched Autoproduct Processing. *The Journal of the Acoustical Society of America*, **In Progress**.

Geroski, D.J., Dzieciuch, M.A., & Dowling, D.R. 2021b. Measurements of the correlation of the frequency-difference autoproduct with acoustic and predicted-autoproduct fields in the deep ocean. *The Journal of the Acoustical Society of America*, **149**, 853–865.

Gerstoft, P., and Xenaki A., & Mecklenbauker, C.F. 2015. Multiple and single snapshot compressive beamforming. *The Journal of the Acoustical Society of America*, **138**, 2003.

Gingras, D.F., & Gerr, N.L. 1993. Minimax robust matched-field processing. *The Journal of the Acoustical Society of America*, **93**, 2798–2808.

Greene, C.A., & Moller, R.T. 1962. The effect of normally distributed random phase errors on synthetic array gain patterns. *ITE Transactions on Military Electronics*, **2**, 130–139.

Hald, J. 2017. Removal of incoherent noise from an averaged cross-spectral matrix. *The Journal of the Acoustical Society of America*, **142**, 846–854.

Hald, J. 2019. Denoising of cross-spectral matrices using canonical coherence. *The Journal of the Acoustical Society of America*, **146**, 399–408.

Hamilton, E.L. 1978. Sound velocity-density relations in sea-floor sediments and rocks. *The Journal of the Acoustical Society of America*, **63**, 366.

Han, X., Jin, R., Li, X., & Wang, S. 2014. Soil Moisture Estimation using cosmic-ray soil moisture sensing at heterogeneous farmland. *IEEE Transactions on Geoscience and Remote Sensing*, **11**, 1659–1663.

Harrington, R.F. 1967. Matrix methods for field problems. *Proceedings of the IEEE*, **55**, 136–149.

Heat, Light, & Sound Inc. 2021. Ocean Acoustics Library: Acoustics Toolbox.

Hirota, R. 2004. *The Direct Method in Soliton Theory*. Cambridge University Press.

Huang, H., Tsang, L., Njoku, E.G., Colliander, A., Liao, T., & Ding, K. 2017. Propagation and scattering by a layer of randomly distributed dielectric cylinders using Monte Carlo simulations of 3D Maxwell equations with applications in microwave interactions with vegetation. *IEEE Access*, **5**, 11985–12003.

Hursky, P., Porter, M.B., Siderius, M., & McDonald, V.K. 2004. Highfrequency (8-16 kHz) model-based source localization. *The Journal of the Acoustical Society of America*, **115**, 3021–3032.

Ishimaru, A. 1977. Theory and Application of Wave Propagation and Scattering in Random Media. *Proceedings of the IEEE*, **65**, 1030–1061.

Jackson, J.D. 1999. *Classical Electrodynamics*. J. Wiley Sons.

Jensen, F.B., Kuperman, W.A., Porter, M.B., & Schmidt, H. 2011. *Computational Ocean Acoustics*. American Insitute of Physics.

Jiang, Y., Chapman, N.R., & Badley, M. 2007. Quantifying the uncertainty of geoacoustic parameter estimates for the New Jersey shelf by inverting air gun data. *The Journal of the Acoustical Society of America*, **121**, 1879.

Jin, J. 2010. *Theory and Computation of Electromagnetic Fields*. J. Wiley Sons.

Johnson, J.E., Takenaka, T., & Tanaka, T. 2008. Two-dimensional time-domain inverse scattering for quantitative analysis of breast composition. *IEEE Transactions on Biomedical Engineering*, **55**, 1941–1945.

Kinsler, L.E., Frey, A.R., Coppens, A.B., & Sanders, J.V. 1999. *Fundamentals of Acoustics*. J. Wiley Sons.

Kovesi, P. 2015. Good colour maps: how to design them. *arXiv:1509:03700v1*.

Kratsov, Y.A., & Orlov, Y.I. 1999. *Caustics, Catastrophes and Wave Fields*. Springer.

Krolik, J.L. 1992. Matched-field minimum variance beamforming in a random ocean channel. *The Journal of the Acoustical Society of America*, **92**, 1408–1419.

Lane, R.G., Glindemann, A., & Dainty, J.C. 1992. simulation of a Kolmogorov phase screen. *Waves in Random and Complex Media*, **2**, 209–224.

Lax, M. 1952. Multiple Scattering of Waves. II. The Effective Field in Dense Systems. *Physical Review*, **85**, 621–629.

Lee, S., & Makris, N.C. 2006. The array invariant. *The Journal of the Acoustical Society of America*, **119**, 336–351.

Lewinski, D.J. 1983. Nonstationary Probabalistic Target and Clutter Scattering Models. *IEEE Transactions on Antennas and Propagation*, **31**, 490–498.

Li, E.S., & Sarabandi, K. 1999. Low grazing incidence millimeter-wave scattering models and measurements for various road surfaces. *IEEE Transactions on Antennas and Propagation*, **47**, 851–861.

Lipa, J.E., Worthmann, B.M., & Dowling, D.R. 2018. Measurement of autoproduct fields in a Lloyd's Mirror environment. *The Journal of the Acoustical Society of America*, **143**, 2419.

Lunkov, A.A., & Petnikov, V.G. 2014. The coherence of low-frequency sound in shallow water in the presence of internal waves. *Acoustical Physics*, **60**, 61–71.

Mantzel, W., Romberg, J., & Sabra, K. 2011. Compressive Matched-Field Processing. *arXiv; 1109.0318*.

Maurice, E.W., Jardetzky, W.S., & Press, F. 1957. *Elastic Waves in Layered Media*. McGraw Hill.

McCargar, R., & Lang, R.E. 2020. Out-of-plane enhancement in a discrete random halfspace. *Waves in Random and Complex Media*, 490–498.

McNairn, H., Jackson, T.J., Wiseman, G., Belair, S., Berg, A., Bullock, P., Colliander, A., Cosh, M.H., Kim, S., Magagi, R., Moghaddam, M., Njoku, E.G., Adams, J.R., Homayouni, S., Ojo, E.R., Rowlandson, T.L., Shang, J., Gotta, K., & Hosseini, M. 2015. The Soil Moisture Active Passive Validation Experiment 2012 (SMAPVEX12): Prelaunch Calibration and Validation of the SMAP Soil Moisture Algorithms. *IEEE Transactions on Geoscience and Remote Sensing*, **53**, 2784–2801.

Mookerjee, A., & Dowling, D.R. 2017. Far-field coherent backscatter enhancement from random aggregations of scatterers and comparisons to backscattering from single isolated spheres. *The Journal of the Acoustical Society of America*, **141**, 1214–1225.

Morgan, D.R., & Smith, T.M. 1990. Coherence effects on the detection performance of quadratic array processors, with applications to large-array matched-field beamforming. *The Journal of the Acoustical Society of America*, **87**, 737–747.

Munk, W., Worcester, P., & Wunsch, C. 1995. *Ocean Acoustic Tomography*. Cambridge University Press.

Niu, H., Ozanich, E., & Gerstoft, P. 2017. Ship localization in Santa Barbara Channel using machine learning classifiers. *The Journal of the Acoustical Society of America*, **142**, EL455–EL460.

Oh, Y., & Hong, J. 2007. Moment method/Monte Carlo simulation of the microwave backscatter of wet-land rice fields. *2007 IEEE International Geoscience and Remote Sensing Symposium*, 69–72.

Omar, A.S., & Akhtar, M.J. 2005. A generalized technique for the reconstruction of permittivity profiles with a controllable resolution in an arbitrary coordinate system. *IEEE Transactions on Antennas and Propagation*, **53**, 294–304.

Ozanich, E., Gerstoft, P., Worcester, P.F., Dzieciuch, M.A., & Thode, A. 2017. Eastern Arctic ambient noise on a drifting vertical array. *The Journal of the Acoustical Society of America*, **142**, 1997–2006.

Pierce, A.D. 1994. *Acoustics: An Introduction to Its Physical Principles and Applications*. Springer.

Polder, D., & van Santen, J. 1946. The effective permeability of mixtures of solids. *Physica*, **12**, 1257–1271.

Popstefanija, I., McQueen, D.S., & McIntosh, R.E. 1993. A stepped-frequency delta-K microwave radar for oceanographic studies. *IEEE Transactions on Geoscience and Remote Sensing*, **31**, 681–691.

Porter, M. 1992. The KRAKEN normal mode program. *Defense Technical Information Center*.

Porter, M.B., & Bucker, H.P. 1987. Gaussian beam tracing for computing ocean acoustic fields. *The Journal of the Acoustical Society of America*, **82**, 1349–1359.

Quijano, J.E., & Zurk, L.M. 2017. Beamforming using subspace estimation from a diagonally averaged sample covariance. *The Journal of the Acoustical Society of America*, **142**, 473.

Richardson, A.M., & Nolte, L.W. 1991. A posteriori probability source localization in an uncertain sound speed, deep ocean environmen. *The Journal of the Acoustical Society of America*, **89**, 2280–2284.

Sarabandi, K. 1997. k-radar equivalent of interferometric SAR's: A theoretical study for determination of vegetation height. *IEEE Transactions on Geoscience and Remote Sensing*, **35**, 1267–1276.

Sarabandi, K., & Nashishibi, A. 1996. A novel bistatic scattering matrix measurement technique using a monostatic radar. *IEEE Transactions on Antennas and Propagation*, **44**, 41–50.

Sarabandi, K., & Siqueira, P.R. 1997. Numerical scattering analysis for two-dimensional dense random media: characterization of effective permittivity. *IEEE Transactions on Antennas and Propagation*, **45**, 858–867.

Schmidt, H., Baggeroer, A.B., Kuperman, W.A., & Scheer, E.K. 1990. Environmentally tolerant beamforming for high-resolution matched field processing: Deterministic mismatch. *The Journal of the Acoustical Society of America*, **88**, 1851–1862.

Silva, S., Cunha, S., Matos, A., & Crus, N. 2008. Sub-Band Processing of Synthetic Aperture Sonar Data. *Proceedings of the OCEANS 2008 MTS/IEEE Conference*.

Siqueira, P.R. 1996. Wave Propagation and Scattering in Dense Random Media. *University of Michigan Deep Blue*.

Siqueira, P.R., & Sarabandi, K. 1996. Method of Moments evaluation of the two-dimensional quasi-crystalline approximation. *IEEE Transactions on Antennas and Propagation*, **44**, 1067–1077.

Siqueira, P.R., Sarabandi, K., & Ulaby, F.T. 1994. Numerical simulation of scatterer positions in a very dense media. *IEEE Antennas and Propagation Conference Digest*.

Skarsoulis, E.K., & Cornuelle, B.D. 2004. Travel-time sensitivity kernels in ocean acoustic tomography. *The Journal of the Acoustical Society of America*, **116**, 227.

Skarsoulis, E.K., Cornuelle, B.D., & Dzieciuch, M.A. 2009. Travel-time sensitivity kernels in long-range propagation. *The Journal of the Acoustical Society of America*, **126**, 2223.

Skolnik, M.I. 1980. *Introduction to Radar Systems*. McGraw Hill.

Snieder, R., van Wijk, K., & Haney, M. 2008. The cancellation of spurious arrivals in Green's function extraction and the generalized optical theorem. *Physical Review E*, **78**, 036606.

Soares, C., Siderius, M., & Jesus, S.M. 2002. Source localization in a time-varying ocean waveguide. *The Journal of the Acoustical Society of America*, **112**, 1879–1889.

Song, H.C., de Rosny, J., & Kuperman, W.A. 2003. Improvement in the matched field processing using the CLEAN algorithm. *The Journal of the Acoustical Society of America*, **113**, 1379–1386.

Spiesberger, J.S. 2005. Probability distributions for locations of calling animals, receivers, sound speeds, winds, and data from travel time differences. *The Journal of the Acoustical Society of America*, **118**, 1790–1800.

Stark, H., & Woods, J.W. 1986. *Probability, Random Processes, and Estimation Theory for Engineers*. Prentice-Hall.

Strauss, W.A. 2008. *Partial Differential Equations: An Introduction*. J. Wiley Sons.

Svigelj, J., Michielssen, E., & Mittra, R. 1992. Absorbing Properties of Layers of Stacked Helices. *IEEE Microwave and Guided Wave Letters*, **4**, 495–496.

Tai, C.T. 1993. *Dyadic Green's Functions in Electromagnetic Theory*. IEEE Press.

Tan, S., & Tsang, L. 2017. Scattering of waves by a half-space of periodic scatterers using broadband Green's function. *Optical Letters*, **42**, 4667–4670.

Tan, S., & Tsang, L. 2019. Efficient broadband evaluations of lattice Green's functions via imaginary wavenumber components extractions. *Progress in Electromagnetic Res.*, **164**, 63–74.

Tatarskii, V.I., & Clifford, S.F. 1995. On the Theory of k Radar Observations of Ocean Surface Waves. *IEEE Transactions on Antennas and Propagation*, 843–850.

Tollefsen, D., Gerstoft, P., & Hodgkiss, W.S. 2017. Multiple-array passive acoustic source localization in shallow water. *The Journal of the Acoustical Society of America*, **141**, 1501.

Tolstoy, A. 1989. Sensitivity of matched field processing to sound-speed profile mismatch for verticals arrays in a deep water Pacific environment. *The Journal of the Acoustical Society of America*, **85**, 2394.

Tsang, L., & Ishumaru, A. 1987. Radiative wave equations for vector electromagnetic propagation in dense non-tenuous media. *Journal of Electromagnetic Waves – Applied*, **1**, 59–72.

Tsang, L., & Kong, J.A. 1978. Radiative Transfer Theory for Active Remote Sensing of Half-Space Random Media. *Radio Science*, **13**, 763–773.

Tsang, L., Ding, K.H., Liao, T.H., & Huang, S. 2018. Modeling of scattering in arbitrary-shape waveguides using broadband Green's function with higher order low wavenumber extractions. *IEEE Transactions on Electromagnetic Computation*, **60**, 16–25.

Tucker, J.B., & Wage, K.E. 2019. Performance weighted blending of multiplicative and min processors. *Proceedings of the Meetings on Acoustics*, **36**, 055004.

Ulaby, F.T., & El-Rayes, M.A. 1987. Microwave dielectric spectrum of vegetation – Part II: dual-dispersion model. *IEEE Transactions on Geoscience and Remote Sensing*, **25**, 550–557.

Ulaby, F.T., Whitt, M., & Sarabandi, K. 1990a. AVNA based scatterometers. *IEEE Antennas and Propagation Magazine*, **32**, 6–17.

Ulaby, F.T., Sarabandi, K., McDonald, K., Whitt, M., & Dobson, M.C. 1990b. Michigan microwave canopy scattering model. *International Journal of Remote Sensing*, **11**, 1223–1253.

Ulaby, F.T., Sarabandi, K., & Nashishibi, A. 1992. Statistical properties of the Mueller matrix of distributed targets. *IEEE Proceedings F – Radar and Signal Processing*, **139**, 136–146.

Ulaby, F.T., & Long, D.G. 2014. *Microwave Radar and Radiometric Remote Sensing*. University of Michigan Press.

Urick, R.J. 1976. Multipath propagation and its effects on sonar design and performance in the real ocean. *Proceedings Of ICASSP '76. IEEE International Conference on Acoustics, Speech, and Signal Processing*, April 12–14.

Urick, R.J. 1996. *Principles of Underwater Sound*. Peninsula Publishing.

Usher, T. 1964. Signal detection by arrays in noise fields with local variations. *The Journal of the Acoustical Society of America*, **36**, 1444–1449.

Van Uffelen, L.J, Nosal, E., Howe, B.M., Carter, G.S., Worcester, P.F., Dzieciuch, M.A., Heaney, K.D., Campbell, R.L., & Cross, P.S. 2013. Estimating uncertainty in subsurface glider position using transmissions from fixed acoustic tomography sources. *The Journal of the Acoustical Society of America*, **134**, 3260–3271.

Wan, L., Zhou, J.X., Rogers, P.H., & Knobles, D.P. 2009. Spatial coherence measurements from two L-shape arrays in shallow water. *Acoustical Physics*, **55**, 383–392.

Wang, J.G., Lu, M.Y., & Michielssen, E. 2000. A time-domain volume-integral equation approach for analyzing scattering from 2-D nonlinear objects under TM illumination. *Microwave and Optical Technical Letters*, **26**, 419–423.

Wegert, E. 2012. *Visual Complex Functions: An Introduction with Phase Portraits*. Birkhauser.

Weissman, D. 1973. Two frequency radar interferometry applied to the measurement of ocean wave height. *IEEE Transactions on Antennas and Propagation*, **21**, 649–656.

Westervelt, P.J. 1963. Parametric acoustic array. *The Journal of the Acoustical Society of America*, **35**, 535–537.

Worcester, P.F., Dzieciuch, M.A., van Uffelen, L.J., Rudnick, D.L., Cornuelle, B.D., & Munk, W.H. 2006. The SPICEX (Spice Experiment) component of the 2004 North Pacific Acoustic Library (NPAL) experiment: An Overview. *The Journal of the Acoustical Society of America*, **120**, 3020.

Worcester, P.F., Dzieciuch, M.A., Mercer, J.A., Andrew, R.K., DuShaw, B.D., Baggeroer, A.B., Heaney, K.D., D'Spain, G.L., Colosi, J.A., Stephen, R.A., Kemp, J.N., Howe, B.M., Van Uffelen, L.J., & Wage, K.E. 2013. The North Pacific Acoustic Laboratory deep-water acoustic propagation experiments in the Philippine Sea. *The Journal of the Acoustical Society of America*, **134**, 3359–3375.

Worthmann, B.M., & Dowling, D.R. 2017. The frequency-difference and frequency-sum acoustic-field autoproducts. *The Journal of the Acoustical Society of America*, **141**, 4579.

Worthmann, B.M., & Dowling, D.R. 2020a. Autoproducts in and near acoustic shadow zones created by barriers. *The Journal of the Acoustical Society of America*, **147**, 1863.

Worthmann, B.M., & Dowling, D.R. 2020b. The effects of refraction and caustics on autoproducts. *The Journal of the Acoustical Society of America*, **147**, 1955.

Worthmann, B.M., Song, H.C., & Dowling, D.R. 2015. High frequency source localization in a shallow ocean using frequency-difference matched field processing. *The Journal of the Acoustical Society of America*, **138**, 3549.

Worthmann, B.M., Song, H.C., & Dowling, D.R. 2017. Adaptive frequency-difference matched field processing for high frequency source localization in a noisy shallow ocean. *The Journal of the Acoustical Society of America*, **141**, 543–556.

Wright, J.A., Ganesh, A., Rao, S., Peng, Y., & Ma, Y. 2009. Robust principal component analysis: Exact recovery of corrupted low-rank matrices via convex optimization. *NIPS'09: Proceedings of the 22nd International Conference on Neural Information Processing Systems*, **22**, 2080–2088.

Wu, M., Barmin, M. P., Andrew, R. K., Weichman, P. B., White, A. W., Lavely, E. M., Dzieciuch, M. A., Mercer, J. A., Worcester, P. F., & Ritzwoller, M. H. 2019. Deep water acoustic range estimation based on an ocean general circulation model: Application to PhilSea10 data. *The Journal of the Acoustical Society of America*, **146**, 4754–4773.

Xie, L, Sun, C., & Tian, J. 2020. Deconvolved frequency-difference beamforming for a linear array. *The Journal of the Acoustical Society of America*, **148**, EL440.

Yang, T.C. 1990. Effectiveness of mode filtering: A comparison of matched-field and matched-mode processing. *The Journal of the Acoustical Society of America*, **87**, 20472–2084.

Yin, C., & Bo, Y. 2014. An improved model for computing the scattering amplitude coefficient of the chaff cloud. *IEEE Workshop on Advanced Research and Technology (WARTIA)*, 1371–1374.

Zeng, Y., Li, J., Liu, Q., Huete, A.R., Xu, B., Yin, G., Fan, W., Ouyang, Y., Yan, K., Hao, D., & Chen, M. 2020. A Radiative Transfer Model for Patch Landscapes Based on Stochastic Radiative Transfer Theory. *IEEE Transactions on Geoscience and Remote Sensing*, **49**, 988–1000.

Zhang, K., & Gasiewski, A.J. 2020. Fast 3-D inhomogeneous radiative transfer model using a planar-stratified forward algorithm and horizontal perturbation series. *IEEE Transactions on Geoscience and Remote Sensing*, **58**, 6861–6873.

Zhang, L., & Wu, Z. 2019. Simulation of full-polarization electromagnetic backscattering characteristics of large number of high-density chaff clouds. *2019 Crs. Strt. Quad-Reg. Rad. Sci. and Wireless Tech. Conf*, 1–3.

Zhuravlev, V., Kobozev, I., & Kravtsov, Y. 1989. Dislocations of a phase front in an ocean waveguide and their manifestation in acoustic measurements. *Soviet Physics Acoustics-Ussr*, **35**, 156–159.